Full analysis of the background for the search of neutrinoless double beta decay in GERDA

DISSERTATION

der Mathematisch-Naturwissenschaftlichen Fakultät
der Eberhard Karls Universität Tübingen
zur Erlangung des Grades eines
Doktors der Naturwissenschaften
(Dr. rer. nat.)

vorgelegt von
ANN-KATHRIN SCHÜTZ
aus Pforzheim

Tübingen
2019

Gedruckt mit Genehmigung der Mathematisch-Naturwissenschaftlichen Fakultät der
Eberhard Karls Universität Tübingen.

Tag der mündlichen Qualifikation:	07.11.2019
Dekan:	Prof. Dr. Wolfgang Rosenstiel
1. Berichterstatter:	Prof. Dr. Peter Grabmayr
2. Berichterstatter:	Prof. Dr. Josef Jochum

Abstract

The GERmanium Detector Array (GERDA) experiment aims for the discovery of neutrinoless double beta decay ($0\nu\beta\beta$) decay in ^{76}Ge. The second phase (Phase II) of GERDA started data taking in Dec 2015 with the design goal of increasing the sensitivity to $T^{0\nu}_{1/2} = O\left(10^{26}\right)$ yr by reducing the background by one order of magnitude. To achieve the target background level, a multitude of supplementary background suppression techniques have been applied in Phase II. Such techniques can only be built on the knowledge and estimation of the background sources observed in the energy spectrum. In this work, a full analysis of the background is presented where all available information on the background has been incorporated in order to develop a detailed background model describing the decomposition of the measured energy spectrum. For the first time, the single- and two-detector data have been combined in a multivariate Bayesian fit approach. Additionally, the background model focuses further on two prominent features in the energy spectrum: the α events dominating the high energy part of the spectrum and the count rates of the potassium γ lines at 1525 keV and 1461 keV. Thanks to the modularity of the detector array, a study of the coincident events in the two-detector data which can provide further information regarding the location of contaminations has been integrated. Using the background model, important information on the main sources and their locations contributing to the background around the Q-value of the decay ($Q_{\beta\beta}$) can be deduced. Besides, the spectral shape of the total background around $Q_{\beta\beta}$ can be extracted. Both are crucial inputs for reliable results on the ^{76}Ge $0\nu\beta\beta$ signal search. According to the background model, the main background contributions around $Q_{\beta\beta}$ come from ^{42}K, energy-degraded α decays from ^{210}Po, ^{228}Th, ^{214}Bi and ^{60}Co, with fractions depending on the assumed source locations. Furthermore, the reconstruction of the different processes due to the individual contributions in the energy spectrum provides many interesting physics results. A direct outcome of this work is the determination of the half-life of the two-neutrino accompanied double beta decay which has been determined as $T^{2\nu}_{1/2} = (2.03 \pm 0.11) \cdot 10^{21}$ yr. This result is in good agreement with the result obtained in Phase I.

Zusammenfassung

Das GERmanium Detector Array (GERDA) Experiment strebt danach den neutrinolosen Doppelbetazerfall in ^{76}Ge zu entdecken. Die Datennahme der zweiten Phase von GERDA startete im Dezember 2015 mit dem Ziel, den Untergrund um eine Größenordnung zu reduzieren, um die Sensitivität auf $T^{0\nu}_{1/2} = O\left(10^{26}\right)$ yr zu erhöhen. Um das vorgenommene Untergrundniveau zu erreichen, wurden eine Vielzahl von ergänzenden Untergrundunterdrückungsmethoden angewendet. Diese Methoden konnten nur auf der Grundlage des Verständnisses und der Bewertung der beobachteten Untergrundquellen im gemessenen Energiespektrum entwickelt werden. In dieser Arbeit wird eine umfassende Analyse des Untergrunds präsentiert, welche alle zur Verfügung stehenden Informationen über den Untergrund einbindet. Dabei wurde ein detailliertes Untergrundmodell entwickelt, welches die Zusammensetzung des gemessenen Energiespektrums beschreibt. Erstmals wurden die Daten von Detektor-anti-koinzidenter Ereignissen in einem Multivariaten Bayesian-Fit-Anstatz mit den Daten von Detektor-koinzidenter Ereignisse kombiniert. Außerdem richtet das Untergrundmodell zusätzlichen seinen Schwerpunkt auf zwei Besonderheiten im Energiespektrum: die α-Ereignisse, die den hochenergetischen Teil des Spektrums dominieren, und die Zählraten der Kalium γ-Linien bei 1525 keV und 1461 keV. Durch die Modularität der Detektoranordnung konnte die Untersuchung der koinzidenten Ereignisse in den zwei-Detektor Daten integriert werden, welche weitere Erkenntnisse in Anbetracht auf mögliche Kontaminationsquellen liefert. Mithilfe des Untergrundmodells können wichtige Informationen im Hinblick auf die dominierenden Quellen, welche zum Untergrund um den Q-Wert des Zerfalls beitragen, abgeleitet werden. Zudem kann die spektrale Form des Gesamtuntergrunds extrahiert werden. Beides sind essenzielle Informationen um zuverlässige Ergebnisse für die Suche des neutrinolosen Doppelbetazerfalls. Gemäß dem Untergrundmodell sind die dominierenden Beiträge um den Q-Wert α Zerfällen von ^{210}Po und aus der ^{226}Ra Zerfallsreihe, sowohl β und γ Zerfälle von ^{42}K, ^{228}Th, ^{214}Bi und ^{60}Co zuzuschreiben. Hierbei hängen deren Anteile vom angenommenen Ort der Entstehung ab. Zusätzlich liefert die Rekonstruktion der unterschiedlichen Prozesse der einzelnen Beträge im Energiespektrum interessante Physik. Ein direkt ableitbares Ergebnis ist die Bestimmung der Halbwertszeit des zwei-Neutrino-behafteten Doppeltenbetazerfalls in ^{76}Ge. Es wurde eine Halbwertszeit von $T^{2\nu}_{1/2} = (2.03 \pm 0.11) \cdot 10^{21}$ yr bestimmt, welche konsistent mit den Ergebnissen aus Phase I ist.

Table of contents

Introduction **xi**

1 Theoretical and experimental aspects of neutrinoless double beta decay **1**

1.1 Neutrinos as a window to physics beyond the Standard Model 1

1.1.1 Massive neutrinos and the Standard Model 3

1.1.2 Dirac and Majorana neutrinos 7

1.2 Search for neutrinoless double beta decay 10

1.2.1 General properties of double beta decay 11

1.2.2 Half-life of neutrinoless double beta decay 12

1.3 Experimental aspects of $0\nu\beta\beta$ decay search 18

1.3.1 Detection and experimental constraints of $0\nu\beta\beta$ decay search . . . 19

1.3.2 Experimental approaches of $0\nu\beta\beta$ decay search 20

1.4 Results on ^{76}Ge $0\nu\beta\beta$ signal search 23

2 The germanium detector array: Physics goals and design **27**

2.1 The GERDA experiment: Phase I and Phase II goals 27

2.2 The GERDA experimental design 29

2.3 Germanium detectors 31

2.3.1 Semiconductor properties 31

2.3.2 Particle interactions in germanium 33

2.3.3 Signal formation of germanium semiconductors 35

2.3.4 High purity germanium detector types 37

3 GERDA Phase II background reduction strategies 41

3.1 GERDA Phase II background sources and contributions 41

3.2 GERDA Phase II background reduction strategies 49

3.2.1 Screening measurements 49

3.2.2 Detector anti-coincidences 50

3.2.3 Muon veto 50

3.2.4 LAr veto 52

3.2.5 Pulse shape discrimination 54

3.3 Phase II background contributions after analysis cuts 59

4 Monte Carlo Simulation of the GERDA Experiment 61

4.1 Monte Carlo simulations and probability density functions 61

4.2 Monte Carlo event processing 65

4.3 Simulated background sources 68

4.4 Conclusion 78

5 Background model of the GERDA Phase II energy spectrum 81

5.1 Statistical analysis method 82

5.1.1 The Bayesian approach 82

5.1.2 Prior probability distribution 85

5.1.3 Parameter estimate 87

5.1.4 Goodness-of-fit and model comparison 88

5.2 Modeling of the high energy region (α-model) 90

5.3 Modeling of the potassium γ lines (K-model) 93

5.4 Global background model (global model) 95

5.5 Background prediction at $Q_{\beta\beta}$ 103

5.6 Stability of the background model 106

5.7 Conclusion 112

6 Measurement of the 2νββ half-life of ^{76}Ge 115

6.1 Result on the 2νββ half-life of ^{76}Ge 116

6.2 Systematic uncertainties 117

6.3 Discussion 119

7 Conclusion and outlook 123

List of figures 127

List of tables 133

Appendix A 135

A.1 My Contribution 135

Appendix B 137

B.1 GERDA Phase II screening measurement results 137

B.2 Decay scheme 138

B.3 GERDA Phase II detector parameters 141

B.4 Global model 142

B.4.1 Parameter correlations 142

B.4.2 Background composition at $Q_{\beta\beta}$ 143

B.5 Statistical Methods 143

B.5.1 Count rate analysis 143

References 145

Introduction

The neutrinoless double beta ($0\nu\beta\beta$) decay is presently the only feasible way to establish the Majorana nature of neutrinos which would imply that neutrinos are their own anti-particles. Therefore, experiments searching for $0\nu\beta\beta$ decay turned into a key probe of physics beyond the Standard Model of particle physics, since it is known that neutrinos have mass. Being a lepton number violation process, the observation of $0\nu\beta\beta$ decay would support extensions of the Standard Model of particles physics which try to explain the dominance of baryonic matter over anti-matter in our universe. One experiment searching for $0\nu\beta\beta$ decay in ^{76}Ge is the GERmanium Detector Array (GERDA) experiment located at the Laboratori Nazionali del Gran Sasso in Italy. GERDA uses high-purity Germanium detectors enriched in the isotope ^{76}Ge, which are directly immersed into liquid argon. In the second phase of GERDA (Phase II), the radio-pure cryogenic liquid acts not only as cooling medium for the detectors and passive shielding but also as active shielding.

Although the $0\nu\beta\beta$ decay has a clear signature due to the expected monochromatic peak at the Q-value of the decay ($Q_{\beta\beta}$), $0\nu\beta\beta$ decay is a rare second order process. The search relies on a rare peak in presence of background events in the same energy region. Obviously, each source producing a similar energy deposition increases the background level which must be kept as low as possible to fully reach the maximum sensitivity. In addition, the aim of a high sensitivity requires a large mass and a long time of data taking while keeping energy resolution and background reduction as high as possible. In order to further optimize the signal-to-background ratio in the energy region of interest (ROI), a multitude of supplementary background reduction techniques were applied in Phase II.

Thanks to the increased detector mass, a more strict radio-purity material selection criteria and the active background suppression techniques, the background level of a few counts/(ROI·ton·yr) has been reached in Phase II. This made GERDA the first $0\nu\beta\beta$ experiment being "background-free" up to its design exposure of 100 kg·yr. However, background reduction techniques can only be built on the knowledge and estimation of the present background sources observed in the energy spectrum. In this dissertation, a background model based on Monte Carlo simulations has been developed to identify and quantify the main background contributions which compose the shape of the measured energy spectra at $Q_{\beta\beta}$. The experimental spectra have been reconstructed by using a multivariate Bayesian fitting algorithm on simulated source spectra and furthermore the activities of the background contributions have been evaluated.

The structure of this thesis is the following: First, the neutrino properties and the $0\nu\beta\beta$ decay are introduced in Chapter 1. In Chapter 2 and 3, a brief outline of the GERDA experiment, its background components and the applied background suppression systems are given. In Chapter 4, a set of simulated background sources and their effect on the energy spectrum are discussed. Furthermore, an overview on the implementation of the GERDA simulation setup and the post-processing of the simulated spectra is given. In Chapter 5, the statistical method of the Bayesian fitting approach is introduced. In the following sections, the fit results of the background model are discussed and their uncertainties are presented. in Chapter 6 the result on the obtained half-life of two-neutrino accompanied double beta decay is evaluated and discussed. Finally, Chapter 7 summaries the most important outcomes of this thesis, and provides the impact of the results and gives an outlook.

Chapter 1

Theoretical and experimental aspects of neutrinoless double beta decay

Neutrinos are perhaps the most elusive particles in our universe. To complete the neutrino picture, the missing information regarding their mass and whether neutrinos are Majorana particles could be provided by the observation of a process called neutrinoless double beta ($0\nu\beta\beta$) decay. Furthermore, neutrino physics is a benchmark for new theories in elementary particle physics and for the understanding of the evolution of the Universe. The objective of this chapter is to motivate the search for $0\nu\beta\beta$ decay through a selective overview of the historical context leading to the requirement of a non-zero neutrino mass. The historical approach is then followed by an introduction to the theoretical and experimental aspects of $0\nu\beta\beta$ decay.

1.1 Neutrinos as a window to physics beyond the Standard Model

The remarkable history of the neutrino begins with the investigation of the β decay. To recover the energy conservation of the β decay, a new particle was postulated theoretically in 1930 by Pauli. In his famous letter addressed to participants of a nuclear physics conference in Tübingen, he proposed the existence of a light neutral particle with spin 1/2. This new hypothetical particle should be emitted alongside with the electron and carry away the excess energy converting the β decay to a three-body-problem. The absence of an observed spectral distortion in the high energy part of the β spectrum caused by a finite neutrino mass lead to the assumption of a zero neutrino mass at that time. Fermi integrated Pauli's "neutron" into his ground-breaking theory of β decay and renamed Pauli's particle the "neutrino". Pauli claimed that it would be almost impossible to detect this new particle. In fact, the experimental proof of the Pauli-Fermi neutrino hypothesis succeeded 23 years later with the pioneering reactor neutrino experiments by Reines and Cowan [1]. To detect the anti-neutrino with a scintillator, Reines and Cowan exploit the β^- decay which the fission products of the nuclear reactor undergo and took advantage of the $\overline{\nu}_e + p \to e^+ + n$ reaction to capture the anti-neutrino. In 1962, the detection of the muon neutrino followed by Lederman, Schwartz and Steinberger [2]. And in 1990, Large Electron–Positron (LEP) Collider experiments at CERN showed the existence of a third neutrino family, the so-called flavor, through the width of the Z-boson [3]. This neutrino was finally detected in 2000 at the Fermi National Laboratory by the DONUT collaboration [4].

After the discovery of the parity violating nature of the weak interaction [5], Landau [6], Lee and Yang [7], and Salam [8] explored the idea of combining the findings with the upper bound from β decay experiments. The authors came up with a so-called two-component theory, decoupling the left- and right-handed neutrino fields in the Dirac equation by assuming a zero neutrino mass (i.e. reducing the Dirac field to two degrees of freedom instead of four). The predictions of the two-component theory were in perfect agreement with numerous experiments investigating weak processes. In 1958, Goldhaber extracted the neutrino helicity from the circular polarization of the photon emitted in the chain reaction induced by an electron capture in ^{152}Eu [9]. It turned out that neutrinos exist as particles of left helicity and anti-neutrinos as particles of right helicity. The Standard Model (SM) of particle physics was consistently developed under the presumption of the massless two-component neutrino theory.

During the following years until the late 1990, little was known about neutrinos beyond the existence of three flavors, and their zero - or at least very small - mass. This picture changed after the findings made by the earliest radiochemical experiment, Homestake [10], based in a gold mine in South Dakota. Measurements of the electron-neutrinos produced in fusion reactions in the core of the Sun uncovered an apparent flux deficit of solar neutrinos. Being sensitive only to the relatively high energy ^{8}B neutrinos, Homestake measured only approximately a third of the flux calculations suggested. This deficit of solar neutrinos was confirmed by the subsequent gallium solar neutrino experiments, SAGE [11] and GALLEX [12], which measured low-energy neutrinos from the first step of the pp chain. Two decades later, an abnormal ν_μ/ν_e ratio of neutrinos produced by the pion decay in the Earth's atmosphere provided the first indication of the disappearance of neutrinos of a specific flavor in flight due to neutrino oscillations. In analogy to the phenomenon of $K^0 \rightleftharpoons \overline{K}^0$ oscillations, the existence of neutrino oscillations was pointed out earlier in 1957 by Pontecorvo [13]. No supporting evidence was provided until the anomaly of atmospheric neutrinos was discovered by the Japanese Super-Kamiokande experiment in 1998 [14]. Shown by the SNO experiment [15], the consequences of flavor conversion could finally solve the solar deficit puzzle. Further investigations in long-baseline accelerator experiments like K2K [16], MINOS [17] and T2K [18], in addition to reactor experiments like Daya Bay [19], RENO [20] and Double Chooz [21] established the concept of neutrino oscillations which requires at least one non-zero neutrino mass. Since the existence of the $0\nu\beta\beta$ decay is related to the neutrino mass, the $0\nu\beta\beta$ decay gained increasing importance with the discoveries made by the oscillation experiments. Each model requiring neutrinos to be massive is a hint of physic beyond the SM.

1.1.1 Massive neutrinos and the Standard Model

According to the SM, neutrinos are electrically neutral and massless particles with three active flavors (ν_e, ν_μ and ν_τ) and their corresponding anti-particles ($\overline{\nu}_e$, $\overline{\nu}_\mu$ and $\overline{\nu}_\tau$) . The neutrinos take part only in the weak interaction which violates the symmetry of parity. This implies that the charged current always includes the left chiral projectors, meaning the gauge bosons of the weak interaction couple only to left-handed particles (negative chirality) or right-handed anti-particles (positive chirality). The left-handed neutrino is incorporated by a doublet together with the left-handed electron, whereas the right-handed counterpart is included by a singlet.

In contradiction to the assumption in the SM, neutrino oscillations unambiguously prove non-zero neutrino masses. It stems from the fact that the theory of neutrino oscillations only holds true, if two assumptions are made. First, neutrinos must have non-vanishing and distinguishable masses, and second, the flavor eigenstates which enter the charge current weak interaction do not coincide with the mass eigenstates of neutrinos and are rather a mixture of them. Thus, neutrino oscillations are a quantum mechanical consequence of the existence of nonzero neutrino masses and neutrino (lepton) mixing. In what follows, a sketch of the derivation for oscillation probabilities in vacuum will be given. A more complete derivation can be found in [22]. Furthermore, the presence of matter can drastically change the pattern of neutrino oscillation due to interactions of the neutrinos with particles forming the matter.

On the premise of the criteria mentioned, the neutrino flavor eigenstate ν_α (referred to as the neutrino flavor α) propagates as a linear quantum superposition of three (or more) mass eigenstates ν_i $(i = 1,2,3)$

$$|\nu_\alpha\rangle = \sum_i U^*_{\alpha i}|\nu_i\rangle, \quad \alpha = e, \mu, \tau \tag{1.1}$$

until it interacts and the wave function collapses into a flavor eigenstate. Here, $U_{\alpha j}$ are the elements of the Pontecorvo-Maki-Nakagawa-Sakata (PMNS) lepton mixing matrix [23] which contain fundamental parameters of the lepton flavor sector of the SM. Through irreducible complex phases δ_{CP} accommodated in the PMNS matrix, it provides a source of charge-parity (CP) violation in the lepton sector which might account for the dominance of matter over anti-matter in the Universe.

The evolution of the states $|\nu_i\rangle$ can be described by stationary plain-wave solutions

$$|\nu_i(t)\rangle = e^{-iE_it}|\nu_i\rangle \tag{1.2}$$

with a time dependence t, mass m_i, momentum p and the relativistic energy relation $E_i = \sqrt{p^2 + m_i^2} \approx p + \frac{m_i^2}{2p}$. Consequently, a pure flavor state $\nu_\alpha = \sum_i U^*_{\alpha i}|\nu_i\rangle$ at time $t = 0$ propagates with time to

$$|\nu_\alpha(t)\rangle = \sum_i U^*_{\alpha i} e^{-iE_it}|\nu_i\rangle = \sum_\beta \sum_i U^*_{\alpha i} e^{-iE_it} U_{\beta i}|\nu_\beta\rangle \tag{1.3}$$

with $\beta = \mathrm{e}, \mu, \tau$. The expression of the probability for migrating from ν_α to ν_β can be cast in the form:

$$P(\nu_\alpha \to \nu_\beta) = |\langle\nu_\beta|\nu_\alpha(t)\rangle|^2 = \sum_{i,j} U^*_{\alpha i} U_{\beta i} U_{\alpha j} U^*_{\beta j} e^{-i\frac{\Delta m_{ij}^2 L}{2|\mathbf{p}|}} \tag{1.4}$$

where $\Delta m_{ij}^2 = m_i^2 - m_j^2$ is the neutrino mass squared difference and L the distance traveled from the source. At least two neutrinos should not be degenerate in mass to give rise to lepton mixing. Driven by the fact that the mass eigenstates propagate along the distance from the source with different phases, the mixing changes and likewise the flavor composition. The respective proportions vary periodically with the characteristic oscillation length $\sim \frac{4\pi p}{|\Delta m_{ij}^2|}$.

The three mixing angles and the two linearly independent mass squared differences have been determined from solar and atmospheric neutrino oscillation data [24]:

$$\Delta m_{sol}^2 = m_2^2 - m_1^2 \approx 7.37 \cdot 10^{-5}\ \mathrm{eV}^2, \tag{1.5}$$

and

$$\left|\Delta m_{atm}^2\right| = \left|m_3^2 - m_2^2\right| \approx 2.56(2.54) \cdot 10^{-3}\ \mathrm{eV}^2. \tag{1.6}$$

Unfortunately, the sign of the atmospheric mass splitting is still unknown, so the question of whether or not m_2 is heavier than m_3 remain open. In contrast, the sign of the solar mass splitting Δm^2_{21} is positive due to the observation of matter effects in the Sun which constrains the product $\Delta m^2_{21} \cdot \cos(2\theta_{12})$ to be positive. As a result, two possible mass distributions, shown in Fig. 1.1, arise:

- normal hierarchy (NH): $m_1 < m_2 < m_3$, ν_1 is the lightest neutrino and $\Delta m^2_{31} > 0$.
- inverted hierarchy (IH): $m_3 < m_1 < m_2$, ν_3 is the lightest neutrino and $\Delta m^2_{31} < 0$.

Depending on the electron neutrino content of each mass eigenstate, matter effects raise or lower the energy state of the mass eigenstates. Therefore, the mass ordering can be determined taking advantage of matter effects inside the Earth, and by involving atmospheric or long baseline accelerator experiments. Up to now, experiments like Super-Kamiokande [25], NOνA [26] and T2K [27],[28] have not enough sensitivity to distinguish between the two hierarchies, but in the near future they may provide a 3 to 5 σ evidence. Since the proposal by Pauli, the mass of neutrinos has been a topic of intense experimental and theoretical investigations. And nevertheless we still have no measurement of the neutrino mass. Looking at the energy spectrum of electrons produced in the β decay of nuclei, spectral distortions due to a finite neutrino mass can determine the absolute mass scale by extracting the effective neutrino mass

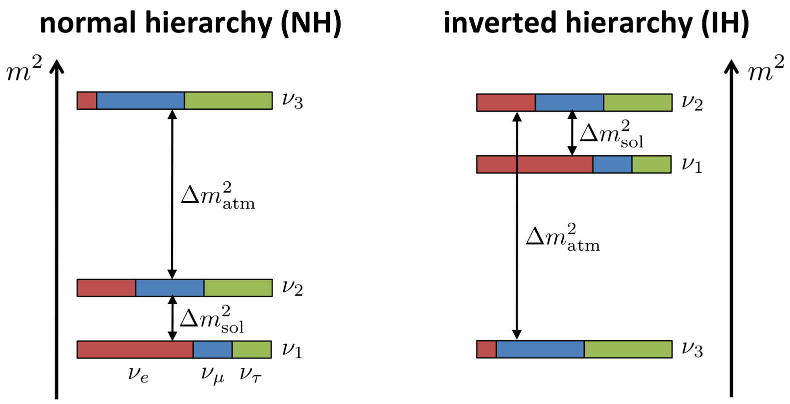

Fig. 1.1 Pattern of neutrino masses eigenstates for the normal (left) and inverted (right) hierarchies shown as function of mass squared. The fractional flavor content (e, μ,τ) of the mass eigenstates (ν_1,ν_2,ν_3) is indicated by the color code. $\Delta m^2_{atm} \sim |\Delta m^2_{32}|$ and $\Delta m^2_{sol} \sim \Delta m^2_{21}$ are the atmospheric and the solar mass-squared splitting, respectively [29].

$$m_\beta = \sqrt{|U_{e1}|^2 m_1^2 + |U_{e2}|^2 m_2^2 + |U_{e3}|^2 m_3^2}. \tag{1.7}$$

Without any assumptions, the mass determination relies only on energy conservation providing very robust and model-independent results. But a high sensitivity requires high energy resolution and large β decay source strength for good statistics at low spectral strength. Upper bounds on the neutrino mass given by measurement of the kinematic endpoint in the tritium β decay are

$$m_\beta < 2.05 \text{ eV at } 95 \text{ \% CL.} \qquad \text{and} \qquad m_\beta < 2.3 \text{ eV at } 95 \text{ \% CL.} \tag{1.8}$$

obtained by the Troitsk [30] and Mainz [31] experiments, respectively. An upcoming experiment that further investigates neutrino mass in laboratory is the KATRIN experiment [32],[33]. KATRIN aims to reach a sensitivity of $m_\beta \sim 0.20$ eV, an improvement of one orders of magnitude compared to current upper limits. With its first results, KATRIN placed an upper limit of 1.1 eV (90% confidence level (C.L.)) on the absolute neutrino mass scale [34].

On grounds that neutrino masses potentially affect the evolution of the Universe, cosmological observations are sensitive to the sum of the neutrino masses. The cosmological access to the determination of neutrino mass is based on the impact neutrinos have on the structure formation of the Universe and on the primordial nucleosynthesis. An upper limit on the sum Σ of the three neutrino masses m_j can be set. Without losing sight of the fact that the cosmological mass probe depends strongly on the model complexity and the input data used, PLANCK [35] and other surveys which determine the parameters of the Λ-CDM model (the current standard model of cosmology) bring along the most stringent constraints in the sub-eV range:

$$\Sigma = \sum_j m_j < 0.23 \text{ eV} \tag{1.9}$$

An additional approach originates from $0\nu\beta\beta$ decay search (discussed in Sec. 1.2) where the effective Majorana mass

$$\langle m_{\beta\beta} \rangle = \left| \sum_i U_{ei}^2 m_i \right| = \left| \sum_i |U_{ei}|^2 m_i \right| \tag{1.10}$$

is one observable of interest. Except for two additional phases which do not come from neutrino oscillations, all parameters can be determined by neutrino oscillations. Hence, the dependence on oscillation parameters restricts the specific structure of the allowed parameter space. Currently, estimates of the half-life for $0\nu\beta\beta$ decay place an upper bound on the

Majorana neutrino mass of

$$\langle m_{\beta\beta} \rangle < (0.15 - 0.44)\ \text{eV}\ [36] \tag{1.11}$$

But one should keep in mind that the effective Majorana neutrino mass is only valid under the assumption of Majorana neutrinos (see Sec. 1.1.2). From this point of view, it represents a complementary probe compared to the direct measurement by the β decay.

1.1.2 Dirac and Majorana neutrinos

The origin of the small mass of the neutrino which is at least six orders of magnitude [37] lower than that of other fermions is still a mystery. The underlying physics for neutrino masses may contain neutrino mass terms of two different kinds: Dirac and Majorana. Combined, both produce the seesaw picture of the lightness of neutrinos. This picture predicts that neutrinos are Majorana particles leading to $0\nu\beta\beta$ decay discussed in Sec.1.2.

Before manifesting massive neutrinos by the formalism of Dirac or Majorana masses, it is worth to recall the basic considerations according to the Dirac equation and the resulting two-component theory. Pursuant to the Dirac equation, one would expect the existence of four component neutrinos: a left-handed neutrino, a right-handed neutrino, a left-handed anti-neutrino and a right-handed anti-neutrino. But only the left-handed neutrino and the right-handed anti-neutrino have been observed in previous experiments so far. From the absence of right-handed neutrinos and left-handed anti-neutrinos, two situations can be conceived. First, the right-handed neutrino and the left-handed anti-neutrino appear as sterile particles which interact only gravitationally because they will not couple to the weak gauge bosons. In this case neutrinos are Dirac particles. Second, the neutrino is its own anti-particle, a so-called Majorana particle, and the question for the right-handed neutrino and the left-handed anti-neutrino does not arise. A short review of the theoretical framework of the two scenarios will be presented, following the discussion in [22] and [38].

The dynamics of each of the charged fermions are described by the Dirac equation of relativistic quantum mechanics, deduced from a linear approach of the Hamiltonian operator in time and space. The Dirac Lagrangian for a free fermion field ψ is given by

$$\mathcal{L} = \overline{\psi} \left(i\gamma^{\mu} \frac{\partial}{\partial x^{\mu}} - m \right) \psi \tag{1.12}$$

where the first part of the equation corresponds to the kinetic energy and the second to the mass term. Accordingly, the first scenario can be pictured by the gauge invariant Dirac mass term m_D

$$\mathcal{L}_D = -m_D \overline{\nu}\nu = -m_D\left(\overline{\nu_L}\nu_R + \overline{\nu_R}\nu_L\right) \tag{1.13}$$

where $\nu = \nu_L + \nu_R$ is the neutrino field segmented in its chiral components ν_L and ν_R, and m_D is the standard Dirac mass.

Applying the Dirac mass term, the left-handed fermion fields couple to the right-handed ones, such that it requires both a left- and a right-handed Dirac neutrino to produce such a mass term. It leads to four distinguishable neutrinos, whilst only two of them actively participate in the weak interaction.

The Dirac mass term can be generated by the standard Higgs mechanism of the mass generation. When the electroweak symmetry breaks down and the neutral Higgs field gets a vacuum expectation value $\langle \psi_H \rangle$, an effective Dirac mass, m_D, for the neutrinos stems from the Yukawa coupling f_ν:

$$m_D = f_\nu \langle \psi_H \rangle \tag{1.14}$$

If we suppose the neutrino mass to be in the order of 0.05 eV, corresponding to the mass scale suggested due to observations from atmospheric neutrino oscillations. Then, the Yukawa coupling requires a very small coupling strength of the order of 10^{-13}. Such an infinitesimal coupling constant is at least 10 orders of magnitude smaller than for charged leptons. Hence, it appears highly unsatisfactory to be the ultimate explanation of the neutrino mass, another mechanism for generating neutrino mass might be present.

Without breaking the gauge invariance of the SM, additional terms formed by a singlet of a right-handed neutrino or a left-handed anti-neutrino can be added to the Lagrangian. Moreover, a Majorana mass is generated by a Lagrangian mass term with a single chiral fermion field only. In order to find a right-handed function of the left-handed neutrino ν_L, the convention on the left-handed anti-neutrino representing the CP conjugate defined by

$$\psi^c = \hat{C}\hat{P}\psi = i\gamma^2\gamma^0\psi^\star \tag{1.15}$$

is considered, where the CP conjugate field for the right-handed neutrino, $(\nu_R)^c$, corresponds to a left-handed anti-neutrino. The Majorana mass term can subsequently be constructed out of a chirally right-handed neutrino field ν_R alone

$$\mathcal{L}_{M_R} = -\frac{1}{2} m_R \left(\overline{(\nu_R)^c}\nu_R + \overline{\nu_R}(\nu_R)^c\right). \tag{1.16}$$

or analogously, out of a left-handed neutrino field alone

$$\mathcal{L}_{M_L} = -\frac{1}{2} m_L \left(\overline{\nu_L} (\nu_L)^c + \overline{(\nu_L)^c} \nu_L \right) \tag{1.17}$$

The Majorana mass term provides a direct coupling between a particle and an anti-particle. This implies that the Majorana mass term converts a particle into an anti-particle with opposite charge. As a consequence, charge is not conserved, but charge violation is not allowed for electrically charged fermions. However, for electrically neutral particles like neutrinos there is no violation. The question then arises which mechanism can generate such a mass term.

The most general renormalizable Lagrangian includes a combination of both the Dirac and the Majorana mass terms. Considering, that $\overline{\nu_L} \nu_R$ is equivalent to $\overline{(\nu_R)^c} (\nu_L)^c$, it follows

$$\mathcal{L}_{DM} = -\frac{1}{2} \left[m_D \overline{\nu_L} \nu_R + m_D \overline{\nu_R^c} \nu_L^c + m_R \overline{(\nu_R)^c} \nu_R \right] + h.c. \tag{1.18}$$

or, equivalently in matrix notation,

$$\mathcal{L}_{DM} = -\frac{1}{2} \left(\overline{\nu_L}, \overline{(\nu_R)^c} \right) \begin{pmatrix} 0 & m_D \\ m_D & m_R \end{pmatrix} \begin{pmatrix} (\nu_L)^c \\ \nu_R \end{pmatrix} + h.c. \tag{1.19}$$

where h.c. stands for the corresponding Hermitian conjugate. The left-handed Majorana mass term is forbidden by the symmetries of the SM since it is not invariant under SU(2)xU(1) transformations. Remember, the right-handed Majorana mass term defined by a singlet is allowed by the gauge symmetry. When disregarding the addition of the right-handed chiral field, Eq. 1.18 and 1.19 are allowed in the framework of the SM, if the left-handed Majorana mass term has no explicit term ($m_L = 0$) [22].

Since the Dirac mass term is generated through the Higgs mechanism of the SM, it is natural to expect the Dirac mass m_D to be in the same order of magnitude as the corresponding charged lepton mass of the same generation. The right-handed Majorana mass, on the other hand, is not protected by the SM symmetries and can be generated by new physics beyond the SM. In contrast to the Dirac mass, the Majorana mass term is completely independent of any other mass scale. Nothing in the SM requires the right-handed Majorana mass to be small, one can assume $m_R >> m_D$. Based on this assumption, a mass eigenvalue for a light neutrino ν and for a heavy neutrino state N is obtained by diagonalizing the mass matrix in Eq. 1.19:

$$|m_\nu| \approx \frac{m_D^2}{m_R} \quad \text{and} \quad \mathrm{m_N} \approx \mathrm{m_R} \tag{1.20}$$

At fixed Dirac mass m_D, the heavier the hypothetical heavy neutrino the lighter the neutrino state ν. There exist a variety of seesaw mechanisms, the scenario described here is known as the Type I seesaw, providing an explanation of why the neutrino mass is much smaller than the other SM fermions [39], [40], [41]. The seesaw mechanism allows a light neutrino ν to exist, which is essentially the same as the massless left-handed neutrino of the SM. In order to induce the light neutrino mass in the order of eV, given a Yukawa coupling in the order of one, a right handed neutrino needs to be introduced at a high mass scale of 10^{13} GeV which is just below the the Grand Unification Scale (GUT) where new physics for neutrino masses resides.

As any model that includes Majorana masses, the seesaw mechanism predicts that the neutrino mass eigenstates will be Majorana type. Obviously, uncovering the nature of massive neutrinos is of fundamental importance in order to understand the origin of neutrino masses and mixing along with the symmetries governing the lepton sector of particle interactions.

1.2 Search for neutrinoless double beta decay

If neutrinos are their own anti-particles, then neutrinoless double beta ($0\nu\beta\beta$) decay is presently the only feasible way to establish the Majorana nature of neutrinos. Since it is known that neutrinos have mass, experiments searching for $0\nu\beta\beta$ decay turned into the key probe of physics beyond the SM. The observation of $0\nu\beta\beta$ decay would reveal the neutrino nature and, under certain assumptions, the neutrino mass hierarchy. In addition, $0\nu\beta\beta$ can constrain parameters beyond SM, e.g. show the existence of heavy neutrinos, depending on the underlying mechanism that may contribute to this decay mode. Models for $0\nu\beta\beta$ host particles from sub-eV to multi-TeV resulting in a variety of potential consequences for particle physics and cosmology. But apart from any particular mechanism that drives $0\nu\beta\beta$, it brings along lepton number violation that breaks a global conservation law of the SM. The violation of the lepton number plays an important role in physics beyond the SM, since in the framework of leptogenesis connected with baryogenesis it may explain the observed matter-antimatter imbalance of the Universe. On that basis, it is worth trying to clarify the nature of these particles not only to understand the underlying symmetries that govern leptons, but also to shed more light on the baryogenesis and the evolution of the Universe.

1.2.1 General properties of double beta decay

The $\beta\beta$ decay is a nuclear transition to an isobar daughter nucleus two nuclear charges away:

$$(A,Z) \rightarrow (A,Z+2)+2e^- + 2\overline{\nu}_e + Q_{\beta\beta} \tag{1.21}$$

It can be understood as a simultaneous β decay of two neutrons in an unstable nucleus. The $\beta\beta$ decay is expected for β-stable mother nuclides (A,Z) with the neighboring daughter nucleus (A,Z+1) whose ground state lies energetically higher. In consequence, the single β decay is energetically forbidden. In case the adjacent nucleus with charge variation by two units lies energetically lower ($m(A,Z+2) < m(A,Z)$), two subsequent single β decays are penalized by an energy barrier which can be tunneled by the second order $\beta\beta$ decay (see Fig.1.2).

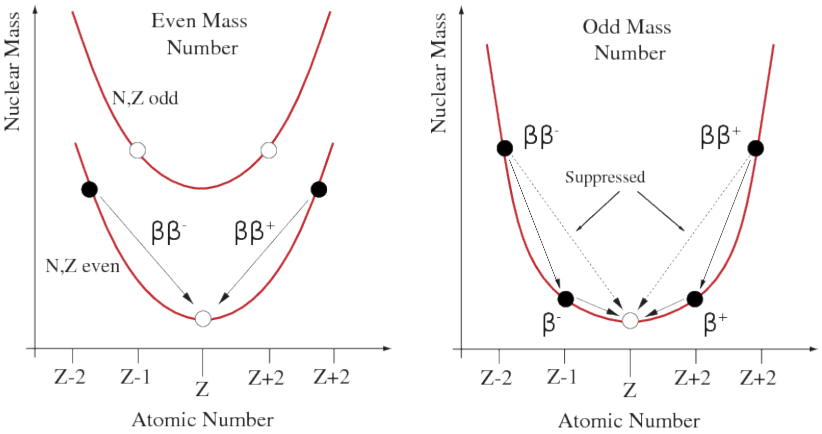

Fig. 1.2 Atomic mass parabola for an isobar candidate with A even (left) and A odd (right) showing the necessary configuration for β decay and $\beta\beta$ decay [42].

Since the first experiment in 1987 [43], the standard process with emission of two electron anti-neutrinos has been observed in a dozen nuclei. Nevertheless, the $\beta\beta$ decay is a very rare second order process of the weak interaction with typical half-lives of $> 10^{19}$ yr. According to the number and type of the released leptons there exist several possible decay modes. Already in 1939 [44] it was suggested that, if neutrinos are Majorana particles [45], the neutrino emitted by one of the nucleons can be absorbed by another one, giving rise to the following decay mode

$$(A,Z) \rightarrow (A,Z+2)+2e^- + Q_{\beta\beta} \tag{1.22}$$

which is called neutrinoless double beta ($0\nu\beta\beta$) decay. The $0\nu\beta\beta$ decay is not observed yet experimentally and the best current half-life limits of $> 10^{26}$ yr have been extracted.

Compared to the SM forbidden zero-neutrino decay mode, the anti-neutrino accompanied transition mode is completely compatible with the SM while zero and nonzero neutrino masses are allowed. However, the $2\nu\beta\beta$ decay can provide information about nuclear structure, and can help to investigate the violation of Lorentz symmetry in the neutrino sector.

1.2.2 Half-life of neutrinoless double beta decay

In principle, every mechanism with non-conserving lepton number ($\Delta L = 2$) or a combination of mechanisms could trigger $0\nu\beta\beta$ decay. The lepton number is an accidental global symmetry whose conservation can not be attributed to a known symmetry requirement. It results from the interactions occurring within the SM. Apart from the standard interpretation, the aforementioned mechanisms embrace a wide range of supersymmetric theories with R-parity violation [46], left-right symmetry theories [47], model with spontaneously broken lepton number, etc. Lepton number violating (LNV) processes that might contribute to $0\nu\beta\beta$ decay can be probed by collider experiments. The collider approaches to LNV are complementary approaches to $0\nu\beta\beta$ decay searches and can be used as a consistency check [48]. But these searches can not probe the Majorana against Dirac character of the neutrino. In the most considered scenario, the $0\nu\beta\beta$ decay process is mediated via the exchange of a light Majorana neutrino by the (V-A) charged current weak interaction which is illustrated schematically in Fig. 1.3. As stated by the experimentally confirmed V-A theory of the β decay, the neutrino exchanged in the first vertex is a right-handed anti-neutrino while the particle absorbed in the second vertex is a left-handed particle. In order to take place anyway, the neutrino must have Majorana nature by being identical to his own anti-particle. But still, without helicity flip the $0\nu\beta\beta$ decay would not be possible even in the Majorana case. Commonly, it is assumed that a single mechanism dominates over the remaining ones, but

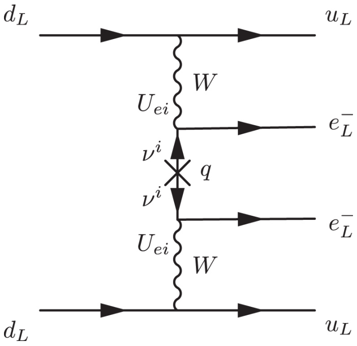

Fig. 1.3 Feynman diagram of the standard mass mechanism of $0\nu\beta\beta$ process light Majorana neutrinos as mediator [49].

independently of the mechanism which underlies $0\nu\beta\beta$ decay there is a generic relation between the decay amplitude and the Majorana mass term for neutrinos [50]. Accordingly, the theoretical expression of the reciprocal half-life of the process can be factorized as:

$$(T_{1/2})^{-1} = G_{0\nu}(Q,Z) \sum_x \left| M'^{0\nu}_x \right|^2 |f_x(m_i, U_{ei})|^2 \tag{1.23}$$

where $G_{0\nu}$ is the phase-space factor, $M'^{0\nu}_x$ the nuclear matrix element associated with mechanism x, and $f_x(m_i, U_{ei})$ includes the physics which lie beyond the SM by involving the neutrino masses m_i and the mixing matrix elements U_{ei}. According to Eq.1.23, $0\nu\beta\beta$ requires Majorana neutrino mass independently of the actual mechanism.

Under the assumption of 3-ν mixing and neutrinos being massive Majorana particles, we have $f_x(m_i, U_{ei}) = \frac{m_{\beta\beta}}{m_e}$ and thus the half-life is proportional to the effective Majorana squared mass $m^2_{\beta\beta}$. In this work, the focus lies on the standard light neutrino mass mechanism of $0\nu\beta\beta$ decay as the leading active mechanism and non-standard interpretations will be neglected. A review on the various beyond the mechanisms for $0\nu\beta\beta$ can be found in [51]. Furthermore, for a description of combined contributions of other mechanisms, the reader is referred to [50].

Effective Majorana mass ($m_{\beta\beta}$) The leptonic part of the transition amplitude arises from the weak-interaction vertex along which the virtual neutrino propagates. Introducing neutrino mixing, the corresponding operator $L_{\mu\nu}$ is proportional to $U_{ei}\nu_i(x)\overline{\nu^c_i}(y)U_{ei}$. In order to correct the helicity mismatch, the neutrino propagator yields $\sim m_i$ when the two neutrino fields contract. Finally, a quantity of great interest deduced from the half-life measurement is the effective Majorana mass which has the actual form:

$$m_{\beta\beta} = \left| \sum_i U^2_{ei} m_i \right| = \left| \sum_i |U_{ei}|^2 e^{i\alpha_i} m_i \right| \qquad (m_i \geq 0) \tag{1.24}$$

with the neutrino mass eigenstates, m_i, weighted by $U = U_{PMNS} \cdot diag\left(1, e^{i\alpha_2}, e^{i\alpha_3}\right)$ which contains the elements of the PMNS mixing matrix in combination with the additional unknown Majorana CP phases α_i which do not affect neutrino oscillations. If CP is not conserved $\alpha_i \neq 0, 2\pi$.

The effective Majorana mass is sensitive to the neutrino mass hierarchies and a possible presence of additional mass eigenstates which mix into the electron neutrino. How the picture would change when varying the numbers of mixing neutrino states is treated in [53]. Expressed as a function of the lightest neutrino mass eigenstate m_{min}, Fig. 1.4a shows

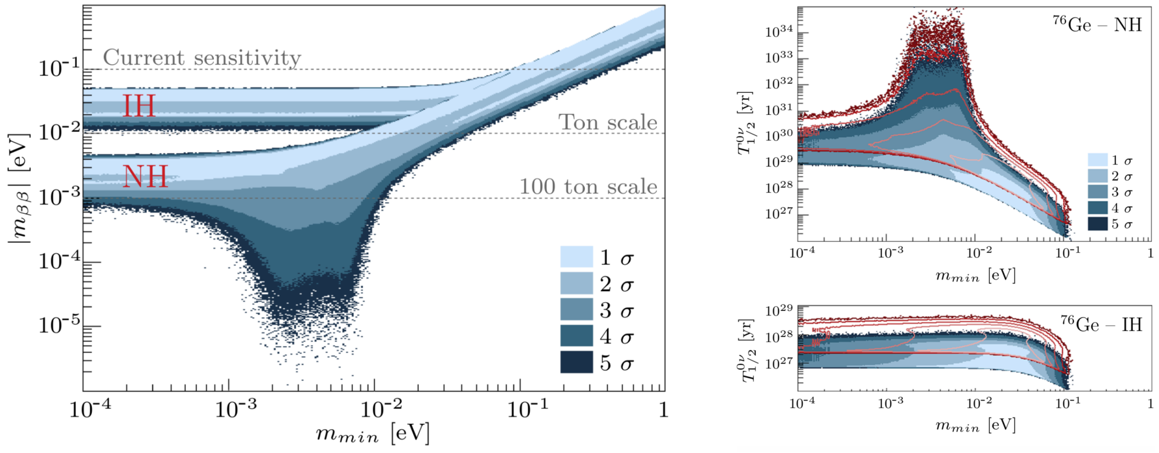

(a) (b)

Fig. 1.4 (a) Effective Majorana mass as a function of the lightest neutrino mass for the normal and inverted ordering. (b) $0\nu\beta\beta$ decay half-life of ^{76}Ge as a function of the lightest neutrino mass for $|M'^{0\nu}| = 5.16$ (blue region) and $|M'^{0\nu}| = 2.81$ (red curves). The $1,...,5\sigma$ coverage regions are indicated by the different color shadings. See [52] for details.

the allowed values of the effective Majorana mass for the corresponding mass hierarchies. Compared to the included uncertainties on the four oscillation parameters, the strongest spread of the values can be attributed to the unknown Majorana phases which define the extreme cases of $m_{\beta\beta}$ assuming CP conservation. While for $m_{\beta\beta} > 0.1$ eV both hierarchies superimpose each other, the realization of the NH would rule out the region of $m_{\beta\beta} > 0.01$ eV in case of non-zero masses. Due to the different combination of the Majorana phases, the effective Majorana mass can vanish in the region of $m_{min} \in [10^{-3}, 10^{-2}]$ eV for the NH. In case the IH is the underlying ordering, the effective Majorana mass can not be less then $15 - 20$ meV, which should be the natural aim for next generation "Ton scale" experiments indicted by the horizontal line in Fig. 1.4a.

The comparison do not contain any statement whether nature choose either of both hierarchies with higher probability. However, oscillation data slightly favor the NH over the IH supported by tensions in Δm^2_{31} and θ_{13} from long baseline and reactor experiments. Nevertheless, the authors of [54] demonstrate that even for the NH, several experiments can reach a probability of discovery of over 50 %.

If the exchange of a virtual light Majorana neutrino is not the dominant mechanism, the corresponding neutrino mass will be difficult to determine. Additional mechanisms would drastically modify the neutrino mass spectrum. However, the general Schechter-Valle (Black Box) theorem [55] states that once $0\nu\beta\beta$ has been observed, the Majorana neutrino mass necessarily arises within gauge theories regardless of the underlying mechanism. A conclusive clarification of the contributing mechanisms requires the observation of $0\nu\beta\beta$ decay in multiple isotopes or the tracking of the full kinematics [42], [56].

$0\nu\beta\beta$ decay is not simply a neutrino mass probe, it has the much more fundamental goal of experimentally testing lepton number violation as it has been stressed in the motivation of this chapter.

Nuclear matrix element ($M'^{0\nu}$) All nuclear structure effects in the $0\nu\beta\beta$ searches are contained in the nuclear matrix element (NME) defined as

$$M'^{0\nu} = g_A^2 M^{0\nu} = g_A^2 \left(M_{GT}^{0\nu} - \left(\frac{g_V}{g_A} \right)^2 M_F^{0\nu} + M_T^{0\nu} \right) \tag{1.25}$$

with the Fermi (M_F, spin independent interaction), Gamow-Teller (M_{GT}, spin-spin interaction) and tensor (M_T) matrix elements. Here, g_A and g_V are the axial and vector coupling constants of the nucleon. $M^{0\nu}$ depends on the knowledge of the nuclear transition between the initial and final states. In contrast to the case of the $2\nu\beta\beta$ decay, it can not be measured separately for the $0\nu\beta\beta$ decay. It relies on the assumed theoretical nuclear models and calculations which presently carry large uncertainties. Although a wide variety of nuclear models exist all approaches miss certain physical features leading to predicted values with a spread of factors of up to about three. The most notable techniques used are: the shell models (SM Mi and SM St-M,Tk), the interacting boson model (IBM), different implementations of the quasiparticle random-phase approximation (QRPA), relativistic and non-relativistic energy density functional theory (EDF). The circulating methods vary mainly due to choice of type of nucleon-nucleon correlations and the model space of single-particle orbitals included in the calculations. From comparisons of recent results by the different methods (see Fig. 1.5), it can be deduced that in most cases the values for the NMEs obtained by the shell model calculations are lower, while the ones obtained by IBM or QRPA are higher. A full treatment of the nuclear correlations according to ISM calculations seem to underestimate the NMEs by about 25 % due to the limited number of orbits in the valence space. By contrast, truncated variants treating large single particle model space according to QRPA and IBM overestimate the NMEs attributed to lack of multipole correlations.

The next generation of $0\nu\beta\beta$ decay experiments will explore the whole region of $m_{\beta\beta} >$ 10 meV covering the parameter space of the inverted mass hierarchy. Due to the inverse proportionality of the isotopic mass to the half-life, an uncertainty of a factor of three in the NME can lead to an order of magnitude of uncertainty in the amount of material required to be sensitive to any particular neutrino mass (see Fig. 1.5, bottom). In Fig. 1.4b, the author compares the impact of two extreme scenarios of NME calculations on the $0\nu\beta\beta$ decay half-life for ^{76}Ge as a function of the lightest neutrino. To fully explore the IH, it is needed to reach a sensitivity starting at $6-7\cdot10^{27}$ yr up to $4\cdot10^{28}$ yr depending on $M'^{0\nu}$ [52]. Obviously, the determination of the neutrino mass properties can be only as good as the knowledge of NMEs. To fully exploit the maximum potential of the future $0\nu\beta\beta$ experiments, there is still a high need for better quantifying and understanding the current discrepancies of the models in order to converge the calculations. Progress in use of chiral effective field theory to understand nuclear interactions, and nonperturbative methods to solve nuclear many-body problem promise reliable NME values over the next decade.

Regarding the sensitivity per unit mass of different isotopes, all nuclei show an inverse correlation between the phase space factor and the square of the nuclear matrix element as observed by [57]. In consequence, no isotope is either favored or disfavored and from theoretical side all have roughly equivalent sensitivity.

For further reading on this topic, [58] contains a detailed description of the current status and future prospects of NME for neutrinoless double beta decay, here only the key aspects of [58] have been pointed out.

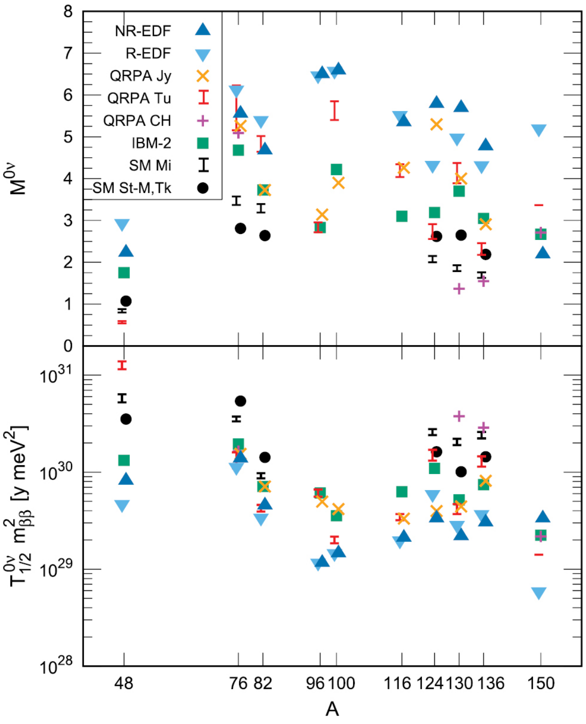

Fig. 1.5 Top: Nuclear matrix elements for $0\nu\beta\beta$ decay candidates as a function of mass number A with the assumption that the axial coupling constant g_A is unquenched. Bottom: Associated $0\nu\beta\beta$ decay half-lives, scaled by the square of the unknown parameter $m_{\beta\beta}$. See [58] for details.

The quenching problem Another controversial open issue in the context of nuclear matrix elements is whether or not the strength of the spin-isospin Gamow-Teller operator has to be modified in $0\nu\beta\beta$ decay as is common for β decays. Introduced by the dominant Gamow-Teller matrix element (see Eq. 1.25), the NME is approximately proportional to the square of the axial vector coupling constant g_A. As a result from comparison of β and $2\nu\beta\beta$ decay experiments with theory [59], g_A may be decreased ("quenched") which leads to a renormalization in nuclear models:

$$M'^{0\nu} = \left(\frac{g_A^{eff}}{g_A}\right)^2 M^{0\nu} \tag{1.26}$$

Here, g_A^{eff} is the quenched effective value of g_A. An analog quenching in $0\nu\beta\beta$ can translate into 6 to 34 times weaker constrains on the effective Majorana mass by a given half-life than currently assumed [60]. Even though $2\nu\beta\beta$ and $0\nu\beta\beta$ share initial and final states and have similar spin-isospin structure, the momentum transfered by the virtual neutrino in $0\nu\beta\beta$ is much larger (about 100 MeV) compared to $2\nu\beta\beta$ (few MeV) [58]. Nevertheless, the source of the quenching is still unknown, and consequently the necessity of the quenching for $0\nu\beta\beta$.

Phase space factor ($G_{0\nu}$) Beside the nuclear matrix elements, the phase space factor largely defines the order of magnitude of lifetime needed to derive neutrino properties. Apart from the Q-value ($Q_{\beta\beta} = m(A,Z) - m(A,Z+2) - 2m_e c^2$, the kinetic energy available in the decays), and the nuclear radius, the main ingredients for the evaluation of the phase space factor are the electron wave functions, leading to

$$G_{0\nu} \sim \int F(Z,\varepsilon) p \varepsilon \delta(E_0 - \varepsilon) d\varepsilon \tag{1.27}$$

where ε and p are the energy and electron momentum and E_0 is the total energy released in the decay. $F(Z,\varepsilon)$ is the usual Fermi function [61] obtained in a non-relativistic approximation. It considers the distortion of the electron plane waves in the Coulomb field of the nucleus. Although it depends on the total energy available in the decay and on details of the kinematics it can be calculated sufficiently accurate by taking into account the nuclear Coulomb effect on the emitted electron. With $G_{0\nu} \sim Q_{\beta\beta}^5$, the phase space factor is typically in the order of $10^{-15} - 10^{-16}$ yr^{-1} for most of the emitters of interest.

1.3 Experimental aspects of $0\nu\beta\beta$ decay search

The experimental observation of $0\nu\beta\beta$ decay relies on the kinematic parameters of the two electrons. Since the recoil energy of the daughter nucleus is negligibly small, the sum of the energies of the two electrons in the final state is equal to the Q value of the transition, $Q_{\beta\beta}$. The signal search is carried out in an energy window around $Q_{\beta\beta}$ whose choice is defined depending on the energy resolution of the detector and the expected signal peak width ΔE. The number of expected signal events $N^{0\nu}$ in the so-called region of interest (ROI) can be estimated by

$$N^{0\nu} = \ln(2)\frac{N_A}{m_A}\left(\frac{a\cdot\varepsilon\cdot M\cdot t}{T^{0\nu}_{1/2}}\right) \tag{1.28}$$

were N_A is the Avogadro number, m_A is the molar mass of the isotope, a is the isotope abundance, ε is the detection efficiency, and t is the measuring time.

Although the $0\nu\beta\beta$ decay has a clear signature due to the expected monochromatic peak at $Q_{\beta\beta}$, $0\nu\beta\beta$ decay is still a rare process in presence of background events in the same energy region. Obviously, each source producing a similar energy deposition increases the background level which must be kept as low as possible to fully reach the maximum sensitivity. Of special interest is a background level that is low enough that the number of expected background events in the ROI over the lifetime t of the experiment is not exceeding unity:

$$M\cdot t\cdot BI\cdot\Delta E \leq 1 \tag{1.29}$$

The background level is commonly given in terms of the background index BI, i.e. the number of background counts weighted by the width of ROI, source mass, and measurement time. In the aforementioned case an experiment performs under so-called background-free conditions and the sensitivity of the half-life $T^{0\nu}_{1/2}$ scales linearly with the exposure $M\cdot t$:

$$T^{0\nu}_{1/2} \sim \begin{cases} a\cdot\varepsilon\cdot M\cdot t, & \text{without background} \\ a\cdot\varepsilon\cdot\sqrt{\frac{M\cdot t}{BI\cdot\Delta E}}, & \text{with background} \end{cases} \tag{1.30}$$

Unlike the background-free regime, in presence of a flat distributed background the observed signal events are approximated as a 1σ fluctuation of the background with the result that the sensitivity scales with $\sqrt{M\cdot t}$.

Table 1.1 Natural abundance and Q value for all candidate isotopes under study [51].

isotope	isotopic abundance (%)	$Q_{\beta\beta}$ [MeV]
^{48}Ca	0.187	4273.7
^{76}Ge	7.8	2039.1
^{82}Se	9.2	2995.5
^{96}Zr	2.8	3347.7
^{100}Mo	9.6	3035.0
^{116}Ca	7.6	2809.1
^{130}Te	34.5	2530.3
^{136}Xe	8.9	2461.9
^{150}Nd	5.6	3367.3

1.3.1 Detection and experimental constraints of 0νββ decay search

In the context of Eq. 1.30, the aim of an high sensitivity translates practically in the requirement of a great mass and a long time of data taking by keeping energy resolution and background reduction as high as possible. Therefore, the choices made when designing an experiment preferable for $0\nu\beta\beta$ search captures the optimization of a subset of the following desirable features:

High Q-value According to nuclear physics, there is no isotope favored over others for the $0\nu\beta\beta$ search, since all seem to have qualitatively the same decay rate per unit mass (see Sec. 1.2.2). Generally, a high $Q_{\beta\beta}$ value is a favorable criterion when choosing an isotope. It is directly related to the potential sources of background present in the ROI. In an ideal case, the $Q_{\beta\beta}$ value is higher than the endpoint of the natural γ radioactivity (the highest γ-line at 2615 keV from ^{208}Tl) and the endpoint of the β energy (Q_β = 3279 keV) from ^{214}Bi. Both radioisotopes are progenies from the U and Th chains which are ubiquitously contained in the detector suspension and their surrounding parts. However, using the isotope with the highest $Q_{\beta\beta}$ does not necessarily promises the highest sensitivity. Out of the 35 isotopes capable of $\beta\beta$ decay, Tab. 1.1 lists all candidate emitters which have been studied so far.

Good energy resolution An excellent energy resolution is a fundamental requirement to identify the signal peak in presence of background. The number of expected background events scale with the energy resolution. With a better understanding of the detector system and its environment, the present background can be eliminated, but the $2\nu\beta\beta$ is an irreducible intrinsic background that can only be significantly reduced with a high energy resolution at $Q_{\beta\beta}$.

Very low background All experimental installations are located underground to be protected from cosmic rays. Keeping the background as low as possible presupposes not only the use of a proper passive and active shielding against the environmental radioactivity, but also of radio-pure materials for the detector suspension. In order to further reduce the backgrounds, experiments need to take into consideration the whole spectrum of possible background suppression techniques, e.g. track reconstruction, event topology based algorithms, etc.

Large isotope mass The sensitivity according to Eq. 1.30 scales linearly with the exposure $M \cdot t$, but the live time of an experiment cannot exceed several years. Since the background interactions are primarily generated at the outer regions of the detector, some experiments take advantage of the self-shielding by the detector itself, and define an inner fiducial region as the active mass. Recent experiments deploy isotope masses of the order of some tens of kg up to a few hundreds of kg. To rule out the IH region with next generation experiments, the isotope masses have to increase up to tons. Therefore, a technique with the opportunity of high less costly scalability has a clear advantage.

High isotopic abundance Of course, a sufficiently large mass can only be accompanied by a high isotopic abundance. All relevant isotopes in Tab. 1.1, except tellurium, have a natural fraction of less than 10%. The $0\nu\beta\beta$ isotope fraction can be increased by enrichment, but usually this involves more costly manufacturing processes. Furthermore, in view of the next generation experiments, the availability of the large masses required could be limited by the annual world production of the isotope.

High detection efficiency Opposed to a detector with an external source approach, a system, in which the source is embedded in the detector itself, can reach a much higher detection efficiency.

1.3.2 Experimental approaches of $0\nu\beta\beta$ decay search

Unfortunately, it is impossible to design an experimental concept that optimize all parameters simultaneously in a single detector. Finally, the chosen experimental approach is a compromise of all these parameters in order to achieve the best sensitivity. Currently there is a broad field of experimental techniques used in $0\nu\beta\beta$ searches. One branch of technologies can be characterized by the use of high energy resolution detectors like semiconductors or cryogenic detectors.

Semiconductor detectors To search for the decay of the ^{76}Ge $\rightarrow$ ^{76}Se, semiconductor detectors of high purity germanium (HPGe) crystals have been used by several groups - for the first time in 1967 [62]. Among other advantages, Germanium detectors feature an excellent energy resolution of a full width half maximum (FWHM $= 2.35\sigma$) typically better than 0.2 % at $Q_{\beta\beta}$. Being source and detector simultaneously, a rather important improvement in sensitivity can be achieved by deploying crystals enriched to 86% (rather than 7.8%) with the isotope ^{76}Ge instead of crystals with natural germanium composition. Two experimental efforts in this sector are the GERDA and Majorana Demonstrator [63] experiments. While GERDA adopted a new approach of submerging an array of enriched HPGe detectors directly in liquid argon, the Majorana Demonstrator operates inside a more conventional low-background passive lead and copper shield with an active muon veto. Currently, the GERDA and Majorana community intend to merge and pursue a joint tonne-scale $0\nu\beta\beta$ decay experiment, LEGEND [64], that combines the best technologies from both collaborations. A more detailed description of GERDA will be given in Ch. 2. Except for the low $Q_{\beta\beta}$ value of ^{76}Ge, the achievable targets of large volume, high purity and very good energy resolution demonstrated by GERDA and the Majorana Demonstrator convert this detector technology suitable for $0\nu\beta\beta$ decay search.

Cryogenic detectors Cryogenic detectors are very sensitive detectors with high resolution operating at very low temperatures. These detectors are able to measure very small amounts of energy deposited by ionization or heat. The energy deposition in the crystal caused by decays results in a rise of the crystals temperature measured by a highly sensitive sensor mounted on the crystal surface. CUORE [65] is such a cryogenic approach setup by a calorimetric system of natural tellurium oxide crystals to search for $0\nu\beta\beta$ decay of ^{130}Te $\rightarrow$ ^{130}Xe ($Q_{\beta\beta} = 2.53$ MeV). In the future, CUORE will be upgraded to its envisioned successor experiment CUPID [66] with isotopically enriched Zn^{82}Se crystals and a coupled light read-out for additional particle identification. Furthermore, CUPID is intended to reject contamination on or near the crystal surface, in particular α contaminations, that had turned out to be a major drawback of CUORE.

Ionization detectors The third type are ionization based detectors including gaseous or liquid detectors with the capability of track reconstruction to search with the best possible spatial and temporal resolution for two electron tracks that originate simultaneously from the same location. In the sector of ionization experiments, time projection chambers (TPC) have proven to be suitable tracking detectors for $0\nu\beta\beta$ search. TPCs provide a partially good energy resolution of better than 4 % FWHM at $Q_{\beta\beta}$ (~ 0.1 % for gas, ~ 4 % for liquid) compensated by the high event pattern identification and the capability of employing large detector modules. TPCs have the advantage of being monolithic, homogeneous detectors with the benefit of self-shielding, which scales linearly with the detector dimensions. In the context of TPCs used in the search for $0\nu\beta\beta$ decay, two major efforts have to be mentioned:

The EXO-200 experiment [67] has a baseline concept that comprises a single-phase liquid xenon (LXe) TPC with three-dimensional event reconstruction and additional scintillation light detection produced by particle interactions. Its successor, the nEXO experiment [68], is currently under research and development. It will consist of TPCs filled with about 5 tons of LXe enriched to about 80 % ^{136}Xe. The experimental upgrade includes improved self-shielding with larger mass and increased segmentation for refined event reconstruction. To achieve an improved energy resolution, which depends on the accuracy of the registered amount of drifting electrons and the number of scintillation photons, a position-resolving, low-noise charge readout and very efficient light collection and detection are considered. In order to tremendously suppress the background level, nEXO might adopt a new, unique technology to directly tag the daughter barium ion of the ^{136}Xe decay [69]. A second ^{136}Xe approach is proposed by the NEXT experiment [70] which is based on the use of enriched gaseous xenon in an electroluminescent high-pressure TPC. Through the lower density of the gas, the path, which the electrons emitted in $0\nu\beta\beta$ decay were traveling, can be reconstructed in the TPC. Furthermore, the increased ionization energy loss at the end of the electron tracks yields a specific structure that allows for rejection of background electrons and external γ rays. In contrast to liquid TPC and liquid scintillators, the application of electroluminescent amplification promises an improved energy resolution of 0.5 to 0.7 % FWHM at the $Q_{\beta\beta}$. A possible upgrade would include further developments on the usage of magnetic fields and the technology of Barium-tagging.

Liquid scintillators The last branch are liquid scintillator detectors loaded with the $0\nu\beta\beta$ isotope. These detectors suffer a poor energy resolution ($\sim$ 10 % FWHM at $Q_{\beta\beta}$) with no particle identification methods for β/γ. This gets compensated by the scalability to very large masses of isotope. Liquid scintillator experiments for $0\nu\beta\beta$ decay were originally developed for neutrino oscillation experiments in the energy region of $\sim$ MeV. KamLAND-Zen [71] and SNO+ [72] loaded with 383 kg of Xe enriched to 91.7 % in ^{136}Xe and with 0.3–0.5% natural tellurium (equivalent to 800 kg of ^{130}Te), respectively, have similar designs. Inward looking photomultiplier tubes (PMTs) are set on the inner surface of a about 18 m diameter stainless steel spherical tank or structure and about 1000 tons of liquid scintillator is stored in a 13 m diameter nylon base balloon (KamLAND-Zen) or 12 m diameter acrylic spheric vessel (SNO+). The emitted scintillation light is detected by the PMTs and the event vertex is reconstructed by hit timing. However, thanks to purification processes, liquid scintillator detectors realize ultra low background environments for radiation from uranium, thorium, and other metals.

Presently, the most stringent limits on the $0\nu\beta\beta$ half-life are derived using ^{76}Ge, ^{136}Xe, ^{130}Te and ^{82}Se by the GERDA, KamLAND-Zen, CUORE and CUPID experiments, respectively. Tab. 1.2 summarizes the parameters of the $0\nu\beta\beta$ experiments which are crucial for a high sensitivity. So far no evidence of $0\nu\beta\beta$ has been found and a few of these projects currently probe the effective Majorana neutrino mass scale of ~ 100 meV, corresponding to half-lives of $O(10^{26})$ yr.

Table 1.2 Summary of the performance parameters of selected $0\nu\beta\beta$ experiments: energy resolution FWHM, background rate *BI* and detection efficiency ε. Furthermore, the sensitivity is compared in terms of the background rate, energy resolution and detection efficiency ($\mathrm{B_{FWHM}} = \mathrm{FWHM} \cdot \mathrm{B}/\varepsilon$) [36].

technology	Experiment	Isotope	FHWM (keV)	ε	BI [cts/(keV · t · yr)]	$\mathrm{B_{FWHM}}$ [cts/(t · yr)]
semiconductor detectors	GERDA	^{76}Ge	3.3	0.5	0.6	4
	Majorana Demonstrator	^{76}Ge	2.5	0.71	5	18
liquid gas TPC	EXO200	^{136}Xe	71	0.66	1.6	170
loaded liquid scintillators	KamLAND-Zen	^{136}Xe	270	1.0	0.45	120
cryogenic bolometers	CUORE	^{130}Te	7.4	0.23	14	450
+ light read-out	CUPID	^{82}Se	23	0.40	3.6	210

1.4 Results on ^{76}Ge $0\nu\beta\beta$ signal search

Among the other experimental approaches which aim to detect $0\nu\beta\beta$ decay in ^{76}Ge, GERDA has the greatest sensitivity for discovering the $0\nu\beta\beta$ decay. GERDA is the first experiment which has surpassed a sensitivity for the $0\nu\beta\beta$ decay half-life of $T^{0\nu}_{1/2} \sim 10^{26}$ yr (90% C.L.) while operating under background-free conditions, i.e. the expected number of background events is < 1 in the ROI at the target exposure. This achievement together with the superior energy resolution of Ge detectors makes GERDA competitive with the best experiments which use significantly larger masses.

The Phase II spectrum after all analysis cuts (see Ch. 3.2) for the two different geometries (coaxial ($^{\mathrm{enr}}$Coax) and Broad Energy Ge ($^{\mathrm{enr}}$BEGE) detectors (see Ch. 2.3.4)) used in GERDA are shown separately in Fig. 1.6. The analysis window ranges from 1930 keV to 2190 keV excluding peaks caused by known γ-lines. The GERDA collaboration applies a blinded procedure of removing all events with an energy deposition in the interval of $Q_{\beta\beta} \pm 25$ keV from the data stream until all analysis parameters have been frozen. After unblinding, only 3 events in the $^{\mathrm{enr}}$Coax and 5 events in the $^{\mathrm{enr}}$BEGE data sets of Phase II recorded with 53.9kg·yr remain in the analysis window. GERDA thus reaches an exceptionally low background rate of $\left(5.6^{+4.1}_{-2.6}\right)$ counts/(keV · kg · yr) for the $^{\mathrm{enr}}$Coax and $\left(5.6^{+3.4}_{-2.4}\right)$ counts/(keV · kg · yr) for the $^{\mathrm{enr}}$BEGE detectors.

Following the statistical methods described in [73], an unbinned maximum likelihood fit has been performed simultaneously to the different data sets combining those of GERDA Phase I and Phase II. The combined likelihood function is defined by flat background distributions independent for each data set and a Gaussian distribution for a possible signal at $Q_{\beta\beta}$ with corresponding resolution taken from calibration data individually for the seven data sets (see Tab. 1.3). For the best-fit, the likelihood yields a maximum for zero signal strength, $1/T^{0\nu}_{1/2} = 0$, translating into a lower limit of

$$T^{0\nu}_{1/2} > 0.9 \cdot 10^{25}\ \mathrm{yr}\ (90\%\ \mathrm{C.L.}) \tag{1.31}$$

for which a mean sensitivity of $1.1 \cdot 10^{26}$ yr (90% C.L.) has been derived by an ensemble of MC with the same parameters of GERDA and zero signal strength. The event at 2042.1 keV in the $^{\mathrm{enr}}$BEGE data set which is 2.4 standard deviations away from $Q_{\beta\beta}$ (see Fig.1.6) is responsible for a lower limit compared to the median sensitivity, since the statistical analysis characterizes it as a background event. In addition, a Bayesian evaluation was carried out. The posterior on $1/T^{0\nu}_{1/2}$ is obtained after the marginalization over all nuisance parameters by Markov chain Monte Carlo numerical integration within the Bayesian Analysis Toolkit (BAT) software package [74]. The a priori constraint for the background rate is a flat distribution between 0 and 0.1 cts/(keV·kg·yr) and for the $1/T^{0\nu}_{1/2}$ it is also a flat distribution up to a maximum of 10^{-24}yr^{-1}. The best fit yields again zero signal strength, $1/T^{0\nu}_{1/2} = 0$, and the 90 % lower limit is

$$T^{0\nu}_{1/2} > 0.8 \cdot 10^{25}\ \mathrm{yr}\ (90\%\ \text{credible interval}) \tag{1.32}$$

with a median sensitivity of $0.8 \cdot 10^{25}$ yr. The probability to obtain a stronger limit than GERDA is 63% and 59% for Frequentist and Bayesian approach, respectively. The half-life sensitivity of $1.1 \cdot 10^{25}$ yr converts into a sensitivity to the effective Majorana neutrino mass of 0.07 - 0.16 eV when combining with other $0\nu\beta\beta$ decay searches listed in Tab. 1.2. Furthermore, this corresponds to a sensitivity to the absolute mass scale in β decay of 0.16 - 0.45 eV, and to the cosmologically relevant sum of neutrino masses of 0.46 - 1.3 eV. The GERDA results presented here have been taken from [36] which gives a comprehensive presentation of the latest GERDA results and is recommended for further reading on this topic.

Table 1.3 Parameters for the seven GERDA Phase I and Phase II analysis data sets. Given are the respective exposure $\mathcal{E}$, energy resolution (FWHM) at $Q_{\beta\beta}$, total efficiency ε and the respective background index BI evaluated in the ROI [36].

dataset name	$\mathcal{E}$ (kg·yr)	FWHM (keV)	ε	BI (cts/(keV · kg · yr)
PhaseI-Golden	17.9	4.3(1)	0.57(3)	$(1.1 \pm 0.2) \cdot 10^{-2}$
PhaseI-Silver	1.3	4.3(1)	0.57(3)	$(3.0 \pm 1.0) \cdot 10^{-2}$
PhaseI-BEGe	2.4	2.7(2)	0.66(2)	$\left(5.4^{+4.0}_{-2.5}\right) \cdot 10^{-3}$
PhaseI-Extra	1.9	4.2(1)	0.58(4)	$\left(4.6^{+4.3}_{-2.5}\right) \cdot 10^{-3}$
PhaseII-Coax1	5.0	3.6(1)	0.52(4)	$\left(3.5^{+2.1}_{-1.5}\right) \cdot 10^{-3}$
PhaseII-Coax2	23.1	3.6(1)	0.48(4)	$\left(5.7^{+4.1}_{-2.6}\right) \cdot 10^{-4}$
PhaseII-BEGe	30.8	3.0(1)	0.60(2)	$\left(5.6^{+3.4}_{-2.4}\right) \cdot 10^{-4}$

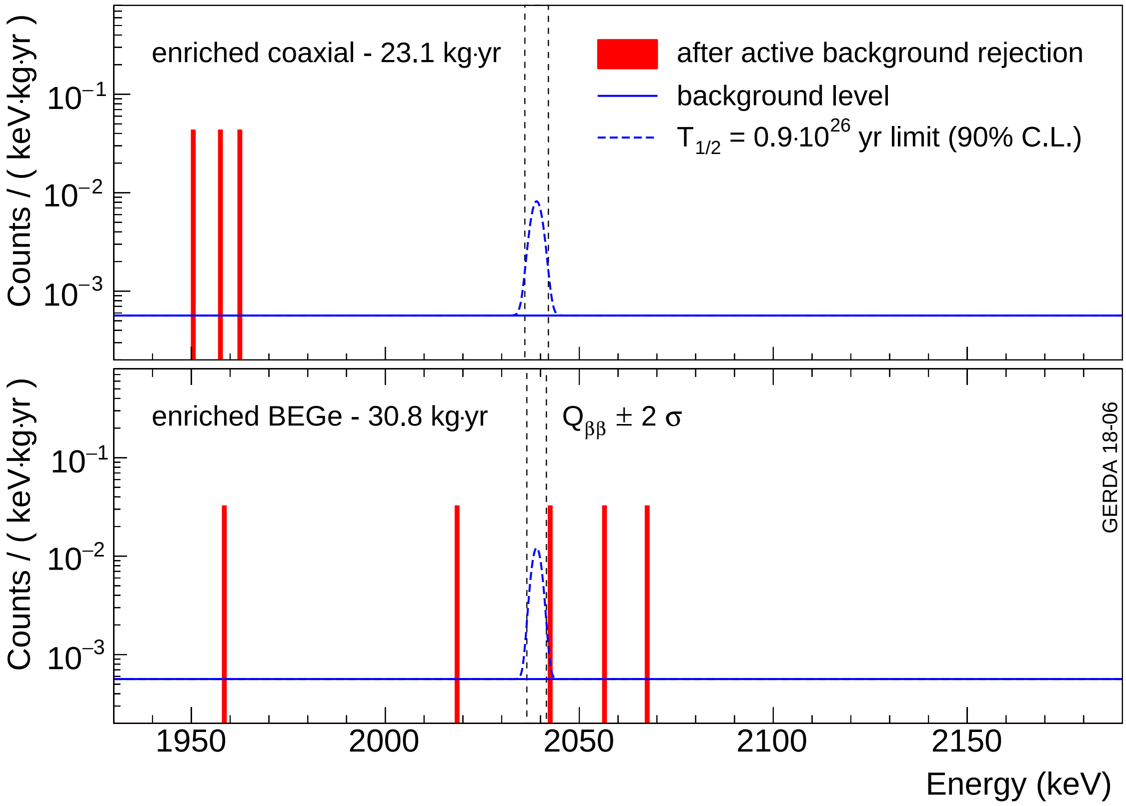

Fig. 1.6 The Phase II energy spectra zoomed to the ROI are shown separately for the ${}^{\mathrm{enr}}$Coax and ${}^{\mathrm{enr}}$BEGE data sets after all analysis cuts. The spectra are superimposed with the expectations based on the 90% C.L. limit for a $0\nu\beta\beta$ signal of $T^{0\nu}_{1/2} = 0.9 \cdot 10^{26}$ yr (dashed line) obtained by the combined analysis of GERDA Phase I and Phase II [36].

Chapter 2

The germanium detector array: Physics goals and design

Among other experimental approaches (see Ch. 1.3.2), the GErmanium Detector Array (GERDA) is designed to search for $0\nu\beta\beta$ decay of $^{76}\mathrm{Ge} \rightarrow ^{76}\mathrm{Se}$. Acting as source and detector simultaneously, germanium crystals isotopically enriched in ^{76}Ge are directly immersed into a cryostat filled with liquid argon (LAr). The well-established germanium detector technology, a high signal efficiency and, the best energy resolution compared to other competitive detection systems convinces to compensate for the low $Q_{\beta\beta}$ value and the rather low natural ^{76}Ge fraction of 7.8 %. In this chapter the basic concept of the GERDA design will be presented. A review on the germanium detectors will deal with the basic properties and physical characteristics of semiconductors, and the most important interactions of particles with matter. Moreover, the two detector configurations used in GERDA will be summarized. Focusing deeply on the subject of semiconductor detectors is out of scope of this work, therefore it is recommended to consult [75] and [76].

2.1 The GERDA experiment: Phase I and Phase II goals

Initially, GERDA, in particular GERDA Phase I, had been proposed to verify or refute a claim of discovery of neutrinoless double beta decay by Heidelberg-Moscow [77] in 2004. In addition, it was expected that the basic concept of GERDA allows for a background reduction by up to two orders of magnitudes with respect to early state-of-art experiments (~ 0.1 cts/(keV $\cdot$ kg $\cdot$ yr)). The operation was conceived to proceed in two phases. The second phase was intended to probe half-lives in the range of 10^{26} yr by collecting a design exposure of 100 kg·yr in a substantially reduced background regime of about 10^{-3} cts/(keV·kg·yr).

The first physics runs (GERDA Phase I) with eight ^{76}Ge detectors corresponding to 15.2 kg of ^{76}Ge were completed in September 2013. The GERDA collaboration applies a blinded procedure of removing all events with an energy deposition in the interval of $Q_{\beta\beta} \pm 25$ keV from the data stream until all analysis parameters have been frozen. With no signal found and a background level of $\sim 10^{-2}$ cts/(keV·kg·yr) in the ROI, GERDA reached already in Phase I its goal of reducing the background by a factor 10 with respect to previous experiments scrutinizing the earlier claim of a signal. Fig. 2.1 shows the half-life sensitivity with 90 % discovery probability plotted versus the exposure under different background conditions. The half-life for the claimed observation of $0\nu\beta\beta$ in ^{76}Ge is indicated by the blue line. Meanwhile, GERDA Phase II was launched in December 2015 after a major upgrade. Thanks to the increased detector mass and active background suppression techniques, among with an additional implementation of a LAr veto system detecting the LAr scintillation light, the background level has been reduced further down to $< 10^{-3}$ cts/(keV·kg·yr). A detailed presentation of the combined results of Phase I and Phase II comprising an exposure of 23.5 kg·yr and 58.9 kg·yr, respectively, can be found in Ch.1.4.

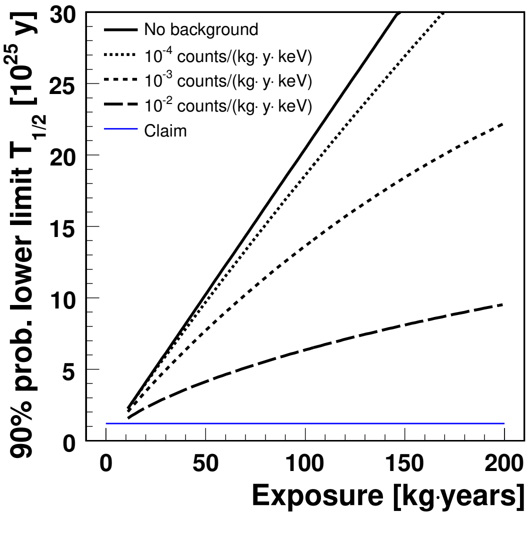

Fig. 2.1 Sensitivity of the GERDA experiment as function of exposure for various background conditions. The half-life for the claim of discovery of $0\nu\beta\beta$ in ^{76}Ge [77] is also shown in blue.

2.2 The GERDA experimental design

The GERmanium Detector Array (GERDA) experiment [78] is located at the underground Laboratori Nazionali del Gran Sasso (LNGS) of INFN in Italy. A rock overburden of about 3500 m water equivalent (m.w.e.) removes the hadronic components of cosmic rays and reduces the muon flux by six orders of magnitude. GERDA operates high purity germanium detectors (HPGe) which are isotopically enriched to 87 % in ^{76}Ge. The HPGe detectors are directly operated in liquid argon (LAr) which is used both to cool the detectors to their operating temperature (90 K) and to shield against external radiation originating from the walls. This innovative layout was already suggested by G. Heusser [79] in 1995, since the concept allows to reduce the mass of nearby components and materials. Apart from this, the detector array is surrounded by low Z shielding, a fact that allows to minimize the background produced by interactions of cosmic rays compared to the traditional concepts. A schematic view of the GERDA installation is given in Fig. 2.2a. The passive shield is completed by a 590 m^3 water tank surrounding the 64 m^3 LAr cryostat. Above the water tank there is a clean room with a glove box and a lock used for the insertion of the germanium detector array and the integration of the LAr veto system.

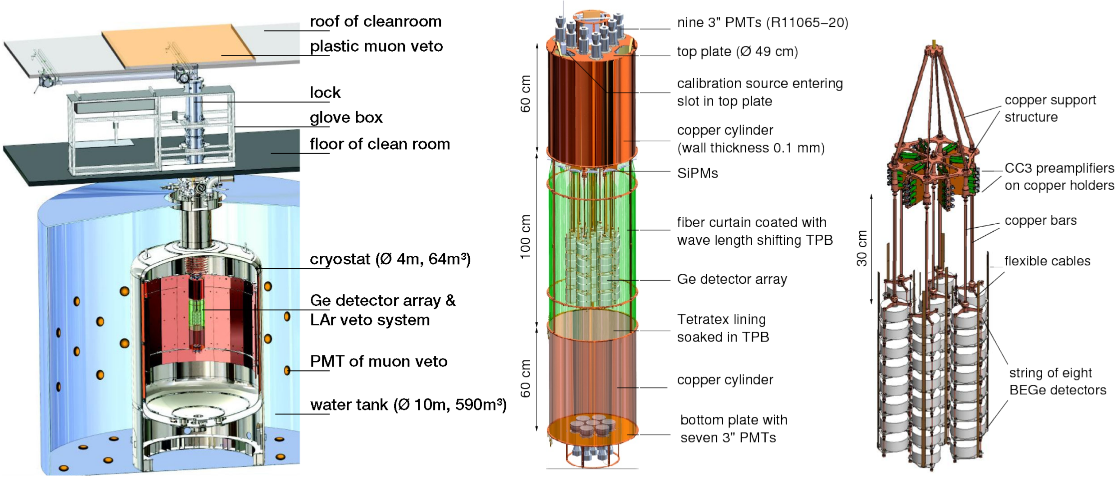

(a) (b) (c)

Fig. 2.2 (a) Schematic layout of the GERDA Phase II setup. (b) Zoom of the Ge detector array surrounded by the LAr veto system (c) Sketch of the full assembled detector array, with the seven detector strings with preamplifiers. [80]

Muon veto In order to collect the Cherenkov light produced by cosmic muons, the water tank is equipped with 66 8 inch photomultipliers (PMTs) distributed on the floor and the walls of the tank [81][82]. The roof of the clean room has been covered by an additional plastic panel veto system to prevent the detection escape of muons passing through the neck region of the cryostat.

Liquid Argon veto In order to further reduce the background index compared to Phase I, a second veto system within the LAr has been applied. It detects radiation in the vicinity of the germanium detectors which deposit energy in LAr. The system has been conceived as a hybrid system composed of PMTs and wave length shifting (WLS) fibers with SiPM read-out covering a cylindrical volume (Fig. 2.3b). By building kind of a curtain surrounding the detector array, the scintillation light created in the vicinity of the array can be detected. The scintillation light is collected by low-radioactive PMTs, which are installed on copper plates separated from the fiber section by copper shrouds of 60 cm height - nine PMTs mounted above and seven PMTs below the detector array. The inner surface of the two copper shrouds are lined with a Tetratex® foil which diffuses and shifts the wave length of the UV scintillation light into the visible range.

Detector array The core of the experiment, the germanium detector array (Fig. 2.3c), bases on p-type high-purity germanium (HPGe) crystals which can be distinguished by two different detector types: the semi-coaxial and the $^{\mathrm{enr}}$BEGE detectors (see Sec. 2.3.4). Building up the array, all detectors are assembled into 6 strings circularly arranged by surrounding a central 7th string. On average each string consists of either 8 $^{\mathrm{enr}}$BEGE or 3 semi-coaxial detectors, except one string which carries a mixture of both types.

The GERDA germanium detectors are finally divided into the following groups: the 7 enriched semi-coaxial ANG and RG detectors ($^{\mathrm{enr}}$Coax) [78] from the former Heidelberg-Moscow [83] and IGEX [84] experiments, the 30 enriched newly produced Broad Energy Germanium detectors ($^{\mathrm{enr}}$BEGE) [85] and, the 3 natural semi-coaxial GTF detectors ($^{\mathrm{nat}}$Coax) [78] with a natural isotopic composition (^{76}Ge abundance of 7.8 %). The mass enriched in ^{76}Ge totals 15.578(7) kg for the semi-coaxial and 20.024(30) kg for the $^{\mathrm{enr}}$BEGE detectors. Tab. B.2 reports the main parameters of all detectors used in GERDA Phase II and quotes the full energy peak (FEP) detector efficiencies ε_{fep} for the $0\nu\beta\beta$ decay in ^{76}Ge.

Each detector string is placed inside a nylon cylinder to limit the LAr volume from which active ions (like the ^{42}K ion) may be collected on the outer detector surface. The total array measures a height of 40 cm at a diameter of about 30 cm. Above the array in a distance of about 30 cm, the front end electronics are placed.

2.3 Germanium detectors

Germanium detectors are semiconducting devices which are based on mono-crystalline semiconducting materials, typically silicon or germanium. The detection principle of semiconducting detectors is analog to the generation of charge carriers by excitation in gas-filled ionization detectors. But the energy necessary to create such an electron-hole pair is much smaller than for gas ionization detectors. Therefore, the produced number of charge carriers for a given energy is one order of magnitude higher, associated with the strongly increased energy resolution of up to $0.1\ \%$. In addition, semiconductors do have a higher absorption capacity due to its higher density. Furthermore, these devices, which are widely used in charged particles (silicon) or γ ray (germanium) spectroscopy, are characterized by compact sizes and relatively fast timing characteristics.

2.3.1 Semiconductor properties

Band structure In order to understand the working principle of semiconductor devices, it is useful to introduce the basic concept of band structure. In an atom, an electron occupies a discrete energy level. When bringing two atoms together, the energy level splits up in two. Bring many atoms together, the discrete energy levels of the electrons can be replaced with band levels of energy states. Obviously, the energy bands are filled up by the electrons starting at the lowest energy level. The latest partially or nearly filled bands are the valence band and the higher lying conduction band. The two bands are separated by the so-called band gap of characteristic size, categorizing the material to be of non-, semi- or conducting type (see Fig. 2.3). For an insulator the band gap is typically in the order of 9 eV while for semiconductors it is in the order of 1 eV. In particular, germanium, as a semiconductor, has a band gap of 0.67 keV at room temperature. Electrons of either a totally filled or a totally empty band cannot contribute to any current conduction. Only electrons in the conduction band can migrate freely through the crystal and contribute to the electrical conductivity of the material. The ability of electrical conductivity is thereby given by the number of electrons in the conduction band and, consequently, by the band gap size of the crystal.

Detection principle In case of a semiconductor the valence band is highly populated, while the conduction band is nearly empty. By excitation, an electron can be lifted from the valence band to the conduction band. Typically, semiconductors like germanium are elements from Group IV with four valence electrons. In order to prevent thermal generation of charge carriers, germanium detectors have to be cooled. Apart from thermal excitation,

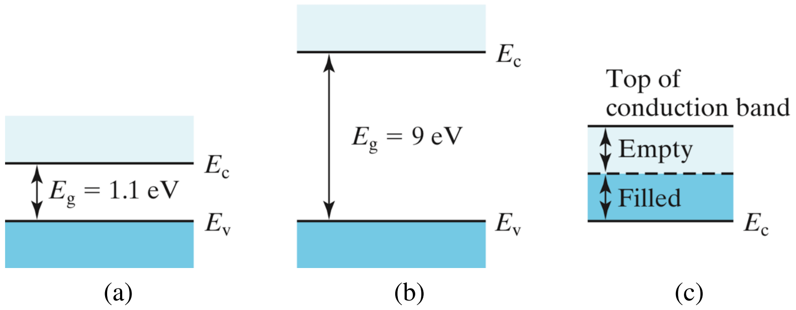

Fig. 2.3 Band structure diagram for a semiconductor (a), an isolator (b) and a conductor (c) in electron energies .

interacting radiation can also induce the excitation of the electron to overcome the band gap. The positively charged vacancy left in the valance band is referred to as hole. More precisely, when particles interact with a detector material electron-hole pairs get created building drifting charge carriers. The charge carriers migrate then through the detector by drifting to the opposite electrode, where they get collected by charge-sensitive preamplifiers.

p-n junction Through doping with a certain concentration of impurities the number of available charge carriers can be controlled. Doping atoms, which can be incorporated in the crystal lattice, can create extra energy levels. An energy level close to the conduction band is generated by adding a dopant from Group V, a donor, that delivers an extra electron. An analogue principle holds for acceptor dopants from Group III, which create an extra hole in the valence band with an resulting extra energy level close to the valence band. According to the dominant charge carrier type, a material can be identified as a n- (electrons) or p-type (holes) semiconductor. A p-n-junction can be fabricated by implanting or diffusing a high concentration of donors into a p-type substrate such that a layer of semiconductor is converted into n-type. When a p-type and n-type material are interfaced together, the free charge carriers from both sides of the junction diffuse into the opposite region. There they recombine giving rise to a zone without free charge carriers (depletion zone) on both sides of the p-n-junction. In case an external voltage is applied with reversed bias, the electric field extends across the depleted region whose the extension increases. A current flow of free charges e.g. generated by the creation of electron hole pairs can only pass in one direction. The contacts built by the n-type and p-type layers close to the crystal surface remain undepleted. These undepleted regions are typically called p+ and the n+ dead layer which extend a few hundreds of µm and 2 mm, respectively, into the crystal volume. Both dead layers are assumed to be in first order insensitive to the incident radiation.

2.3.2 Particle interactions in germanium

Indeed, whether and how many electron-hole pairs are created by incident radiation depends largely on the band gap energy. But the charge carrier clouds generated in the germanium detector arise in different ways and with different characteristics depending on the type and energy of incident radiation. The most common source of radiation in an environmental application of germanium detectors are radioisotopes that decay by spontaneous emission of α or β particles. If necessary, the isotopes can further decay or deexcite emitting γ rays to reach a more stable nuclear configuration. According to the (background) radiation intended to detect with GERDA(which has typically an energy below 10 MeV), the interaction processes of heavy charged particles, electrons and photons are of primary concern. For this reason, the following compilation will be limited to these tree categories. More descriptions of particle interactions, including neutron processes, can be found in [76].

Charged particles Heavy ($m \gg m_e$) charged particles, such as α particles, lose their energy in matter almost exclusively due to the electromagnetic interaction with the orbital electrons. Inelastic collisions with the shell electrons lead to the excitation (raise the electron to a higher-lying shell) or ionization (remove completely the electron from the atom) of the atoms in the interaction medium. The average energy loss per path length depends on the properties of the medium as well as on kinematics of the incident particle. Due to the much smaller mass, electrons and positrons lose their energy likewise through ionization and excitation of atoms within the absorber material, but also through Bremsstrahlung emission. While at low energies electrons and positrons primarily lose their energy by ionization, Bremsstrahlung losses rise and dominate exceeding an energy of a few tens of MeV.

Ionization Bohr's classical formula extended by quantum mechanics and relativistic effects results in the Bethe-Bloch formula which describes the specific energy loss through ionization [76]. According to the Bethe-Bloch formula, the specific energy loss decreases with increase of the kinetic energy of the incoming particle:

$$\frac{dE}{dx} \propto \frac{z^2 e^4 n_e}{m_e v^2} \left(\ln \frac{2 m_e v^2}{\langle E_b \rangle} - \ln(1-\beta^2) - \beta^2 \right) \tag{2.1}$$

with the charge $z \cdot e$ and velocity v of the incident particle, the electron density n_e, the electron mass m_e, the ratio $\beta = v/c$, and the average binding energy of the electrons E_b. Furthermore, the specific energy loss scales proportional to the electron density of the material $n_e \propto \rho Z/A$ and to the square of the atomic number Z. Nevertheless, it does not depend significantly on the material, except through its density. In case of electrons, the assumption that the penetrating particle is not deflected in the Coulomb field of the nucleus is no longer correct. On the other hand, the ionization process in this case is an interaction between identical particles. Both points have to be included in the Bethe-Bloch calculations

Bremsstrahlung Because of the deflection in the Coulomb field of the atomic nuclei, the electron undergoes a deceleration and therefore radiates photons in the electrostatic field of the nucleus. As the Bremsstrahlung radiation depends on the strength of the field acting on the electron, the shielding of the nucleus by the inner electrons plays a central role. The energy loss per path length due to radiation grows linearly with energy of the electron and on a quadratic scale with Z. Above a critical energy, Bremsstrahlung constitutes the main contribution compared to ionization which reaches a plateau with $\sim Z \cdot \ln(E)$ at high energies.

Photons Only charged particles interact with electrons of the atoms through ionization, a γ ray creates no direct ionization or excitation of the material while passing through. Nevertheless, γ rays can be detected because they create charged particles in the absorber material by transferring all or part of its energy E_γ. The electrons generated along the track have a typical mean free path of a few millimeters and provide indirect information about the incident γ ray. Three mayor interaction mechanisms which play a role for γ rays to yield electrons in matter are: photoelectric absorption, Compton scattering, and pair production. Apart from the atomic number of the interaction medium, the relative contribution of these various processes depends on the γ ray energy which ranges from a few keV to several MeV for emissions in radioactive decays. The photoelectric absorption dominates at low-energy γ rays (up to several hundred keV), pair production dominates for high-energy γ rays (above 5-10 MeV), and Compton scattering is the most probable process over the range of energies around 1 MeV.

Photoelectric Absorption An incoming photon with high enough energy $(E = E_\gamma - E_b)$ is absorbed by a shell electron. The incident γ ray transfers all its energy to an electron of the absorber atom, which then is ejected off from its shell (most likely from the K shell). The vacancy is filled by rearrangement of an electron of a higher shell accompanied X-ray radiation with characteristic binding energy. This process dominates for lower energies ($<$ 200 keV) and happens between a photon and an entire atom. Since the photon is absorbed, the energy and momentum conservation can only be fulfilled at the same time as the atom absorbs part of the momentum (recoil).

Compton Scattering As result of a Compton scattering, a recoil electron scatters off due to an energy transfer by the γ ray. The energy transfered can vary from zero to large energy fractions of the incident γ ray dependent on the deflection angle θ. Hence, the energy of the scattered γ ray is given by

$$E'_\gamma = \frac{E_\gamma}{1 + \frac{E_\gamma}{m_0 c^2}(1 - \cos\theta)} \tag{2.2}$$

where m_0c^2 is the rest energy of the electron. From Eq. 2.2, it can be deduced that a continuum of energies can be transferred to the electron reaching the maximum Compton recoil electron energy, the so-called Compton edge, when the γ ray is backscattered ($\theta = \pi$). Since the γ ray still carries some energy, a gap arises between the Compton edge and the incident γ ray energy. The Compton scattering is the dominant process at intermediate energies between the two extremes.

Pair production When the energy of the photon exceeds twice the electron mass, the incident photon can produce an electron-positron pair in the Coulomb field of the atomic nucleus. The entire energy of the photon is transferred to the electron positron pair and the nuclear recoil. After slowing down while traveling though the medium, the positron will annihilate and a photo-peak (i.e. full energy peak (FEP)) at E_γ can be observed in the energy spectrum. If one or both γ rays from the subsequent annihilation are not absorbed in the detector volume, escape lines at $\mathrm{E}_\gamma - \mathrm{m_0c^2}$ keV (single escape peak (SEP)) and $\mathrm{E}_\gamma - 2\mathrm{m_0c^2}$ keV (double escape peak (DEP)) appear in the recorded energy spectrum. The cross section of the process depends on the atomic number of the material and scales logarithmically with the photon energy turning almost constant at very high energies ($E_\gamma \gg m_e c^2$).

2.3.3 Signal formation of germanium semiconductors

The final recorded charge signal is characterized by its 1 µs long leading edge formed during the charge collection and its exponential decay tail folded in by the preamplifier. The shape of the rising part of the pulse depends on the position at which the charge carriers are produced within the active volume. The charge collection times are not likely to be the same because of different drift distances and mobilities. Due to approximately equivalent collection times, the signal formation relies on both electrons and holes. But, in case charge carriers are created at a position near either edge of the active volume the pulse shape is formed primarily due to the motion of only one type of charge carrier. Both types must be completely collected as a measure of the energy deposited by the particle. If no charge carrier gets lost during drift trough the active volume, the charge will be directly proportional to the absorbed energy. For instance, charge losses can be provoked by impurities or defects in the crystal lattice giving rise to recombination centers due to additional levels in the forbidden gap where electrons from the conduction band or holes from the valance band can be captured. Apart from that, charges can get retained in shallow traps followed by a sudden release after some time. This effect causes an increased charge collection time or even charge losses, if the release time is longer than the collection time.

Since the charge carriers migrate with a speed which depends almost linearly on the electric field until it saturates, the electric field governs the charge collection process. The signal shape and timing behavior are consequently dependent on the variation of its strength. While the electric field itself depends on the detector geometry, the applied bias voltage and the density of the electrically active impurities. Nevertheless, the individual charge collections can be resolved by the Shockley-Ramo's theorem [86]. It is used to calculate the time development of the charge q in each electrode by solving the Poisson's equation

$$\nabla^2\phi(\mathbf{x}) = \frac{\rho(\mathbf{x})}{\varepsilon} \tag{2.3}$$

for given boundary conditions, where ϕ is the electric potential, $\rho(\mathbf{x})$ the stationary space charge, and ε the permittivity of the detector medium. The influence of any electrode S_j on a given space-point is characterized by an electrostatic potential, the so-called weighting potential φ_i. It describes the potential that exists at the position x_0 of the point charge, where the potential on the signal electrode $(S_j, j = i)$ equals unity and the reference $(S_j, j \neq i)$ electrodes are grounded. The charge Q_{qi} induced on electrode S_i by a point charge q at position x_0 is

$$Q_{qi} = -q \cdot \varphi_i(\mathbf{x}_0) \tag{2.4}$$

with the weighting potential given by

$$\nabla^2\varphi_i(\mathbf{x}) = 0 \qquad \phi|_{S_j} = \delta_{ij}. \tag{2.5}$$

Since the weighting potential is considered as static, it may be calculated only once and tabulated for a reasonably space grid with interpolation of the intermediate spaces. For further reading on the detection principle and the weighting potential [76] and [86] are recommended.

2.3.4 High purity germanium detector types

As mentioned in the previous Sec. 2.2, the germanium detectors setting up the array can be distinguished by two different types: the semi-coaxial and the ^{enr}BEGE detectors. Considering the different detector types, the electric field strength across the detectors active volume can vary markedly for different detector types, since it determines the drift velocity of the charge carriers. Consequently, the properties of pulse shape, timing behavior, and completeness of the charge collection process are effected. A sketch of both used detector types reporting their typical geometrical dimensions, electrodes and grooves is shown in Fig. 2.4a.

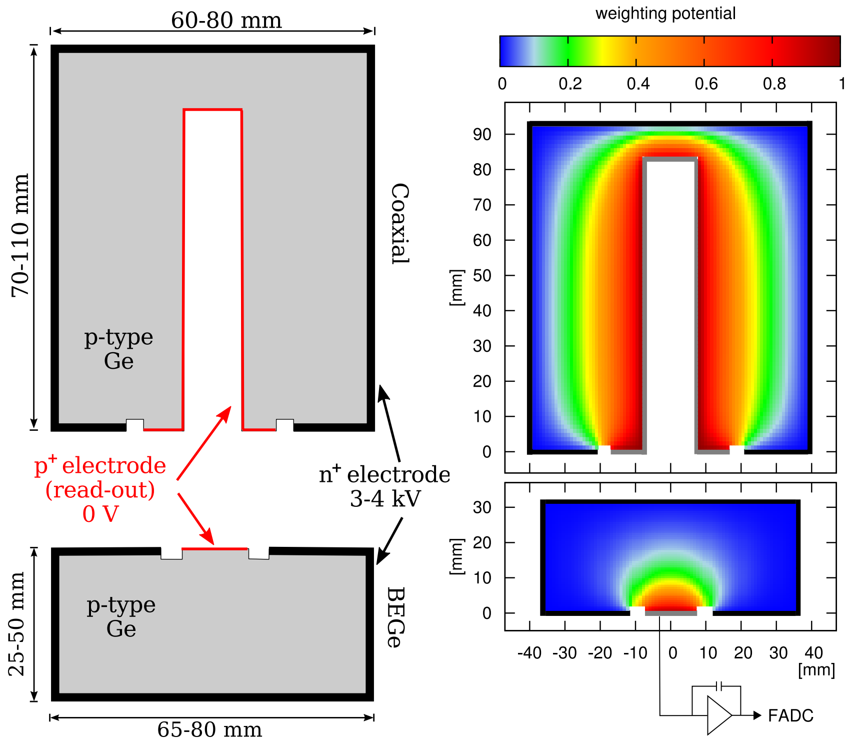

(a) (b)

Fig. 2.4 (a) Cross section of a semi-coaxial detector (top) and a ^{enr}BEGE detector (bottom). The p^+ and n^+ electrodes are indicated in Grey and black, respectively. The electrodes are separated by an insulating groove. (b) Weighting potential of a semi-coaxial (top) and a ^{enr}BEGE detector (bottom) shown with color profiles.[80]

Semi-coaxial detectors The semi-coaxial detectors are characterized by a cylindrical shape with a bore hole on one of the flat surfaces. The core of the crystal is either removed completely (true-coaxial) or partially (semi-coaxial). The lithium diffused n^+ electrode extends across the outer mantle and top surface. It is separated by a circular groove from the boron-implanted p$^+$ read-out electrode. The p$^+$ electrode covers the bore hole surface with a thickness of only about 1 µm and connects to a charge sensitive amplifier (see Fig. 2.4a, top left). Generally limited by the maximum depletion depth of only several centimeters, compared to $^{\mathrm{enr}}$BEGE detectors much larger active volumes can be achieved for semi-coaxial detectors with masses exceeding 2 kg. Due to the core position of the electrode, the detectors height can be extended to about 10 cm in axial direction (compared to typical height of 2 to 4 cm for $^{\mathrm{enr}}$BEGE detectors). The detectors were operated by biasing the n$^+$ electrode with high voltages reaching from 3 to 4.6 kV.

The electric field configuration of the coaxial configuration varies inversely with the radial distance from the detector axis, resulting in a strongly inhomogeneous weighting potential. Because of the radial variation the drift velocities change as the carriers are collected. The effect of the different mobilities of the electron and hole is clearly reflected in the resulting pulse. This generally brings the ability to resolve the radial dependence of the interaction position within the detector volume, but involves an existing library of position dependent pulse shapes or further analysis based on multi-parameters. In Sec. 3.2.5, a compilation of the pulse shape strategy applied by GERDA will be presented.

Broad energy germanium detectors The $^{\mathrm{enr}}$BEGE detectors are likewise cylindrically shaped, but enclose a small-sized boron-implanted p$^+$ electrode on one of the flat surfaces (see Fig. 2.4a, bottom left). Along with the minimized capacitance of the detector it reduces the electric noise. Thereby, a superior energy resolution and a lower energy threshold can be achieved with respect to the standard semi-coaxial detectors. But the small area of the p$^+$ electrode disables the realization of large volume diodes with a feasible depletion voltage. Hence, the crystals are on average 2-3 times smaller than the semi-coaxial detectors, with diameters from 58.3(1) mm to 79.0(1) mm, heights from 22.9(3) to 35.3(1) mm and masses below 900 g. To maximize the number of detectors to get out of the Ge ingots, conical tail slices were used leading to 9 detectors with a conical shape. The average active volume (AV) fraction f_{av} and the total active mass M_{act} of all $^{\mathrm{enr}}$BEGE detectors have been determined. The values include a correction which considers a growth of the full charge collection depth (FCCD) by 0.2 to 0.3 mm due to storage at room temperature over a period of three years before deployment in GERDA [87], as specified in Tab. B.2. All crystals feature different doping and impurity properties and, consequently, exhibit slightly different electrical properties. Prior to installation, all $^{\mathrm{enr}}$BEGE detectors have been characterized by their leakage currents, their detection efficiencies, as well as their spectroscopic and pulse-shape discrimination (PSD) performance [85],[87].

Arising from the small area of the p^+ electrode, the $^{\mathrm{enr}}$BEGE detectors possess a characteristic electric field distribution. The weighting potential has a strong variation concentrated around the small p^+ electrode. Elsewhere throughout the detector volume, it is relatively weak (see Fig. 2.4b). Consequently, the length of the path to reach the strong weighting potential, thus the drift times of the charge carriers, depend on the site of the interaction and cause differences in the rising part of the induced pulse. Besides, the majority of the charge is collected only at the very end of the trajectory of the charge drift. Moreover, the contribution by the electron is expected to have only an influence at the beginning of the pulse with a negligible amplitude for the most of the interaction points within the detector volume. The induced signal remains small until the charge arrives the electrode and then increases strongly until the holes are collected. Compared to the usual coaxial detectors, the pulse shape analysis enables a superior event classification used for background rejection. How GERDA takes advantage of the capability to discriminate background events from signal events will be presented in Sec. 3.2.5.

Chapter 3

GERDA Phase II background reduction strategies

In Phase II, GERDA aimed to increase the sensitivity by reducing the background by one order of magnitude. To achieve such a low background level, the second phase of GERDA required supplementary background suppression systems with respect to Phase I. Besides, a more strict radio-purity criteria has been pursued when selecting construction materials. In order to further optimize the signal to background ratio at $Q_{\beta\beta}$, a multitude of background reduction techniques were applied. However, such techniques can only be built on the knowledge and estimation of the background sources observed in the energy spectrum. This chapter will start with the background composition of the observed energy spectrum and pass then to the description of the developed strategies.

3.1 GERDA Phase II background sources and contributions

A total exposure of 60.2 kg·yr has been accumulated between December 2015 and April 2018, with a live-time of 683.2 d, for the whole data set for the present work. This includes all $^{\mathrm{enr}}$BEGE (32.1 kg·yr) and $^{\mathrm{enr}}$Coax (28.1 kg·yr) detectors of Phase II. The natural semi-coax detectors are excluded from the analysis. The observed energy spectrum in the energy range from 100 keV up to 5500 keV is presented in Fig. 3.1. The energy spectrum is displayed for events with a detector multiplicity (M) of one (single-detector, M1) and for events with a detector multiplicity of two (two-detector events, M2) (see Sec. 3.2.2) both after removing μ-tagged events (see Sec. 3.2.3). In case of the two-detector events, the summed energy deposition is shown with no further differentiation between the two detector types. The signal processing of digitized traces and the energy reconstruction are performed by an off-line analysis in the GELATIO software framework [88].

Weekly energy calibrations were performed with ^{228}Th sources to determine the energy scale. Through monitoring of the long-term stability of the energy scale, the variation has been identified to be typically smaller than 1 keV [73]. Data or detectors with temporary instabilities of the energy scale are excluded from the analysis for these periods. Accordingly, the effective resolution at $Q_{\beta\beta}$ has been estimated to 3.0(1) keV FWHM for the $^{\mathrm{enr}}$BEGE detectors and 3.6(1) keV FWHM for the $^{\mathrm{enr}}$Coax detectors [36]. For two-detector events the reconstructed energy has to be corrected for cross-talk effects measured by dedicated calibrations and by the γ line of ^{42}Kdecay in the physics data. In order to achieve a full reconstruction efficiency, an energy threshold of 100 keV applies to all detectors in all data sets. The given exposure might differ from the one of the $0\nu\beta\beta$ analysis, since the quality requirements for e.g. the pulse shape discrimination are not necessary for the background analysis prior to these analysis cuts. The quality cuts applied in this work comprise a set of necessary parameters to ensure the rejection of non-physical events [73]. Besides, if not explicitly pointed out, by implication all energy spectra shown in this work are energy distributions of single-detector events after the anti-coincidence (AC) and the muon veto selection. Unless the energy spectra is referred to two-detector events (with muon veto selection), which is explicitly pointed out.

The main background sources have been identified by their prominent features and structures in the observed energy spectrum of the individual data sets:

^{39}Ar & ^{85}Kr Below 565 keV, the GERDA energy spectrum is dominated by the β decay of ^{39}Ar. ^{39}Ar is produced through cosmic rays with a specific activity of (1.01 ± 0.08) Bq/kg in natural argon, corresponding to a ratio ^{39}Ar/$^{\mathrm{nat}}$Ar of $(8.0 \pm 0.6) \cdot 10^{-16}$g/g [89]. In the earth's atmosphere, the long-living ^{40}K captures an electron producing ^{40}Ar, which then creates ^{39}Ar through ^{40}Ar(n,2n)^{39}Ar and similar reactions. Atmospheric argon is liquified for the coolant of GERDA's detectors. ^{39}Ar has a half-life of 268 yr and is a pure β emitter (Q_{β} = 565.1 keV). The resulting spectral shape of the β decay is strongly affected by slight differences of the n^{+} dead layer geometry and composition, particularly on the low energy side. In the two-detector data set, the contribution of ^{39}Ar is less considerable, since the probability of detector coincidences caused by β particles of ^{39}Ar is reduced. Besides ^{39}Ar, the same energy region is also populated by ^{85}Kr up to its β endpoint at 687.1 keV. Although ^{85}Kr decays primarily by β emission ($T_{1/2}$= 10.8 yr), it disintegrates with a branching ratio of 0.44% left in a meta stable state of ^{85}Rb and followed by the emission of a γ ray ($E_{\gamma} = 514$ keV). As a fission

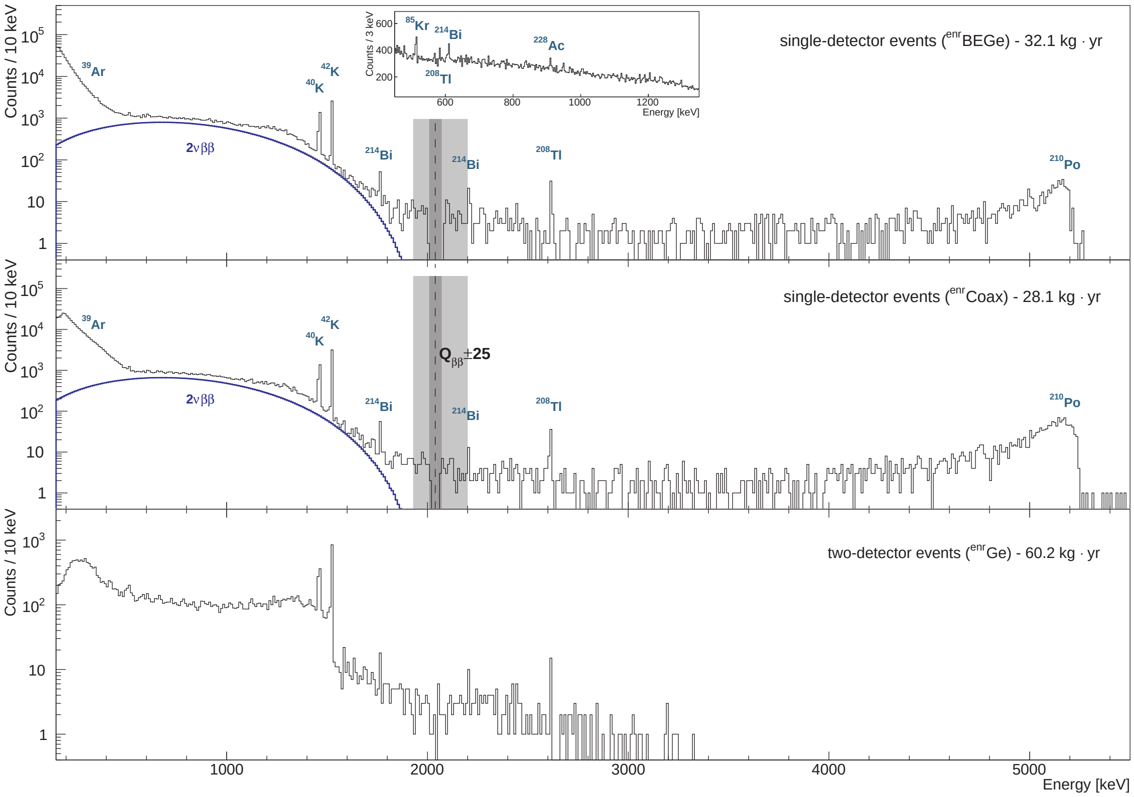

Fig. 3.1 Energy spectra of the single-detector (M1) and two-detector (M2) events collected in the enriched detectors between Dec 2015 and May 2018 corresponding to a total exposure of 60.2 kg·yr. The light grey shaded area represents the ROI in which the BI is evaluated, the dark grey shaded are indicates the blinded energy region. Additionally the most prominent γ lines and structures are marked.

product of uranium and plutonium, it is present in the atmosphere with an abundance in the order of 1 Bq/m^3 [89], but it can be substantially reduced during the liquification of LAr.

$2\nu\beta\beta$ Above the endpoint of the β decay from ^{39}Ar, the energy spectrum is largely dominated by the continuous spectrum due to the $2\nu\beta\beta$ decay of ^{76}Ge. The $2\nu\beta\beta$ is a transition to the 0^+ ground state of the final nucleus which is perfectly allowed by the SM. Apart from that, $2\nu\beta\beta$ is an irreducible background to $0\nu\beta\beta$ search, which can only be reduced through narrowed energy resolution at its endpoint at $Q_{\beta\beta}$ = 2039 keV. No contribution is expected in the two-event data set, since the $2\nu\beta\beta$ takes place localized within a tiny volume due to the minimal separation of the emitted electrons within Ge. The dominating continuous energy distribution attributed to the $2\nu\beta\beta$ decay might superimpose some γ lines resulting barely visible in the energy spectrum in this region, as shown by the enlarged inset of Fig. 3.1. Nevertheless, γ lines of ^{42}K (1524.7 keV), ^{40}K (1460.9 keV), ^{60}Co (1332.5 keV), ^{208}Tl (2614.5 keV), ^{214}Bi (609.3 keV), ^{214}Pb (351.9 keV), ^{234m}Pa (1001.0 keV) and ^{228}Ac (911.2 keV) could be identified unambiguously.

^{42}K The most intense γ line of all data sets appears at 1524.7 keV, stemming from the decay of ^{42}K, the daughter of ^{42}Ar. The isotope of argon, ^{42}Ar, is a cosmogenically produced isotope which undergoes a β decay with a half-life of 32.9 yr. As it has been detected in the LAr of the cryostat, a homogeneous distribution is expected. It decays through a single β (Q_β = 599.0 keV) and has no characteristic γ lines. Since the energy loss of electrons in the n$^+$ dead layer shifts the energy close to or mostly below the analysis threshold of 100 keV. Contributions close to the p$^+$ surface, where the electrons are not effected by the energy shift of the dead layer, were negligible. The decay product of ^{42}Ar is the shorter-lived daughter ^{42}K ($T_{1/2}$ = 12.4 h). It undergoes a β decay with Q_β = 3525.2 keV to the stable ^{42}Ca (see Fig. B.2b). In 17.2% of the cases, ^{42}K decays to an excited level of ^{42}Ca, which de-excites under emission of a 1524.7 keV γ ray. The decay product is in an ionic state and drifts inside the electric field close to the detectors. In consequence, a non-homogeneous distribution and potential hot spot contaminations are expected due to the electric field and an additional transportation by convective flows in LAr.

^{40}K For detectors in a cryogenic environment the electronic components such as resistors or capacitors need a special attention, because of their placement in the direct neighborhood of the detectors. Especially the ceramics of these electronics are carriers of a relatively high concentration of primordial radionuclides. ^{40}K, a naturally occurring radioisotope of potassium, is one of these. Its characteristic γ line at 1460.9 keV has been observed with high significance in the energy spectrum of all data sets. ^{40}K decays to ^{40}Ca through β decay (Q_{β} = 1311.1 keV) with a half-life of $1.3 \cdot 10^{9}$ yr and a branching ratio of 89.3% (see Fig. B.2a). The ground state of ^{40}Ca is populated with 100%. To a less significant degree, it undergoes further transitions to the stable isobar ^{40}Ar via electron capture (Q_{β} = 1504.7 keV) accompanied by γ radiation ($E_{\gamma} = 1460.9$ keV), and with a minor probability of 0.001% through β^{+} decay. As both Q-values, 1311.1 keV and 1504.7 keV, are well below the $Q_{\beta\beta}$, no particular material selection regarding ^{40}K is needed.

^{60}Co ^{60}Co is one of the most common anthropogenic radionuclides with significant amounts, present in construction materials as a consequence of the widespread industrial application of ^{60}Co. With a half-life of 5.3 yr, ^{60}Co undergoes two transitions via β emission followed by γ rays. The more dominant β branch (Q_{β} = 317.3 keV) with 99.88% probability is an allowed transition accompanied by a two photons cascade of 1173.2 keV and 1332.5 keV (see Fig. B.5). The two successively emitted γ rays can be detected simultaneously resulting in a summation peak. The summation peak at 2505.7 keV is additionally populated by only about $\sim 10^{-6}$ % of γ rays from de-exitation with direct transition to the ground stated. The second β decay is an unique second forbidden transition in coincidence with a single γ ray at 1332.5 keV. Besides background contributions stemming from contaminations in man-made construction materials, ^{60}Co can be produced in the bulk of the detectors via cosmic spallation reactions in Ge. The activity of cosmogenically induced ^{60}Co can be estimated according to the known exposition to cosmic rays of the detectors. Even though, some contributions to the energy spectrum due to cosmogenic activation might be expected after several years of underground storage of the Ge detectors, but in view of the known history of the GERDA detectors, these contributions can be neglected in Phase II.

^{238}U & ^{232}Th decay chains The main concern in most $0\nu\beta\beta$ experiments is the natural radioactivity from impurities of ^{238}U and ^{232}Th, which are omnipresent in mineral materials (or earth's crust). Consequently, all progenies are inevitably contained. The selection of components with sufficient radiopurity is therefore essential. Constructing a detector environment with materials of tolerable concentrations can only be guaranteed by controlling the radiopurity by screening measurements prior to application (see Sect. 3.2.1). Even though, a careful selection of materials was pursued, GERDA observes γ lines of several isotopes from the natural decay chains of ^{238}U and ^{232}Th.

The activities among the various members in the decay chain may differ due to a possible lack of secular equilibrium, if the data taking time is in the order of or shorter than the half-life of the decay. Furthermore, a previous processing of material can selectively remove

Table 3.1 Natural decay chain of ^{238}U. The values are taken from [90]

nuclide		$T_{1/2}$	decay mode	Q-value
^{238}U		$4.5 \cdot 10^9$ yr	α	4269.7
	^{234}Th	24.1 d	β/γ	272.0
	^{234m}Pa	1.2 min	β/γ	2269.0
^{234}U		$2.5 \cdot 10^5$ yr	α	4857.7
^{230}Th		$7.5 \cdot 10^4$ yr	α	4769.8
^{226}Ra		$1.6 \cdot 10^3$ yr	α	4870.6
	^{222}Rn	3.8 d	α	5590.3
	^{218}Po	3.1 min	α	6114.7
	^{214}Pb	26.9 min	β/γ	1019.0
	^{214}Bi	19.8 min	β/γ	3270.0
	^{214}Po	162.3 μs	α	7833.5
^{210}Pb		22.2 yr	β	63.5
	^{210}Bi	5.0 d	β	1162.1
	^{210}Po	138.4 d	α	5407.5

nuclide		$T_{1/2}$	mode	Q-value
^{232}Th		$1.4 \cdot 10^{10}$ yr	α	4082.8
^{228}Ra		5.8 yr	β/γ	45.8
	^{228}Ac	6.2 h	β/γ	2123.8
^{228}Th		1.9 yr	α	5520.0
	^{224}Ra	3.7 d	α	5788.9
	^{220}Rn	55.8 s	α	6404.7
	^{216}Po	0.1 s	α	6906.3
	^{212}Pb	10.6 h	β/γ	569.9
	^{212}Bi	60.6 min	α	6207.3
			β/γ	2252.1
	^{212}Po	0.3 μs	α	8954.1
	^{208}Tl	3.1 min	β/γ	4999.0

intermediate members of the decay chain and thus no reliable conclusions can be drawn regarding the presence or absence of daughter nuclides. As a consequence the decay chains are divided into several sub-sequences. In Tab. 3.1, the ^{238}U and ^{232}Th decay chains are listed with a highlighting of the long-lived isotopes for identification of the sub-sequences (or see Fig. B.1 for an overview of the relevant isotopes in the two decay chains).

^{238}U & its progenies The first daughter where the the decay series is broken off is the long-living ^{234}U. The next point where the equilibrium is broken is at ^{234}U. The presence of the intermediate member ^{234m}Pa was indicated by the screening measurements. ^{234m}Pa would account for a background around 2 MeV, since ^{234m}Pa decays via β emission to ^{234}U with a Q-value of 2269 keV and a probability of 98.85%. It disintegrates into the ground state or an excited state of ^{234}U accompanied by γ emission. The weak γ line at 1001.4 keV (with only 0.86% probability) has not been observed with a high significance.

No candidates of the proceeding sub-sequence containing the two long-living α emitters, ^{234}U and ^{230}Th, were observed in the data spectra so far. The presence of the γ lines from ^{214}Bi confirms the presence of the progenies from the sub-sequence starting at ^{226}Ra with several α and β emitters. A particular attention is payed to ^{214}Bi decaying via β (Q_β= 3270 keV) and γ emission (609.3 keV (46.4%), 768.4 keV (5%), 1120.3 keV (15.1%),1238.1 keV (5.9%), 1764.5 keV (15.4%) and 2204.2 keV (4.9%)), which contribute to a large extend to the background in the ROI (see Fig. B.4). On one hand, the γ can deposit energy via Compton scattering in a detector and then release the remaining energy in LAr producing scintillation light. On the other hand, it can undergo a Compton scattering in one detector getting absorbed via photo-effect in another detector.

Finally, ^{238}U chain can be broken at ^{210}Pb and at ^{210}Po. The presence of ^{210}Po is confirmed by peak-like structure around 5.3 MeV, since the passage through the p^{+} dead layer reduces the α energy compared to the original 5407.5 keV. The isotopes in the decay chain preceding ^{210}Po are the two β emitters ^{210}Pb and ^{210}Bi with Q-values of 63.5 keV and 1162.1 keV, which do not leave traces in the high-energy region and cannot be distinguished via characteristic γ lines. The presence or absence of this isotopes can only be assessed by the analysis of the time structure of the ^{210}Po decays. The constituents of the ^{238}U decay chain are categorized by the kind of particles the isotopes emit (α versus γ/β emitter).

^{232}Th & its progenies With maximal energy released in the considered energy range above 575 keV, the isotopes of the ^{232}Th decay chain with potential contributions are ^{228}Ac, ^{212}Bi and ^{208}Tl. The decay chain of ^{232}Th breaks in the second sub-sequence after ^{228}Ac, indicated by the 911.2 keV (26.5%) and the 968.9 keV (16.1%) γ lines, whereas ^{212}Bi and ^{208}Tl are part of a sub-sequence starting with ^{228}Th. The presence of the sub-sequence of ^{228}Th demonstrated by the observed lines at 583.2 keV (86.7%), 860.5 keV and 2614.5 keV (100%) from ^{208}Tl. Additionally, the 511 keV line from photons emitted in the ^{208}Tl decay, as well as by the photons resulting from e^{+}e^{-}-annihilation can be observed. No indications for the presence of α emitting isotopes in the ^{232}Th and corresponding sub-sequences could be found, so all contributions from far sources can be neglected.

^{208}Tl decays via β decay to various excited levels of ^{208}Pb (see Fig B.3). The most prominent γ ray from ^{208}Tl is the 2614.5 keV γ ray which is preceded by the emission of a 583.2 keV γ ray with 86.7% probability. The γ ray with 2614.5 keV is part of a γ cascade in the de-excitation of ^{208}Pb, since there exists no direct β decay to the 2614.5 keV level or the ground state of ^{208}Pb.

α emitting isotopes Above the Q-value of ^{42}K, several peak-like structures at 4.7 MeV, 5.3 MeV, 5.4 MeV and 5.9 MeV can be observed. Since the highest γ line which can be attributed to a natural occurring isotope is at 2614.5 keV from ^{208}Tl and the highest Q_{β} value is at 3525.2 keV from ^{42}K, these structures are attributed to α decays from the ^{238}U decay chain, mainly from ^{210}Po, but also from ^{226}Ra and ^{222}Rn, and their progenies. The peak-like tail is almost exclusively expected from the ^{210}Po contamination close to the p^{+} surface with a slightly lower maximum than the corresponding decay energy. As can be seen in the two-detector energy spectrum of Fig. 3.1, no coincidence contribution is expected in multiple detectors, since the range of α particles in LAr is limited.

Cosmogenic induced isotopes If the crystals are exposed to cosmic radiation during the transportation or the manufacturing process, different short-and long-living isotopes can be generated. The resulting intrinsic activation of the crystals is caused mostly by spallation reactions of fast nucleons from cosmic rays and by smaller contributions due to capture of stopped negative muons and muon induced fast neutrons. Beside ^{60}Co, ^{68}Ge is worth considering as it is a β emitter decaying with $T_{1/2}$= 270.8 d to ^{68}Ga which further disintegrates within minutes via β decay (Q_β = 2921.1 keV), electron capture and β^+ decay. Nevertheless, in view of the exposure history and underground storage for several years it can be assumed that the majority of the contamination produced during their exposure to cosmic radiation during production and refurbishing does not contribute significantly to the energy spectrum.

Muons-induced neutrons can create isotopes by inelastic scattering (n,X) reactions when passing the water tank or the LAr cryostat. Moreover, thermalized neutrons can be captured by the Ge crystals or the liquid argon. The formed isotopes typically de-excite with prompt emission of single or multi γ cascades. However, transitions through β decay or to a meta-stable state can occur. Three neutron-induced isotopes can be empathized: $^{77(m)}$Ge due to neutron capture on ^{76}Ge, $^{75(m)}$Ge due to neutron capture of ^{74}Ge and ^{41}Ar due to neutron capture on ^{40}Ar. Even though the predicted contribution of $\sim 10^{-4}$ cts/(keV·kg·yr) at $Q_{\beta\beta}$ is lower than the target background index of Phase II, the main concern raised by muon-induced isotopes with potential background contribution in the ROI is addressed to $^{77(m)}$Ge [91]. A study of potential contribution to the energy spectrum originating from neutron-induced isotopes could only place an upper limit [92].

Anthropogenic isotopes As it is the case for ^{137}Cs and ^{110m}Ag, ^{207}Bi is an anthropogenic isotope which is released into the environment in accidents of nuclear plants or weapon tests. Previous investigations of the relative strengths of γ lines in the measured energy spectrum of the individual data sets yield information on a possible presence of ^{207}Bi. The long-lived bismuth nuclide that disintegrates to ^{207}Pb by electron capture ($T_{1/2} = 32.9$ yr and $Q_\beta = 2397.5$ keV) and simultaneous emission of γ rays (the main ones being at 569.7 keV (97.8%) and 1063.6 keV (74.6%)). In the Phase II spectra, a vague indication for a γ line at the 1063.6 keV from ^{207}Bi could be assigned to the enriched coaxial detectors, giving a hint on the presence of a possible contamination in this detector type. Anyway, the low energy line at 569.7 keV is not visible and the enhancement in the region of the expected γ line at 1063.6 keV is not significant enough to favor a clear evidence for the presence of this isotope. Furthermore, the GERDA energy spectrum could not provide an evidence for the presence of further long-living anthropogenic nuclides.

3.2 GERDA Phase II background reduction strategies

The experimental signature for $0\nu\beta\beta$ decay is a sharp peak at the Q-value given by the summed energy of the two released electrons. Because of the short range of the two electrons in Ge a $0\nu\beta\beta$ event taking place in the detector bulk volume will manifest itself as an absorption of the two β particles within a small, localized volume. A localized energy deposition is commonly referred to as a single-site event (SSE). Thus, events in which more than one Ge detector has an energy deposit (AC cut) are rejected as background events. While γ rays can be distinguished by multiple Compton scatterings separated by ≈ 1 cm in Ge (multi-site event, MSE), external α or β rays can be characterized by their energy deposit on the detector surface. A pulse shape analysis allows to manifest event topologies which can be used for discrimination.

Furthermore, nearby radio-active contaminated solids can either release β particles which mostly get absorbed in the contaminated solid itself or release γ rays which can deposit energy around the $Q_{\beta\beta}$ in Ge and additionally deposit the excess energy in LAr. For that purpose, light sensors have been installed in order to identify and veto background signals coincident with the Ge signal within 5 µs (LAr veto).

Efficient suppression strategies have been chosen which take into account the characteristics of event classes and topology of the individual background contributions already brought up in the previous section. The following sub-sections will present a short overview and motivation for the rejection and suppression strategies applied in Phase II, more precisely for the radio-purity selection criterion, the detector anti-coincidence (AC) cut, the muon veto cut, the LAr veto cut and the pulse shape discrimination (PSD). For a higher comprehension on the strategies presented, [80], [82], [93], [94] and [95] are recommended.

3.2.1 Screening measurements

To achieve a reduction by one or two orders of magnitude, all used materials were selected carefully in preparation of Phase II. Therefore, state-of-the art screening techniques have been used: gamma ray spectroscopy with HPGe spectrometers, gas counting with ultra-low background proportional counters and mass spectrometry with Inductively Coupled Plasma Mass Spectrometers (ICP-MS). Tab. B.1 shows the results of the measurements from materials installed nearby the detector array. The dominating decay modes and the corresponding total energies are given.

With the purpose of reducing the amount of construction materials and improving their radio-purity, the following components have been replaced: The copper holder plates which serve to position the vertical copper bar taking the weight of the Ge detectors have been substituted by extremely radio-pure ones made from mono-crystalline silicon. Also the signal and high voltage cables which are attached with bronze clamps to the plates have been replaced by cleaner ones. Furthermore, the charge sensitive preamplifiers have been substituted by cleaner ones. The copper mini-shrouds were substituted by nylon mini-shrouds to permit the scintillation light generated near the detectors to be seen by the LAr veto system.

3.2.2 Detector anti-coincidences

While the $0\nu\beta\beta$ event is apparently a localized energy deposition in the crystal bulk, a γ ray is likely to Compton scatter out of one detector before depositing all of its energy due to the crystals small diameter and thickness of only few centimeters. Leaving one detector, it might create simultaneous pulses in additional detectors that can be used to effectively suppress this background type. Thus, multiple detector hits are discarded by a detector anti-coincidence cut as background events.

3.2.3 Muon veto

The rock overburden already reduces the μ flux by a factor of 10^6. However, the remaining flux is a non-negligible background in the ROI when increasing the sensitivity and aiming a background index below 10^{-2} cts/(keV·kg·yr). The cosmogenically produced μs have an average energy of about 270 GeV, leading to a specific energy loss of 2 MeV per $(\mathrm{g} \cdot \mathrm{cm}^2)$. Therefore, a μ can create an enormous amount of Cherenkov light in the water as well as scintillation light in the inner LAr cryostat. Consequently, the water tank is used as active Cherenkov veto to tag μs depositing energy directly or through decay radiation of spallation products. An event tagged as μ requires either at least 5 out of 66 PMTs in the water tank or a triple coincidence of the plastic veto on the roof of the GERDA clean room. Besides, the trigger condition for the PMTs of the water tank requires the collection of more than 0.5 photo-electrons within 60 ns. If a μ tagged event precedes a Ge trigger by less than 10 µs, the Ge event is rejected leading to a dead time of less than 0.1%.

A mean daily rate of 3164(6) μs was measured in Phase II which translates into a μ rate of $3.54 \cdot 10^{-4}/(\mathrm{m}^2 \cdot \mathrm{s})$. This result is consistent with Phase I and differs only by 1.8% from the mean rate of Phase I. The daily rate of an arbitrary selection of PMTs, representative for the majority of all 66 PMTs, is shown in Fig. 3.2, demonstrating the long-term stability of the whole veto system for more than 2.5 years.

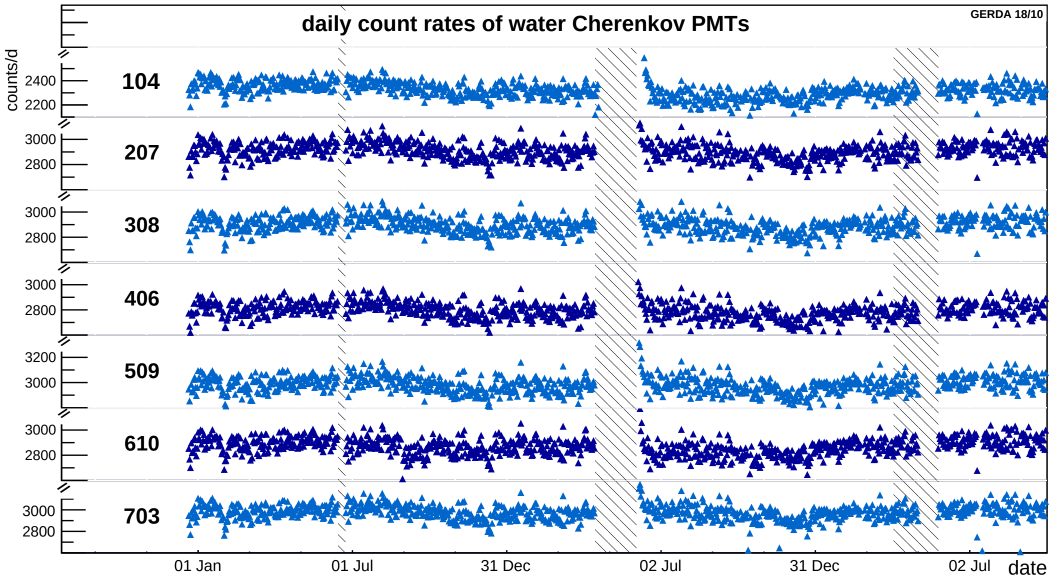

Fig. 3.2 Daily rate of 7 representative water Cherenkov PMTs from December 2015 till July 2018. The numbers indicated on the left denote the PMT labels defining the position and data channel.

A total of 5478 events tagged as μs with an energy deposition in one or more enriched Ge detectors ($^{\mathrm{enr}}$BEGE and $^{\mathrm{enr}}$Coax) was found in the aforementioned data sets. The energy distribution of these μ coincident Ge events is displayed in Fig. 3.3a. Muons are most likely to deposit energy in more than one Ge detector which then can be vetoed by the AC cut with a survival probability of about 75%. A volume separated from the main water tank (denoted as the pillbox) is located directly below the LAr cryostat. It is instrumented with six PMTs out of which one PMTs is broken. The objective of the pillbox is to detect muon coming from straight above crossing eventually the detector array depositing only a small amount of energy in the main water tank. This holds for only one muon event which does not traverse the main water tank such that it deposits enough energy to fulfill the necessary trigger condition for the PMTs of the water tank, but this event is seen by the pillbox. Conversely, a fraction of 5.8% of the μs do not pass through the pillbox, but are seen by the water tank PMTs. Even tough a fraction of 1% of the muons escape detection through scintillation light in the LAr veto, the LAr veto consolidates the μ rejection power of the muon veto. All these events which escaped detection though scintillation light populate the low energy part of the spectrum far below the ROI, such that these events do not contribute to a background at $Q_{\beta\beta}$. Unfortunately, no unambiguous μ identification in the LAr veto can be determined, because of a missing veto trigger of the LAr veto independent from the Ge trigger. Hence, μs escaping detection by the muon veto system can not be verified by the LAr veto.

The benefit of the systems shows the improved background index due to the muon veto in the ROI which would have led without the muon veto to a contribution of

$$3.18 \cdot 10^{-3} \mathrm{cts}/(\mathrm{keV} \cdot \mathrm{kg} \cdot \mathrm{yr}). \tag{3.1}$$

Extracted from MC simulation for Phase I, the entire veto reaches a detection efficiency of

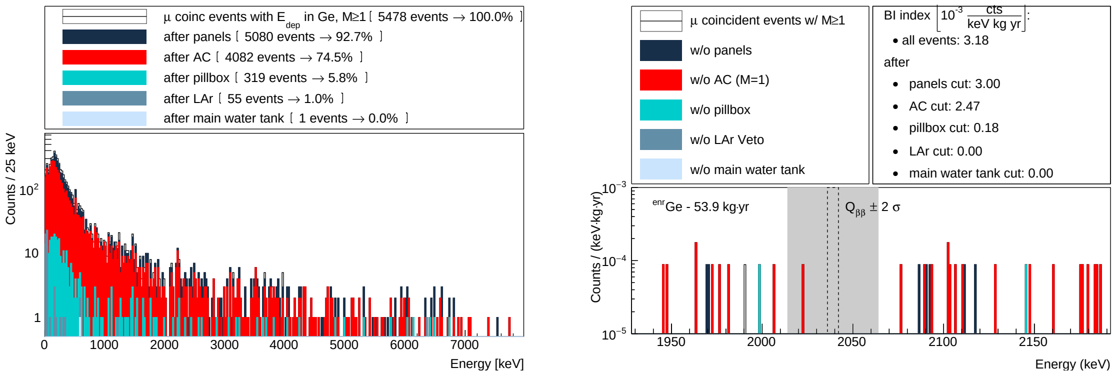

(a) (b)

Fig. 3.3 (a) The measured energy spectrum of $^{\mathrm{enr}}$BEGE and $^{\mathrm{enr}}$Coax detectors for μ coincident Ge events without AC cut ($M \geq 1$) before and after various cuts whereby the muon veto trigger condition is applied to PMT supgroups depending on the PMT position: panels, pillbox (volume below LAr cryostat) and main water tank. (b) Shows the energy spectrum for μ coincident Ge events with $M \geq 1$ before and after various cuts in the analysis window around $Q_{\beta\beta}$.

$(99.935 \pm 0.015)\%$ for muons with energy deposition in the Ge detectors [82]. Assuming this rejection, the background index of Eq. 3.1 converts to a remaining BI of

$$2.07 \cdot 10^{-6} \mathrm{cts}/(\mathrm{keV} \cdot \mathrm{kg} \cdot \mathrm{yr}) \tag{3.2}$$

after applying the muon veto cut. How the aforementioned cuts affect the energy distribution in the ROI is shown in Fig. 3.3b.

3.2.4 LAr veto

If ionizing radiation passes though the LAr a number of scintillation photons are produced by the superposition of the decays of an unstable (singlet) and meta-stable (triplet) excited dimers (so-called excimer) state [96]. By the de-excitation process of the Ar_2^* excimer, 41,000 extreme ultra-violet (XUV) photons are generated per MeV which peak at a wavelength of 128 nm of electron-equivalent energy deposition [97] for the fast (singlet) and slow (triplet) component. The veto condition is fulfilled when at least one photo-electron is detected within an optimized time window of 6 µs around the Ge trigger.

A strong rejection power is expected mainly for particles released in LAr, especially γs originating from contaminations of the solids in the vicinity of the array or the close-by materials. Concerning γ lines, the FEP can occur without releasing energy in LAr causing only random coincidences. In contrast, a significant suppression is expected for the SEP at 511 keV and the DEP at 1022 keV. A potential trigger due to Compton scattered events depends on the total energy of the γ ray. The energy which remains after an energy deposition in ROI can create scintillation light. Depending significantly on the exact location and the residual energy, β particles might escape an efficient detection, because of the short absorption length in Ge and LAr.

The capabilities of the LAr veto are revealed by the energy spectrum shown in Fig. 3.4a. The spectrum in coincidence with the LAr veto contains practically only the Compton continuum hiding the SEP and DEP peaks due to poor statistics. However, the 583 keV and 609 keV γ lines of ^{208}Tl and ^{214}Bi, respectively, appear visible in the coincidence spectrum, since the γ rays are emitted as part of γ cascades. Additionally, the strong reduction power of the LAr veto is demonstrated by the population of events in the 1525 keV line of ^{42}K. Due to a β and γ cascade of which the β particle can release up to 2 MeV in the LAr itself, the γ line at 1525 keV is suppressed by typically a factor 5 (see inset of Fig. 3.4b). On the other hand, the ^{40}K line at 1461 keV is barely reduced due to the electron capture without further energy release in LAr. The induced dead time due to this γ line can be used to calculate the LAr veto acceptance independent of the test pulser injected in the data set. In order to verify the stability and performance of the system, the two potassium lines at 1525 keV and 1461 keV have been monitored continuously during data taking. A potential $0\nu\beta\beta$ signal loss due to random coincidences predominately caused by ^{39}Ar leads to an exposure weighted dead time of $(2.3 \pm 0.1)\%$.

Furthermore, the performance of the LAr veto system has been tested by determining suppression factors from ^{228}Th and ^{226}Ra sources. Apart from depending strongly on the source position, suppression factors for the events in the region around $Q_{\beta\beta}$ are 98 ± 4 for the ^{228}Th Compton continuum and only 5.7 ± 0.2 for ^{226}Ra, respectively. With quenching factors reaching from 0.85 up to 0.88 at 1 MeV, the number of scintillation photons produced by an α particle is smaller than the one by γ or β particles of the same energy [98]. This is the reason why a background reduction with less extent is expected for the ^{226}Ra chain, since ^{226}Ra and its progenies decay primarily through α decays on the detector surface. Except

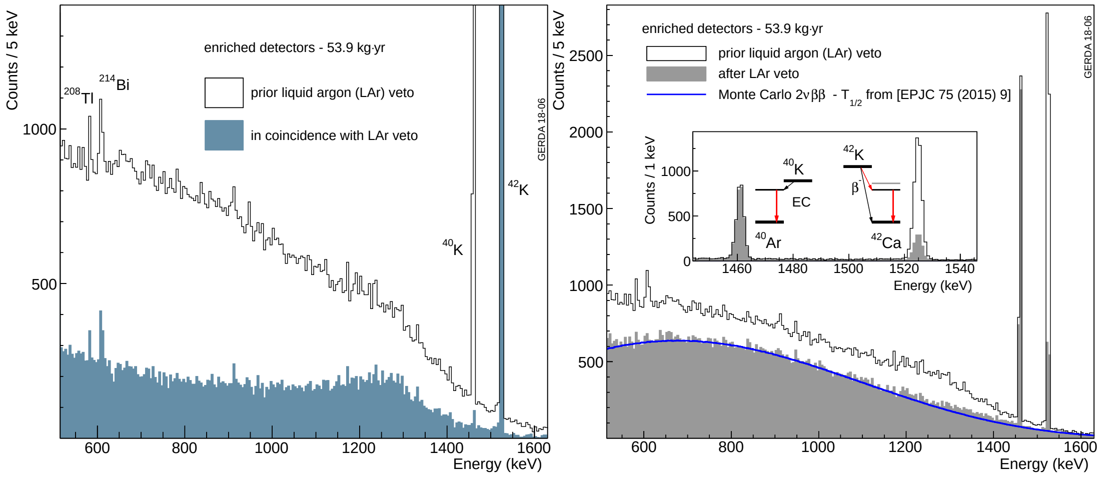

(a) (b)

Fig. 3.4 (a) Spectrum in the $2\nu\beta\beta$ decay dominated energy region prior to and in coincidence with the LAr veto. (b) Energy spectrum in the same energy range after the LAr veto suppression together with a spectrum of simulated $2\nu\beta\beta$ decays (solid line). Inset shows a zoom of the full energy γ lines from ^{40}K and ^{42}K.

^{214}Bi which is the only progeny which can be further discriminated by several orders of magnitude using the fraction of the prompt ^{214}Bi β and γ signal deposited in the LAr.

The total efficiency of the veto can be characterized by the interplay of suppression efficiency in a certain energy range and the $0\nu\beta\beta$ signal acceptance. The signal acceptance is estimated through test pulser injected in the data set leading to $((97.7 \pm 0.1)\%)$. Both suppression factor and veto acceptance depend strongly on the veto window and energy threshold defining the rejection or acceptance. The reduction of the veto acceptance due to random coincidences, mainly due to ^{39}Ar, is additionally cross-checked by calculation of the survival fraction of single γ lines of the FEP from ^{40}K.

3.2.5 Pulse shape discrimination

The $^{\text{enr}}$BEGE detector configuration implies an electric field profile (see Fig. 2.4b, bottom) that results in a specific time profile of its current pulse. This allows for a powerful discrimination between event topologies. In case of a SSE, the charge clusters have a spatial extent so small that the electric field does not change significantly across its width. The charges drift towards the respective electrodes, resulting in only one peak in the current signal with an amplitude proportional to the charge contained in the cluster. Thus, the current signal is also proportional to the total energy deposited. Independent from the location in the active volume, except for a small region around the read-out electrode, the ratio between the amplitude and the energy remains constant for a given total energy (see Fig. 3.5, top left).

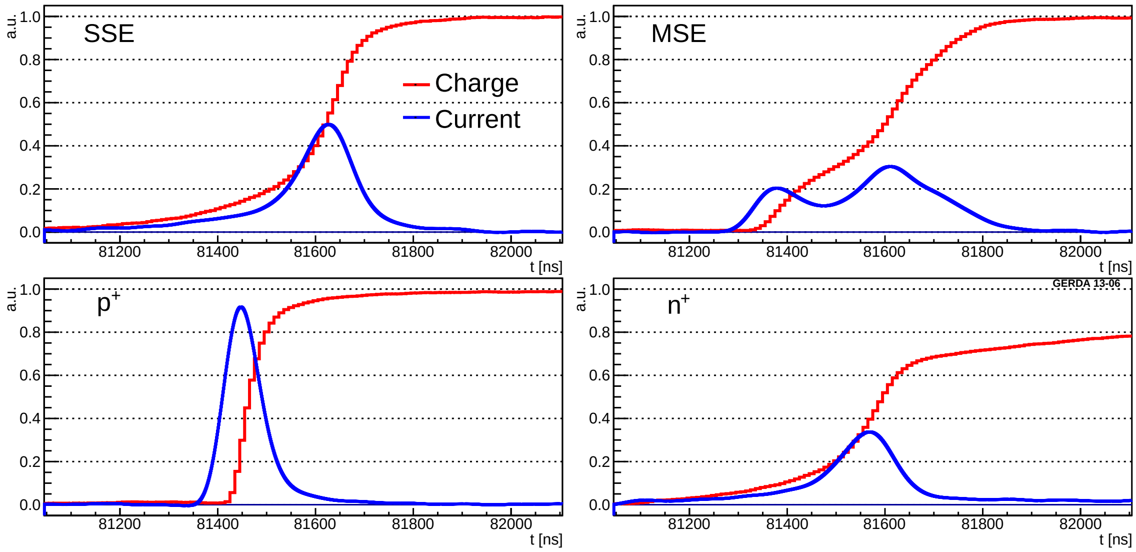

Fig. 3.5 Pulse shapes illustrative for a SSE (top left), MSE (top right), p^+ electrode event (bottom left) and n^+ surface event (bottom right). The charge pulses (red solid line) are shown as a function of time together with its interpolated derivative, i.e. the current (blue solid line). The amplitudes of the maximal charge pulse are normalized to unity. [99]

Since the electrons drift mostly though the volume of a weak electric field, the electrons have much longer drift times and the holes predominantly contribute to the formation of the charge signal. In case of multiple Compton scattering, the energy is divided between smaller spatially separated charge clusters, which create several current peaks with smaller amplitudes (see Fig. 3.5, top right). The resulting signal is kind of a superposition of several SSE energy depositions, which are shifted in time. The time shifts arises from the different drift times until the charges reach the region of the strong weighting potential. Compared to a pure SSE of the same total energy, a reduced amplitude of the highest peak in the current pulse (differentiated charge signal) can be expected. The charge collection on the signal electrode yields different time-structures of the current signal. β events have small penetration depths and are partially absorbed in the dead layer, which is separated from the active volume by a transition layer. In the transition layer, the detector is not completely insensitive to particle interactions. Instead of drifting towards the read-out electrode, the charge carriers diffuse slowly causing a dilated time profile of the rising edge of the charge signal (see Fig. 3.5, bottom right). Consequently, a reduced ratio A/E of the amplitude A of the current pulse and the total energy E can be expected for such a slow pulse. Due to the fact that the main background at $Q_{\beta\beta}$ is caused by nearby sources of the U/ Th progenies,

^{42}K, and α surface events, the time profile can be used to discriminate SSE against MSE or surface background events by the single parameter A/E [99].

A calibration spectrum for ^{228}Th is displayed in Fig. 3.6a. The DEP at 1593 keV from ^{208}Tl, which consists predominantly of SSEs, is barely diminished by the A/E cut with a survival probability of about 87% (see Tab. 3.2). On the other hand, the SEP at 2104 keV and the FEPs at 1621 keV and 2615 keV are significantly reduced to a level of less than 15% due to a high fraction of MSEs. Accordingly, the lower threshold of the A/E cut is chosen according to a 90% acceptance of DEP events of ^{208}Tl. For each detector the exact value of the cut parameter was optimized with calibration data for each time period and at different energies.

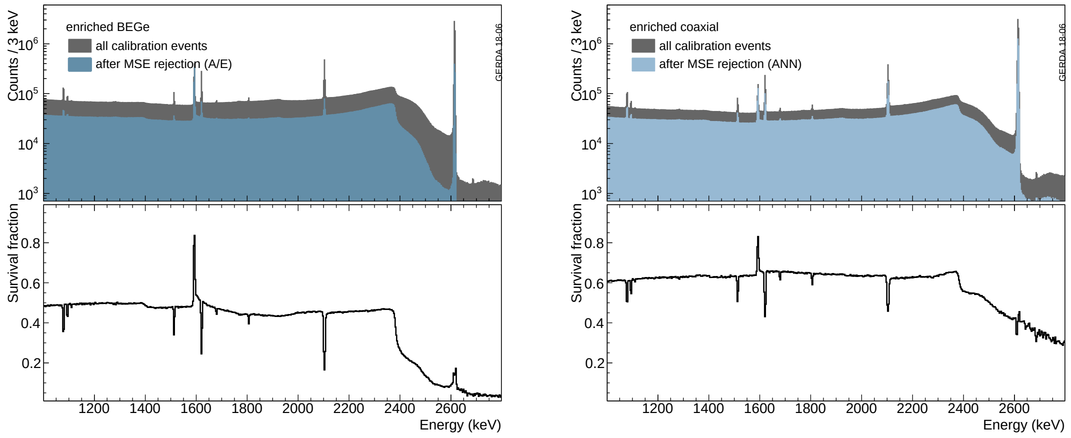

(a) (b)

Fig. 3.6 ^{228}Th calibration spectra of $^{\text{enr}}$BEGE (a) and coaxial detectors (b) before and after multi-site event rejection using the two different PSD techniques. The respective bottom panels shows the survival fraction as a function of energy, i.e. the ratio of the spectra with and without PSD.

In Figure 3.7a, left side, the PSD classifier $(A/E-1)/\sigma(E)$ is shown versus energy, which is the corrected A/E parameter normalized by the energy-dependent A/E resolution σ. Events which survive the LAr veto selection are accepted SSE-like events and are marked in blue. The two potassium peaks and Compton scattered γs are reconstructed at negative A/E values while all α events at higher energies exhibit a high A/E value. A lower value of the A/E parameter is typical for MSEs compared to SSEs and surface events. α particles can only penetrate very thin layers like the insulating groove ring between n$^+$ and p$^+$ electrodes or the p$^+$ contact, where the gradient of the weighting potential is largest. As a consequence, the electrons contribute also to the signal creation. The current signal induced close to the read-out electrode has a larger amplitude and a steeper slope leading to normalized A/E values > 1, because the induced current signal has the largest amplitude when charges

Table 3.2 Event suppression fractions of one-sided low and high A/E cuts together with the survival fractions of a two-sided cut given for the SEP, two FEPs and the DEP from physics and calibration of the $^{\mathrm{enr}}$BEGE detectors [80].

Region	Low cut (%)	High cut (%)	s.f. (%)
DEP (1593)	10.0(2)	2.68(6)	87.3(2)
FEP (1621)	83.5(3)	1.62(8)	14.9(3)
FEP (2615)	83.58(3)	1.82(1)	14.60(2)
SEP (2104)	87.8(2)	1.55(4)	10.6(2)
(2039 ± 35) keV	52.5(1)	2.20(2)	45.3(1)

drift though the volume of the strongest weighting potential. The enhanced A/E value can then be used to discriminate events triggered in this region. A survival fraction of $(87.6 \pm 0.1(stat) \pm 2.5(syst))\%$ has been estimated for $0\nu\beta\beta$ events.

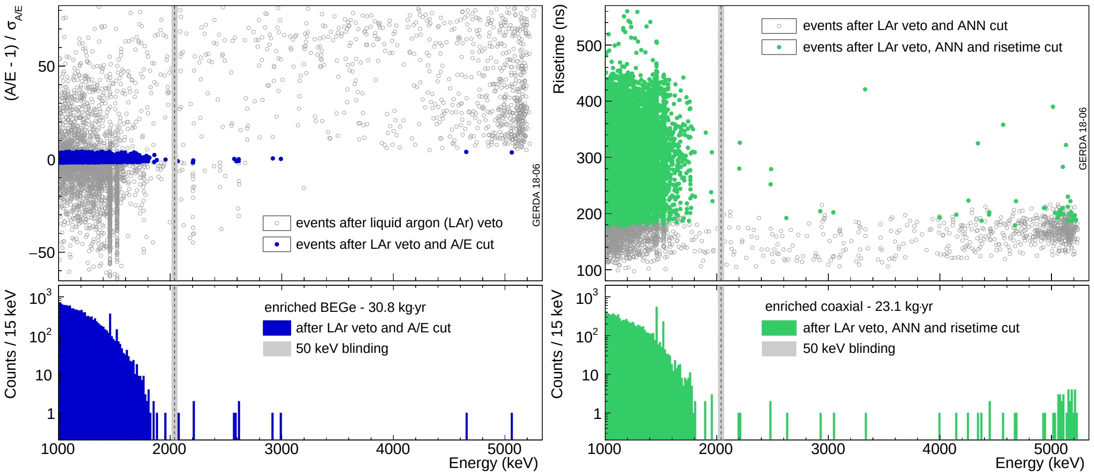

(a) (b)

Fig. 3.7 The measured GERDA Phase II energy spectrum of $^{\mathrm{enr}}$BEGE (a) and semi-coaxial (b) detectors after the various background rejection cuts.

The semi-coaxial detectors possess a more inhomogeneous weighting potential (see Fig. 2.4b, top) with inferior capability for pulse shape analysis. Hence, the potential is non-zero in most of the detector volume and both charge carrier types contribute to the charge collection. Huge differences can arise at the very beginning or end of the pulse depending on the carrier drift. As illustrated by a collection of simulated pulse shapes for SSE in Fig. 3.8a varying along the radial distance from the bore hole, the contribution of the electrons and holes highly depends on the location of the energy deposition. Even the current signal of a SSE may feature two peaks, thus the A/E parameter is not suitable. Still, the digitized charge trace contains all relevant information on events occurring within the bulk volume.

A multi-parameter analysis method based on an artificial neural network (ANN) provides an alternative classifier with best performance. The input parameters are extracted from the rising parts of the linearly interpolated charge pulse samples, reaching from 1% to 99% of the full normalized amplitude in increments of 2%. The point where the pulse reaches 50% of its amplitude is used as a reference (see Fig 3.8b). The ANN-based pulse shape analysis discrimination is carried out by using the Toolkit for Multivariate Data Analysis (TMVA) implemented in ROOT [100]. It studies systematically the given input parameters and classifies the events as signal-like or background-like events. The output of the neural network is a qualifier number between 0 (background-like) and 1 (signal-like event).

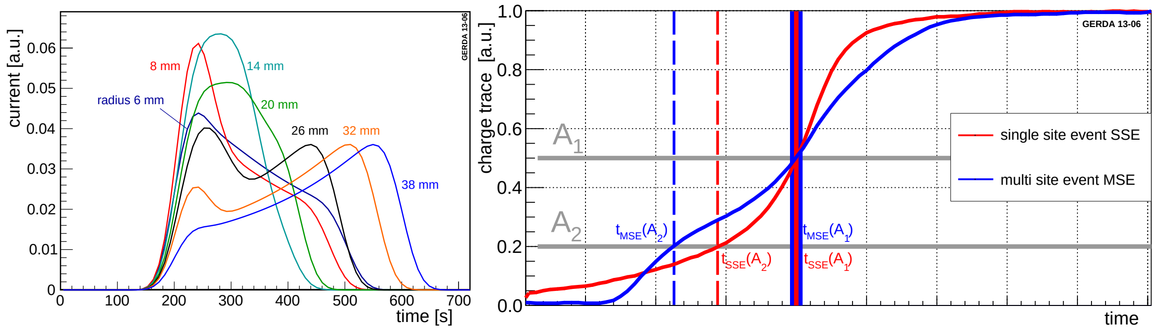

(a) (b)

Fig. 3.8 (a) Simulated current pulses for SSE events at various locations of a semi-detector normalized to its integral. The pulse shapes are calculated for different location starting at the outer n^+ surface going along a radial line at the mid-plane towards the bore hole. (b) Recorded physics data pulses for SSE and MSE candidate events. The extraction of the input parameters for the neutral network is shown. The colored lines give the corresponding reference times at 20% (A_2) and 50% (A_1) of the maximum pulse amplitude. [99]

Again the events of the DEP in 1593 keV ± FWHM represent a proxy for SSE, while the FEP of ^{212}Bi around 1621 keV contains dominantly MSEs and is therefore used as a sample for background events. Consequently, for a MSE based ANN rejection the DEP and the FED are used to create training libraries of signal-like and background-like events, respectively. To correctly identify events, the training has been performed using ^{228}Th calibration data. The survival fraction of ^{228}Th calibration spectrum is displayed in Fig. 3.6b demonstrating that contributions originating from the FED and the Compton continuum are significantly reduced while the contribution from the DEP remains almost untouched. Analogously, the qualifier has been adjusted to keep 90% of the DEP events of the 2.6 MeV γ line of ^{208}Tl decay. The cut threshold is determined individually for each detector and period, which varies between 0.302 and 0.455. A study of possible volume effects and energy dependence of the efficiency $0\nu\beta\beta$ decay has been carried out with events at the Compton edge (rich with

SSE) and at slightly higher energies (almost pure MSE) leading to a systematic uncertainty of about 5% [99].

A separate ANN is used to reject surface α events on the p+ electrode. The α event sample is trained by using $2\nu\beta\beta$ events remaining after the LAr-veto cut and events with an energy deposition above 3500 keV [99]. Furthermore, the α rejection is consolidated by a complementary rise time (RT) selection performed on the noise reduced and interpolated signal. It is specified by the time difference between the intermediate rise times at 10% and 90% of the maximum signal amplitude. The RT cut value is optimized in such way that it maximizes the $2\nu\beta\beta$ acceptance by simultaneous minimization of the survival fraction of surface α events. The RT cut is not affected by volume effects and does not show any energy dependence.

3.3 Phase II background contributions after analysis cuts

The final energy spectra after applying all aforementioned suppression techniques are shown in Fig. 3.9. After the LAr veto cut, in both data sets less than 5% of background events left in the energy region between 600 keV and 1300 keV remain in addition to the $2\nu\beta\beta$ decay. This 5% background contribution can be further reduced by both PSD methods. Furthermore, the LAr veto cuts mostly emitters of β/γ cascades, in particular ^{42}K and ^{214}Biand their Compton continuum. Besides, the combination of the ANN and RT selection provides a suppression of 96% for α events in the high energy region of the $^{\mathrm{enr}}$Coax spectrum ($E > 3500\ keV$). But the A/E cut is in no way inferior and removes equally or even more efficient almost all high energy αs. Finally, more then 95% of the background can be rejected with a $0\nu\beta\beta$ signal acceptance of $(87.6 \pm 0.1(\mathrm{stat}) \pm 2.5(\mathrm{syst}))$ % and (71.2 ± 4.3)% for the $^{\mathrm{enr}}$BEGE and $^{\mathrm{enr}}$Coax detectors, respectively [36].

The energy window ranging from 1930 keV to 2190 keV defines the ROI of GERDAused for background evaluation. It excludes two 10 keV windows around the known γ lines at 2104 keV and 2119 keV arising from the decays of the isotopes ^{208}Tl and ^{214}Bi. A zoom to the ROI of the energy spectra is shown in Fig. 3.10. After unblinding, only 3 events in the $^{\mathrm{enr}}$Coax and 5 events in the $^{\mathrm{enr}}$BEGE data sets of Phase II recored with 53.9kg·yr remain in the analysis window. GERDA thus reaches an unprecedented low background rate of $\left(5.6^{+4.1}_{-2.6}\right)$ counts/(keV $\cdot$ kg $\cdot$ yr) for the $^{\mathrm{enr}}$Coax and $\left(5.6^{+3.4}_{-2.4}\right)$ counts/(keV $\cdot$ kg $\cdot$ yr) for the $^{\mathrm{enr}}$BEGE detectors.

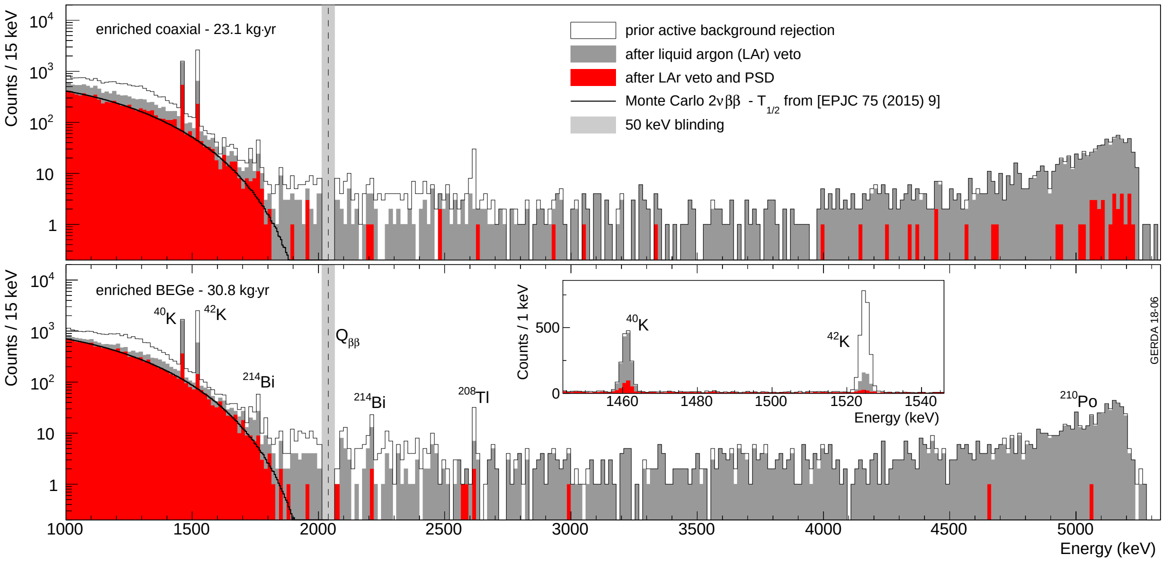

Fig. 3.9 Energy spectra before (open histogram) and after the LAr veto cut (grey shaded) and PSD selection (red shaded) for the $^{\mathrm{enr}}$Coax (top) and $^{\mathrm{enr}}$BEGE (bottom) detectors together with the expected $2\nu\beta\beta$ spectra (solid line) from a recent half-life measurement of GERDA [101]. In addition, a zoom of the $^{\mathrm{enr}}$BEGE spectrum into the energy region around the two potassium lines is shown [36].

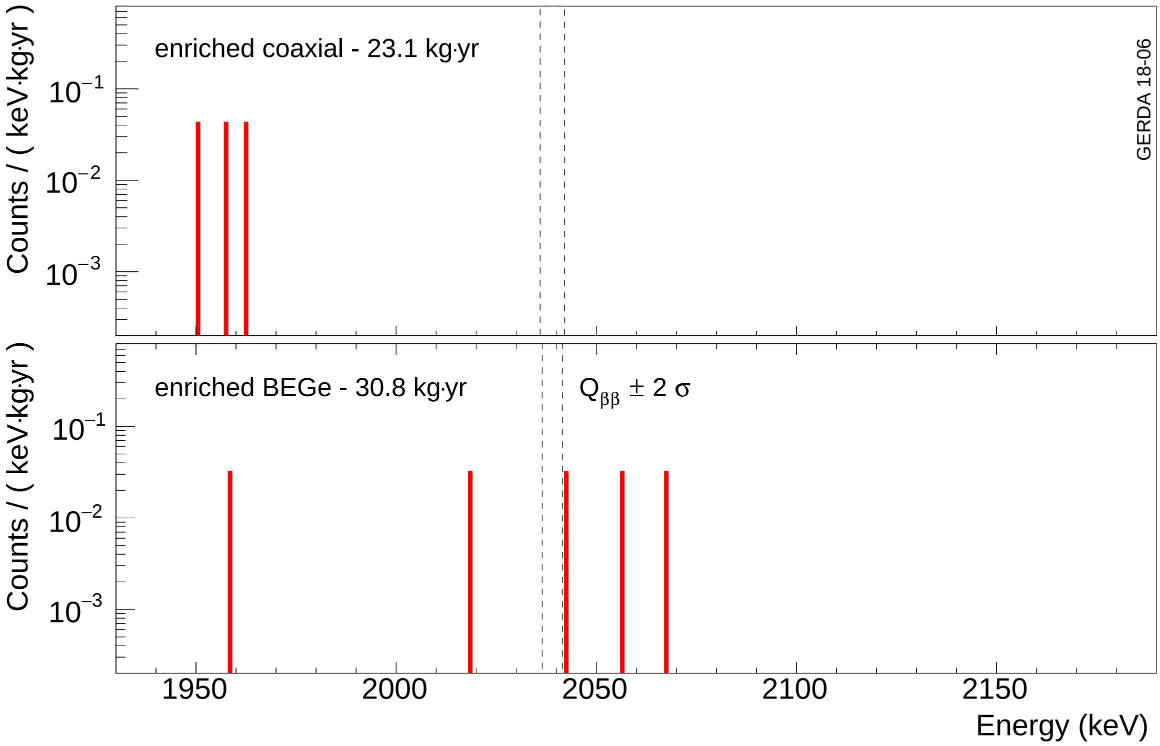

Fig. 3.10 The Phase II energy spectra zoomed to the ROI are shown separately for the $^{\mathrm{enr}}$Coax and $^{\mathrm{enr}}$BEGE data sets after the LAr veto and PSD cuts [36].

Chapter 4

Monte Carlo Simulation of the GERDA Experiment

In cooperation with the analysis groups from Padova and Dresden (see Appx. A.1), a Monte Carlo (MC) campaign [102] has been performed in order to study the observed structures in the energy spectrum of the individual data sets (see Ch. 3.1). Since the shape of the energy distribution strongly depends on the assumed source location, the effects of various source positions on the spectral shape have been studied quantitatively by means of MC simulations. This chapter will give an overview on the MAGE implementation of the GERDA Phase II simulation setup and the post-processing. In addition, the simulated spectra define the probability density functions (PDF) which form the basis of the GERDA Phase II background model elaborated in Ch.5. For this reason, the obtained simulated spectra will be described in terms of differences which can be extracted from the simulated backgrounds in view of their potential origins. The attention is drawn to spectral differences that later might influence the modeling of the decomposition of the recorded background spectrum presented in Ch. 5.4.

4.1 Monte Carlo simulations and probability density functions

The MC simulations were performed with using the GEANT4-based MAGE framework [103]. It is a physics MC framework jointly developed by the MAJORANA and GERDA collaborations. MAGE provides a full implementation of all the relevant components of the GERDA Phase II arrangement with the complete germanium detector array and the forty individual detectors. MAGE has been used to simulate the propagation of particles and nuclei through matter providing the interaction points and the corresponding energy losses within the crystals, including all the physical processes involved in the passage of γ rays or charged particles. Decays originating from intrinsic and in particular from surface contaminations of the following GERDA setup components have been simulated: germanium detectors, the detector holding structure, the detector cables, mini-shrouds, the LAr veto system, the front-end electronics and the LAr around the detector array. Figure 4.1 shows a 3D model of the implementation of the individual components simulated for the background model.

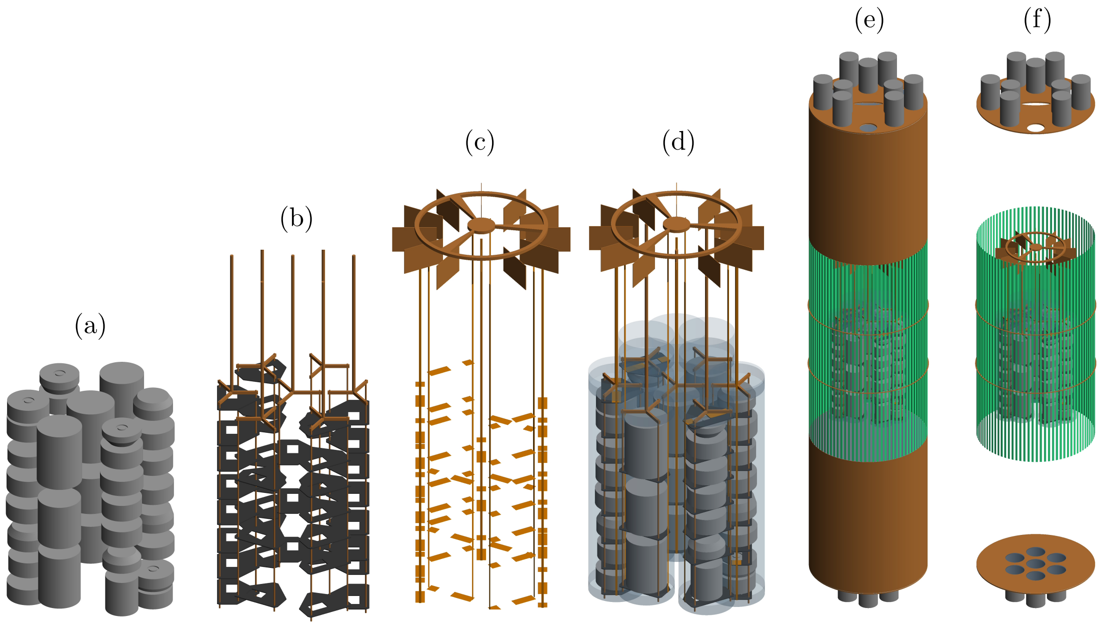

Fig. 4.1 Rendering of GERDA Phase II MAGE components without cryostat: (a) Raw Ge crystals without holding structure showing in the front row from left to right starting with string 4 with eight $^{\text{enr}}$BEGE detectors, string 5 with three semi-coaxial, and string 6 and 1 with six $^{\text{enr}}$BEGE plus one semi-coaxial and eight $^{\text{enr}}$BEGE detectors, respectively. (b) Copper support structures of the crystals together with the Si holder plates. (c) The front-end components located on a copper support structure in about 30 cm distance to the detectors. Layout of the signal and high voltage cables shown together with their connection bars. (d) Arrangement of the seven detector strings with high voltage and signal cables, holder plates and read-out electronics. Each string is enclosed by a transparent nylon mini-shroud. (e) The Ge detector array enclosed by the LAr veto system. Top and bottom plate with nine and seven PMTs, respectively and the copper cylinder. (f) Fiber curtain surrounding the detector array together with the top and bottom plate showing the shifted alignment of the veto with respect to the center of the detector array [104].

Conform with the GERDA Phase II, in MAGE the detectors are positioned in seven detector strings with 40 detectors in total. The middle string consists of 3 natural semi-coaxial detectors while the surrounding strings consist of either 8 $^{\text{enr}}$BEGE or 3 enriched semi-coaxial detectors except for one string which is a mixture of 7 $^{\text{enr}}$BEGE and one semi-coaxial detector. The height of the array is about 40 cm, with a diameter of about 30 cm. The detector placing is applied according to the distribution shown in Fig. 4.2.

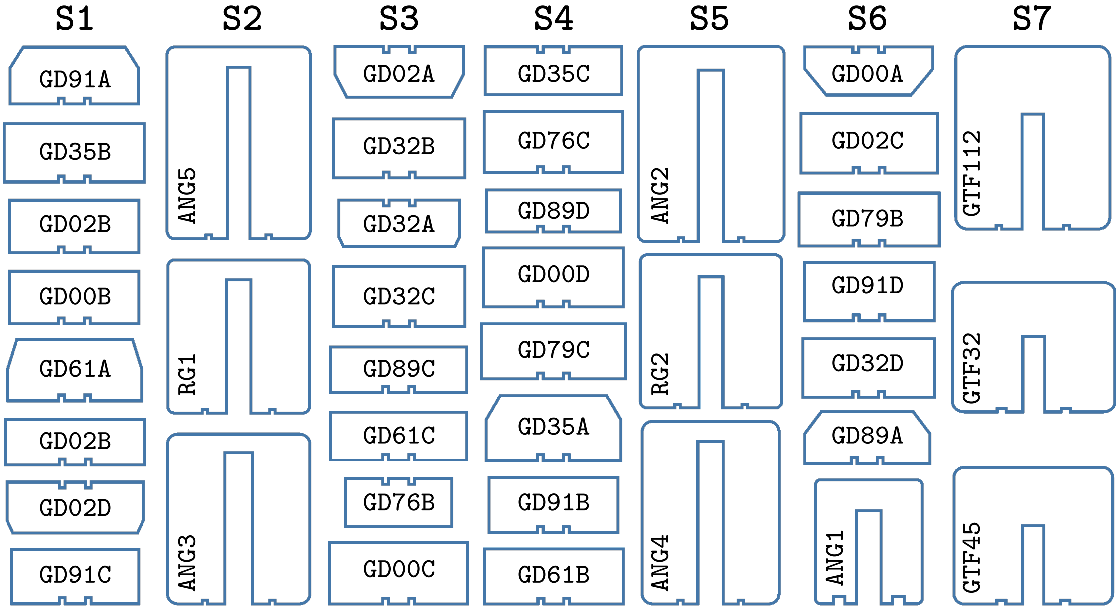

Fig. 4.2 String arrangement of the enriched $^{\mathrm{enr}}$BEGE (GDxxx), the enriched (RGx and ANGx) and natural (GTFxxx) semi-coaxial detectors of the GERDA Phase II detector array. Each detector is labeled by a number between 0 and 39 depending on its position starting in string S1 with 0 continuing from top to bottom string by string. In addition, for each detector the groove orientation and the geometrical configuration including conical shapes are indicated [104].

The geometries and dimensions such as radius, height and dead layer thickness of each detector as determined by the characterization campaign [85] have been included. The density of Ge has been adapted to cryogenic temperatures for enriched and natural Ge with 5.56 g/cm^3 and 5.34 g/cm^3, respectively [105]. The n$^+$ surface dead layer is set individually for each detector while a generic dead layer thickness of 400 nm was used for the p$^+$ surface except for simulations of α surface decays. Since the short range in Ge of α events lead to a strong sensitivity on the p$^+$ dead layer thickness, simulations of α decays on or close to the p$^+$ surface have been carried out for thicknesses ranging from 100 nm to 800 nm in 100 nm steps. In both cases, the dead layer has been assumed to be inactive with a sharp transition to the active volume. No partial charge collection was taken into account.

Each germanium detector is mounted on a silicon holder plate with a thickness of 1.5 mm (see Figure 4.1(b)). Vertical bars and star holder bars on the top of the detectors, are constructed by Cu, complete the detector holding structure. The copper support has not been taken into account, since in the ROI a background contribution of $< 10^{-5}$cts/(keV·kg·yr) for

^{228}Th and ^{214}Bi has been predicted by the screening measurements [80]. Decays originating from the detector holder plates are expected to be distributed relatively homogeneously among the detectors, when neglecting the volume differences of the detectors.

Regarding the detector cables, one signal and one HV cable per detector run along the side of each detector in a string, reaching from the detector's plate up to the front-end electronics (see Figure 4.1(c)). In MAGE, the cables are generically modeled by Kapton with a density of $\rho = 1.53$ g/cm^3. A higher concentration of background decays from impurities in the cable material are expected in the top detectors due to the higher amount of cable layers in the upper part of each string. The impurities are assumed to be homogeneously distributed in the cable material.

Transparent nylon tubes, the so-called mini-shrouds, enclose each of the seven strings separately (see Figure 4.1 (d)). Each mini-shroud consists of three sub-pieces: a tube, a bottom and a top volume. The sub-volumes of each mini-shroud have been glued with additional vertical stripes to seal up the main tube of the mini-shrouds. In addition, the tube have been glued with the top and bottom by additional rings. The three sub-volumes and the additional rings are considered in the simulation.

The main front-end board consist of copper support and copper holders equipped with custom-produced preamplifiers, the so-called CC3 preamplifiers. The front-end circuit is connected to the detectors by cables made of Pyralux or Cuflon at a distance of 30 cm. In Figure 4.1 (c) and (d) the representation of the front-end electronics in the simulation is indicated by the vertical bares in the upper part. Due to the installation above the array (see 4.1) a higher background contribution in the top detectors is expected from the front-end electronics.

As the illustration of the LAr veto system in Fig. 4.1 (e) shows, a hybrid system of photomultipliers (PMTs) and wavelength shifting fibers with silicon-photomultiplier (SiPM) read-out has been adopted in GERDA. Since each component can vary in its potential contamination, the LAr veto has been split to four sub-volumes in the simulation.

In the GERDA setup, a cylindrical volume is lined by fibers which cover 50% of the surface area. The fiber shroud is supported by a lightweight copper frame that also carries the weight of a bottom plate. The fibers are bent around the shroud, building a curtain of fibers with a total surface of about 2.9 m^2. Less events should reach the detector's active volume in the central string due to the shielding of the outer strings. However, the central string contains only the natural semi-coaxial detectors which are excluded from the analysis in the present work. The copper support structure for the fiber curtain and the SiPMs is not fully implemented in the geometry, but the expected activity is considered later in the background model.

The ends of the fibers are coupled to custom packaged 3x3 mm^2 SiPMs placed on Cuflon holders and bonded to copper stripes. The holders are covered with a thin layer of transparent epoxy glue. In the simulated geometry, a ring on top of the fiber shroud which is coupled to the fibers represents this hardware component. The top ring is closer to the array and hence the top detectors should be affected more by contaminations of the top ring. The active or passive electronic components are installed outside the LAr cryostat and can be neglected in the simulation.

The PMT system consists of nine PMTs pointing downward to the detector array from the top and seven PMTs pointing upwards from the bottom which are installed on copper plates at the ends of the cylindrical LAr volume (see Figure 4.1 (f)). The two plates are separated from the central fiber section by copper shrouds of 60 cm height whose center is shifted towards the upper part with respect to the center of the detector array. In GERDA, the cabling of the PMTs runs from the bottom plate along the outside of the shrouds and the fiber curtain. In the analysis, contaminations of the cabling are accounted for by the simulated volume of the copper shroud.

The copper shroud with a diameter of 75 cm encloses the fiber curtain. The copper shroud consists of 100 μm thick copper foils which carry flanges at both ends for the connection to the PMT plates and the fiber section. The inside of the shrouds are lined with Tetratex PTFE foil of 254 μm thickness. As a result from screening measurements, the Tetratex foil is expected to be contaminated with ^{40}K. Therefore, decays originating from the inner surface of the cylindrical shroud have been simulated.

And finally, simulations of decays originating from contaminations in LAr were performed by adjusting the different sizes and placements of volumes from which the decays were sampled according to the attenuation length and position of the simulated source. For α decays, a small volume close to the simulated detector p^+ surface was used, while for all remaining sources a volume surrounding the whole array was simulated.

4.2 Monte Carlo event processing

Internal and external background contaminations have been simulated in the detector bulk and in the components of the detector setup, respectively, by using the full detector array which considers all detectors as present simultaneously in the simulation. As generator of the simulated events, the G4gun of GEANT4 was used to sample the decays from the final state of the isotopes. All decays were sampled uniformly within the material of the hardware components. The simulation output contains a list of hits with energy deposition in the active volume of the detector crystals. Each simulated event follows then the same analysis stream as real data, taking into account the detection and reconstruction effects as well as detector run parameters. Various post-processing steps were introduced including necessary parameters not incorporated in the used simulation mode (detector's lifetime, energy threshold...). During post-processing, the energy of each event in the simulation was smeared by a Gaussian distribution with the standard deviation determined from the average energy resolution obtained for each detector using calibration data. In addition, for each event the detector operation modes were sampled according to the valid run configurations weighted by the corresponding lifetime. This step considers the exclusion of individual detectors during certain runs due to temporary instabilities. Furthermore, the post-processing comprises an energy cut of 40 keV applied to the simulated events to account for the hardware threshold.

To obtain the final probability density function $\Phi(E)$ of a subset d of detectors, the simulated spectrum $\Phi_j(E)$ of the each detector j is scaled by the detector's lifetime fraction given as the sum of the considered run lifetimes t_i of detector j

$$t_j = \sum_{i=1}^{N_{runs}} t_i \delta_{ij} \quad with \quad \delta_{ij} = \begin{cases} 1 & \text{j is ON in run i} \\ 0 & \text{j is OFF in run i} \end{cases} \tag{4.1}$$

Accordingly, the total spectrum of a subset is the sum of the scaled single detector spectra:

$$\Phi_d^{ext}(E) = \sum_{j=1}^{N_{dets}} \frac{t_j}{T} \Phi_j(E) \quad \text{with} \quad T = \sum_{i=1}^{N_{runs}} t_i \tag{4.2}$$

Considering an internal background contamination (in e.g. ^{76}Ge), to achieve an uniform distribution of the primary vertices in the contaminated intrinsic mass M all over the detector array, the number of events simulated in each detector is weighted by the detector's fraction of the total mass M. In case of ^{76}Ge as source of the contamination, the enrichment of the different detector classes has been approximated by an equal enrichment fraction f_{76} whereby M is replace by the mass of ^{76}Gewith $f_{76} \cdot M$. The final probability density function of a detector subset is analogous to the previous discussed procedure except for the additional weighting:

$$\Phi_d^{int}(E) = \sum_{j=1}^{N_{dets}} \frac{M_j}{M} \frac{t_j}{T} \Phi_j(E) \tag{4.3}$$

Since no transition layer has been considered, decay without energy deposition in the detector's active volume are excluded. Therefore, the simulations have been performed separately for the detector's active volume (AV) and the dead layer volume (DL). Both contributions have been summed up according to the active volume fraction (f_{AV}) leading to the following simulated spectrum:

$$\Phi_j(E) = f_{AV,j}\Phi_j^{AV}(E) + (1 - f_{AV,j})\Phi_j^{DL}(E). \tag{4.4}$$

where $\Phi_j^{AV}(E)$ and $\Phi_j^{DL}(E)$ are the normalized energy distributions of the detector j for simulated for decays taking place in the active and dead volume of detector j.

In case of α emitting isotopes on the detectors surface, simulations were carried out by simulating a single detector instead of simulations with the whole array setup. As consequence of the short range in LAr or Ge, α events do not scatter through the detector array and do not markedly contribute to the two-detector events spectrum. Besides the argument of the scattering probability, the spectral shape caused by energy depositions of emitted α particles is almost independent on detector dimensions and geometrical variations between $^{\mathrm{enr}}$BEGE and semi-coaxial detectors. Since geometrical differences have a negligible impact on the resulting spectral shapes, GD91C has been chosen to be generic for both the $^{\mathrm{enr}}$BEGE and semi-coaxial detectors in this case. The strongest impact on the shape comes from the dead layer thickness. Therefore, the single detector mode simulations have been carried out for several p$^+$ surface thicknesses in 100 nm steps between 100 nm and 800 nm.

A complete set of MC simulations in the energy space were prepared for a single-detector data set, i.e. anti-coincidence of the $^{\mathrm{enr}}$BEGE (`M1-enrBEGe`) and of the enriched semi-coaxial (`M1-enrCoax`) detectors as well as a two-detector data set (`M2-enrGe`), i.e. multiplicity of two, containing all enriched detectors. Obviously, the two-detector events data set has not been generated for α emitting isotopes. In addition, a set of MC simulations in detector space has been generated only for a selection of background sources in specific energy regions which will be discussed in the framework of the K-model(see Ch. 5.3). While the energy space denotes the energy distribution of the events, the detector space represents the number of counts distributed over the detector IDs in a certain energy range.

4.3 Simulated background sources

The simulated background sources were chosen due to contributions observed in the recorded background spectrum. As already discussed in Sec.3.1, radioactive isotopes from the natural decay chains of ^{232}Th and ^{238}U, as well as ^{42}K, ^{40}K, ^{60}Co and the intrinsic $2\nu\beta\beta$ of ^{76}Ge are taken into consideration. Due to its low Q-value of 565 keV, ^{39}Ar has been removed from the analysis. The low Q-value would require an extremely detailed knowledge not only of the detector dead layer geometry, but also of the trigger efficiency at small energies. Only with this knowledge the correct modeling of the ^{39}Ar β decay spectrum can be achieved.

Further background contributions with expected BI of less than 10^{-4} cts/(keV·kg·yr) estimated in previous works have not been considered in this work. This includes contributions of the cryostat and the water tank [106], the calibration source [107],[80] and expected neutron [92] and muon fluxes [81]. In the following, only the simulated spectra in energy space are discussed.

$2\nu\beta\beta$ The simulated spectral shape induced by the intrinsic $2\nu\beta\beta$ decay of ^{76}Ge is shown in Fig. 4.3 for the $^{\mathrm{enr}}$BEGE and $^{\mathrm{enr}}$Coax data sets. The decays have been simulated homogeneously distributed in the detector crystals sampled from each detector bulk volume individually. For technical reasons, decays inside the active volume and inside the dead layer were simulated separately and later summed up weighted by their mass fraction. The energy is deposited exclusively by electrons and Bremsstrahlung photons and the continuous spectrum is characterized by a broad maximum around 700 keV. The probability of generating two-detector events for intrinsic $2\nu\beta\beta$ decays is negligible. Above the β endpoint of ^{39}Ar, $2\nu\beta\beta$ is the dominating background compared to the smaller contributions in that energy range. This can lessen the significance of γ-lines below 2 MeV or even hide some of them. The analysis of the measured spectrum allows for the precise determination of the rate of the SM allowed $2\nu\beta\beta$ process.

^{42}K Due to the electric field of the detectors dispersed in LAr, a not negligible background contribution at $Q_{\beta\beta}$ is expected when the ^{42}K ions are attracted to the detector surfaces to which they can stick. To reproduce potential non-uniform distributions with specific hot-spot locations, various volumes in LAr close to the p^{+} and n^{+} surfaces as well as inside and outside the mini-shrouds have been adopted. The simulated spectral shapes of the energy distribution corresponding to the individual scenarios are shown in Fig. 4.4. Depending on the dominating decay processes the simulated spectra show quite distinct features. However,

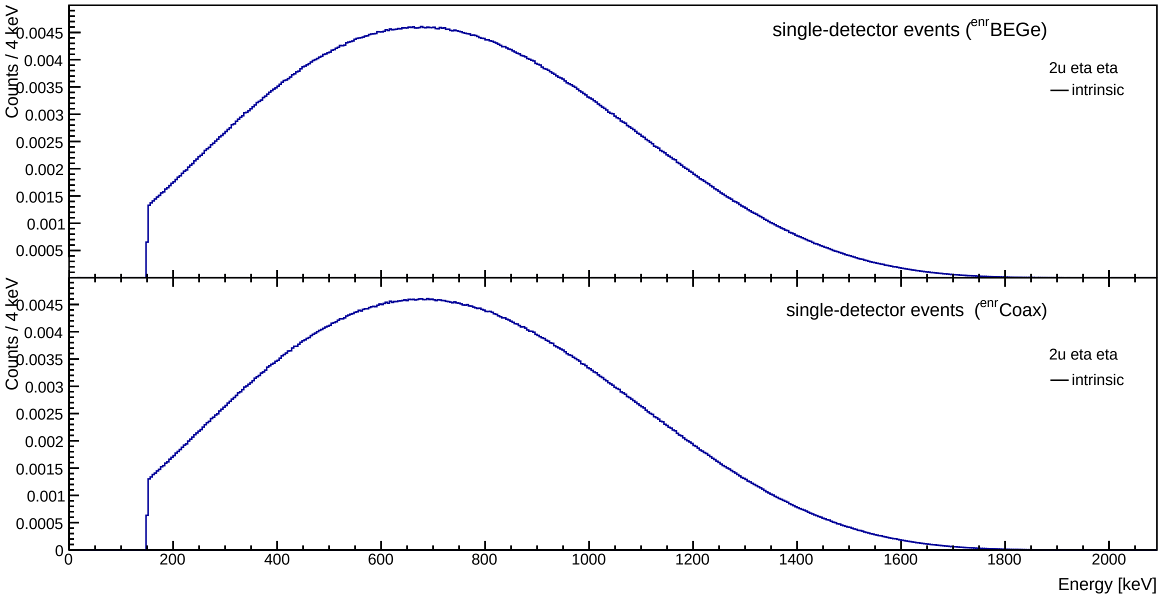

Fig. 4.3 Simulated energy spectra of intrinsic $2\nu\beta\beta$ decays corresponding to single-detector events of the enriched ^{enr}BEGE and ^{enr}Coax data sets. Each spectrum is normalized to the number of total number events in the energy range between 100 keV and 8000 keV.

the spectral shapes can be described by two most opposite scenarios and further intermediate ones.

In case the distance is to large for the electrons to reach the detector's active volume, the major contribution can be attributed to photons, a pronounced photon peak appears along with a large peak-to-continuum ratio. Additionally, the continuum drops above the FEP due to the absence of the dominating contribution from Compton scattered photons. Furthermore, the detectors are enclosed by nylon mini-shrouds which avoid the ^{42}K ions to be attracted resulting in a quasi field free configuration with an almost homogeneous distribution in LAr outside of the mini-shrouds. For decays on the detector surfaces, the continuum attributed to the electrons is enhanced resulting in a reduced peak-to-continuum ratio. Even though, one has to differentiate between the two surface areas considering the dead layer thickness. Compared to the much thicker n^{+} dead layer, the p^{+} dead layer thickness is only in the order of µm which practically does not degrade the energy of the electrons. Consequently, the energy spectrum reaches up to almost the Q-value of the decay. Obviously, strong surface contamination is a potential background in the ROI already at much smaller concentrations.

All further scenarios are intermediate combinations of the two extreme cases with a re-weighting of the contributions from photons and electrons described above. Comparing the sensitivity on the dead layer surface, with increasing dead layer thickness the peak-to-continuum ratio increases and the sudden drop above the γ lines gets stronger. The spectral shape is not expected to vary strongly among the detectors due to geometrical differences, but due to dead layer characteristics. The larger the distance of the electrons emitted in the decay of ^{42}K to the detectors, the higher the barrier to reach the detectors' active volume analogous to a larger dead layer thickness. This is effect is visible in the simulated energy spectrum of ^{42}K distributed in LAr inside the mini-shrouds. In this context, a smooth transition is observed between the spectral shape generated by decays on detector surface and by decays inside the mini-shroud depending on the dead layer thickness. In case of the coaxial detectors, the dead layer has, on average, a thickness of about 2 mm, while for the $^{\text{enr}}$BEGE detectors about 1 mm. Notice, the average dead layer has a thickness comparable to the absorption length in Ge of the electrons emitted in the ^{42}K decays. For this reason, the β spectrum for decays on the detector surface can be equally suppressed to the one from electrons originating from inside the mini-shrouds. Since the energy of the electrons gets shifted towards lower energies correlated with the barrier they have to overcome before reaching the detector's active volume. A semi-active transition layer has not been taken into account. In contrast to the photons on which it has only a minor impact, it would influence the energy distribution of the electrons close to the n$^+$ electrode and shift their energies towards higher energy regions.

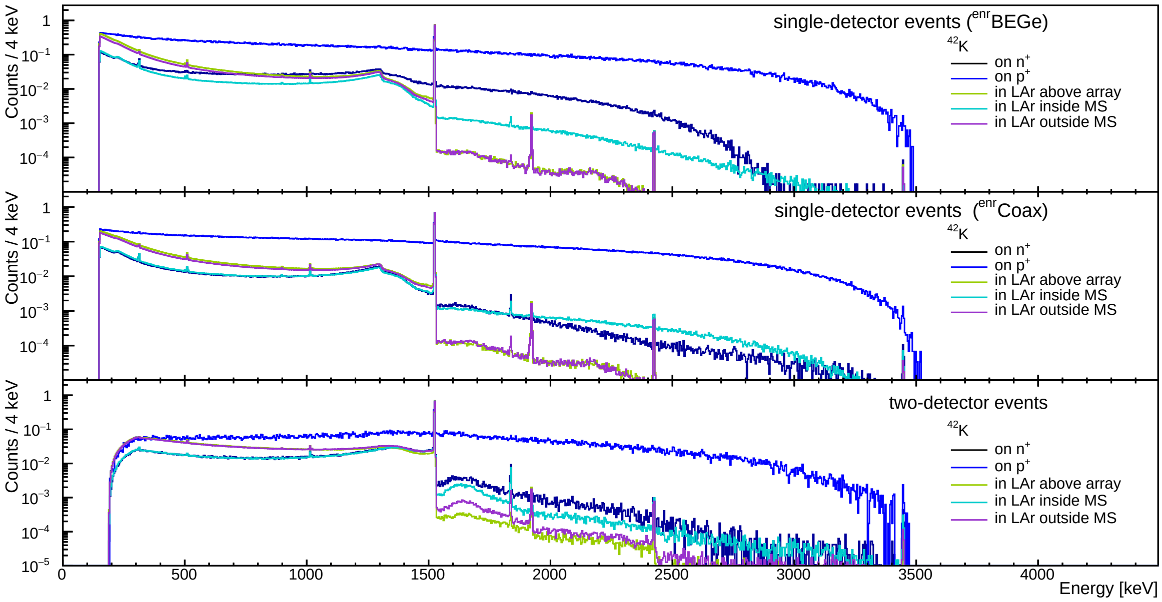

Fig. 4.4 Simulated energy spectra of the ^{42}K decays for different source positions corresponding to the single-detector and two-detector event data sets for enriched $^{\text{enr}}$BEGE and $^{\text{enr}}$Coax. All spectra are normalized to the number of events in the bins containing the FEP at (1524.7 ± 2) keV.

Apart from Compton scattered γ rays, events surviving the multiplicity two cut are due to Bremsstrahlung γ rays leaving the detector volume and depositing their energy in a second detector or due to the β and γ cascade release in the decay of ^{42}K. Especially for ^{42}K events directly on the surface the probability gets higher to create multiple interactions over various detectors.

According to the observed data, the count rate distribution of the γ line at 1524.7keV over the detector IDs, in the so-called detector space, exhibits a top-bottom asymmetry, thus an additional position scenario was introduced. To represent the observation, decays of ^{42}K were sampled from a volume surrounding the upper part of the detector array. In the simulated energy spectrum summed over multiple detectors in top and bottom position, this asymmetric effect is washed out and thus not replicated. Decays taking place in an upper volume around the detector array may produce a summed energy spectrum which differs only slightly from a homogeneous distribution outside the mini shrouds with an high peak-to-continuum ratio and smaller contribution at higher energies.

^{40}K The screening measurements indicate ^{40}K in materials close to the detectors and in materials of the LAr veto system. Therefore, it has been simulated in the detector assembly, the nearby front-end electronics, and in several parts of the LAr veto support. Fig. 4.5 shows the resulting post-processed energy spectra for the various source contaminations normalized to the single γ ray line at 1460.9 keV in the spectrum. The main difference in the spectral shapes stemming from the various locations can be attributed to the ratio of the peak to Compton continuum. The β endpoint is below 2 MeV, thus ^{40}K does not contribute in the ROI at $Q_{\beta\beta}$, but the energy distribution falls in the energy region dominated by $2\nu\beta\beta$ decay of ^{76}Ge. Consequently, the sensitivity to small variations in the shape of the energy distribution as expected for various source positions is limited. Nevertheless, the more distant the source origin is away the flatter the rise in the continuum near the Compton edge of the FEP at 1460.9 keV and consequently the smaller the ratio of the peak to the continuum region. Parts of the detector array support are positioned at an equal distance from the detectors. Thus, the energy distributions of the individual components are hardly distinguishable. In all data sets, the DEP is visible, along with the SEP and the 511 keV peak due to annihilation radiation produced by pair production interactions in the surrounding. In case of the two-detector events, the Compton edge and continuum are less pronounced.

^{60}Co Screening measurements suggest ^{60}Co contaminations in the signal and high-voltage cables besides possible traces in the detector holders (see Tab. B.1). Fig. 4.6 displays the resulting simulated energy spectra of ^{60}Co decays originating from the two components for the single-event $^{\mathrm{enr}}$BEGE and $^{\mathrm{enr}}$Coax sum data set and the two-event data set, respectively. The successive photon peaks at 1173.2 keV and 1332.5 keV and the summation peak at

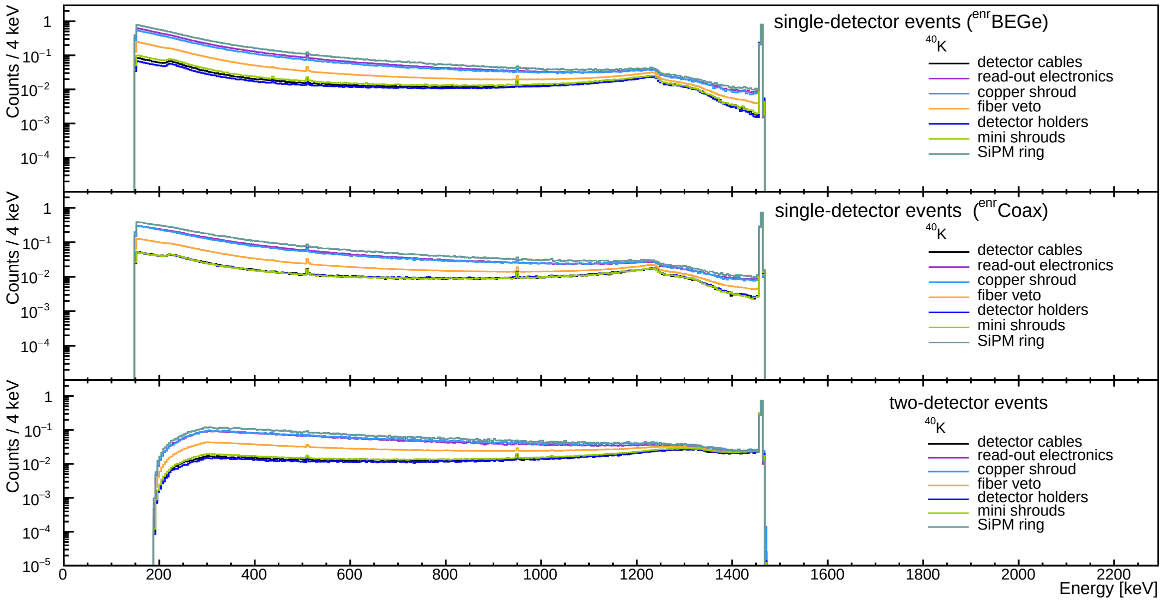

Fig. 4.5 Simulated energy spectra of the ^{40}K decays for different source positions corresponding to the single-detector and two-detector event data sets for enriched $^{\text{enr}}$BEGE and $^{\text{enr}}$Coax. All spectra are normalized to the number of events in the bins containing the FEP at (1460.9 ± 2) keV.

2505.7 keV are clearly visible. Various source positions show spectral distortions only to a very small extent in the Compton region of the summation peak, in particular for the $^{\text{enr}}$BEGE detectors. For energies below the two photon peaks, the spectra for corresponding positions do not differ significantly. Above the FEP at 1332.5 keV, in the $^{\text{enr}}$BEGE data set the contribution for the cables drops. Nevertheless, no unambiguous distinction between the two positions is expected given the limited statistics in the observed data spectrum.

^{238}U chain Contaminations of ^{238}U or its progenies are assumed to be omnipresent in the very close vicinity of the detector array. The sub-chains consist primarily of α and β emitting radionuclides, but α particles originating from distances of more than hundreds of µm from the detectors are absorbed before reaching the detector's active volume. Since the mean attenuation length of α particles with an energy between 4 MeV and 9 MeV ranges from 14 to 41 µm in Ge and 34 to 113 µm in LAr, even the n$^+$ surface serves as a barrier. Therefore, if α particles reach the detector's active volume these α particles can only stem from a very close distance to the detectors p$^+$ or groove surface. For this reason, only β and γ emitting isotopes with measurable half-lives have been simulated in the main parts of detector assembly (cabling, holding structure and mini-shrouds) and in components of the LAr veto system according to expectations from screening measurements. Since the sub-chain is broken after $^{234\text{m}}$Pa, it has been simulated and treated separately from the ^{226}Ra

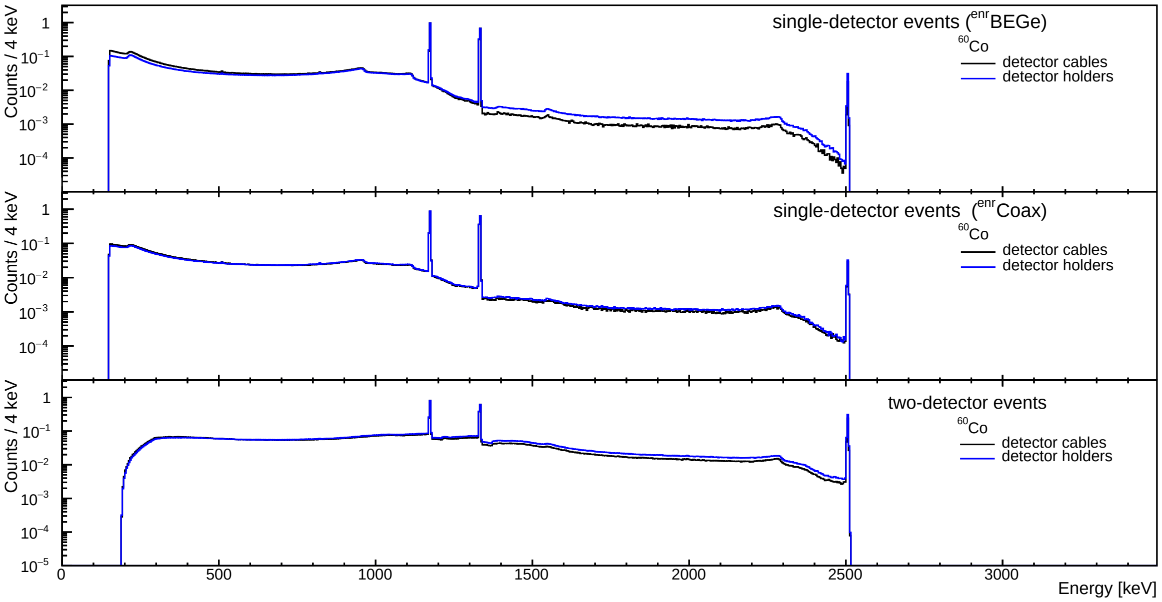

Fig. 4.6 Simulated energy spectra of the ^{60}Co decays for different source positions corresponding to the single-detector and two-detector event data sets for enriched $^{\text{enr}}$BEGE and $^{\text{enr}}$Coax. All spectra are normalized to the number of events in the bins containing the FEP at (1332.5 ± 2) keV.

sub-chain containing ^{214}Pb and ^{214}Bi. The production of ^{214}Pb is directly followed by ^{214}Bi ($T_{1/2} = 26.8$ min) and the corresponding energy distributions of both isotopes have been added with the respective branching ratio.

^{214}Bi and ^{214}Pb decays are expected to originate from materials with ^{226}Ra contamination. However, due to the mobility of the intermediate progeny ^{222}Rn, the production location in non metallic materials can be different from the original contamination of ^{226}Ra or even break the secular equilibrium. Furthermore, as an impact of ^{226}Ra migration and ^{222}Rn emanation, additional ^{214}Bi and ^{214}Pb contaminations on the detector surfaces are expected. The obtained energy spectra for the corresponding sub-chains of ^{238}U are depicted in Figs. 4.7 and 4.8. The simulated spectra have been normalized to the number of events in the bin containing (1001.4 ± 2) keV or (609.3 ± 2) keV, respectively.

In the case of the protactinium isotope, the metastable isomer $^{234\text{m}}$Pa is formed which decays predominantly via β decay ($Q_\beta = 2269$ keV) and γ emissions with 766.7 keV (0.33%) and 1001.4 keV (0.86%). ^{214}Pb emits lower-energy γ rays and the three most abundant ones are at 242 keV (13.7%), 295.2 keV (27.3%), and 351.9 keV (47.96%). ^{214}Bi has a higher number of dominant γ rays in the energy range from 600 keV to about 2.5 MeV. The γ rays with the highest yields are at 609.3 keV (46.4%), at 1120.3 keV (15.1%), at 1238.1 (5.9%), at 1764.5 keV (15.4%) and 2204.2 keV (4.9%). The remaining ones have individual yields not higher than about 5%.

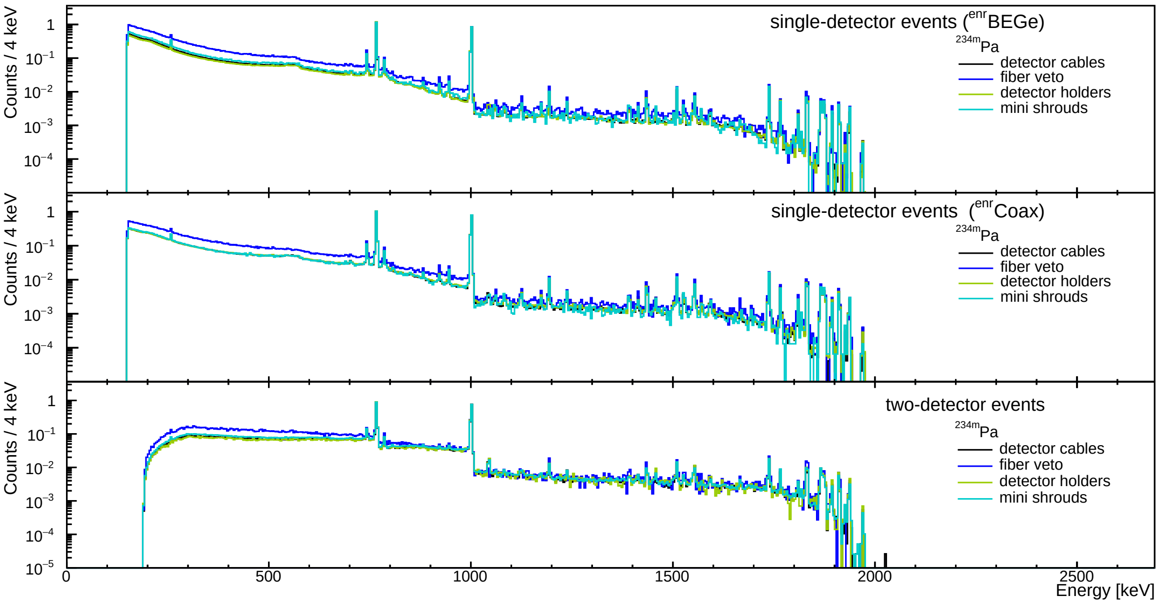

Fig. 4.7 Simulated energy spectra of the $^{234\text{m}}$Pa decays for different source positions corresponding to the single-detector and two-detector event data sets for enriched $^{\text{enr}}$BEGE and $^{\text{enr}}$Coax. All spectra are normalized to the number of events in the bins containing the FEP at (1001.4 ± 2) keV.

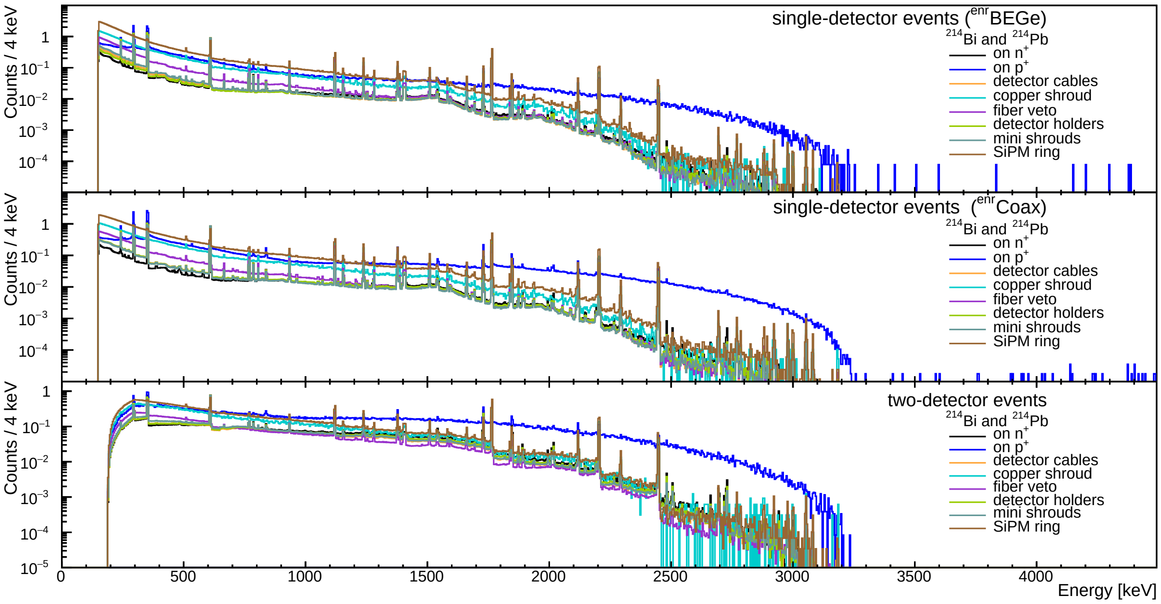

Fig. 4.8 Simulated energy spectra of the ^{226}Ra sub-chain decays for different source positions corresponding to the single-detector and two-detector event data sets for enriched $^{\text{enr}}$BEGE and $^{\text{enr}}$Coax. All spectra are normalized to the number of events in the bins containing the FEP at (609.3 ± 2) keV.

In both sub-chains, the majority of the electrons released in the decay are absorbed in the LAr or the n$^+$ dead layer. With an increasing source distance of more than a few millimeters, the contribution from electrons in the spectrum decreases. Moreover, the γ lines are amplified reflecting the distance by the peak-to-continuum ratio. Since all near contaminations including the n$^+$ surface are located in a distance of less then 3 cm, the spectra do not differ significantly. The fibers are in medium distance of about 10 cm to the detector array. While for higher energies (above 1 MeV (1.5 MeV), the corresponding spectral shape resembles the one of sources in the direct detector vicinity, the γ lines are less pronounced for lower energies. In case of the far sources, i.e. the SiPM ring and the copper shroud, the source location has a distance of more than 30 cm to the detector array resulting in an even stronger reduced peak-to-continuum ratio for the whole energy range. For background contaminations on the p$^+$ surface of the latter isotopes, the peak structures are washed out compared to the enhanced continuum due to electrons released in the decay of ^{214}Bi.

All α decays of the ^{226}Ra, ^{210}Pb sub-chain and the ^{210}Po decay have been simulated separately on the p$^+$ surface and homogeneously distributed in LAr close to the p$^+$surface. ^{222}Rn as intermediate member of several decay series can escape by recoil or by diffusion. So, the Po isotopes can additionally originate from ^{222}Rn and daughters dissolved in LAr. As a consequence of the boron implantation process, the dead layer thickness can vary non-uniformly among the surface. An effective dead layer thickness can be determined by modeling the inhomogeneous dead layer composition through a superposition of different dead layer thicknesses. To account for this effect, decays on or close to the p$^+$ surface were simulated for thicknesses ranging from 100 nm to 800 nm. If a particle is emitted perpendicular to the detector surface it will cross the shortest path of the dead layer, lose minimal energy and produce a peak reduced in energy by the minimal energy loss. With shallower emission angles it results in a distribution towards lower energies, similar to traveling longer distances through the LAr or the dead layer. The energy distribution results in a degraded tail toward lower energies with potential background contribution in the ROI. With increasing dead layer thickness, the maximal energy is shifted in the energy spectrum towards lower values similarly like it is the case of α particles emitted with reduced energy (e.g. ^{222}Rn vs. ^{210}Po). The spectral features of the individual α emitting isotopes are in principle the same apart from the maximal residual energy (compare Fig. 4.9a and Fig. 4.9c). The decays in LAr close to the p$^+$surface have been sampled from a volume on the p$^+$ surface extending 1 cm into LAr. The energy distribution of these homogeneously distributed α decays is characterized by a broad continuum truncated below the maximum energy without prominent peak structures (see Fig. 4.9b).

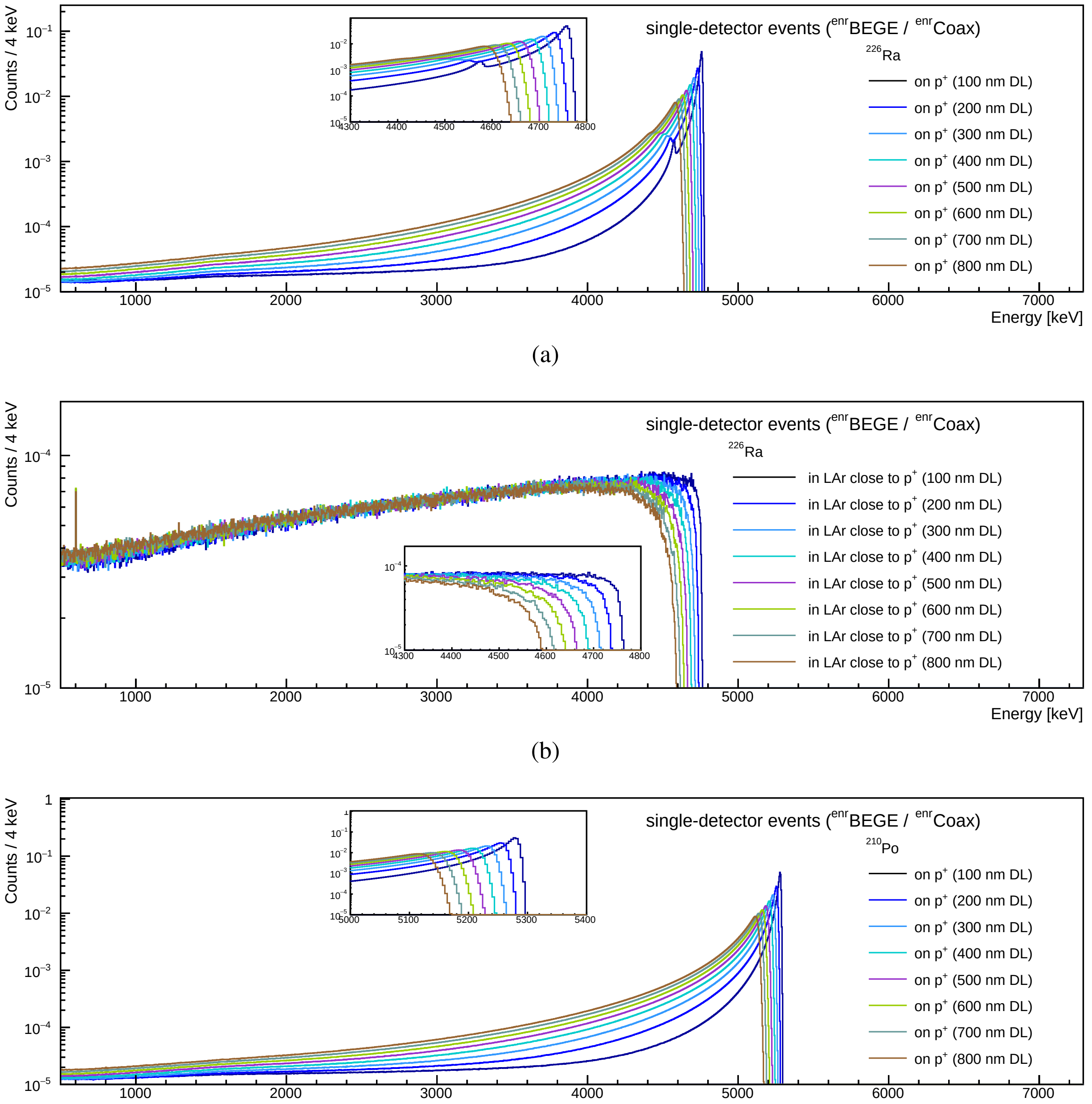

(a)

(b)

(c)

Fig. 4.9 Simulated energy spectra of the ^{226}Ra decays on p$^+$ surface (a) and in LAr close to the p$^+$ surface (b), and the ^{210}Po decays on p$^+$ (c) for p$^+$ dead layer thicknesses between 100 nm and 800 nm corresponding to singe-detector events of enriched $^{\mathrm{enr}}$BEGE and $^{\mathrm{enr}}$Coax. All spectra are normalized to the number of total events in the energy spectrum.

^{232}Th chain Neither features in the observed energy spectrum nor screening measurements have given rise to expect non-negligible surface contaminations due to ^{232}Th and its progenies. In consequence, no α decays are considered in the analysis, and furthermore radionuclides with β or γ ray emissions below 575 keV have been excluded from the analysis. Only the contributions from ^{228}Ac, ^{212}Bi, and ^{208}Tl decays have been simulated. Representing the sub-chain of ^{228}Th, it has been assumed that ^{212}Bi is in secular equilibrium with ^{208}Tl. Therefore, the corresponding energy spectra have been summed by down-scaling to the branching ratio. The final energy spectra for ^{228}Ac and the ^{228}Th sub-chain are shown in Figs. 4.10 and 4.11 corresponding to the ^{enr}BEGE and ^{enr}Coax sum data sets as well as the summed two-event data set.

In case of ^{228}Ac, the largest differences in the spectral shapes can be attributed to the peak-to-continuum ratio, with an enhanced continuum correlated with the distance of the sources. These spectral differences start to diminish for energies above 1 MeV and wash out for energies above about 1.6 MeV, especially for the two-detector events.

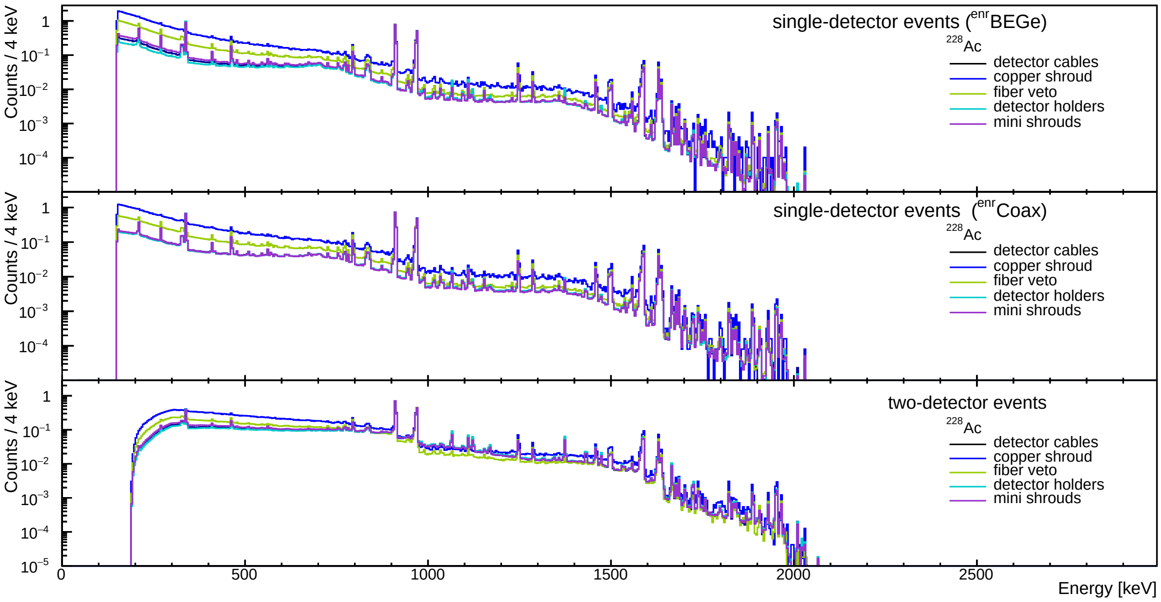

Fig. 4.10 Simulated energy spectra of the ^{228}Ac decays for different source positions corresponding to the single-detector and two-detector event data sets for enriched ^{enr}BEGE and ^{enr}Coax. All spectra are normalized to the number of events in the bins containing the FEP at (911.2 ± 2) keV.

For the ^{228}Th sub-chain, the spectral shapes of the near and medium distant sources largely overlap below 2382 keV, the Compton edge of the 2614.5 keV γ line. Similarly, the far sources resemble each other, but with an increased continuum for the single-detector events. This amplification effect seems to be reversed for the two-detector events. For higher energies above the FEP at 2614.5 keV, the contribution can be correlated to the source distance, in particular in case of the ${}^{\text{enr}}$BEGE detector. The farther away the source location, the stronger the contribution above the 2.6 MeV γ line is suppressed. Even for the near sources, different suppressions are evident. The emission of the 2614.5 keV γ ray (100%) is accompanied in 86.7% of the cases by a 583.2 keV γ ray. Evidently, the high energy contribution is due to the summation of γs or to the coincidence of β and γ events.

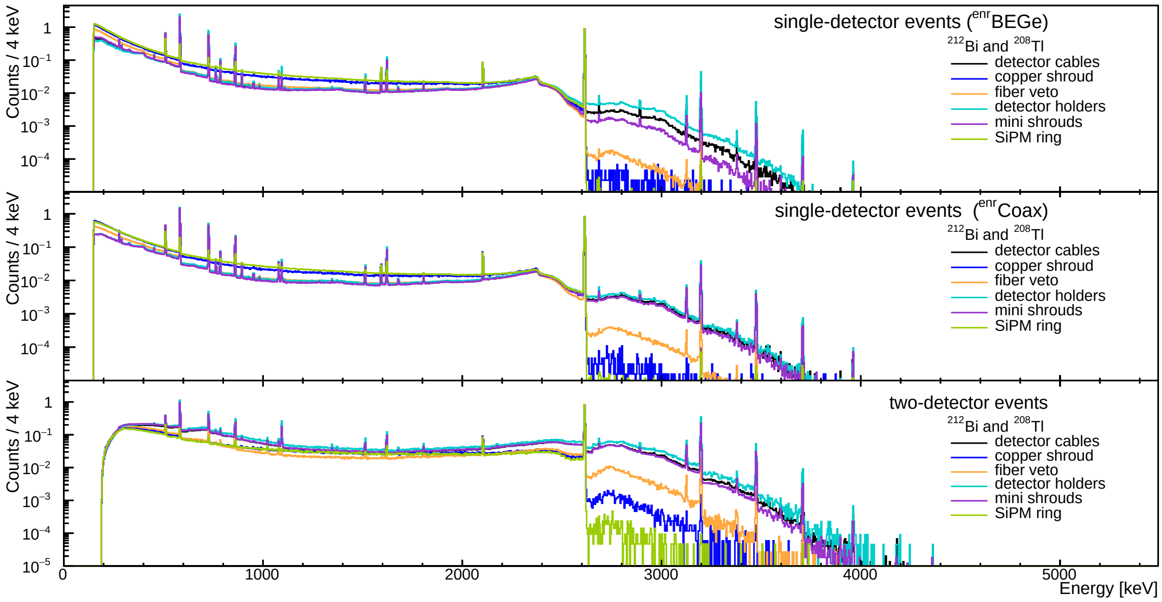

Fig. 4.11 Simulated energy spectra of the ^{228}Th sub-chain decays for different source positions corresponding to the single-detector and two-detector event data sets for enriched ${}^{\text{enr}}$BEGE and ${}^{\text{enr}}$Coax. All spectra are normalized to the number of events in the bins containing the FEP at (2614.5 ± 2) keV.

4.4 Conclusion

The background sources expected from observation in the data spectrum or from screening measurements have been simulated using a GEANT4-based MC code called MAGE. The simulation generates and propagates the primary and any secondary particles through the GERDA Phase II geometry until they are detected in the Ge crystals. The simulations are further processed by applying the detectors' response functions and incorporating other post-processing features. The obtained simulated spectra provide the PDFs for the background model described in Ch. 5.

Since the shape of the energy distribution strongly depends on the assumed source location, the effects of various source positions on the spectral shape have been studied quantitatively. The obtained simulated spectra have been described in terms of differences which can be extracted from the simulated backgrounds in view of their potential origins. Attention has been drawn to spectral differences that later might influence the modeling of the decomposition of the recorded background. Depending on the attenuation length of particles emitted by the isotope, the spectral shape of a source decaying at a certain location in the surrounding of the detector array can be characterized by several general features.

Due to the attenuation length in the order of few milliliters, the majority of the electrons released in the decays are absorbed in the LAr or the n^+ dead layer except for decays occurring in the proximity of the p^+ or n^+ surface. Consequently, the contribution from electrons in the spectrum decreases drastically with an increasing source distance of more than a few millimeters. γ rays can be characterized by their high penetration power such that the main difference in the spectral shapes stemming from the various locations can be attributed to the peak-to-continuum ratios. Since parts of the detector array support are positioned in an equal distance from the detectors, the sensitivity to small variations in the shape of the energy distribution due to γ as expected for various source positions is limited. In particular, all near contaminations including the n^+ surface are located in a distance of less then 3 cm. In consequence, the corresponding spectral shapes of the sources in direct detector vicinity resemble each other. In contrast, the far sources, i.e. the SiPM ring and the copper shroud, have a distance of more than 30 cm to the detector array resulting in spectral shapes that exhibit stronger reduced peak-to-continuum ratios. The attenuation length of α particles with an energy between 4 MeV and 9 MeV is less than a few hundreds of µm in Ge and LAr, such that even the n^+ surface serves as a barrier for α particles. Consequently, if α particles reach the detectors' active volume, these α particles can only stem from the p^+ or groove surface. α particles emitted on the p^+ surface produce a peak in the energy distribution which is reduced in energy due to the energy lost by passing through the dead layer. With increasing path length through the dead layer, the energy distribution results in a degraded tail toward lower energies with potential background contribution in the ROI. The energy distribution of α decays homogeneously distributed in LAr close to the p^+ surface is characterized by a broad continuum truncated below the maximum energy without prominent peak structures.

Chapter 5

Background model of the GERDA Phase II energy spectrum

A background model describing the observed data energy spectra has been developed. The background model defined by a spectral fit yields the specific contribution of isotopes to the background rate in the whole energy spectrum as well as in the ROI and the source locations by which one can evaluate the effects of contaminations in different components of the experimental setup. Thus, it can give hints where experimental design modifications could mitigate effects from contamination for next generation experiments.

The Phase II background model has been built on the basis of the earlier approach used in [108] and [109], but with the goal to focus further on two prominent features in the energy spectrum: the α events dominating the energy range above 3500 keV of the spectrum (**α-model** [110]) and the ^{42}K and ^{40}K events from the 1525 keV and the 1461 keV γ-lines (**K-model** [111]). Thus, the full background model consists of a spectral fit over the whole energy spectrum above the ^{39}Ar end-point (**global model**) integrating the two additional model parts, which were studied individually in detail. The full background model has been developed in cooperation with the analysis groups of Padova and Dresden (see Appx.A.1), whereas the global model has been conceived in the context of this work. The global model incorporates both the α-model and K-model into the full background model. These parts are an important input to the global model influencing the outcome. In this chapter, the construction and results of the GERDA Phase II background model will be presented. For completeness, the presentation will include the α- and K-model.

5.1 Statistical analysis method

5.1.1 The Bayesian approach

The statistical data analysis is performed using a binned maximum likelihood fit to the data count rate spectra in energy space or detector space. Applying a Bayesian approach, the posterior probability distribution of the model $P(\lambda|n)$, which provides the probability of a certain model described by a set of parameters λ given the data n, is defined as

$$P(\lambda|n) = \frac{P(n|\lambda)P_0(\lambda)}{\int P(n|\lambda)P_0(\lambda)\mathrm{d}\lambda} \tag{5.1}$$

where $P(n|\lambda)$ denotes the likelihood $\mathcal{L}(n|\lambda)$ evaluated with the observed data n given the set of parameters λ. The additional term $P_0(\lambda)$ includes the prior knowledge on the parameters λ or its possible boundaries. In contrast to the common Frequentist approach, it expresses the degrees of belief about λ and updates to the posterior probability distribution. The posterior probability distribution $P(\lambda|n)$ constructed according to Eq. 5.1 summarizes the whole knowledge concerning λ by both the prior belief and the information provided by the experimental data n. The denominator in Eq. 5.1 represents a normalization factor.

The number of observed counts n_i in each bin follows a Poisson distribution. The likelihood for the observed data spectra results from the product of the probability of the data given the model and parameters in each bin i for each data set d such that it has the actual form

$$\mathcal{L}(n|\lambda) = \prod_d \prod_i Pois(n_{i,d}|\lambda_{i,d}) = \prod_d \prod_i \frac{e^{-\lambda_{i,d}} {\lambda_{i,d}}^{n_{i,d}}}{n_{i,d}!} \tag{5.2}$$

with $n_{i,d}$ the observed number of events and $\lambda_{i,d}$ the number of events expected from the model in the i-th bin, each of data set d.

The model prediction can be described as a composition of all components with potential contribution to each observed energy spectrum obtained from MC simulations. Hence, the predicted number of events in the i-th bin of data set d is the sum of the expected number of events from each model component c in that bin:

$$\lambda_{i,d} = \sum_c \lambda_{i,d}^c \tag{5.3}$$

The expected number of counts $\lambda_{i,c}$ from a component c in the i-th bin is given by

$$\lambda_{i,d}^{c} = N_d^c \int_{\Delta E_i} \Phi_d^c(E)\mathrm{d}E \tag{5.4}$$

where $\Phi_d^c(E)$ is the probability density function (PDF) of component c for data set d integrated over bin i, obtained by the normalized simulated spectrum of component c projected in energy (detector) space. The number of total counts, N_d^c, can depend on various quantities of interest (e.g. activity, number of events, half-life,...) for individual components.

The full background model consists of three independent model parts: the α-model, the global model and the K-model. Each part is carried out by a spectral fit with the parameter of interest defined by the number of events N_d^c of each component c in the spectrum of data set d. Combining the individual model parts yields the following factorization of the likelihood

$$\mathcal{L}(n|\lambda) = \mathcal{L}_{glob}(n|\lambda)\cdot\mathcal{L}_{K}(n|\lambda)\cdot\mathcal{L}_{\alpha}(n|\lambda) \tag{5.5}$$

where $\mathcal{L}_x$ is the likelihood function from the x-th model part with $x \in \{\text{glob}, \alpha, \text{K}\}$. The likelihood function of each part is defined according to Eq. 5.2. Finding the model parameters that yield the maximum likelihood estimates according to the preceding procedure, was achieved with the Markov Chain Monte Carlo (MCMC) technique provided by the Bayesian Analysis Toolkit software package [74].

α-model The α-model is designed to investigate the high edge of the energy spectra of the single-detector events (M1) of $^{\text{enr}}$BEGE and $^{\text{enr}}$Coax data dominated by α events from emitting isotopes in the neighborhood of the detectors. The energy spectra are fitted in the range from 3500 keV to 5270 keV with the parameters of interest defined according to Eq. 5.4. Since α particles have a very short range in LAr and in Ge, these events are only able to reach a detector's active volume through the thin p$^+$ surface. Therefore, it's contribution depends strongly on the surface contamination of each detector resulting in a α events distribution which is detector individual. Consequently, the data sets are uncorrelated and can be processed for each data set $d \in \{\text{BEGe},^{\text{enr}}\text{Coax}\} \times \{\text{M1}\}$ separately.

Global model The global model consists of a fit over the whole energy spectrum above the ^{39}Ar end-point up to 5260 keV including the high energy range of the α-model. In order to connect model contributions from different data sets of the same decay, the activity or the half-life of a decay, which can be the same for different data sets, can be introduced. This applies for the global model which combines the single-detector events of $^{\text{enr}}$BEGE and $^{\text{enr}}$Coax as well as the two-detector events data (M2) with $d \in \{\{\text{BEGe},^{\text{enr}}\text{Coax}\} \times \{\text{M1}\},\{\text{M2}\}\}$. To extract the activity A_c of a decay from a certain component c, the total number of counts N^c_d from Eq. 5.4, can be replaced by the relation $N^c_d = A_c \cdot \varepsilon^c_d \cdot t_d$ by inserting at the same time the lifetime t_d and the detection efficiency ε^c_d of component c which are data set inherent properties. For the inverse half-life $1/T^c_{1/2}$, the total number of counts N^c_d can be substituted according to Eq. 1.28. In both cases, the detection efficiency of component c is extracted from the MC simulations.

K-model In the framework of the K-model, the number of counts in certain energy intervals around the 1461 keV and 1525 keV γ lines of ^{40}K and ^{42}K, respectively, have been studied by their distribution over the detector ID (detector space). Each bin in the spectrum is attributed to one detector whereby the bin content corresponds to the total counts in the particular K line in this detector. Due to the high statistics in these γ lines, the K-model has the benefit of disentangling potential top-down and rotational asymmetries in the ^{40}K and ^{42}K distributions. Furthermore, the two-detector events are included by the count rates of one detector versus another resulting in a two-dimensional spectrum in the detector space. Therefore, the product of the likelihood runs over the two detectors i and k and Eq. 5.2 is extended by:

$$\mathcal{L}_K(n|\lambda) = \prod_d \left(\prod_i Pois\left(n^{M1}_{i,d}|\lambda^{M1}_{i,d}\right) \cdot \prod_{i<k} Pois\left(n^{M2}_{ik,d}|\lambda^{M2}_{ik,d}\right) \right). \tag{5.6}$$

Each data set consists of two so-called line-bands (K40 and K42) containing the counts in an energy interval of ±4 keV (M1) or ±6 keV (M2) around the γ lines and three so-called side-bands covering the energy range from 1405 keV to 1450 keV (SB1), 1470 keV to 1515 keV (SB2), and 1535 keV to 1580 keV (SB3) (see Fig. 5.1). The side-bands serve to determine the continuous background under the γ lines.

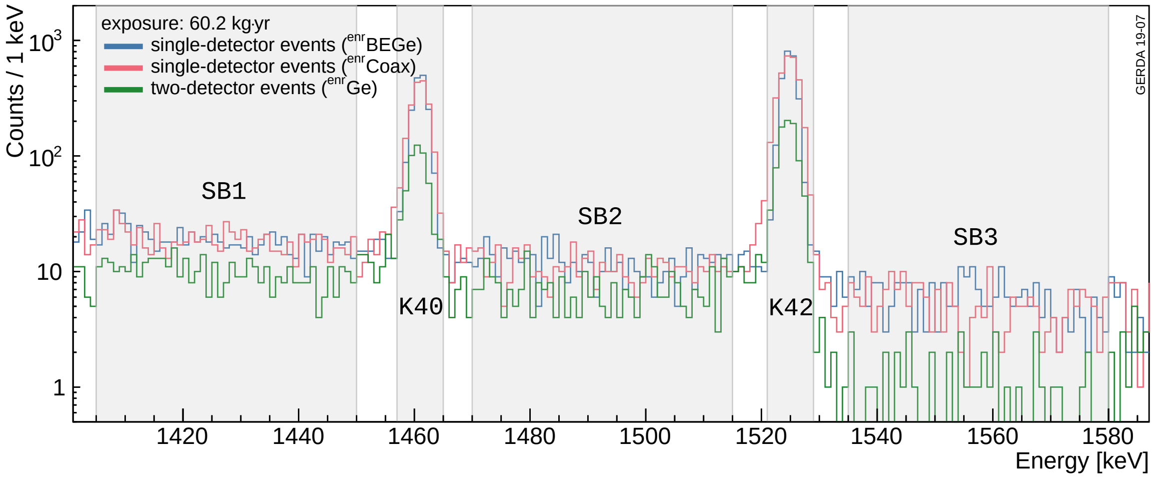

Fig. 5.1 Energy spectrum between 1410 keV and 1590 keV for single-detector and two-detector events of ^{enr}BEGE and ^{enr}Coax illustrating the selection of the five energy bands composing the data sets of the K-model [104].

5.1.2 Prior probability distribution

Choosing a prior is an essential part of the Bayesian approach. The prior probability function introduces preconceptions about possible values and defines the parameters range, making the choice of a suitable prior necessary although the preconceptions are sometimes unknown or arbitrary. There is no unique rule for constructing the prior containing one's degree of belief in the different possible values of a specific parameter λ. If some experimental knowledge about λ exists from a previous experiment, the prior can be deduced from the posterior probability density function of the previous experiment. Faced with the problem of finding an adequate prior when there is no previous measurement, the most evident prior seems to be a prior that expresses prior ignorance. According to Eq. 5.1, the posterior is proportional to the product of likelihood and prior distributions. The posterior can be understood as a combination of two sources of informations. If one carries more information, the posterior will be pulled toward it. Thus, a noninformative prior is a prior which has minimal impact on the posterior distribution of λ such that the posterior will resemble the information in the data.

In fact, if there is no previous measurement which can be consulted, in a first approximation you naively consider all possibilities equally likely. Then the most obvious candidate for a noninformative prior is a prior density uniform over the range of λ. When moving the endpoints of the parameter interval to finite values, the uniform distribution (also known as flat distribution) is given by

$$p_0^{uni}(\lambda) = \frac{1}{\lambda_{max} - \lambda_{min}} \tag{5.7}$$

with the cut-offs λ_{min} and λ_{max}, it becomes normalizable. If λ_{max} is big enough the posterior is almost independent of λ_{max}. If a constant prior is used, the parameter estimation by using the value with the highest posterior density (the maximum of the posterior probability distribution commonly called the mode) is equivalent to the maximum likelihood estimation over the used parameter range. Although the uniform prior gives reasonable results for a Poisson distribution, it is not invariant under non-linear parameter transformations. Image the parametrization of λ has been change to function of λ, for instance one may choose the half-life as parameter of interest instead of the count rate. The resulting transformed parameter might not have an uniform prior distribution due to the dependence on whether the prior is uniform in λ, $1/\lambda$ or etc.

Based on the argument of scale invariance, an alternative prior given by

$$p_0^{log}(\lambda) \sim 1/\lambda \tag{5.8}$$

is used in order to present a non-informative prior distribution. It is uniform on the log-scale of the parameter space λ and goes to zero smoothly for large λ. Unfortunately, $p_0^{log}(\lambda)$ is an improper prior, since it is not integrable over $[0,\infty)$. Still, an improper prior does not necessarily cause a problem when the posterior yields well-defined results which is the case for the Poisson likelihood, since the resulting posterior probability density results normalizable. Analogue to Eq. 5.7, $p_0^{log}(\lambda)$ becomes normalizable to unit area in $[\lambda_{min}, \lambda_{max}]$ by

$$p_0^{log}(\lambda) = a \cdot \frac{1}{\lambda} \quad \text{with } a = 1/\log\left(\frac{\lambda_{max}}{\lambda_{min}}\right) \tag{5.9}$$

with the cut-offs λ_{min} and λ_{max}. Finally, it should be noted that for the uniform prior the mode of the posterior probability distribution $P(\lambda|n)$ equals n which is the maximum of the likelihood estimation, while for the scale-invariant prior the mode is smaller than the maximum of the likelihood estimation. But when considering the expectation value of the posterior probability distribution, for the scale-invariant prior the expectation value of the posterior equals n, while for the flat prior the expectation value is $n+1$.

In the particular case of the analysis presented in this work, the screening measurements presented in Ch. 3.2.1 could be used as previous "experiment" in order to extract a prior information on certain parameters. For backgrounds which have been measured, the prior probability distribution is expressed by a Gaussian distribution with the measured value from Tab. B.1 as mean and the corresponding error as sigma uncertainty. In case the screening measurements in Tab.B.1 indicate a source only by an upper limit λ_{lim} with a certain confidence level *CL*, the prior distribution is characterized by an exponential function

$$p_0(\lambda) \sim a \cdot \exp(-a \cdot \lambda) \tag{5.10}$$

which must be normalized in the range between the cut-off 0 and λ_{max}. Additionally, it must have the quantile corresponding to the desired probability at the limit value λ_{lim}. To construct a proper density out of the standard exponential function normalized between zero and infinity, the parameter a must be fixed by the condition of the quantile:

$$\int_0^{\lambda_{lim}} p_0(\lambda)\mathrm{d}\lambda = CL \quad \text{with } a = -\frac{\ln(1-CL)}{\lambda_{lim}} \tag{5.11}$$

Finally, cutting off the range of λ at a finite value λ_{max} yields the probability density function:

$$p_0^{exp}(\lambda) = a \cdot \exp(-a(\lambda - \lambda_{max})) \quad \text{with } a = -\frac{\ln(1-CL)}{\lambda_{lim} - \lambda_{max}}. \tag{5.12}$$

In the ideal case, the problem of choosing the adequate prior should become less important when increasing the amount of data. With increased amount of data, the likelihood should dominate and the posterior probability density function should tend asymptotically toward a Gaussian distribution.

5.1.3 Parameter estimate

The posterior probability distribution of a single parameter λ_k of the model $\lambda = (\lambda_1, \lambda_2, ...,)$ given the data n can be obtained by integrating the global posterior probability distribution over all model parameters except the one of interest:

$$P(\lambda_k|n) = \int_{\lambda_{k\neq l}} P(n|\lambda)P_0(\lambda)\mathrm{d}\lambda_{k\neq l} \tag{5.13}$$

where $P(\lambda_k|n)$ denotes the marginalized posterior distribution of λ_k. The parameter value with the highest probability density in the marginalized posterior distribution of the parameter in question is called the marginalized mode. The marginalized mode has to be distinguished from the global mode which maximizes the global posterior probability distribution. In analogy, a two-dimensional marginalized posterior distribution with respect to two parameters can be obtained. It represents the correlation between the two parameters and the correlation coefficient can be evaluated. Furthermore, an interval estimate for a parameter λ_k with the boundaries $\lambda_{k,min}$ and $\lambda_{k,max}$ can be estimated by a central interval $(\lambda_{k,l}, \lambda_{k,u})$ which is defined such that the probability fraction of each tail equals $(1-\alpha)/2$:

$$\int_{\lambda_{k,min}}^{\lambda_{k,l}} P(\lambda_k|n)\mathrm{d}\lambda_k = \int_{\lambda_{k,u}}^{\lambda_{k,max}} P(\lambda_k|n)\mathrm{d}\lambda_k = \frac{1-\alpha}{2} \tag{5.14}$$

Analogously, when the marginalized distribution is compatible with zero, an upper limit can be analogously calculated by a one-sided interval. The calculated parameter interval describes the degree of belief that the true value of λ lies with a probability α within this interval and therefore is called a credible interval (C.I.).

5.1.4 Goodness-of-fit and model comparison

p-value To draw conclusions about the ability of a model as representation of the data, the p-value is used as a goodness-of-fit test which quantifies the probability that a result as extreme or more extreme than the observed data could have occurred under the assumption that the model in question is the correct description of the physical situation (being the null hypothesis) [112]. Accordingly, the p-value is the probability that a discrepancy variable will have larger value (or smaller value depending on the definition of the discrepancy variable) than the observed value n under the assumption of the best fit parameters λ of the model. With the likelihood chosen as discrepancy variable, the p-value has been evaluated according to

$$p = \frac{\int_{\forall x:\mathcal{L}(x|\lambda)<\mathcal{L}(n|\lambda)} \mathcal{L}(x|\lambda)dx}{\int_0^\infty \mathcal{L}(x|\lambda)dx} \tag{5.15}$$

In consequence, the p-value results in the probability to obtain a lower likelihood for a possible set of observations x within the context of the best fit parameters λ than for the observed data set n. Small values of the p-value are taken as evidence against the model in question. Commonly, the significance level is set at 0.05 such that the model in question is rejected in case of a p-value smaller than 0.05.

z-score The results of the performed fits are displayed by showing the best fit model and data plotted together with the residuals and the uncertainty intervals placed on the model predictions. The residual of each bin is estimated by the so-called z-score. Analogous to definition of the p-value in Eq. 5.15, the probability $\mathscr{P}$ that a result as extreme or more extreme than the data point n_i in the i-th bin given the model expectation λ_i is defined by

$$\mathscr{P}(n_i|\lambda_i) = \frac{\int_{\forall x:P(x|\lambda_i)<P(n_i|\lambda_i)} P(x|\lambda_i)dx}{\int_0^\infty P(x|\lambda_i)dx} \tag{5.16}$$

where $P(x|\lambda_i)$ is the discrepancy variable given by the Poisson distribution such that $P(x|\lambda_i) = Pois(x|\lambda_i)$. The probability $\mathscr{P}(n_i|\lambda_i)$ of the data point n_i is then converted into an equivalent significance z, the z-score. It is interpreted as the $\mathscr{P}(n_i|\lambda_i)$-quantile normalized to the standard normal distribution $\mathscr{N}(0,1)$, and thus defined by

$$Z(n_i|\lambda_i) = \Phi^{-1}(\mathscr{P}(n_i|\lambda_i) - 0.5) \tag{5.17}$$

where $\Phi(z)^{-1}$ is the inverse cumulative distribution function of $\mathcal{N}(0,1)$. The z-score is given in terms of the number of standard deviations σ the data point is above ($Z(n_i|\lambda_i) > 0$) or below ($Z(n_i|\lambda_i) < 0$) the mean. Three uncertainty intervals corresponding to 1σ, 2σ and 3σ are shown with green, yellow and red bands, respectively. The comparison plots with the color-coded uncertainty intervals give an indication whether the observations are within reasonable statistical fluctuations of the expectations, and hence also allow for judging the validity of a model.

Bayes factor Although, the p-value allows ranking different models, it is not suitable for model selection since the p-value is a measure of the statistical significance level of a model in question validating it without reference to other models. Even if the model with the largest p-value gives the best representation, any model yielding a reasonable p-value should be taken into consideration [112]. A more convenient measure of the evidence for an alternative model is the Bayes factor. Suppose one aims to compare an alternative model M_A to a base model M_B (null hypothesis). Then, the Bayes factor is defined as the ratio of their marginalized posterior probability distributions:

$$BF = \frac{\int P(n|\lambda_A, M_A) P_0(\lambda_A) d\lambda_A}{\int P(n|\lambda_B, M_B) P_0(\lambda_B) d\lambda_B} \tag{5.18}$$

To assess the evidence, the scale for the obtained Bayes factor can be interpreted by the categorization listed in Tab. 5.1. Note that the testing through the Bayes factor gives the null hypothesis a preferred status and considers the evidence against it.

Table 5.1 Scale for Bayes factor to assess the evidence of model M_A against model M_B [113].

BF	Evidence against M_B
< 3	barely worth mentioning
$3 - 20$	positive
$20 - 150$	strong
> 150	very strong

The calculation of the Bayes Factor requires the normalization of the posterior probability function which is not trivial to compute, since it is an integral over a high dimensional parameter space requiring numerically more or less sophisticated procedures. In fact, in case of the global model the numerical integration procedure of the likelihood over all parameters failed. Since solving the numerical integration was beyond the scope of this work, different competing models obtained by the global fit have been evaluated by their respective p-values.

If the p-values have been approximately at the same significance level, the principle of simplicity following Occam's razor has been applied and the model containing the fewest assumptions was preferred [114].

5.2 Modeling of the high energy region (α-model)

The modeling of the high energy region considers only the α-emitting constituents of the ^{238}U decay chain. Using the statistical method described in Sec. 5.1.1, a spectral fit in the energy space is performed over the high energy range between 3500 keV and 5270 keV divided in 10 keV wide bins. The fit window is dominated by ^{210}Po decays, below which ^{226}Ra decays ($E_\alpha = 4.8$ MeV) on the p$^+$ surface or in LAr are expected to contribute as well. The number of events is determined as a free parameter for each component of ^{210}Po and ^{226}Ra in addition to its short lived daughter nuclei.

The spectral shape due to α decays is influenced by the p$^+$ dead layer thickness, but a single dead layer thickness assumption can not describe the observed data spectra sufficiently accurate. As an effect of the boron implantation process of the p$^+$ surface, resulting inhomogeneous layers among the surface could cause a kind of transition layer with partly disturbed charge collection. Taking this effect into account a superposition of energy distributions arising from different dead layer thicknesses without a partly active layer is assumed be equivalent to the approach described in [108]. The weights of the single dead layer thicknesses between 100 nm and 800 nm are determined as free parameters of a separate fit in the region of the ^{210}Po peak.

Apart from ^{210}Po, simulations of decays on the p$^+$ surface of ^{226}Ra, ^{222}Rn, ^{218}Po and ^{214}Po are included, but each subsequent isotope in a sub-chain shows a systematic decrease in intensity due to the reduced detection efficiency of the emitted αs. The probability that the daughter nucleus with typically about 100 keV recoil energy after an α decay, reaches the active volume of the detector is about 50% due to kinematics and the stopping ranges of a few tens of μm. Based on kinematics, the α particle and the daughter nucleus will have momenta with opposite directions, hence the α particle will be detected through energy deposition in the active volume and the daughter nucleus will recoil away from the surface. The subsequent emitted α particle will escape detection due to the short range in LAr. Assuming the reverse scenario where the nucleus stays at the detector surface, the α particle escape detection and the subsequent α will be detected. As consequence of the low event statistics around the peaks at 5.3 MeV (^{222}Rn), 5.9 MeV (^{218}Po) and 5.2 MeV (^{214}Po) the count rate of each progeny can be determined individually. Thus, accounting for the effect of escaping detection the energy spectra of the sub-sequent α emitting isotopes of the ^{226}Ra sub-chain (^{226}Ra, ^{222}Rn, ^{218}Po and ^{214}Po) are summed up with a decreasing branching of 50% from daughter nucleus to daughter nucleus.

Table 5.2 Summary of the fit results of the α-model for single-detector data of $^{\mathrm{enr}}$BEGE and $^{\mathrm{enr}}$Coax. The global and marginalized modes along with the central 68% C.I. are reported. Values are given in cts in the full PDF range from 40 to 8000 keV [104].

data set	component	contact [nm]	global mode [cts]	marg. mode 68% C.I. [cts]
$^{\mathrm{enr}}$BEGE	^{210}Po	400	49	50 (34,76)
		500	162	165 (107,222)
		600	346	342 (278,391)
		comb.	–	555 (523,586)
	^{226}Ra chain	500	20	20 (15,29)
	energy deg.	–	–	845 (698,948)
$^{\mathrm{enr}}$Coax	^{210}Po	300	167	165 (140,208)
		400	363	368 (272,430)
		500	182	175 (83,338)
		600	433	420 (233,582)
		700	404	410 (295,537)
		comb.	–	1555 (1511,1609)
	^{226}Ra chain	100	58	59 (49,70)
	energy deg.	–	–	485 (426,599)

The spectral shapes of the peak-like structures from p$^+$ surface simulations (see Figs. 4.9a and 4.9c) can not describe the observed spectrum below 4.6 MeV sufficiently. A contribution from an approximately flat component is necessary to describe the whole energy spectra below the peak-structures. Besides, an unexpected kind of events with a delayed charge collection to which the energy reconstruction algorithm has not been adjusted, was observed in the data. Evidence suggests a contamination of ^{210}Po located on the groove surface causing a delayed charge collection resulting in wrongly reduced energy reconstruction [115]. The perturbed charge collection degrades the energy distribution towards lower energies. The energy distribution of events due to slow charge release is expected to be a broad continuum without a peak structure modeled by a first order polynomial cut off below the maximum of the ^{210}Po peak at 5.3 MeV. The first order polynomial has been modeled by a flat offset and a degraded slope. If no hot spot can be traced, a first degree polynomial shape is in agreement with either location scenarios, i.e. with decays in LAr close to the p^+ or in the groove with inefficient charge collection.

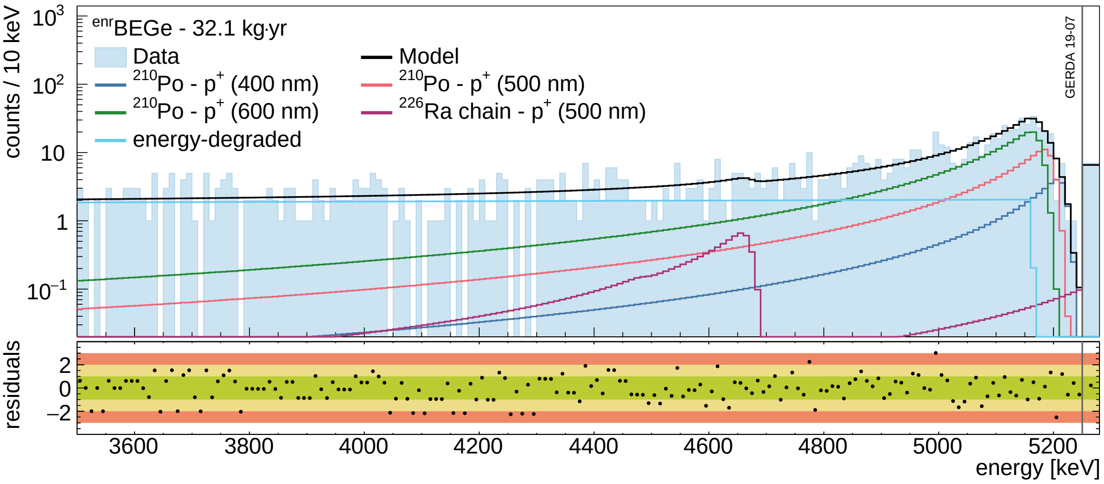

(a)

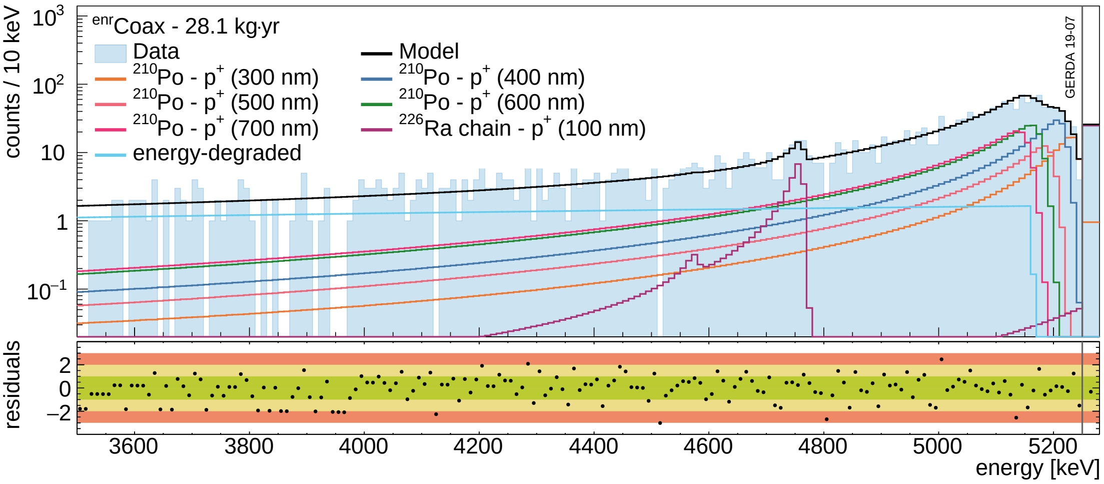

(b)

Fig. 5.2 Experimental spectrum in the energy region above 3500 keV (filled) and the best fit of the α-model(black line), together with the individual components of the best fit model for the single-detector data sets of ^{enr}BEGE (a) and ^{enr}Coax (b). All events above 5250 keV are contained in the last bin at the high energy edge of the spectrum. The lower panels show the residuals with the shaded bands representing the statistical uncertainties. [104]

Summarizing, the high energy region fit model consists of different dead layer contributions of the α decay of ^{210}Po on the p^+ surface, the decays of the α emitters in the ^{226}Ra sub-chain on the p^+ surface and a flat component modeled by slope and offset. The expected number of α induced events in the whole range between 40 keV and 8000 keV of the final configuration are listed in Tab. 5.2. As it can be seen by the comparison of the α model and the high energy range of the observed data in Fig. 5.2, the α-model fully describes the data and no unidentified structures or missing background components are found. The analytically constructed distribution of the degraded α events can not be constrained completely by the high energy range as it degenerates towards lower energies. Therefore, the α model is split in a high energy part containing the peak-like structures from ^{210}Po and the ^{226}Ra sub-chain, and the offset and slope part, which are added to the full-range model as three probability density functions for each data set. Their total number of counts will be left as a free parameter with non-informative prior probability distribution allowing only for positive values. Furthermore, the decay rate of ^{214}Bi and ^{214}Pb are assumed to be similar to the initial rate of ^{226}Ra, therefore its activity on the p^+ surface is extracted from the α model and then the posterior distribution is folded in as prior distribution in the global model [110].

5.3 Modeling of the potassium γ lines (K-model)

According to the observed data, the count rate distribution of the γ line at 1524.7 keV over the detector IDs, in the so-called detector space, exhibits a top-bottom asymmetry indicating a source near the top. Thus an additional volume surrounding the upper part of the detector array was introduced in the simulation from which decays of ^{42}K were sampled. In the energy spectrum, top-bottom or possible rotational asymmetries are not visible due to the summation over multiple detectors. Decays taking place in an upper volume around the detector array produce a summed energy spectrum which differs only slightly from a homogeneous distribution outside the mini-shrouds. For this reason, the K-model has been integrated to disentangle top-bottom or rotational asymmetries in the spacial distributions of ^{42}K and ^{40}K.

The K lines are the most prominent γ lines in the energy spectra with high enough statistics to analyze the count rates individually for each detector. In the K-model, the count rates are projected in the detector space such that each bin in the spectrum is attributed to one detector where the bin content corresponds to the total counts in the particular K line in this detector. A spectral analysis is performed by fitting the projected spectrum for the regions of the line and side bands according to Sec. 5.1.1. While for ^{42}K flat priors are used, the measured values of ^{40}K from the screening measurements are introduced by Gaussian prior probability distributions. The side bands are integrated in order to determine the continuum below the K lines, which is primarily attributed to decays of the $2\nu\beta\beta$ process in ^{76}Ge and of ^{214}Bi originating from the cables and holders.

Table 5.3 Summary of the fit results of the K-model for single-detector and tow-detector data of $^{\mathrm{enr}}$BEGe and $^{\mathrm{enr}}$Coax combined. The global and marginalized modes along with the central 68% C.I. are reported. The type of prior distributions is indicated with [f] for flat, [g] for Gaussian and [e] for exponential.

source	[prior] location	units	global mode	marg. mode	68% CI or 90% CI upper limit
^{40}K	[g] cables	mBq	3.22	3.25	(1.91, 4.72)
	[g] detector holders		1.72	1.73	(1.24, 2.14)
	[g] mini-shrouds		1.70	1.70	(1.60, 1.79)
	[g] fiber shroud		2.83	2.81	(2.24, 3.38)
	[g] SiPM ring		2.50	2.32	(0.83, 4.13)
	[g] copper shroud		18.4	18.5	(16.6, 20.0)
	[g] read-out electronics		15.8	16.2	(11.4, 20.1)
	[f] close to the array		10.8	10.9	(9.52, 12.08)
	[f] far from the array		330	323	(235, 420)
^{42}K	[f] LAr – outside mini-shrouds	mBq	1848	1912	(1770, 2010)
	[f] LAr – above array		458	459	(442, 476)
	[f] n^{+} (Coax)		0.50	0.39	(0.21, 0.63)
	[f] n^{+} (BEGe)		0	0	<0.55
	[f] p^{+} (Coax)		0.05	0.06	(0.03, 0.10)
	[f] p^{+} (BEGe)		0	0	<0.09
^{214}Bi	[g] cables	mBq	1.36	1.14	(0.85, 1.40)
	[g] detector holders		0	0	<0.31
$2\nu\beta\beta$	[f] germanium	10^{21}yr	2.03	2.06	(2.02, 2.11)

Through calculation and comparison of the respective Bayes factors [104], the final composition of the K-model had been determined iteratively by starting with a minimal model consisting of ^{40}K coming from the source locations predicted by screening measurements and of ^{42}K distributed homogeneously around and above the detector array. It turned out that the minimum model is not sufficient to describe the data, therefore, the final configuration, the so-called base model, comprises additional near and far ^{40}K sources whose exact source locations are unknown. The additional contribution is represented by the PDFs of the mini-shrouds, since reconsiderations point to the applied glue which is expected to be contaminated with ^{40}K. Since the glue has been applied by hand, the amount in the setup is not precisely known and can differ significantly per location and mini-shroud. Furthermore, including surface contributions of ^{42}K leads only to a slightly improved Bayes factor. Nevertheless, these contributions are included in the base model, since additional information is expected by the larger fit window of the global model need in order to constrain these contributions (see Sec. 5.4). Tab. 5.3 lists the parameter estimates of the base model configuration reported by the global modes and the marginalized modes together with the 68% C.I. and the 90% probability limits. Since the energy spectra are not very sensitive to asymmetries of the source locations, the results of the base model yield a satisfactory prior information for the global model although the base model is obtained with a low p-value of 0.06 (see Fig. 5.3(a)-(d)). To improve the accuracy of the description of the data, an extended model has been developed which contains additional rotationally asymmetric components. The extended model is not used in this analysis and therefore the reader is referred to [104] and [111].

5.4 Global background model (global model)

The global model provides a full decomposition of the background spectrum for single-detector and two-detector events of $^{\text{enr}}$BEGe and $^{\text{enr}}$Coax into its individual components. A spectral fit following the statistical method described in Sec. 5.1.1 was performed in the energy range from 570 keV to 5250 keV for the single-detector events spectra of $^{\text{enr}}$BEGe and $^{\text{enr}}$Coax, and from 520 keV to 3500 keV for the two-detector events spectrum with a binning of 1 keV. Each post-processed MC simulation discussed in Ch. 4.3 has been considered providing a PDF in the global model.

The global analysis compares model prediction with data by taking advantage of the two models (α-model and K-model) introduced above. Fig. 5.4 gives a visualization of how the global model incorporates the individual model parts. The α-model is partially decoupled from the global model analysis in the sense that after a pre-definition of the decomposition of the energy spectra above 3500 keV for single-detector events of $^{\text{enr}}$BEGe and $^{\text{enr}}$Coax, it enters the global model as a reduced number of PDFs. Apart from the energy degraded α events, all α-emitting components of the ^{226}Ra and ^{210}Po chains have been summed up according to the α-model results (see Sec. 5.2) in order to be represented by only one remaining PDF each for $^{\text{enr}}$BEGe and $^{\text{enr}}$Coax. Since the global model is uncorrelated with the K-model, the posterior probability density distributions for each K-component can enter as prior information into the global model. The contributions of the components corresponding to ^{42}K and ^{40}K have been pre-analyzed in the context of the K-model and the resulting posterior distributions have been used as prior distributions for the global model. Generally, a surface contamination might be different for the two detector types. In case of ^{42}K, the surface contaminations are expected due to the attraction of the ^{42}K ions by the high voltage potential of the detectors. Since the volumes of the mini-shrouds from which the ions

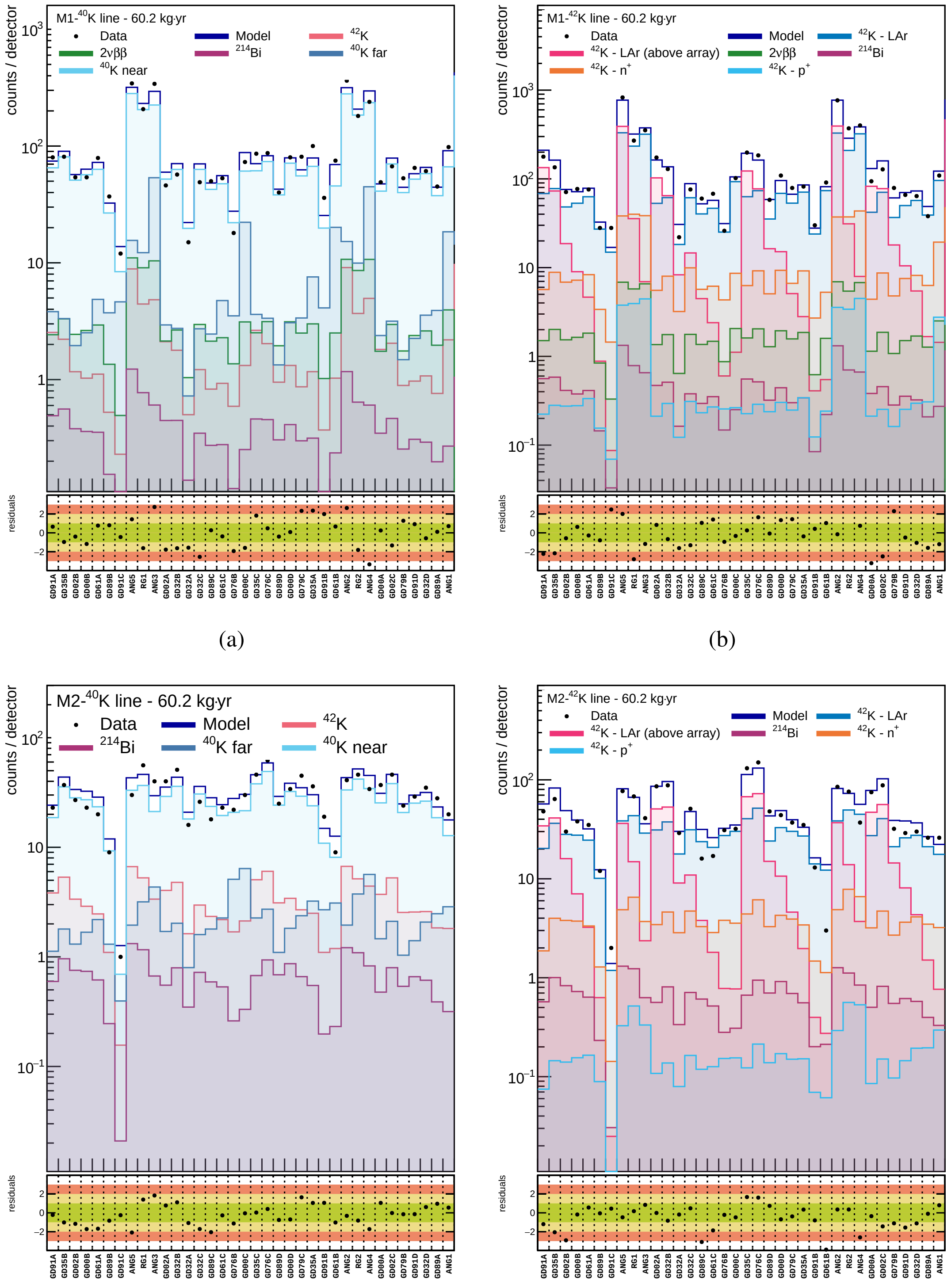

(a)

(b)

(c)

(d)

Fig. 5.3 Experimental count rate in detector space (black marker) of the ^{40}K ((a),(c)) and ^{42}K((a),(c)) lines and the best fit of the base K-model (black line) for the single-detector data ((a),(b)) as well as the one-dimensional representation of the two-detector data ((c),(d)), together with the individual components of the best fit base model. The lower panels show the residuals with the shaded bands representing the statistical uncertainties. [104]

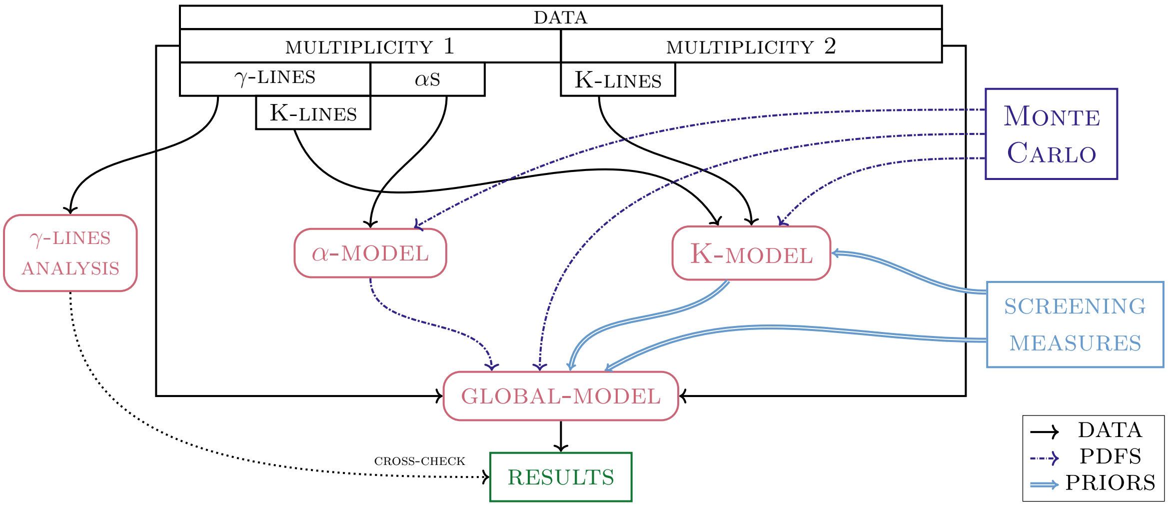

Fig. 5.4 Chart of the global model describing the analysis flow. The energy distribution of the single-detector and two-detector data are fit in the framework of the global model. The simulated spectral shapes and the α-model enter the global model as PDFs while the screening measurements and K-model provide prior probability distributions.

originate are almost equally sized, the surface contaminations are assumed to be correlated additionally taking into account the total surface of the two detector types. For this reason, a correlation between the two detector types has been maintained by inserting the joint two-dimensional marginalized posterior probability distribution involving both parameters of the n^+ for ^{enr}BEGe and ^{enr}Coax data provided by the K-model. In each data set, the energy ranges of the two line bands of the K-model are represented by two single bins containing the corresponding total count rates .

All available results from screening measurements of the materials, as reported in Tab. B.1, have been used as prior information for the background activities of the corresponding isotopes and locations following the description in Sec. 5.1.2. Furthermore, delayed coincidences can provide information on the population of progenies by associating the estimated activity of the parent isotope. Due to the fact that ^{214}Bi and ^{214}Pb are part of the U-series, for a contribution on the p^+ detector contacts the posterior probability density distribution of ^{226}Ra extracted from the α-model has been used as prior probability distribution. Not all of the components in the setup have been assayed, hence a flat prior was selected for these parameters.

For a large number of different isotopes and locations, the source activity has been determined by a scaling parameter estimate in the fit and by the number of simulated events. Fig. 5.5 shows the results which are extracted from a so-called maximum model which consists of 49 fit parameters considering all available PDFs. The results are reported together with the chosen prior and the screening information. In case of a flat prior, the prior is not explicitly indicated in Fig. 5.5. For the fit results, the priors and the screening measurements are quoted by either the marginalized modes with the 68% C.I. or the 90% upper limit. The comparison with the known inventory of the contaminations in the same figure shows that all contaminations expected from screening measurements are contained in the background spectra. As demonstrated in Fig. 5.5 all parameter estimates and their corresponding screening information agree within 68% or within 90% C.I. But the activities identified by screening measurements are not sufficient to explain the total composition of the observed background spectra. The main background contributions are coming from close sources of the detector assembly and the fiber veto instrumentation in medium distance. Without using the information of the screening measurements, the individual close sources (detector holders, cables and mini-shrouds) of the detector assembly can not be identified unambiguously due to the strong correlations (factor between 0.6 and 0.8) resulting from the high resemblance of the spectral shapes of the summed energy spectra.

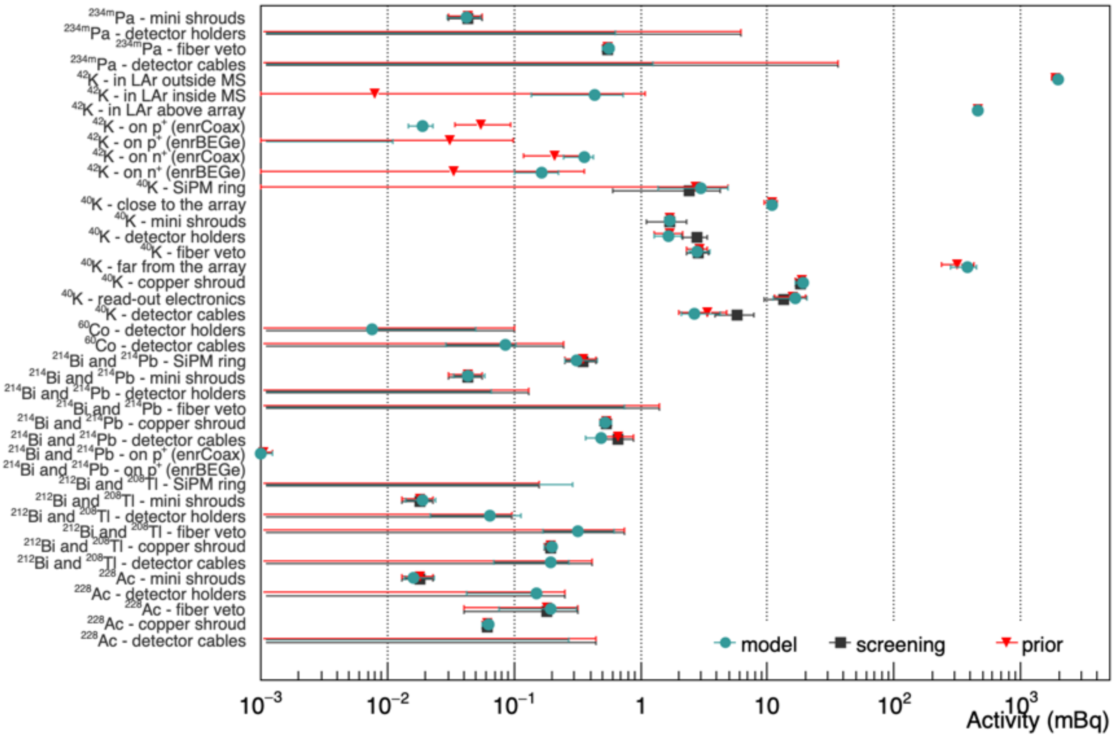

Fig. 5.5 Summary of the parameter estimates obtained by the maximum global model. Flat priors are not indicated. The marginalized modes along with the central 68% C.I. or the 90% upper limit are reported. Furthermore, the parameter estimates are compared to the corresponding prior and screening measurements.

To obtain the final background model, a model has been elaborated on the basis of the maximum model by reducing the number of parameters to a minimal number necessary to describe the observed energy spectra. At the same time, the individual parameters should be preferably identified unambiguously. For this reason, the pairwise correlations among the parameters have been studied. Fig. B.6 displays the correlation matrix for the maximum fit of the global model. Additionally, the impact of the individual parameters on the total number of counts in the spectra under study are shown. If two parameters are correlated in the maximum model, one of the parameters have been selected for the minimum model after the study of the energy spectra and PDfs or in consideration of further informations.

^{42}K Apart from the $2\nu\beta\beta$ decay of ^{76}Ge, the largest background is due to ^{42}K. In the maximum model, the total ^{42}K contribution is represented by all seven different source locations (the p^+ contact and the n^+ surfaces of the enriched BEGe and coaxial detectors, the homogeneous distribution in LAr separated by decays originating from the inside and outside of the mini-shrouds and the arbitrary chosen volume above the array). The top-bottom asymmetric distribution of ^{42}K can not be completely disentangled by the global fit using the summed energy spectra of $^{\mathrm{enr}}$BEGE and $^{\mathrm{enr}}$Coax. However, the posterior obtained by the K-model provides the necessary information of the decays originating from above the array. The activity of this contribution is primarily correlated with the contribution of decays from outside the mini-shrouds. A higher contribution compared to the K-model prior information can be observed for the contributions coming from the detector n^+ surfaces. On the other side, the contributions of the p^+ surface are decreased. The surface contaminations exhibit a higher continuum whose determination relies on larger energy ranges compared to the small side bands used in the K-model. Furthermore, the different activities of ^{42}K on the n^+ surfaces of the two detector types can be explained by differences in the continuum-to-peak ratio and especially in the energy region above the FEP. The spectral shape of decays close to the detector n^+ surface depends strongly on the assumed detector dead layer thickness due to the attenuation length of only a few millimeters for β events. Unfortunately, all surface contributions are strongly correlated by about a factor 0.5, except the p^+ contribution of the $^{\mathrm{enr}}$Coax data. Excluding the contributions of ^{42}K on the n^+ surface leads to an increase of the contribution from ^{42}K homogeneously distributed in LAr inside the mini-shrouds. In addition, it amplifies the contribution of α emitting isotopes and the contribution of ^{208}Tl in the fiber veto. Background coming from the ^{42}K is considered to be one of the most relevant for the GERDA experiment. The spacial distribution of ^{42}K proved to be difficult to determine due to its large continuous spectrum with only a single γ line at 1525 keV. All components due to ^{42}K have to be constraint by the counts in the FEP. The localization of

^{42}K is particularly crucial as electrons released in the decay of ^{42}K with a maximal energy of 3.5 MeV can contribute to background in the ROI depending on the its distance from the detectors' surfaces. Since the marginalized distribution of the contribution from inside the mini-shrouds yield a 90% upper limit, this contribution has been excluded from the minimum model. Compared to Phase I, the rate of ^{42}K has increased by about a factor of 2. This might be explained by the replacement of the Cu mini-shrouds of Phase I by transparent non-metallic mini-shrouds which allow to move the ^{42}K ions in LAr due to the dispersion of the electric field by the unshielded HV cables.

^{40}K ^{40}K can be found in almost all materials in close, medium and far distance from the detector array. Apart from that, a higher ^{40}K contamination than expected from screening measurement is observed. This additional presence of ^{40}K contaminations is compensated in the global fit by the introduction of additional contributions located in short and long distance from the detector array. The additional close contribution is represented by the PDFs of the mini-shrouds, but in contrast to the count rates in detector space, the simulated energy spectra of the close sources do not differ noticeably. Furthermore, a smaller contribution compared to the activity predicted by the screening measurements exists for the detector cables and holders. This effect is already introduced by the prior distributions obtained from the K-model.

^{214}Bi and ^{214}Pb ^{214}Bi and ^{214}Pb is present in the cables, the mini shrouds and the copper shroud. But the main background from ^{214}Bi and ^{214}Pb is due to the detector cables. Normalized to the number of detectors operated in Phase II, this result equals approximately the activity of the close source (detector holders) of the maximum model in Phase I. Despite the different peak-to-continuum ratios of the PDFs, the parameter of the cables is correlated with the holders and the fiber veto by a factor of 0.68 and 0.59, respectively. Both contributions are excluded from the minimum model. The contamination of the p$^+$ surfaces is derived from the ^{226}Ra activity on the p$^+$ surface obtained by the α-model and are below 1 µBq. There might be a contribution from the outer detector surface due to the Li salt which is used for doping of the n$^+$ surface. Even if the Li-induced ^{226}Ra contamination diffuses into the Ge, a negligible background contribution is assumed. With this fact and the strong correlation to the remaining contributions, it has not been taken into account in the minimum model.

^{228}Ac The individual ^{228}Ac contributions are almost consistent with the screening measurements. Since the spectral shapes of the PDFs of close source locations resemble each other, a high correlation is expected. A contamination of cables is indicated only by a

90% upper limit. In case of the mini-shrouds, the prior distribution extracted from the screening measurements dominates the data. The close contributions of the holders and the mini-shrouds to the background turns out to be four times smaller than that of Phase I. The additional contributions in Phase II originate from the LAr veto system introduced by the fibers veto instrumentation and the Tetratex foil of the copper shroud. Especially the dominant contribution from the fiber veto can be emphasized.

^{228}Th The largest contributions of ^{228}Th are coming from the cables and the fiber veto. But the cables contamination contributes more strongly to the background in the ROI compared to the fiber veto contamination due to a larger distance of the fiber veto to the detectors. The contamination of the cables, the holders and the fiber veto are all indicated by the screening measurements with 90% upper limits. The cables contamination is strongly correlated with the one of the holders (-0.85) and the one of the fiber veto (-0.55). Therefore, the cable contribution has been adopted as representation of the two near source contributions, as the assumption on the BIs in the ROI is more pessimistic when attributing the background contribution to the cable contaminations due to the reduced continuum above the FEP (see Fig. 4.11). Different parts in the detector surrounding have been affected by the upgrade to Phase II, in consequence the contaminations of the close source can be different from Phase I. This can be observed for the close source of ^{228}Th (from the cables in Phase II) which is reduced by about a factor of 1.5 compared to the close source of Phase I attributed to the detector assembly.

remaining contributions The background contributions from ^{60}Co and $^{234\mathrm{m}}$Pa are mainly associated with the close sources of the detector assembly and the fiber veto instrumentation in medium distance ($^{234\mathrm{m}}$Pa). For ^{60}Co, the source location can not be identified unambiguously.

α decays The total number of α decays originating from isotopes of the ^{226}Ra and ^{210}Po chain are summarized in one fit parameter in the global model whose overall scaling extracted by the α-model is reduced by 2.4% and 1.5% in the global model for the $^{\mathrm{enr}}$BEGE and $^{\mathrm{enr}}$Coax data, respectively. Events from α decays degraded in energy are represented by two continuous distributions which are obviously highly correlated. In case of the $^{\mathrm{enr}}$Coax detectors, as a result of the spectral tail towards lower energies, the degraded α contribution can not be completely determined by the α-model. Compared to the α-model, the number of decays coming from energy-degraded α is markedly reduced by a factor of 1.5 and 1.2 for the $^{\mathrm{enr}}$BEGE and $^{\mathrm{enr}}$Coax data, respectively, since the contribution is correlated with the other major contribution in the ROI coming from the p^+ and n^+ contamination of ^{42}K.

Though a flat distribution without peak structures which extents towards lower energies could be attributed to α decays taking place in LAr close to the p^+ surface, but contributions from ^{226}Ra and its daughters can not be assessed due the low counting rate above 5.4 MeV (compared to Phase I).

Table 5.4 Summary of the analysis parameter estimates obtained by the minimum model. The global and marginalized modes along with the central 68 % C.I. are reported. The number of reconstructed counts from each component are given. The type of prior distributions is indicated with `[f]` for flat, `[g]` for Gaussian, `[e]` for exponential, `[p`$_\alpha$`]` for posterior obtained from the α-model and `[p`$_K$`]` for posterior obtained from the K-model.

source	location	unit	global mode	marg. mode	(16% C.I.,84% C.I.)	screening	^{enr}Ge (M2)	^{enr}BEGE (M1)	^{enr}Coax (M1)
$2\nu\beta\beta$	`[f]` intrinsic	$10^{-21} yr^{-1}$	0.4938	0.4939	(0.4904,0.4970)		–	45267.8	37863.2
	`[f]` δ_{AV} (^{enr}Coax)	%	4.6	5.1	(3.8,5.8)		–	–	1743.3
^{212}Bi & ^{208}Tl	`[e]` detector cables	μBq	361.71	356.00	(329.73,382.54)	< 413	423.1	399.9	258.5
	`[g]` copper shroud		194.64	196.50	(177.49,215.32)	194±19	1.4	2.9	3.1
	`[g]` mini shrouds		18.19	17.70	(13.34,23.12)	18±5	23.7	20.1	20.5
^{214}Bi & ^{214}Pb	`[`p_α`]` on p^+ (^{enr}BEGE)	μBq	0.3778	0.3705	(0.2673,0.5222)		3.0	6.1	–
	`[`p_α`]` on p^+ (^{enr}Coax)		0.851	1.037	(0.875,1.234)		4.4	–	21.1
	`[g]` detector cables		544.16	536.00	(505.71,577.76)	660±207	896.4	1158.9	728.3
	`[g]` copper shroud		531.43	535.00	(475.04,581.22)	532±53	3.9	9.1	9.9
	`[g]` mini shrouds		44.69	43.50	(31.67,56.93)	43±13	81.2	95.9	94.1
	`[g]` SiPM ring		356.88	325.00	(259.18,451.44)	351±97	2.9	6.5	5.0
^{228}Ac	`[g]` copper shroud	μBq	62.20	62.50	(55.88,68.05)	62±6	0.2	0.5	0.6
	`[e]` detector holders		182.65	182.25	(162.77,208.70)	< 250	346.5	540.3	280.1
	`[g]` mini shrouds		18.50	17.75	(13.27,23.38)	18±5	20.0	28.7	28.1
^{60}Co	`[e]` detector cables	μBq	111.55	113.75	(97.36,129.56)	< 247	327.4	375.6	236.2
^{234m}Pa	`[g]` fiber veto	mBq	0.5519	0.5480	(0.4993,0.5963)	0.55±0.05	1.4	3.2	3.2
	`[g]` mini shrouds		0.0429	0.0435	(0.0281,0.0559)	0.04±0.01	1.0	2.0	2.0
^{40}K	`[g/`p_K`]` detector cables	mBq	2.59	2.93	(2.07,4.20)	6±2	297.5	756.1	465.3
	`[g/`p_K`]` read-out electronics		16.310	16.032	(11.764,20.191)	13±4	45.0	102.1	77.9
	`[g/`p_K`]` copper shroud		18.15	18.22	(16.53,20.16)	18±2	17.0	40.9	44.2
	`[g/`p_K`]` fiber veto		2.79	3.00	(2.32,3.43)	2.9±0.6	56.3	126.8	118.7
	`[g/`p_K`]` detector holders		1.725	1.667	(1.269,2.030)	2.8±0.6	352.1	933.3	501.7
	`[g/`p_K`]` mini shrouds		1.697	1.710	(1.614,1.817)	1.7±0.6	215.0	515.9	473.3
	`[g/`p_K`]` SiPM ring		2.35	2.17	(1.27,4.29)	2±2	2.5	5.7	4.4
	`[f/`p_K`]` close to the array						1448.6	3476.4	3189.1
	`[f/`p_K`]` far from the array						371.8	892.0	964.3
^{42}K	`[f/`p_K`]` on n^+ (^{enr}BEGE)	mBq	0.260	0.255	(0.181,0.303)		161.2	913.5	–
	`[f/`p_K`]` on n^+ (^{enr}Coax)		0.5122	0.5250	(0.3835,0.6227)		169.8	–	842.1
	`[f/`p_K`]` on p^+ (^{enr}BEGE)		0.00185	0.00125	(0.00107,0.00865)		3.1	35.1	–
	`[f/`p_K`]` on p^+ (^{enr}Coax)		0.0214	0.0213	(0.0166,0.0249)		20.6	–	470.2
	`[f/`p_K`]` in LAr above array	Bq	0.4672	0.4570	(0.4467,0.4791)		2625.8	6068.8	4579.4
	`[f/`p_K`]` in LAr outside MS		1.9784	1.9825	(1.9408,2.0384)		4437.7	9986.1	9464.5
α decays	`[f]` ^{210}Po and ^{226}Ra chain (^{enr}BEGE)	cts	561.82	572.77	(540.94,601.97)		–	561.8	–
	`[f]` energy-degraded (^{enr}BEGE)		585.71	605.00	(560.90,663.16)		–	585.7	–
	`[f]` ^{210}Po and ^{226}Ra chain (^{enr}Coax)		1589.8	1590.50	(1546.94,1642.30)		–	–	1589.8
	`[f]` energy-degraded (^{enr}Coax)		402.01	405.00	(371.18,479.81)		–	–	402.0

The finally obtained minimum model is defined by 36 parameters containing the dominant background contributions describing the energy spectra of the single-detector and two-detector data of ^{enr}BEGE and ^{enr}Coax. With a p-value of 0.36, the minimum model is well suited to describe the data. The individual parameter estimates of the minimum model are summarized in Tab. 6.1. The global modes, the marginalized modes and the 68% C.I. of the parameters are quoted together with the corresponding count rates per exposure in the fit range for the single-detector events of ^{enr}BEGE and ^{enr}Coax as well as for the two-detector events. Fig. 5.6 shows the results of the global model minimum fit to the single- and two-detector events of $^{\text{enr}}$BEGE and $^{\text{enr}}$Coax spectra displayed in Fig. 5.6. The observed experimental spectra and the best fit model are displayed together with the individual components according to the best fit parameter estimates in the energy range from 575 keV to 5260 keV. The lower panels in Fig. 5.6(a)-(c) show the corresponding residuals evaluated by the z-score (see Sec. 5.1.4), quantifying the good agreement between the background model expectation and the data.

5.5 Background prediction at $Q_{\beta\beta}$

Using the background model, we can make predictions about the decomposition of the individual background contributions around $Q_{\beta\beta}$. The predicted contributions in the ROI can be found in Tab. 5.5 which lists the global and marginalized modes together with the 68% C.I.. The background evaluation window ranges from 1930 keV to 2190 keV, excluding the intervals $Q_{\beta\beta} \pm 25$ keV, (2104 ± 5) keV and (2119 ± 5) keV. The main contributions in the ROI are due to ^{42}K, energy-degraded α decays, ^{208}Tl, ^{214}Bi and ^{60}Co. The BI composition listed in Tab. 5.5 is visualized in Fig. B.7 which additionally highlights the summed contributions of the isotopes giving a quantitative estimation on the overall contribution of the individual isotopes. The overall fraction of the contributions due to a certain isotope depend strongly on the assumed source origin. The most significant contribution to the BI in the ROI is due to ^{42}K, followed by ^{208}Tl and α decays. In case of the $^{\text{enr}}$Coax data, the α decays dominate over ^{208}Tl. Contributions to the background in the ROI due to $2\nu\beta\beta$ decays, ^{40}K or ^{228}Ac are negligible. With regard to the source origin, one can notice that almost only the close components are important, especially the detector surfaces with high contaminations of ^{42}K. The fiber veto and the remaining parts of the LAr veto can be neglected.

Fig. 5.7 displays the best-fit background model together with the observed single-detector event spectra of $^{\text{enr}}$BEGE and $^{\text{enr}}$Coax in the ROI which is used for the BI evaluation by determining the total number of events in this energy window. The global fits were performed on the experimental spectra with the $Q_{\beta\beta}\pm25$ keV blinding window. After the unblinding in June 2018, the blinded energy window was reduced to $Q_{\beta\beta} \pm 5$ keV. From the best-fit minimum (maximum) model, we expect 19.1 (18.7) and 17.2 (17.6) events for the $^{\text{enr}}$BEGE and the $^{\text{enr}}$Coax data, respectively, in the unblinded energy region of $Q_{\beta\beta}\pm25$ keV excluding $Q_{\beta\beta} \pm 5$ keV. While in the data spectrum, we observe 18 and 19 events for the $^{\text{enr}}$BEGE and $^{\text{enr}}$Coax data, respectively. This translates to a probability of 58.2% (54.7%) and 32.4% (35.7%), respectively, to observe the same number of events or more given the background

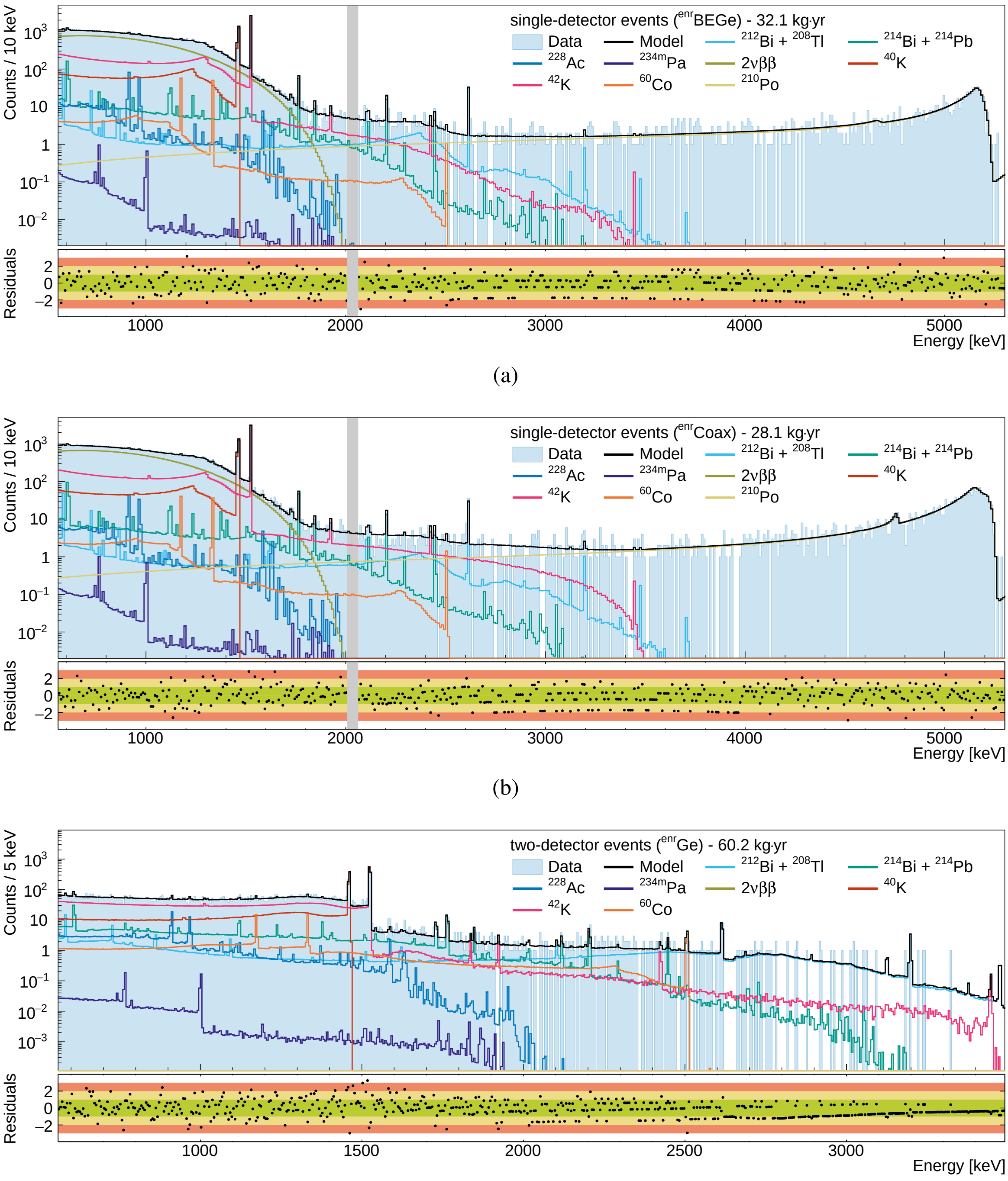

(a)

(b)

(c)

Fig. 5.6 Fit results of the minimal model corresponding to single-detector events for ^{enr}BEGE (a) and ^{enr}Coax (b) and two-detector events (c). The lower panel in each plot shows the residuals evaluated by the z-score with the one (green), two (yellow) and three (red) standard deviation bands.

Table 5.5 The predicted background index and the contributions from the individual background components for single-detector data in the ROI derived from the minimum model are summarized. The results are quoted in units of $10^{-3}\,\frac{\text{cts}}{\text{keV}\cdot\text{kg}\cdot\text{yr}}$ by the global and marginalized modes along with the central 68 % C.I..

source	location	$^{\text{enr}}$BEGE (M1)			$^{\text{enr}}$Coax (M1)		
		global mode	marg. mode	68% C.I.	global mode	marg. mode	68% C.I.
α decays	energy-degraded (slope)	2.85	2.53	(1.97, 2.75)	1.92	1.90	(0.97, 2.10)
	energy-degraded (offset)	0.01	0.03	(0.00, 1.68)	0.44	0.03	(0.00, 2.70)
	^{210}Po and ^{226}Ra chain	0.23	0.24	(0.23, 0.25)	0.74	0.74	(0.72, 0.76)
^{42}K	in LAr outside MS	0.47	0.47	(0.46, 0.49)	0.57	0.58	(0.56, 0.59)
	in LAr above array	0.28	0.27	(0.27, 0.29)	0.26	0.25	(0.25, 0.26)
	on n^+ ($^{\text{enr}}$BEGE)	4.42	4.34	(3.08, 5.16)			
	on n^+ ($^{\text{enr}}$Coax)				0.79	0.81	(0.59, 0.96)
	on p^+ ($^{\text{enr}}$BEGE)	0.33	0.22	(0.19, 1.54)			
	on p^+ ($^{\text{enr}}$Coax)				5.46	5.42	(4.22, 6.35)
^{60}Co	detector cables	0.31	0.32	(0.27, 0.36)	0.33	0.34	(0.29, 0.38)
^{212}Bi & ^{208}Tl	mini shrouds	0.17	0.16	(0.12, 0.21)	0.17	0.17	(0.13, 0.22)
	detector cables	3.15	3.10	(2.87, 3.33)	2.18	2.15	(1.99, 2.31)
	copper shroud	0.03	0.03	(0.03, 0.03)	0.03	0.03	(0.03, 0.04)
^{214}Bi & ^{214}Pb	SiPM ring	0.01	0.01	(0.01, 0.01)	0.01	0.01	(0.01, 0.01)
	mini shrouds	0.19	0.18	(0.13, 0.24)	0.21	0.21	(0.15, 0.27)
	detector cables	2.33	2.30	(2.17, 2.47)	1.70	1.68	(1.58, 1.81)
	copper shroud	0.02	0.02	(0.01, 0.02)	0.02	0.02	(0.02, 0.02)
	on p^+ ($^{\text{enr}}$BEGE)	0.03	0.03	(0.02, 0.05)			
	on p^+ ($^{\text{enr}}$Coax)				0.19	0.23	(0.20, 0.28)
global model		14.28	16.04	(14.56, 16.29)	15.37	15.53	(14.40, 16.06)

model expectation. According to the prediction from the background model, the background distribution in the ROI can be represented by a flat distribution around $Q_{\beta\beta}$ (see Fig. 5.7). A flat distribution is sufficient since a linear interpolation leads to a deviation of the obtained BI of less than 1% (1%) and less than 3% (3%) in the ROI and in $Q_{\beta\beta} \pm 25$, respectively, which is still smaller than the statistical uncertainty obtained by the global fit.

Different parts of the experimental setup have been affected by the upgrade to Phase II. Since the number of detector has been increased, the detectors are deployed in additional strings and the detector mounting has been replaced. In addition, the cables have been optimized and the mini-shrouds made from Cu foil have been exchanged by nylon mini-shrouds. As a result, the expected background level before LAr veto and PSD cut has been reduced by about a factor 1.2 and 2.5 for $^{\text{enr}}$Coax and $^{\text{enr}}$BEGE, respectively, compared to the background model prediction from Phase I. The much higher background of the $^{\text{enr}}$BEGE data in Phase I might carry a comparatively high uncertainty due to the much lower exposure of 1.8 kg·yr used for the analysis. Therefore, the $^{\text{enr}}$BEGE results of Phase I are not

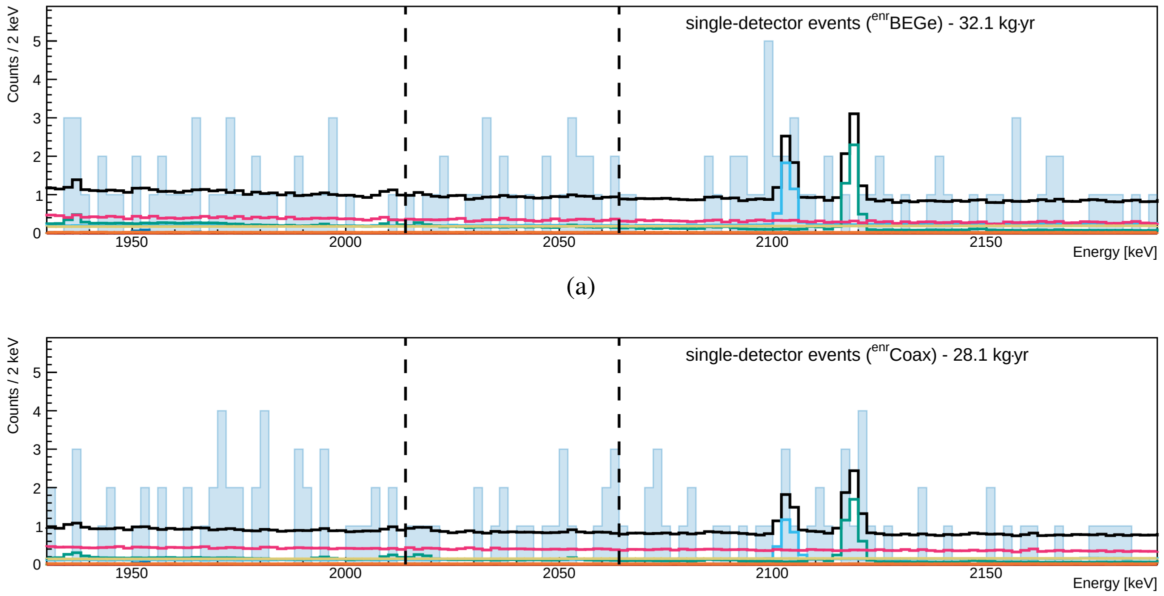

(a)

(b)

Fig. 5.7 Fit results of the minimal model corresponding to single-detector events for ^{enr}BEGE (a) and ^{enr}Coax (b).

considered here. The improved background index is due to the reduction of ^{60}Co by about a factor 3 and reduced contributions from near sources of ^{208}Tl and ^{214}Bi. In addition, the surface contamination of ^{214}Bi is significantly reduced, due to the fact that a large proportion of the α decays are from energy-degraded αs. The overall contribution from α decays including decays from ^{210}Po and from the ^{226}Ra decay chain is slightly higher, but still in the order of the expected level from Phase I. Even though, the total predicted background contribution of ^{42}K stays the same as in Phase I, increased contributions from the surface contaminations can be noted.

5.6 Stability of the background model

The stability of the minimal background model predictions with respect to the choices made according to binning, prior and data set selection was validated by several sanity checks. The deviations are evaluated in comparison to a reference model which is represented by the minimum model listed in Tab. 6.1. The following paragraphs summarize how the assumptions made for the final decomposition of the background model translate to potential systematic errors.

Validation of the fit the validity and robustness of the fitting algorithm against known background sources has been tested with Toy Monte Carlo data. A data spectrum has been artificially generated with a lifetime of 10^9 s which corresponds to 17 times GERDA Phase II. The artificial data spectrum has been once sampled from a reduced number of PDFs (α decays, ^{40}K on holders, ^{42}K homogeneously distributed in LAr and $2\nu\beta\beta$ decay) and fitted with its known constituent. The result has not shown any bias and the fitter has been able to correctly reproduce the toy MC combination of the data spectrum.

Binning The choice of an inappropriate binning can lead to a wash out of spectral shapes, e.g. the distortion of peak structures, or similar spectral shapes might become indistinguishable. For the global model a binning of 1 keV was chosen. The fine binning maintains the spectral shape in the γ region below 3500 keV. But it can become a problem in the high energy α region above 3500 keV due to the low statistics in this energy range. To account for these different structures, an adaptive binning has been chosen by applying a wider binning of 10 keV for the α-model. Since the α components reduced to a minimal number of PDFs are defined by an overall scaling in the global model, no major skewing is expected by the fine binning of the global model. To evaluate the effect of the binning, the global fit was repeated with varying bin size from 2 keV up to 50 keV. For bin sizes smaller than 30 keV, the parameter estimates vary by less than 20% which is smaller than the respective statistical fluctuations. This applies both to the individual components and to the summed contributions of each isotope. The isotope contribution which fluctuates most by changing the bin size is ^{42}K, especially for contaminations on the p^+ and n^+ surfaces. The stronger deviation by bin sizes larger than 30 keV can be attributed to the bad reconstruction of the shapes of the γ lines. Considering the sensitivity of the ROI to the chosen binning, it turns out that the BI of the single-detector data deviates by less than 10% for all bin sizes. For the $^{\text{enr}}$Coax data, the deviations are smaller than the statistical uncertainty, whereby the BI of the $^{\text{enr}}$BEGE data indicate a systematic shift towards decreasing BIs with increasing bin size.

Data sets A study was performed to understand the systematics associated with the global model fitting routine and fitting multiple data sets simultaneously with common parameters. Therefore, the global fit has been repeated separately for each data set used in the background model. Apart from the ^{42}K surface contaminations of the $^{\text{enr}}$Coax data, a deviation is noticeable especially for the parameter associated with the contribution of ^{60}Co. In the case of the $^{\text{enr}}$BEGE data, the amount of ^{60}Co is markedly reduced, while the situation is exactly reversed for the $^{\text{enr}}$Coax data. Less pronounced, the same situation is observable for the ^{214}Bi contamination of the cables. Furthermore, the ^{228}Ac contribution of the holders is reduced in the $^{\mathrm{enr}}$BEGE data compared to the minimum model. Except for the components discussed, the parameter estimates differ by less than 20% for the single-detector data. Roughly speaking, the differences of the two-detector data follow the trend of the $^{\mathrm{enr}}$BEGE data, except that the effects of the already mentioned parameters are even stronger. Nevertheless, apart from the cable contamination of ^{214}Bi, ^{208}Tl, ^{60}Co and the p^{+} contamination of ^{42}K, all fluctuations are smaller than the statistical uncertainties. The half-life of the $2\nu\beta\beta$ decay is affected by 1.5% and 5.7% for the $^{\mathrm{enr}}$BEGE and $^{\mathrm{enr}}$Coax data, respectively. The much higher uncertainty for the $^{\mathrm{enr}}$Coax data can be related to an increased uncertainty on the active volume (see Sec. 6). With a discrepancy of 8% between the global fit performed on the single $^{\mathrm{enr}}$BEGE data set and the minimum model, the BI of the $^{\mathrm{enr}}$BEGE data in the background model might be overestimated, since the observed $^{\mathrm{enr}}$BEGE data indicate as well a lower value for the BI. The reduced BI is especially correlated with the background contributions in the ROI, associated with the cable contaminations of ^{214}Bi, ^{208}Tl and ^{60}Co which are reduced in the global fit performed on the single $^{\mathrm{enr}}$BEGE data. In contrast, the BI of the $^{\mathrm{enr}}$Coax data differs by less than 2.5%.

Prior selection When using noninformative priors (e.g. flat priors or scale-invariant priors) instead of priors containing the screening information or the K-model, the global fit is not able to uniquely identify the degenerate spectra of the close components. For each isotope, the PDFs of the close source locations have been replaced in the global fit by an effective PDF consisting of a combination of cables, holders and mini-shrouds normalized under the assumption that the components have the same contamination per unit mass. Due to the replacement of the close components by an effective component, the activities are no longer directly comparable to the reference minimum model. However, the total contributions of each isotope and the remaining components can be compared. In the first approach, the priors extracted from the screening measurements were replaced by flat priors. It turned out that the flat priors are unsuitable for the distant components, because the flat priors lead to posteriors characterized by a broad continuum extending over the whole parameter ranges. Therefore, the fit was cross-checked and repeated using scale-invariant priors (see Sec. 5.1.2). In this case, the parameter estimates of the distant components have lead to 90% upper limits and the distant components were excluded from a minimum model obtained with either flat or scale-invariant priors. The parameter estimates obtained by using either a flat or a scale-invariant prior are consistent to each other and are much smaller than the statistical fluctuations. It is noticeable that no distant component (copper shroud, SiPM ring or front-end electronics) is required for a minimum model when not considering the screening measurements. The spectra can be completely described by the effective near components of the individual isotopes together with the components of the fiber veto except for ^{228}Ac which is expected only from close components. But this is not surprising considering the total contributions in counts per time and mass of these components to the spectrum of the data sets in the background model (see Tab. 6.1). When replacing the prior information from screening with a flat or scale-invariant prior, $^{234\mathrm{m}}$Pa is not a necessary model component to describe the energy spectra. Regarding the respective contributions in the ROI, the ^{208}Tl and ^{214}Bi contributions of the effective near components are reduced compared to the cable and mini-shroud contribution of the reference background model. Furthermore, an enhancement of the fiber veto components of ^{208}Tl and ^{214}Bi which do not contribute in the minimum background model can be observed. Nevertheless, the total BIs of each single-detector data set are affected by less than 1.5%. This result was confirmed by revising the parameter deviation through global fits in which all parameters are fixed according to the posteriors of the minimum background model except one isotope under study. The priors of the individual components of the isotope under study were thereby replace by scale-invariant priors. The remaining parameter estimates are changed by less than 10%.

Count rate analysis The global fit has been performed by combining three different data sets. For this reason the fit results provided by the minimum model have been cross check with the γ line intensities obtained for each data set from fitting individually the γ peaks with a Gaussian plus a flat background. Furthermore, γ rays may suffer energy losses over large distances such that the intensity decreases with the distance of the source location. Therefore, the intensities can give important information on the distance of the corresponding isotopes. When studying the γ lines one can correlate certain behavior of the systematics of the minimum model regarding the different data sets described in Sec. 5.6. However, if one compares the intensity of different detector types, the configuration and size of the detector also plays a role, since the probability with which the full energy is absorbed decreases with smaller detector sizes.

The count rate of each γ line is determined by fitting the binned data spectra used for the global modeling in the γ peak region with a width of $\pm 3\sigma$ (see Appx. B.5.1). The γ lines of all radioisotopes considered in the background model have been determined. The marginalized mode of count rate together with the 68% C.I., or an upper limit at 90% C.I. are quoted in Tab. 5.6. In all data spectra, the γ lines observed with high significance are from ^{214}Bi, ^{208}Tl, ^{42}K and ^{40}K. The lines of ^{228}Ac, $^{234\mathrm{m}}$Pa and ^{60}Co have been identified with less significance. Furthermore, the count rates obtained from the data are compared to the ones from the minimum model given the best fit parameters. The statistical uncertainties on the count rates resulting from the minimum model are due to the marginalized posterior distributions.

Table 5.6 The observed γ line count rates compared with the predicted count rates from the minimum model derived by the best fit parameters for single-detector and two-detector data. The marginalized modes together with the central 68 % C.I. are quoted in units of $[\mathrm{cts}/(\mathrm{kg}\cdot\mathrm{yr})]$.

source	energy	$^{\mathrm{enr}}$BEGe (M1)		$^{\mathrm{enr}}$Coax (M1)		$^{\mathrm{enr}}$Ge (M2)	
		data	background model	data	background model	data	background model
		marg. mode with 68% CI	marg. mode with 68% CI	marg. mode with 68% CI	marg. mode with 68% CI	marg. mode with 68% CI	marg. mode with 68% CI
^{228}Ac	911.2 (26.5%)	2.94 (2.38, 3.81)	2.72 (2.46, 3.17)	0.66 (0.34, 1.54)	1.84 (1.65, 2.10)	0.25 (0.18, 0.48)	0.34 (0.29, 0.38)
	968.9 (16.1%)	1.19 (0.60, 1.91)	1.55 (1.41, 1.84)	< 4.52	1.11 (0.95, 1.23)	< 0.45	0.20 (0.17, 0.22)
^{214}Bi	609.3 (46.4%)	4.26 (4.12, 5.84)	6.07 (5.69, 6.47)	5.54 (4.53, 6.44)	4.24 (4.09, 4.60)	0.27 (0.14, 0.45)	0.58 (0.56, 0.64)
	934.1 (3.2%)	< 1.01	0.26 (0.24, 0.29)	< 3.03	0.14 (0.13, 0.16)	0.18 (0.06, 0.29)	0.04 (0.03, 0.04)
	1120.3 (15.1%)	0.94 (0.44, 1.48)	1.28 (1.24, 1.43)	2.46 (1.76, 3.08)	1.13 (1.01, 1.17)	0.39 (0.22, 0.56)	0.20 (0.19, 0.22)
	1238.1 (5.9%)	1.46 (0.77, 1.98)	0.58 (0.55, 0.63)	0.31 (0.23, 1.19)	0.55 (0.53, 0.59)	0.28 (0.10, 0.40)	0.07 (0.06, 0.07)
	1377.7 (4%)	0.41 (0.13, 0.81)	0.45 (0.43, 0.50)	< 1.64	0.41 (0.39, 0.45)	< 1.81	0.09 (0.08, 0.09)
	1764.5 (15.4%)	1.23 (1.07, 1.54)	1.80 (1.62, 1.85)	1.55 (1.44, 1.96)	1.57 (1.52, 1.74)	0.26 (0.16, 0.26)	0.30 (0.29, 0.33)
	2204.2 (4.9%) (5%)	0.48 (0.41, 0.68)	0.47 (0.45, 0.51)	0.34 (0.25, 0.49)	0.45 (0.43, 0.50)	0.10 (0.07, 0.16)	0.09 (0.08, 0.09)
^{60}Co	1173.2 (99.9%)	1.30 (0.70, 1.88)	1.70 (1.40, 1.93)	1.35 (1.16, 2.46)	1.43 (1.19, 1.62)	0.10 (0.05, 0.28)	0.25 (0.21, 0.28)
	1332.3 (100%)	0.73 (0.34, 1.21)	1.54 (1.36, 1.83)	2.17 (1.75, 2.89)	1.27 (1.13, 1.53)	< 0.79	0.26 (0.21, 0.29)
^{40}K	1460.9 (10.6%)	48.37 (47.35,50.00)	49.95 (48.66,50.96)	59.88 (58.22, 61.12)	59.23 (58.34, 60.85)	7.21 (7.03, 7.77)	8.25 (7.82, 8.35)
^{42}K	1524.7 (17.2%)	77.14 (75.31,78.62)	80.14 (79.53,81.82)	109.95 (107.51,111.66)	108.39 (107.37,110.56)	13.44 (12.86,13.81)	14.68 (14.47,14.91)
^{234m}Pa	1001.4 (0.9%)	1.05 (0.30, 1.60)	0.02 (0.01, 0.03)	< 4.78	0.03 (0.02, 0.03)	< 0.26	0.01 (0.01, 0.01)
^{208}Tl	583.2 (86.7%)	3.08 (2.17, 3.77)	2.42 (2.22, 2.61)	1.92 (1.72, 3.31)	1.67 (1.61, 1.86)	< 3.89	0.24 (0.22, 0.25)
	860.5 (12.7%)	0.58 (0.26, 1.27)	0.39 (0.37, 0.43)	0.44 (0.21, 1.37)	0.21 (0.18, 0.22)	0.03 (0.02, 0.16)	0.05 (0.04, 0.05)
	2614.5 (100%)	0.93 (0.74, 1.08)	0.96 (0.87, 1.04)	1.31 (1.03, 1.46)	0.96 (0.87, 1.04)	0.24 (0.19, 0.31)	0.19 (0.17, 0.20)

No significant discrepancies between the count rates deduced from the peak intensities observed in the data and resulting from the minimum model have been found. This shows the reliability of the minimum model. The count rates of the γ lines due to ^{208}Tl, ^{42}K and ^{40}K are in agreement being within the 68% uncertainty intervals with the results from the minimum model in the both single-detector and two-detector data. In case of ^{228}Ac and $^{234\mathrm{m}}$Pa, the results are not in perfect agreement within the 68% uncertainty intervals, but the intensities of the γ lines are very low compared to the remaining background contributions in the same energy region and the result can not be assessed. Besides, the number of events in the peak regions of the two-detector data is strongly limited by the available statistic. One can note that the observed count rates of ^{214}Bi and ^{60}Co do not match very well with the results from the minimum model for all data sets. Both isotopes already showed discrepancies when comparing the fits of the global fit performed separately for the $^{\mathrm{enr}}$BEGe and $^{\mathrm{enr}}$Coax data (see Sec. 5.6). Comparing the intensities between data and model or between to γ line of the same isotopes does not give hint for the locations of the sources. For instance, considering the intensities of the γ lines at 1173.2 keV and 1332.3 keV, the ratio of the intensities is slightly bigger than one for all three model spectra, while for the $^{\mathrm{enr}}$Coax data and the two-detector data it is significantly smaller than one. This effect is not fully understood, since both γ lines of ^{60}Co should occur with almost the same intensity such that the ratio of the intensities is in the order of one. For both isotopes, no revealing pattern can be found concerning the intensity ratios, which could provide further information.

5.7 Conclusion

A background model has been developed which describes the observed energy spectra of $^{\text{enr}}$BEGE and $^{\text{enr}}$Coax data with a minimal number of background contributions. For the first time, the single-detector and two-detector data have been combined in a multivariate Bayesian fit approach. Additionally, the background model focuses further on two prominent features in the energy spectrum: the α events dominating the high energy part of the spectrum and the count rates of the potassium γ lines at 1525 keV and 1461 keV. Through the incorporation of the count rates in the γ lines for each detector individually, potential top-bottom and rotationally asymmetric source distributions of ^{42}K and ^{40}K are taken into account. The dominating background sources and locations are largely disentangled by analyzing and fitting the shape of the measured spectra in energy and partially in detector space. For this, the individual contributions to the energy spectra have been reconstructed by GEANT4-based MC simulations, including both physics processes and instrumental effects.

The model comprises several contributions which are either identified by material screening or observed in the measured energy spectra. The individual background contributions and the resulting activity estimates have been determined through the Bayesian fitting algorithm based on prior constraints extracted from the screening assays and the modeling of the potassium γ lines. The background model confirms the ubiquitous presence of backgrounds stemming from the daughters of the ^{238}U and ^{232}Th decay chains, ^{40}K and ^{42}K. Further background contributions are due to the $2\nu\beta\beta$ decay in ^{76}Ge and ^{60}Co. The contamination levels yielded by the background model are very well in agreement with the ones predicted by the screening measurements. This result shows the validity of both the background model and the screening measurements. Nevertheless, the activities identified by the screening measurements are not sufficient to explain the total composition of the observed background spectra. Subsequent handling, machining and assembly seem to have introduced additional or varying contaminations as it is the case for ^{40}K. It has been found that additional contaminations of ^{40}K have been introduced most probably by the gluing process of the min-shrouds (close distance) and by the LAr veto (far distance).

Apart from that, background coming from ^{42}K is considered to be one of the most relevant for the GERDA experiment. The spacial distribution of ^{42}K proved to be difficult to determine due to its continuous spectrum with only a single FEP at 1525 keV. All components due to ^{42}K have to be constrained by the counts in the FEP. The localization of ^{42}K is particularly crucial as electrons released in the decay of ^{42}K with a maximal energy of 3.5 MeV can contribute to the background in the ROI depending on the its distance from the detectors' surfaces. In consequence, the BI varies greatly with different distribution of ^{42}K in LAr or on the detector's surfaces. In view of further comprehensive studies on the distribution of ^{42}K decays, the integration of a transition layer in the simulation should be considered. However, the concern regarding ^{42}K can be mitigated, since [116] has demonstrated that the combination of the LAr veto and PSD cut are an excellent method to efficiently suppress ^{42}K background by three orders of magnitude.

The stability of the model has been tested by checking the dependence on priors, and estimating the systematic uncertainties, especially those affecting the background contribution in the ROI. A number of global fits varying the binning, the input data spectra, the priors, and the list of background contributions have been performed. In addition, the background model has been verified by comparing the γ line intensities observed in the spectra of single- and two-detector data to the ones resulting from the background model. No significant deviations have been found which would lessen the validity of the background model.

Using the background model, we can make predictions about the decomposition of the individual background contributions around $Q_{\beta\beta}$. Besides the expected number of background events, the spectral shape of the total background around $Q_{\beta\beta}$ can be extracted from the full decomposition obtained by the background model. Both are crucial input informations for reliable results on the ^{76}Ge $0\nu\beta\beta$ signal search presented in Ch. 1.4. As a result, the background at $Q_{\beta\beta}$ is dominated by close sources originating from the LAr or contaminations of the detector assembly where the individual fractions depend on the assumed source locations. Besides ^{42}K and α decays originating from close to the p^{+} or groove surface, the highest contribution in the ROI of interest is due to nearby contaminations of ^{228}Th, ^{214}Bi and ^{60}Co. The background model has shown that the installation of the LAr veto has introduced a non-negligible background contributing to the observed energy spectra. Nevertheless, due to its location in medium distance from the Ge detectors and in a scintillating medium, these backgrounds contribute only marginally to the background in the ROI.

The background model has been developed by exclusion of the 50 keV wide blinded energy region, thus it has been tested for consistency by reducing the blinded energy region to a window of 10 keV around $Q_{\beta\beta}$. It has been shown that in the ROI the expected background is uniformly distributed and that no significant peak like structures are expected. The statistical uncertainty on the BI prediction from interpolation is smaller than the systematic uncertainty due to deviations from the final decomposition of the background model. The BIs interpolated into the blinded region are $14.9 \cdot 10^{-3}$ cts/(keV $\cdot$ kg $\cdot$ yr) and $15.3 \cdot 10^{-3}$ cts/(keV $\cdot$ kg $\cdot$ yr) for the ^{enr}BEGe and ^{enr}Coax data, respectively, which is consistent with the full ROI and within the uncertainties. Furthermore, during the upgrade from Phase I to Phase II, extensive efforts has been taken in material screening and selection of the components in the detector surroundings where the goal has been to minimize the external background in the ROI. The results of the background model rewards the efforts taken and shows that it has been achieved to reduce the background at $Q_{\beta\beta}$ even before the LAr veto and PSD.

Chapter 6

Measurement of the $2\nu\beta\beta$ half-life of ^{76}Ge

The neutrino accompanied $\beta\beta$ decay is a rare nuclear physics process whose measurement in ^{76}Ge has been explored by several groups in the field even though from the point of view of particle physics, $0\nu\beta\beta$ is of course the most interesting decay mode. However, the estimations of the $0\nu\beta\beta$ half-life suffer large theoretical uncertainties (see Ch.1.2.2). Nevertheless, the nuclear process most related to $0\nu\beta\beta$ is $2\nu\beta\beta$. Even though both are different, the calculation are carried out within the same model framework and both rely on similar model assumptions. $2\nu\beta\beta$ can help to derive constraints on NME of $0\nu\beta\beta$ and might reduce to some extent the uncertainties and the spread of the calculations for the $0\nu\beta\beta$ process. Furthermore, $2\nu\beta\beta$ results have been used to calibrate QRPA calculations, in particular the quenching of g_A is a hot topic. The verification by experiments might eventually lead to improved theoretical models and a better understanding of experimental results.

Apart from that, there is the possibility of exploring physics beyond the SM with the $2\nu\beta\beta$ decay through the analysis of deviations in the conventional shape of the electron sum spectrum. Predicted by a number of grand unification theories, a massless or light boson can couple to the neutrino. Consequently, the $2\nu\beta\beta$ decay can proceed with the emission of one or two so-called Majoron bosons entailing a likewise continuous energy sum spectrum. Accordingly, the Lorentz invariance violation may become apparent as a distortion of the electron sum spectrum due to an additional contribution of the Lorentz-violating perturbation.

Through background reconstruction the background model allows to measure the half-life of the $2\nu\beta\beta$ decay in ^{76}Ge with increased accuracy. In 2015, GERDA published for Phase I data the $2\nu\beta\beta$ half-life measured with the highest accuracy compared to previous measurements [117]. Thereby the source of the largest uncertainty on the obtained half-life has been due to the background decomposition resulting from the corresponding background model. In addition, the active volume of the $^{\mathrm{enr}}$Coax detectors is affected by large uncertainties. To achieve a reduced uncertainty, data recorded with more exposure should be used as well as new and more precise measurements of the active volume should be consulted. Here, the exposure of the Phase II data has been increased compared to the result in [117], but more precise numbers of the active volume have not been available. This work aims to reduce the uncertainty due to background by using the improved background model, with better characterized and constrained background components, e.g. by including larger number of data sets, the incorporation of further information due to the properties of the backgrounds, etc. (see Ch. 5).

6.1 Result on the $2\nu\beta\beta$ half-life of ^{76}Ge

The contribution of the $2\nu\beta\beta$ decay of ^{76}Ge to the observed spectra resulting from the global model can be used for deriving the half-life of the process. According to Eq. 1.28, the number of expected decays $\lambda_{i,2\nu}$ in the i-th bin in the summed energy spectrum of data set comprising N_{det} detectors obeys

$$\lambda_{i,2\nu} = (T_{1/2}^{2\nu})^{-1} \frac{\ln 2 N_A}{m_A} \sum_{j=1}^{N_{dets}} M_j t_j f_{AV,j} f_{76,j} \varepsilon_j^{2\nu} \int_{\Delta E_i} \Phi_j^{2\nu}(E) dE \tag{6.1}$$

where $(T_{1/2}^{2\nu})^{-1}$ is the signal strength of the decay, N_A is the Avogadro's constants and m_A is the molar mass of ^{76}Ge. The sum runs over all detectors in data set where f_{76} is the mass fraction of ^{76}Ge, $f_{AV,j}$ is the active volume fraction and $\varepsilon_j^{2\nu}$ the detection efficiencies obtained from MC simulation corresponding to the probability that events release their entire energy inside the detector considering the reconstruction and analysis cuts. The normalized energy distribution $\Phi_j^{2\nu}(E)$ and the detection efficiency $\varepsilon_j^{2\nu}$ corresponding to detector j are deduced from simulations of $2\nu\beta\beta$ decays taking place in the active volume and dead layer part considering the weight of the active volume fraction, such that the right part of Eq. 1.28 is analogous to Eqs. 4.3 and 4.4 with the additionally introduced detection efficiency and omitted normalization. Each detector related parameter has been taken into account separately.

The first determination of the half-life of $2\nu\beta\beta$ in this work revealed discrepancies between the parameters for the half-life of $2\nu\beta\beta$ extracted from the $^{\mathrm{enr}}$BEGE and $^{\mathrm{enr}}$Coax data. This result confirmed the suspicion of a wrongly assumed total active volume of the

$^{\mathrm{enr}}$Coax detectors, because the active volume of the $^{\mathrm{enr}}$BEGE detectors is better determined. To account for a potential deviation of the total active volume of the $^{\mathrm{enr}}$Coax detectors, an additional parameter δ_{AV} was introduced in the global model, while keeping an unique parameter $1/T^{2\nu}_{1/2}$. The parameter δ_{AV} is derived from the number of excess counts ($\delta_{AV} \geq 0$ in [cts]) of the $2\nu\beta\beta$ process in ^{76}Ge due to the potential underestimated total active volume of the $^{\mathrm{enr}}$Coax detectors. The half-life of $2\nu\beta\beta$ was determined from the marginalized posterior distribution of $1/T^{2\nu}_{1/2}$ which yields

$$\mathrm{T}^{2\nu}_{1/2} = (2.02^{+0.01}_{-0.01}\ \mathrm{stat}\ ^{+0.11}_{-0.09}\ \mathrm{syst}) \cdot 10^{21}\mathrm{yr} = (2.02^{+0.11}_{-0.09}) \cdot 10^{21}\mathrm{yr}. \tag{6.2}$$

The obtained result requires an increase of $(5.1^{+0.7}_{-1.3})\%$ of the active volume of the $^{\mathrm{enr}}$Coax detectors compared to the initially assumed total active volume corresponding to 1743.3 number of excess counts in the analysis window. The $2\nu\beta\beta$ decay of ^{76}Ge produces 45267.8 and 37863.2 counts in the single-detector $^{\mathrm{enr}}$BEGE and $^{\mathrm{enr}}$Coax data, respectively, in the energy range from 600 keV to 2000 keV. The $2\nu\beta\beta$ event fraction is about 60% of the events in the single-detector data for both $^{\mathrm{enr}}$BEGE and $^{\mathrm{enr}}$Coax data, while the backgrounds amount to about $\sim 40\%$.

6.2 Systematic uncertainties

The determination of the $2\nu\beta\beta$ half-life is subject to a number of systematic uncertainties which are summarized in Tab. 6.1. The major contributions are related to uncertainties in the modeling of the signal and background as well as the active ^{76}Ge exposure. All uncertainties have been summed in quadrature separately for downward and upward deviations in the half-life of all systematics.

MC simulation and primary spectrum of $2\nu\beta\beta$ decay The uncertainties introduced by the MC simulation and by the primary spectrum fed in the MC simulation are adopted from the investigations by [101]. Since in [101] and in this work the same simulation framework has been used and the deviation due to later adjustments of MAGE are assumed to be negligible. Uncertainties in the half-life can on one hand derive from the dimensions, displacements or materials upon which the experimental geometry is constructed in GEANT4. On the other hand, the half-life can be affected by the interaction of radiation with matter characterized by cross sections and final state distributions ($< 2\%$). Deviations due to particle transport are at the few-percent level and in first order affect the propagation of the external γ

rays, while the $2\nu\beta\beta$ electrons usually deposit their entire kinetic energy inside the detector's crystal.

The uncertainties related to the shape of the initial $2\nu\beta\beta$ decay spectrum comprise the theoretical calculation of the input shape and detector related effects like energy losses or finite energy resolution taking place in the MC simulation step. Both effects have already been evaluated in [101] to have an impact of less than 0.1% on the $2\nu\beta\beta$ half-life of ^{76}Ge determined in Phase I. Since the primary spectrum has been analogically sampled from the same distribution implemented in DECAY0 [118] and, in addition, an analogical simulation processing in MAGE have been applied, the same effect is expected for the $T_{1/2}^{2\nu}$ determined in this work.

Global model fit components and binning The strongest background contribution in the $2\nu\beta\beta$ energy region between 600 keV and 2000 keV is attributed to ^{42}K with 23.8% and 24.7% of all events in this energy region in the $^{\mathrm{enr}}$BEGE and $^{\mathrm{enr}}$Coax data, respectively. In addition, there is ^{40}K with background contributions of 9.7% and 9.6%, respectively. All remaining background contributions amount to less than 3.5% and 2.6%. Depending on the different combinations of potential distributions of ^{42}K analyzed in Sec. 5.6, an uncertainty on the $2\nu\beta\beta$ half-life of less than 1.1% can be expected. In case of ^{40}K, the Compton tail and the FEP overlap completely with the energy range dominated by $2\nu\beta\beta$. Therefore, fluctuations of ^{40}K are directly correlated with the half-life of $2\nu\beta\beta$. The influence of fluctuations of ^{40}K has been estimated to be less than 2%. All other contributions impact by less than 1%. By comparing the individual data sets, it can be pointed out that for the $^{\mathrm{enr}}$Coax data the uncertainty is amplified by +5.9% compared to the uncertainty of 2.7% for the $^{\mathrm{enr}}$BEGE data. This is due to the strong deviation of the active volume for which the analysis of $T_{1/2}^{2\nu}$ has been correct for by the additional parameter δ_{AV} when combining the $^{\mathrm{enr}}$BEGE and $^{\mathrm{enr}}$Coax data. But this uncertainty is already accounted for in the uncertainty of the active ^{76}Ge exposure of the $^{\mathrm{enr}}$Coax data described in the next paragraph. Therefore, it has been neglected in the context of the global model fit components. Including data set, prior dependence, binning, and selection of background sources, the uncertainty obtained by the global model fit can be estimated to be less than 3.7% and 4.1% for the lower and upper bound, respectively. The estimations given here are derived from the study on the stability of the background model in Sec. 5.6.

Detector parameters The ^{76}Ge exposure can be calculated by

$$\mathcal{E}_{AV,76} = \sum_{j=1}^{N_{det}} M_j t_j f_{AV,j} f_{76,j}. \tag{6.3}$$

The uncertainties of the exposures of the $^{\mathrm{enr}}$BEGE and $^{\mathrm{enr}}$Coax data are not included in the determination of $1/T^{2\nu}_{1/2}$ in Eq. 6.2. The uncertainties are mainly driven by the uncertainties on the active mass fraction $f_{av,j}$ and the isotopic abundances $f_{76,j}$ of ^{76}Ge of each detector. The uncertainties have been estimated by taking the results of [119] which used a Monte Carlo approach by randomly sampling the exposure from a Gaussian distribution with the mean values and standard deviations corresponding to the values of $f_{av,j}$ and $f_{76,j}$ listed in Tab. B.2. Thereby, the correlation terms are taken into account. While the detector mass is determined with an accuracy of less than 0.1%, the uncertainty on the active mass fraction is much larger and results from comparison of simulations and calibration measurements taken with ^{60}Co and ^{214}Am performed by [87]. Apart from the number of decays taking place in the active and dead layer part of the detectors, the active volume fractions have an impact on the shape of the energy spectrum of several background sources located on the n^{+} like ^{42}K. This effect has not been taken into account in this estimation. The uncertainty coming from the live time is derived from the test pulser injected every 20 s resulting in less than 0.5%. In summary, the exposure for the total $^{\mathrm{enr}}$Ge data is 45.2 with an error of ± 1.1 kg $\cdot$ yr or $\pm 2.4\%$.

Data acquisition and selection The efficiency of trigger, the quality cuts and the reconstruction for physical events is as well determined with the injected test pulsers. Since no pulser event above 150 keV is lost by the data acquisition and selection, the efficiency is almost 100% [119]. Hence, it is considered to introduce less than 0.1% of uncertainty.

6.3 Discussion

Fig 6.1 summarized the results of the $2\nu\beta\beta$ half-life measurements over the last three decades. The first direct observation has been made by the ITEP-Yerevan experiment resulting in $T^{2\nu}_{1/2} = (9 \pm 1) \cdot 10^{20}$ yr. Ten measurements followed in the following years. The first three results turned out to be contaminated with internal radioactivity generated by spallation reactions of cosmic ray induced neutrons. These backgrounds events were partially assumed to come from the $2\nu\beta\beta$ decay, resulting in shorter half-lives. The measurement published by GERDA Phase I in 2015 has been obtained with the highest accuracy so far with $T^{2\nu}_{1/2} = (1.926 \pm 0.094) \cdot 10^{21}$ yr at 90% confidence level. When taking into account

Table 6.1 Systematic uncertainties on the measured half-life for the $2\nu\beta\beta$ decay of ^{76}Ge.

	uncertainty on $T^{2\nu}_{1/2}$ [%]	
shape of primary spectrum	< 0.1[101]	
^{42}K	$^{+0.9}_{-1.1}$	
remaining components	$^{+2.6}_{-1.2}$	
binning	< 1.3	
data sets	< 2.7	
fit model total		$^{+4.1}_{-3.4}$
active ^{76}Ge exposure		$\pm$ 2.4[119]
precision of the MC geometry model	$\pm$ 1[101]	
accuracy of the MC tracking	$\pm$ 2[101]	
Monte Carlo simulation		$\pm$ 2.2
Data acquisition and handling		< 0.1[119]
total		$^{+5.2}_{-4.7}$

the deviation of the total active volume of the $^{\mathrm{enr}}$Coax data which has been determined in this analysis, the result of Sec. 6.2 is in very good agreement with the half-life published in Phase I. The measurements have shown that the rate for $2\nu\beta\beta$ decay in ^{76}Ge is at least four orders of magnitude higher compared to the one of $0\nu\beta\beta$ decay. Historically, the value for $T^{2\nu}_{1/2}$ for ^{76}Ge has increased with increasing signal-to-background ratio indicating that the background subtraction is very difficult. As the experiments improve with better performance by increased signal-to-noise ratio, new design concepts or more strict material selection criteria, the background is either reduced or it is better constrained by improved analysis and modeling of background. As a consequence of the two latter conditions, the evaluated half-life increases.

Typically, high purity germanium detectors are operated in a vacuum cryostat with an experimental design based on ultra-low background cryostats and on a shielding consisting of lead. In contrast, GERDA operates its high purity germanium detectors directly in LAr. While the former experiments faced a background mainly dominated by radioactive daughters of ^{238}U and ^{232}Th, ^{42}K is an unique background of GERDA. Each surviving background has to be well understood for a successful subtraction from the observed spectrum. A careful background model is crucial for the separation of the $2\nu\beta\beta$ decay events from the remaining background contributions. Tab. 6.1 shows that the highest uncertainty with 4.1% is attributed

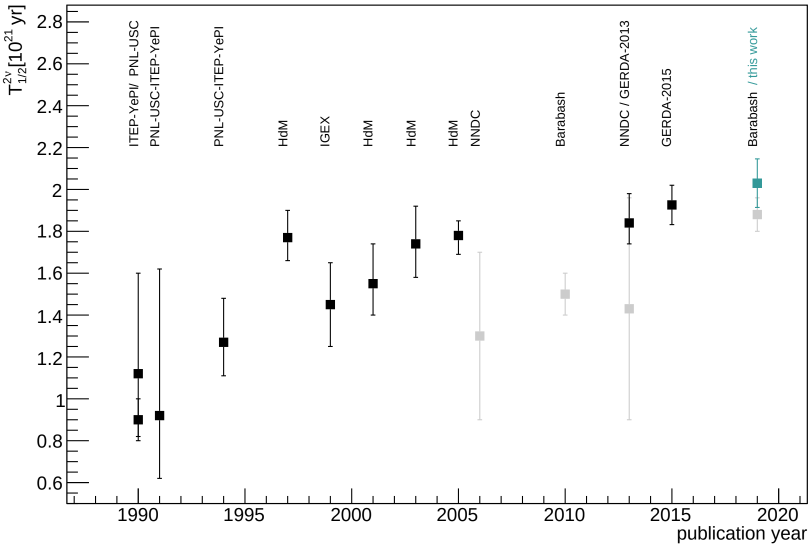

Fig. 6.1 Compilation of the measurements of the half-life of $2\nu\beta\beta$ in ^{76}Ge versus publication year. The experimental results are shown for ITEP-YePV / PNL-USC ([120],[121],[122],[123]), IGEX [124], the former Heidelberg-MoscowHdM ([125],[126],[127]), and GERDA ([101],[117]) experiments. In addition, values recommended values by NNDC ([128],[129]), and estimated by the weighted average due to Barabash [130],[131]) marked in gray.

to the background composition due to global model fit and the ^{76}Ge exposure. Besides the active ^{76}Ge exposure which is further correlated to the spectral behavior of certain background contributions. As the results of this analysis demonstrate, the uncertainty due to the background model components is still comparable with the accuracy of 4.2% reached in Phase I ($T^{2\nu}_{1/2}(1.926 \pm 0.025$ stat $\pm\, 0.091$ sys$) \cdot 10^{21}$ yr and signal-to-background ratio 4:1 [117]). Nevertheless, one should note that the background model of this analysis has integrated much more properties of the background. In addition, the background model accounts for the earlier underestimated total active volume of the $^{\text{enr}}$Coax detectors. In fact, it is impressive that the uncertainties remain comparable to the result of [117], although the background model presented here carriers a much larger number of potential sources of uncertainties and is of increased complexity. A significant more precise result can be achieved by determining the half-life after applying the LAr veto cut. The LAr veto cut suppresses primarily the γ lines from β-γ cascade emitters reducing the ^{42}K and ^{214}Bi background by a factor of 5 and the Compton continuum by a factor of 2. After applying this cut the signal-to-background ratio improves from 3:2 to 30:1[93]. Beyond that, a next generation Ge experiment like LEGEND can benefit from using argon extracted from underground wells depleted in naturally occurring radioactive isotopes of cosmogenic origin. Since ^{42}K is a cosmogenically produced decay product of ^{42}Ar, the deployment of so-called depleted argon would decrease drastically the remaining background not only around $Q_{\beta\beta}$ (see Ch. 5.5) but also in the $2\nu\beta\beta$ dominated energy region improving the signal-to-background ratio.

Chapter 7

Conclusion and outlook

The neutrinoless double beta decay is presently the only feasible way to reveal the Majorana nature of neutrinos, i.e. if neutrinos are their own anti-particles. GERDA aims to discover this process in a background-free search using ^{76}Ge. Located at the Laboratori Nazionali del Gran Sasso in Italy, GERDA operates bare, isotopically enriched, high purity germanium detectors in liquid argon. The second phase of GERDA is intended to probe half-lives in the range of 10^{26} yr by collecting a design exposure of 100 kg·yr in a substantially reduced background regime of about 10^{-3} $\mathrm{cts}/(\mathrm{keV}\cdot\mathrm{kg}\cdot\mathrm{yr})$. After a major upgrade, GERDA Phase II was launched in December 2015. Thanks to the increased detector mass and active background suppression techniques, among with an additional implementation of a LAr veto system detecting the LAr scintillation light, the target background level of $< 10^{-3}$ $\mathrm{cts}/(\mathrm{keV}\cdot\mathrm{kg}\cdot\mathrm{yr})$ has been reached. This result proves that the LAr veto and the pulse shape discrimination (PSD) technique are efficient suppression strategies. Both techniques base on the understanding of the characteristics of event classes and topologies of the individual background contributions which imply the knowledge of the present background in the energy spectrum. Therefore, the goal of this thesis has been a detailed study of the background and the development of a comprehensive model describing the experimental energy spectra of the single- and two-detector data of $^{\mathrm{enr}}$BEGE and $^{\mathrm{enr}}$Coax recorded in Phase II comprising 60.2 kg·yr.

The individual contributions to the energy spectra have been reconstructed by detailed GEANT4-based Monte Carlo simulations, including both physics processes and instrumental effects. Background contributions and estimates of the activities have been determined though a Bayesian approach based on a priori constrains from material screening. The single- and two-detector background spectra have been fitted by using the spectra of the simulated background sources. At the same time, the background contributions present in both the single- and two-detector data have been used to constrain for the first time the parameter estimates in common for all data sets in a multivariate algorithm. As a result, the most significant background sources and their locations in the experimental setup are largely disentangled by the observed γ lines and other prominent features in the energy spectra. Two most striking features are the α decays dominating the high energy part of the spectrum and the significant γ lines of ^{40}K and ^{42}K. Both features have been investigated with an additional emphasis in the context of the α-model and K-model. Thereby, the count rates of the potassium γ lines are studied on the single detector basis in order to assess potential asymmetries in the data spectra due to inhomogeneous source distributions of ^{42}K or ^{40}K. Finally, the stability of the results has been validated by consistency checks varying the binning, the input data spectra, the priors, and the list of background contributions.

Of particular interest for the GERDA experiment is the identification and reduction of those contaminants contributing in the ^{76}Ge $0\nu\beta\beta$ decay energy range between 1930 keV and 2190 keV. In addition, the shape of the measured energy spectra at $Q_{\beta\beta}$ which is composed by the main background contributions is an essential input for reliable results on the $0\nu\beta\beta$ signal search. It has been shown, that after removal of the known γ peaks, the model predicts a flat energy spectrum for the blinded region around $Q_{\beta\beta}$ with a background index before applying the LAr and PSD cuts of $14.9 \cdot 10^{-3}$ cts/(keV $\cdot$ kg $\cdot$ yr) and $15.3 \cdot 10^{-3}$ cts/(keV $\cdot$ kg $\cdot$ yr) for the $^{\mathrm{enr}}$BEGE and $^{\mathrm{enr}}$Coax data, respectively. While depending on the assumed impurity location, the background at $Q_{\beta\beta}$ is dominated by close sources, mainly ^{42}K, α emitting isotopes from ^{210}Po and the ^{226}Ra decay chain, ^{228}Th, ^{214}Bi, and ^{60}Co. Compared to Phase I, the BIs have been reduced even prior to the LAr veto and PSD cuts which shows the success of the efforts undertaken with regard to the Phase II upgrade. In addition, after all suppression cuts GERDA has reached an unprecedented low background rate of $\left(5.6^{+4.1}_{-2.6}\right)$ counts/(keV $\cdot$ kg $\cdot$ yr) for the $^{\mathrm{enr}}$Coax and $\left(5.6^{+3.4}_{-2.4}\right)$ counts/(keV $\cdot$ kg $\cdot$ yr) for the $^{\mathrm{enr}}$BEGE detectors. The assumption of a flat background around $Q_{\beta\beta}$ from this background model has been used in the $0\nu\beta\beta$ analysis of Phase II. Combining Phase I and Phase II data, GERDA has found no evidence for the $0\nu\beta\beta$ decay in ^{76}Ge and set the most stringent half-life limit. When assuming no signal and given the expected background rate after the LAr veto and PSD cuts, the sensitivity is $T^{0\nu}_{1/2} > 1.1 \cdot 10^{26}$ yr (90% C.L.) performing a profile likelihood fit and $T^{0\nu}_{1/2} > 1.1 \cdot 10^{26}$ yr (90% C.I.) using a Bayesian approach.

As a direct outcome of this work, the determination of the half-life of the neutrino accompanied $\beta\beta$ decay in ^{76}Ge with GERDA Phase II is reported. The half-life is determined to be $T^{2\nu}_{1/2} = (2.02 \pm 0.11) \cdot 10^{21}$ yr with an exposure of 45.2 kg·yr of ^{76}Ge. The $2\nu\beta\beta$ decay of ^{76}Ge produces about 60% of the total events in the single-detector spectra in the energy region from 600 keV to 2 MeV. Obviously, a precise determination relies on how well the background can be constrained. Thus, an apparent background characterization and reduction is also essential for the determination of the $2\nu\beta\beta$ half-life of ^{76}Ge. The statistical uncertainty is mainly due to the anti-correlation to the dominating backgrounds of ^{40}K and ^{42}K which are characterized by only a single FEP and a continuous spectrum which overlap that of the $2\nu\beta\beta$ process. Therefore, a significantly improved precision on the half-life is expected after applying the LAr veto cut, since the signal to background ratio in the $2\nu\beta\beta$ energy region will be improved from 3:2 to 30:1.

The key to an increased sensitivity is a reduced background level among a larger active mass and a higher energy resolution. But a minimized background level can only be achieved by efforts devoted to understand the most important backgrounds and their properties. An improved background model with eventually even better characterized and constrained background components could be achieved by considering the individual event classes and topologies of the background contributions by integrating the information obtained by the LAr veto or PSD selection. Furthermore, with increased statistics the K-model could be extended to other prominent γ lines. In particular, the γ line of ^{214}Bi at 609 keV would be a candidate, it still suffers from strong discrepancies between the different data sets when comparing with the intensities in the observed data spectra. Otherwise, if the statistics are not high enough, potential top-bottom and rotational asymmetries could be directly disentangled via dividing the data sets further by taking into account the individual detector positions inside the array.

The superb performance of GERDA with respect to background characterization and discrimination, energy resolution and sensitivity pave the way for LEGEND, a next generation Ge experiment with a goal sensitivity to half-lives of 10^{27} yr and beyond. The knowledge gained by the background model regarding the dominant source and locations of impurities can be fed into the detector design of next generation experiments like LEGEND with an optimized processing and cleaning as well as improved materials selection. The achievements of Phase II give LEGEND the confidence to aim for a background reduction by another order of magnitude.

List of figures

1.1 Pattern of neutrino masses eigenstates for the normal (left) and inverted (right) hierarchies shown as function of mass squared. The fractional flavor content (e, μ,τ) of the mass eigenstates (ν_1,ν_2,ν_3) is indicated by the color code. $\Delta m^2_{atm} \sim |\Delta m^2_{32}|$ and $\Delta m^2_{sol} \sim \Delta m^2_{21}$ are the atmospheric and the solar mass-squared splitting, respectively [29]. 5

1.2 Atomic mass parabola for an isobar candidate with A even (left) and A odd (right) showing the necessary configuration for β decay and $\beta\beta$ decay [42]. 11

1.3 Feynman diagram of the standard mass mechanism of $0\nu\beta\beta$ process light Majorana neutrinos as mediator [49]. 12

1.4 (a) Effective Majorana mass as a function of the lightest neutrino mass for the normal and inverted ordering. (b) $0\nu\beta\beta$ decay half-life of ^{76}Ge as a function of the lightest neutrino mass for $|M'^{0\nu}| = 5.16$ (blue region) and $|M'^{0\nu}| = 2.81$ (red curves). The $1,...,5\sigma$ coverage regions are indicated by the different color shadings. See [52] for details. 14

1.5 Top: Nuclear matrix elements for $0\nu\beta\beta$ decay candidates as a function of mass number A with the assumption that the axial coupling constant g_A is unquenched. Bottom: Associated $0\nu\beta\beta$ decay half-lives, scaled by the square of the unknown parameter $m_{\beta\beta}$. See [58] for details. 16

1.6 The Phase II energy spectra zoomed to the ROI are shown separately for the $^{\mathrm{enr}}$Coax and $^{\mathrm{enr}}$BEGE data sets after all analysis cuts. The spectra are superimposed with the expectations based on the 90% C.L. limit for a $0\nu\beta\beta$ signal of $T^{0\nu}_{1/2} = 0.9 \cdot 10^{26}$ yr (dashed line) obtained by the combined analysis of GERDA Phase I and Phase II [36]. 26

2.1 Sensitivity of the GERDA experiment as function of exposure for various background conditions. The half-life for the claim of discovery of $0\nu\beta\beta$ in ^{76}Ge [77] is also shown in blue. 28

2.2 (a) Schematic layout of the GERDA Phase II setup. (b) Zoom of the Ge detector array surrounded by the LAr veto system (c) Sketch of the full assembled detector array, with the seven detector strings with preamplifiers. [80] 29

2.3 Band structure diagram for a semiconductor (a), an isolator (b) and a conductor (c) in electron energies 32

2.4 (a) Cross section of a semi-coaxial detector (top) and a $^{\mathrm{enr}}$BEGE detector (bottom). The p^{+} and n^{+} electrodes are indicated in Grey and black, respectively. The electrodes are separated by an insulating groove. (b) Weighting potential of a semi-coaxial (top) and a $^{\mathrm{enr}}$BEGE detector (bottom) shown with color profiles.[80] 37

3.1 Energy spectra of the single-detector (M1) and two-detector (M2) events collected in the enriched detectors between Dec 2015 and May 2018 corresponding to a total exposure of 60.2 kg·yr. The light grey shaded area represents the ROI in which the BI is evaluated, the dark grey shaded are indicates the blinded energy region. Additionally the most prominent γ lines and structures are marked. 43

3.2 Daily rate of 7 representative water Cherenkov PMTs from December 2015 till July 2018. The numbers indicated on the left denote the PMT labels defining the position and data channel. 51

3.3 (a) The measured energy spectrum of $^{\mathrm{enr}}$BEGE and $^{\mathrm{enr}}$Coax detectors for μ coincident Ge events without AC cut ($M \geq 1$) before and after various cuts whereby the muon veto trigger condition is applied to PMT supgroups depending on the PMT position: panels, pillbox (volume below LAr cryostat) and main water tank. (b) Shows the energy spectrum for μ coincident Ge events with $M \geq 1$ before and after various cuts in the analysis window around $Q_{\beta\beta}$. 52

3.4 (a) Spectrum in the $2\nu\beta\beta$ decay dominated energy region prior to and in coincidence with the LAr veto. (b) Energy spectrum in the same energy range after the LAr veto suppression together with a spectrum of simulated $2\nu\beta\beta$ decays (solid line). Inset shows a zoom of the full energy γ lines from ^{40}K and ^{42}K. 54

3.5 Pulse shapes illustrative for a SSE (top left), MSE (top right), p^{+} electrode event (bottom left) and n^{+} surface event (bottom right). The charge pulses (red solid line) are shown as a function of time together with its interpolated derivative, i.e. the current (blue solid line). The amplitudes of the maximal charge pulse are normalized to unity. [99] 55

3.6 ^{228}Th calibration spectra of $^{\text{enr}}$BEGe (a) and coaxial detectors (b) before and after multi-site event rejection using the two different PSD techniques. The respective bottom panels shows the survival fraction as a function of energy, i.e. the ratio of the spectra with and without PSD. 56

3.7 The measured GERDA Phase II energy spectrum of $^{\text{enr}}$BEGe (a) and semi-coaxial (b) detectors after the various background rejection cuts. 57

3.8 (a) Simulated current pulses for SSE events at various locations of a semi-detector normalized to its integral. The pulse shapes are calculated for different location starting at the outer n^+ surface going along a radial line at the mid-plane towards the bore hole. (b) Recorded physics data pulses for SSE and MSE candidate events. The extraction of the input parameters for the neutral network is shown. The colored lines give the corresponding reference times at 20% (A_2) and 50% (A_1) of the maximum pulse amplitude. [99] 58

3.9 Energy spectra before (open histogram) and after the LAr veto cut (grey shaded) and PSD selection (red shaded) for the $^{\text{enr}}$Coax (top) and $^{\text{enr}}$BEGe (bottom) detectors together with the expected $2\nu\beta\beta$ spectra (solid line) from a recent half-life measurement of GERDA [101]. In addition, a zoom of the $^{\text{enr}}$BEGe spectrum into the energy region around the two potassium lines is shown [36]. 60

3.10 The Phase II energy spectra zoomed to the ROI are shown separately for the $^{\text{enr}}$Coax and $^{\text{enr}}$BEGe data sets after the LAr veto and PSD cuts [36]. 60

4.1 Rendering of GERDA Phase II MAGE components without cryostat: (a) Raw Ge crystals without holding structure showing in the front row from left to right starting with string 4 with eight $^{\text{enr}}$BEGe detectors, string 5 with three semi-coaxial, and string 6 and 1 with six $^{\text{enr}}$BEGe plus one semi-coaxial and eight $^{\text{enr}}$BEGe detectors, respectively. (b) Copper support structures of the crystals together with the Si holder plates. (c) The front-end components located on a copper support structure in about 30 cm distance to the detectors. Layout of the signal and high voltage cables shown together with their connection bars. (d) Arrangement of the seven detector strings with high voltage and signal cables, holder plates and read-out electronics. Each string is enclosed by a transparent nylon mini-shroud. (e) The Ge detector array enclosed by the LAr veto system. Top and bottom plate with nine and seven PMTs, respectively and the copper cylinder. (f) Fiber curtain surrounding the detector array together with the top and bottom plate showing the shifted alignment of the veto with respect to the center of the detector array [104]. 62

4.2 String arrangement of the enriched $^{\mathrm{enr}}$BEGE (GDxxx), the enriched (RGx and ANGx) and natural (GTFxxx) semi-coaxial detectors of the GERDA Phase II detector array. Each detector is labeled by a number between 0 and 39 depending on its position starting in string S1 with 0 continuing from top to bottom string by string. In addition, for each detector the groove orientation and the geometrical configuration including conical shapes are indicated [104]. 63

4.3 Simulated energy spectra of intrinsic $2\nu\beta\beta$ decays corresponding to single-detector events of the enriched $^{\mathrm{enr}}$BEGE and $^{\mathrm{enr}}$Coax data sets. Each spectrum is normalized to the number of total number events in the energy range between 100 keV and 8000 keV. 69

4.4 Simulated energy spectra of the ^{42}K decays for different source positions corresponding to the single-detector and two-detector event data sets for enriched $^{\mathrm{enr}}$BEGE and $^{\mathrm{enr}}$Coax. All spectra are normalized to the number of events in the bins containing the FEP at (1524.7 ± 2) keV. 70

4.5 Simulated energy spectra of the ^{40}K decays for different source positions corresponding to the single-detector and two-detector event data sets for enriched $^{\mathrm{enr}}$BEGE and $^{\mathrm{enr}}$Coax. All spectra are normalized to the number of events in the bins containing the FEP at (1460.9 ± 2) keV. 72

4.6 Simulated energy spectra of the ^{60}Co decays for different source positions corresponding to the single-detector and two-detector event data sets for enriched $^{\mathrm{enr}}$BEGE and $^{\mathrm{enr}}$Coax. All spectra are normalized to the number of events in the bins containing the FEP at (1332.5 ± 2) keV. 73

4.7 Simulated energy spectra of the $^{234\mathrm{m}}$Pa decays for different source positions corresponding to the single-detector and two-detector event data sets for enriched $^{\mathrm{enr}}$BEGE and $^{\mathrm{enr}}$Coax. All spectra are normalized to the number of events in the bins containing the FEP at (1001.4 ± 2) keV. 74

4.8 Simulated energy spectra of the ^{226}Ra sub-chain decays for different source positions corresponding to the single-detector and two-detector event data sets for enriched $^{\mathrm{enr}}$BEGE and $^{\mathrm{enr}}$Coax. All spectra are normalized to the number of events in the bins containing the FEP at (609.3 ± 2) keV. 74

4.9 Simulated energy spectra of the ^{226}Ra decays on p^{+} surface (a) and in LAr close to the p^{+} surface (b), and the ^{210}Po decays on p^{+} (c) for p^{+} dead layer thicknesses between 100 nm and 800 nm corresponding to singe-detector events of enriched $^{\mathrm{enr}}$BEGE and $^{\mathrm{enr}}$Coax. All spectra are normalized to the number of total events in the energy spectrum. 76

4.10 Simulated energy spectra of the ^{228}Ac decays for different source positions corresponding to the single-detector and two-detector event data sets for enriched $^{\mathrm{enr}}$BEGe and $^{\mathrm{enr}}$Coax. All spectra are normalized to the number of events in the bins containing the FEP at (911.2 ± 2) keV. 77

4.11 Simulated energy spectra of the ^{228}Th sub-chain decays for different source positions corresponding to the single-detector and two-detector event data sets for enriched $^{\mathrm{enr}}$BEGe and $^{\mathrm{enr}}$Coax. All spectra are normalized to the number of events in the bins containing the FEP at (2614.5 ± 2) keV. 78

5.1 Energy spectrum between 1410 keV and 1590 keV for single-detector and two-detector events of $^{\mathrm{enr}}$BEGe and $^{\mathrm{enr}}$Coax illustrating the selection of the five energy bands composing the data sets of the K-model [104]. 84

5.2 Experimental spectrum in the energy region above 3500 keV (filled) and the best fit of the α-model(black line), together with the individual components of the best fit model for the single-detector data sets of $^{\mathrm{enr}}$BEGe (a) and $^{\mathrm{enr}}$Coax (b). All events above 5250 keV are contained in the last bin at the high energy edge of the spectrum. The lower panels show the residuals with the shaded bands representing the statistical uncertainties. [104] 92

5.3 Experimental count rate in detector space (black marker) of the ^{40}K ((a),(c)) and ^{42}K((a),(c)) lines and the best fit of the base K-model (black line) for the single-detector data ((a),(b)) as well as the one-dimensional representation of the two-detector data ((c),(d)), together with the individual components of the best fit base model. The lower panels show the residuals with the shaded bands representing the statistical uncertainties. [104] 96

5.4 Chart of the global model describing the analysis flow. The energy distribution of the single-detector and two-detector data are fit in the framework of the global model. The simulated spectral shapes and the α-model enter the global model as PDFs while the screening measurements and K-model provide prior probability distributions. 97

5.5 Summary of the parameter estimates obtained by the maximum global model. Flat priors are not indicated. The marginalized modes along with the central 68% C.I. or the 90% upper limit are reported. Furthermore, the parameter estimates are compared to the corresponding prior and screening measurements. 98

5.6 Fit results of the minimal model corresponding to single-detector events for $^{\mathrm{enr}}$BEGE (a) and $^{\mathrm{enr}}$Coax (b) and two-detector events (c). The lower panel in each plot shows the residuals evaluated by the z-score with the one (green), two (yellow) and three (red) standard deviation bands. 104
5.7 Fit results of the minimal model corresponding to single-detector events for $^{\mathrm{enr}}$BEGE (a) and $^{\mathrm{enr}}$Coax (b). 106

6.1 Compilation of the measurements of the half-life of $2\nu\beta\beta$ in ^{76}Ge versus publication year. The experimental results are shown for ITEP-YePV / PNL-USC ([120],[121],[122],[123]), IGEX [124], the former Heidelberg-MoscowHdM ([125],[126],[127]), and GERDA ([101],[117]) experiments. In addition, values recommended values by NNDC ([128],[129]), and estimated by the weighted average due to Barabash [130],[131]) marked in gray. 121

B.1 Overview of the relevant isotopes in the two natural decay chains ^{232}Th (Th chain) and ^{238}U (U-Ra chain). Dominating decay modes, decay energies, half-lives and branching ratios are given [132]. 138
B.2 Simplified decay scheme of ^{40}K (a) and ^{42}K (b) [133]. 138
B.3 Simplified decay scheme of ^{208}Tl [133]. 139
B.4 Simplified decay scheme of ^{214}Bi [133]. 139
B.5 Simplified decay scheme of ^{60}Co [133]. 140
B.6 Correlation matrix obtained from the maximum fit of the global model with 51 parameters. Furthermore, the correlation coefficient between the individual parameters and the total count rate in the energy spectra for single-detector events of $^{\mathrm{enr}}$BEGE and $^{\mathrm{enr}}$Coax, and for two-detector events are given. 142
B.7 Estimated background contributions in the ROI shown in $\frac{10^{-3}\mathrm{cts}}{\mathrm{keV\cdot kg\cdot yr}}$. Backgrounds from natural radioactivity from the auxiliary detector materials are shown in blue. Green denotes backgrounds from the environment or those introduced during detector assembly. The contributions sum to $\frac{10^{-3}\mathrm{cts}}{\mathrm{keV\cdot kg\cdot yr}}$ in the single-detector data of $^{\mathrm{enr}}$BEGE and $^{\mathrm{enr}}$Coax. 143

List of tables

1.1 Natural abundance and Q value for all candidate isotopes under study [51]. 19

1.2 Summary of the performance parameters of selected $0\nu\beta\beta$ experiments: energy resolution FWHM, background rate *BI* and detection efficiency ε. Furthermore, the sensitivity is compared in terms of the background rate, energy resolution and detection efficiency ($\mathrm{B}_{\mathrm{FWHM}} = \mathrm{FWHM} \cdot \mathrm{B}/\varepsilon$) [36]. 23

1.3 Parameters for the seven GERDA Phase I and Phase II analysis data sets. Given are the respective exposure $\mathcal{E}$, energy resolution (FWHM) at $Q_{\beta\beta}$, total efficiency ε and the respective background index BI evaluated in the ROI [36]. 25

3.1 Natural decay chain of ^{238}U. The values are taken from [90] 46

3.2 Event suppression fractions of one-sided low and high A/E cuts together with the survival fractions of a two-sided cut given for the SEP, two FEPs and the DEP from physics and calibration of the $^{\mathrm{enr}}$BEGE detectors [80]. 57

5.1 Scale for Bayes factor to assess the evidence of model M_A against model M_B [113]. 89

5.2 Summary of the fit results of the α-model for single-detector data of $^{\mathrm{enr}}$BEGE and $^{\mathrm{enr}}$Coax. The global and marginalized modes along with the central 68% C.I. are reported. Values are given in cts in the full PDF range from 40 to 8000 keV [104]. 91

5.3 Summary of the fit results of the K-model for single-detector and tow-detector data of $^{\mathrm{enr}}$BEGE and $^{\mathrm{enr}}$Coax combined. The global and marginalized modes along with the central 68% C.I. are reported. The type of prior distributions is indicated with [f] for flat, [g] for Gaussian and [e] for exponential. 94

5.4 Summary of the analysis parameter estimates obtained by the minimum model. The global and marginalized modes along with the central 68 % C.I. are reported. The number of reconstructed counts from each component are given. The type of prior distributions is indicated with `[f]` for flat, `[g]` for Gaussian, `[e]` for exponential, `[p`$_\alpha$`]` for posterior obtained from the α-model and `[p`$_K$`]` for posterior obtained from the K-model. 102

5.5 The predicted background index and the contributions from the individual background components for single-detector data in the ROI derived from the minimum model are summarized. The results are quoted in units of $10^{-3}\,\frac{\mathrm{cts}}{\mathrm{keV\cdot kg\cdot yr}}$ by the global and marginalized modes along with the central 68 % C.I.. 105

5.6 The observed γ line count rates compared with the predicted count rates from the minimum model derived by the best fit parameters for single-detector and two-detector data. The marginalized modes together with the central 68 % C.I. are quoted in units of [cts/(kg · yr)]. 110

6.1 Systematic uncertainties on the measured half-life for the $2\nu\beta\beta$ decay of ^{76}Ge. . 120

B.1 Compilation of the specific activity for components of the detector support and the LAr veto obtained by the GERDA Phase II radio-purity screening measurements. The samples were measured with Ge γ spectrometers or ICP-MS assuming secular equilibrium [80]. 137

B.2 Main parameters of the GERDA Phase IIdetectors. All detectors labeled with GD, ANG or RG are made of germanium enriched in ^{76}Ge from 85.5 to 88.3 %, while the GTF detectors are made from natural germanium composition. The position number in a given string increases from top to bottom. The active masses of the newly produced $^{\mathrm{enr}}$BEGE detectors include a correction that considers a full charge collection depth growth occurred during storage at room temperature in the three years before deployment in GERDA. Finally, the full energy peak detector efficiencies ε_{fep} for the $0\nu\beta\beta$ decay in ^{76}Ge are quoted. For more details see Ref. [80]. 141

Appendix A

A.1 My Contribution

For the first two data releases of Phase II, a preliminary background model had been developed on the basis of the Phase I background model involving two people. This model consisted only of the α-model and the global model worked out by Katharina von Sturm and myself, respectively. The development of the preliminary background model has included a first Monte Carlo simulation campaign. The Monte Carlo simulations of the expected background simulations had been run, post-processed and evaluated in a common work involving the two of us. The list of background sources had been selected according to sources we identified in the energy spectra presented in Ch. 4 and according to the screening measurement. Providing the list of simulations had incorporated the compilation and evaluation of all preformed material screening measurements and material assays during the upgrade leading to the numbers given in Tab. B.1.

For the third data release of Phase II in 2018, the concept of the extended background model integrating the K-model has been developed in cooperation with the "background modeling analysis group" involving five people including myself. As a result, the final background model consists of three parts: the α-model, the K-model and the global model which has been further optimized in the context of this thesis. The presented α-model and K-model refer to Katharina von Sturm and Thomas Wester, respectively. The global model, the integration of the other models, the consistency checks and results presented in Ch. 5 and Ch.6 result from my work, except the α-model, the K-model and validity check of the global model fitter performed with a toy MC by Luigi Pertoldi. Furthermore, for the final background model a second Monte Carlo campaign of which the results have been presented in Ch. 4 has been performed by whom. The goal of this campaign has been to revise and improve the existing simulations predominantly regarding the post-processing. This task has been carried out by the "background modeling analysis group". During this, my main task has been providing the list of necessary background sources and cross-checking the simulation outputs.

The measurement of the $2\nu\beta\beta$ decay half-life presented in Ch. 6 is based on the energy spectra acquired during the Phase II data taking. On the basis of the developed background model in Ch. 5, I determined the $2\nu\beta\beta$ decay half-life and the correction of the assumed total active volume. Furthermore, I estimated the systematic uncertainties.

Appendix B

B.1 GERDA Phase II screening measurement results

Table B.1 Compilation of the specific activity for components of the detector support and the LAr veto obtained by the GERDA Phase II radio-purity screening measurements. The samples were measured with Ge γ spectrometers or ICP-MS assuming secular equilibrium [80].

part	method	mass [g]	^{228}Ra [uBq/g]	^{226}Ra [uBq/g]	^{228}Th [uBq/g]
silicon holder plates	Ge γ	640	< 0.39	< 0.21	< 0.15
signal and HV cables	Ge γ	50 pc	< 8.8	13.2 ± 4.2	< 8.2
front-end electronics	Ge γ	191	4.0 ± 2.0	14.0 ± 2.0	< 6.8
nylon mini-shrouds	ICP-MS	197	$(91 \pm 25) \cdot 10^{-3}$	–	0.091 ± 0.025
fibers and mounting	ICP-MS	765 + 3533	$(42 \pm 33) \cdot 10^{-3}$	0.12 ± 0.12	0.042 ± 0.033
SiPM and mounting	ICP-MS + Ge γ	1.3 + 73.1	$< 98 \cdot 10^{-3}$	4.7 ± 1.3	0.2 ± 1.9
top and bottom PMTs	Ge γ	9 + 7 pc	–	< 2840	< 2440
copper shroud with Tetratex® coating	ICP-MS + Ge γ	1688	$(36.7 \pm 3.6) \cdot 10^{-3}$	0.315 ± 0.031	0.115 ± 0.011

part	method	mass [g]	^{60}Co [uBq/g]	^{40}K [mBq/g]	^{238}U [mBq/g]
silicon holder plates	Ge γ	640	< 0.16	0.0043 ± 0.0009	< 0.0097
signal and HV cables	Ge γ	50 pc	0.8 ± 4.2	0.12 ± 0.04	< 0.72
front-end electronics	Ge γ	191	< 1.6	0.070 ± 0.020	< 0.11
nylon mini-shrouds	ICP-MS	197	–	> 0.0086	$(218 \pm 66) \cdot 10^{-6}$
fibers and mounting	ICP-MS	765 + 3533	–	$(81 \pm 16) \cdot 10^{-6}$	$(7.44 \pm 0.70) \cdot 10^{-3}$
SiPM and mounting	ICP-MS + Ge γ	1.3 + 73.1	–	0.032 ± 0.024	–
top and bottom PMTs	Ge γ	9 + 7 pc	–	< 20.6	–
copper shroud with Tetratex® coating	ICP-MS + Ge γ	1688	–	0.0109 ± 0.0011	–

B.2 Decay scheme

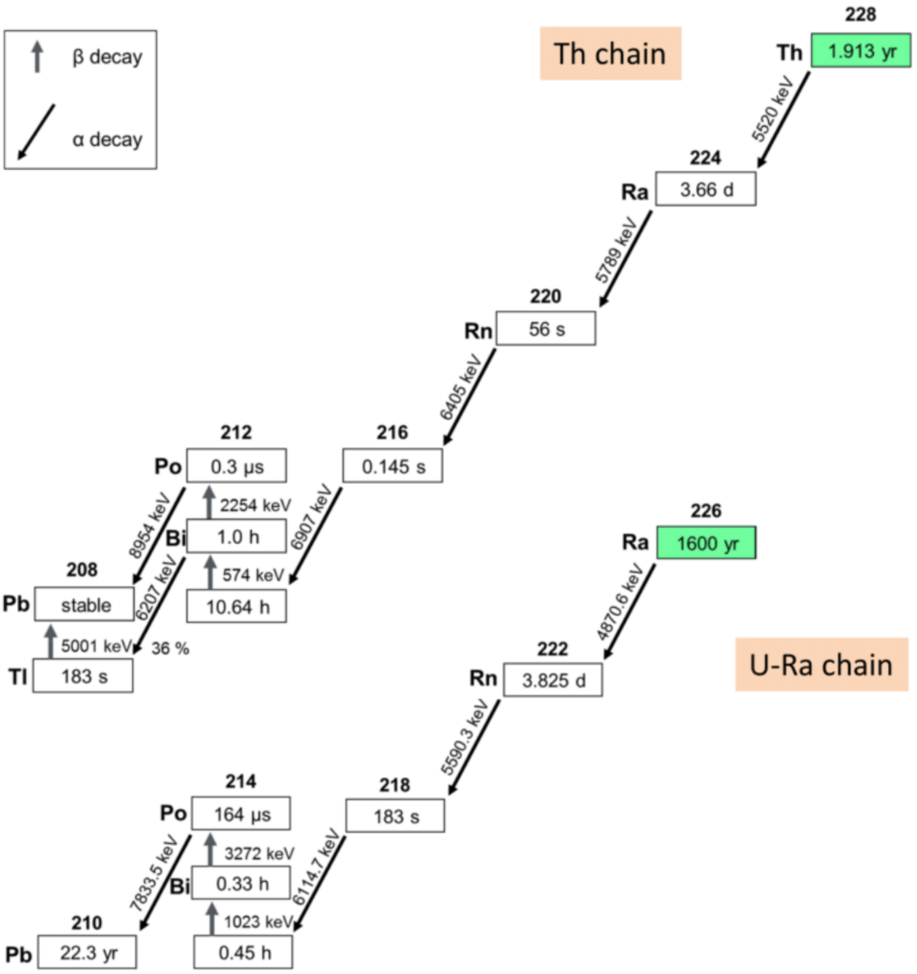

Fig. B.1 Overview of the relevant isotopes in the two natural decay chains ^{232}Th (Th chain) and ^{238}U (U-Ra chain). Dominating decay modes, decay energies, half-lives and branching ratios are given [132].

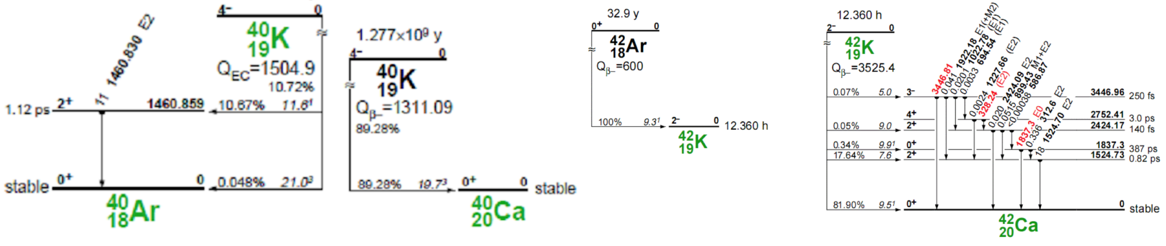

(a)

(b)

Fig. B.2 Simplified decay scheme of ^{40}K (a) and ^{42}K (b) [133].

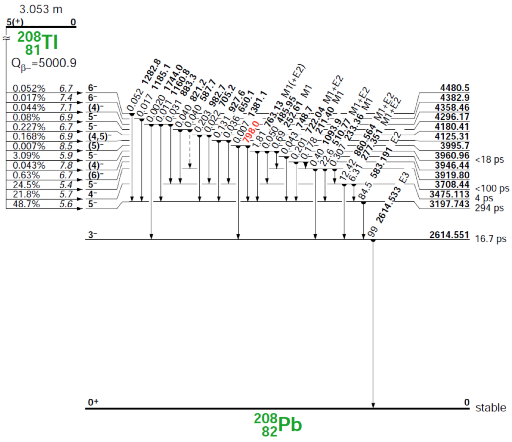

Fig. B.3 Simplified decay scheme of ^{208}Tl [133].

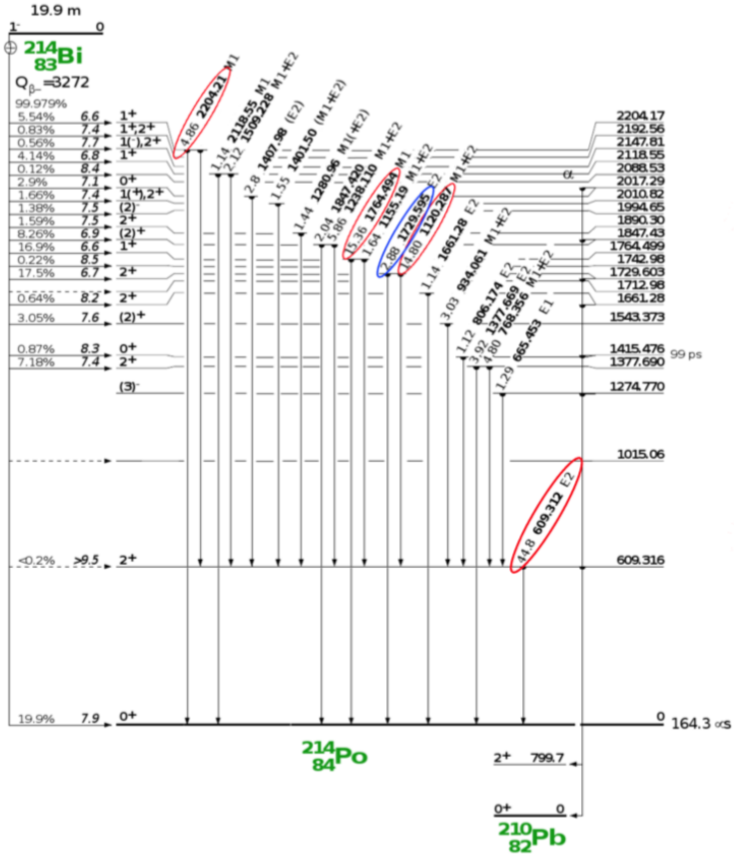

Fig. B.4 Simplified decay scheme of ^{214}Bi [133].

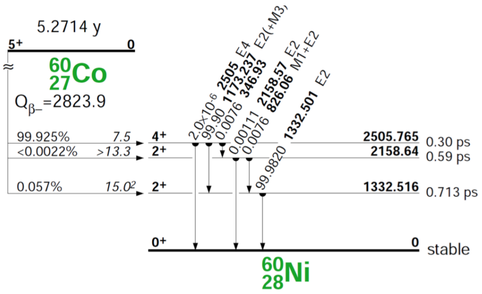

Fig. B.5 Simplified decay scheme of ^{60}Co [133].

B.3 GERDA Phase II detector parameters

Table B.2 Main parameters of the GERDA Phase IIdetectors. All detectors labeled with GD, ANG or RG are made of germanium enriched in ^{76}Ge from 85.5 to 88.3 %, while the GTF detectors are made from natural germanium composition. The position number in a given string increases from top to bottom. The active masses of the newly produced ^{enr}BEGE detectors include a correction that considers a full charge collection depth growth occurred during storage at room temperature in the three years before deployment in GERDA. Finally, the full energy peak detector efficiencies ε_{fep} for the $0\nu\beta\beta$ decay in ^{76}Ge are quoted. For more details see Ref. [80].

Nr.	detector	string position	f_{76}	M_{diode} [g]	$M_{av}{}^{+ucorr+corr}_{-ucorr-corr}$ [g]	$\varepsilon_{fep} \pm ucorr \pm corr$
13	GD32A	III-2	0.877 ± 0.013	458	404^{+10+4}_{-10-2}	$0.888 \pm 0.001 \pm 0.002$
12	GD32B	III-1	0.877 ± 0.013	716	632^{+10+4}_{-10-2}	$0.900 \pm 0.001 \pm 0.002$
14	GD32C	III-3	0.877 ± 0.013	743	665^{+10+4}_{-10-2}	$0.901 \pm 0.001 \pm 0.002$
34	GD32D	VI-4	0.877 ± 0.013	720	657^{+10+5}_{-10-2}	$0.900 \pm 0.001 \pm 0.002$
24	GD35A	IV-5	0.877 ± 0.013	768	693^{+13+3}_{-13-2}	$0.904 \pm 0.001 \pm 0.002$
1	GD35B	I-1	0.877 ± 0.013	810	740^{+11+5}_{-11-2}	$0.902 \pm 0.001 \pm 0.002$
19	GD35C	IV-0	0.877 ± 0.013	634	572^{+9+4}_{-9-3}	$0.893 \pm 0.001 \pm 0.002$
4	GD61A	I-4	0.877 ± 0.013	731	652^{+12+4}_{-11-3}	$0.902 \pm 0.001 \pm 0.002$
26	GD61B	IV-7	0.877 ± 0.013	751	666^{+12+5}_{-12-2}	$0.899 \pm 0.001 \pm 0.002$
16	GD61C	III-5	0.877 ± 0.013	634	562^{+10+5}_{-10-3}	$0.892 \pm 0.001 \pm 0.002$
17	GD76B	III-6	0.877 ± 0.013	384	326^{+7+3}_{-7-2}	$0.883 \pm 0.001 \pm 0.002$
20	GD76C	IV-1	0.877 ± 0.013	824	723^{+12+5}_{-12-2}	$0.902 \pm 0.001 \pm 0.002$
32	GD79B	VI-2	0.877 ± 0.013	736	648^{+13+5}_{-13-2}	$0.897 \pm 0.001 \pm 0.002$
23	GD79C	IV-4	0.877 ± 0.013	812	713^{+11+5}_{-11-2}	$0.900 \pm 0.001 \pm 0.002$
35	GD89A	VI-5	0.877 ± 0.013	524	462^{+10+3}_{-9-2}	$0.893 \pm 0.001 \pm 0.002$
5	GD89B	I-5	0.877 ± 0.013	620	533^{+12+4}_{-12-2}	$0.890 \pm 0.001 \pm 0.002$
15	GD89C	III-4	0.877 ± 0.013	595	520^{+12+5}_{-11-2}	$0.889 \pm 0.001 \pm 0.002$
21	GD89D	IV-2	0.877 ± 0.013	526	454^{+9+5}_{-9-2}	$0.884 \pm 0.001 \pm 0.002$
0	GD91A	I-0	0.877 ± 0.013	627	557^{+10+3}_{-11-2}	$0.898 \pm 0.001 \pm 0.002$
25	GD91B	IV-6	0.877 ± 0.013	650	578^{+10+5}_{-10-2}	$0.897 \pm 0.001 \pm 0.002$
7	GD91C	I-7	0.877 ± 0.013	627	556^{+11+4}_{-11-2}	$0.896 \pm 0.001 \pm 0.002$
33	GD91D	VI-3	0.877 ± 0.013	693	615^{+12+5}_{-12-2}	$0.899 \pm 0.001 \pm 0.002$
30	GD00A	VI-0	0.877 ± 0.013	496	439^{+8+3}_{-9-2}	$0.888 \pm 0.001 \pm 0.002$
3	GD00B	I-3	0.877 ± 0.013	697	613^{+12+5}_{-12-2}	$0.897 \pm 0.001 \pm 0.002$
18	GD00C	III-7	0.877 ± 0.013	815	727^{+14+5}_{-13-2}	$0.903 \pm 0.001 \pm 0.002$
22	GD00D	IV-3	0.877 ± 0.013	813	723^{+13+5}_{-13-2}	$0.902 \pm 0.001 \pm 0.002$
11	GD02A	III-0	0.877 ± 0.013	545	488^{+8+3}_{-8-2}	$0.893 \pm 0.001 \pm 0.002$
2	GD02B	I-2	0.877 ± 0.013	625	553^{+10+4}_{-10-2}	$0.895 \pm 0.001 \pm 0.002$
31	GD02C	VI-1	0.877 ± 0.013	788	700^{+13+5}_{-13-2}	$0.901 \pm 0.001 \pm 0.002$
6	GD02Da	I-6	0.877 ± 0.013	662	552^{+11+0}_{-11-2}	Not defined, see remark
36	ANG1	VI-6	0.859 ± 0.029	958	795^{+43+26}_{-43-26}	0.889 ± 0.018
27	ANG2	V-0	0.866 ± 0.025	2833	$2468^{+121+80}_{-121-80}$	0.918 ± 0.018
10	ANG3	II-2	0.883 ± 0.026	2391	$2070^{+118+60}_{-118-67}$	0.916 ± 0.018
29	ANG4	V-2	0.863 ± 0.013	2372	$2136^{+116+69}_{-116-69}$	0.916 ± 0.018
8	ANG5	II-0	0.856 ± 0.013	2746	$2281^{+109+74}_{-109-74}$	0.918 ± 0.018
9	RG1	II-1	0.855 ± 0.015	2110	$1908^{+109+62}_{-109-62}$	0.915 ± 0.018
28	RG2	V-1	0.855 ± 0.015	2166	1800^{+99+58}_{-99-58}	0.912 ± 0.018
38	GTF32	VII-1	0.078 ± 0.001	2321	2251^{+116}_{-116}	0.92 ± 0.018
39	GTF45	VII-2	0.078 ± 0.001	2312	1965	0.92 ± 0.018
37	GTF112	VII-0	0.078 ± 0.001	2965	2522	0.92 ± 0.018

B.4 Global model

B.4.1 Parameter correlations

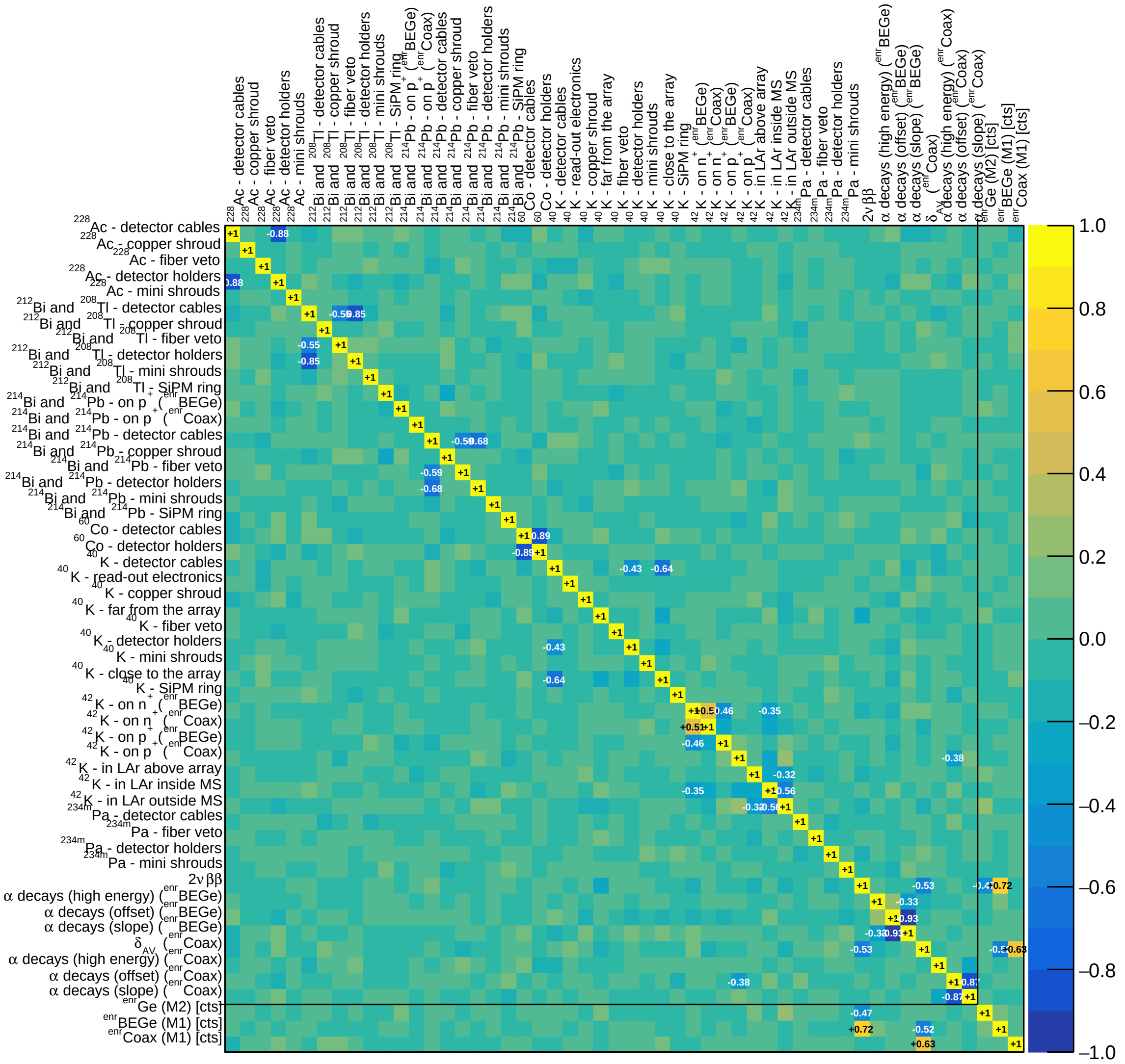

Fig. B.6 Correlation matrix obtained from the maximum fit of the global model with 51 parameters. Furthermore, the correlation coefficient between the individual parameters and the total count rate in the energy spectra for single-detector events of ^{enr}BEGE and ^{enr}Coax, and for two-detector events are given.

B.4.2 Background composition at $Q_{\beta\beta}$

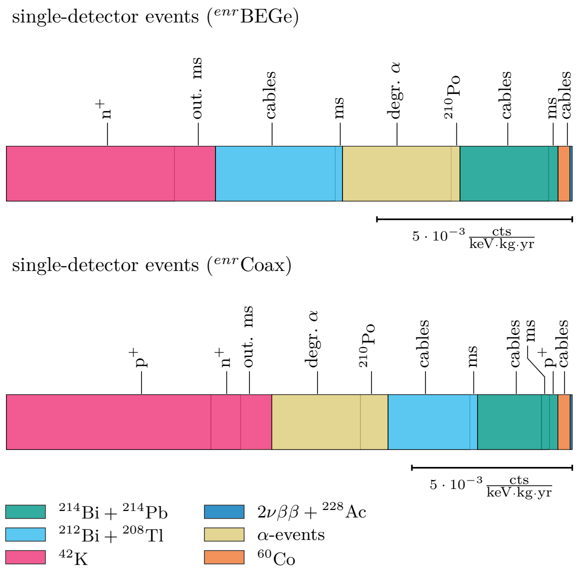

Fig. B.7 Estimated background contributions in the ROI shown in $\frac{10^{-3}\text{cts}}{\text{keV}\cdot\text{kg}\cdot\text{yr}}$. Backgrounds from natural radioactivity from the auxiliary detector materials are shown in blue. Green denotes backgrounds from the environment or those introduced during detector assembly. The contributions sum to $\frac{10^{-3}\text{cts}}{\text{keV}\cdot\text{kg}\cdot\text{yr}}$ in the single-detector data of $^{\text{enr}}$BEGE and $^{\text{enr}}$Coax.

B.5 Statistical Methods

B.5.1 Count rate analysis

The count rate R_S of each γ line is determined by fitting the binned data spectra in the γ ray peak region with a width E_W of $\pm 3\sigma$. The probability distribution of the model and its parameters is given by the Bayes' Theorem, according to Eq. 5.1. The total number of events in the peak region arises from a Poisson process and since the events of a certain γ ray is measured in presence of background, the likelihood can be written as:

$$P(n|\lambda_B, \lambda_S) = \prod_{i=0}^{N_{bins}} Poiss(n|\lambda_{i,B} + \lambda_{i,S}) \tag{B.1}$$

with λ_B being the number of expected background and λ_S being the expected signal events. While the background events are assumed to have a flat energy distribution.

$$\lambda_{i,B} = \int_{\Delta E_i} \frac{R_B}{E_W} dE = \frac{R_B}{E_W} \Delta E_i \tag{B.2}$$

the signal events are given by a Gaussian function centered at the expected peak position energy μ:

$$\lambda_S = \int_{\Delta E_i} \frac{R_S}{\sqrt{2\pi\sigma^2}} \exp\left(-\frac{E-\mu}{2\sigma^2}\right) dE \tag{B.3}$$

The standard deviation σ of the gauss distribution is extrapolated from the data calibration at the respective energy. The prior probability distribution of the other model parameters R_B, R_S and μ are assumed to be flat. As a result, the count rate R_S has been extracted by the marginalized mode of the posterior probability distribution.

References

[1] F. Reines and C. L. Cowan. Detection of the Free Neutrino. *Phys. Rev.* , 92:830–831, Nov 1953.

[2] G. Danby et al. Observation of High-Energy Neutrino Reactions and the Existence of Two Kinds of Neutrinos. *Phys. Rev. Lett.* , 9:36–44, Jul 1962.

[3] S. Schael et al. Precision electroweak measurements on the Z resonance. *Phys. Rep.* , 427(hep-ex/0509008. CERN-PH-EP-2005-041. SLAC-R-774. CERN-L3-304):257. 302 p, Sep 2005.

[4] K. Kodama et al. Observation of tau neutrino interactions. *Phys. Lett.* **B**, 504(3):218 – 224, 2001.

[5] C. S. Wu et al. Experimental Test of Parity Conservation in Beta Decay. *Phys. Rev.* , 105:1413–1415, Feb 1957.

[6] L. D. Landau. On the conservation laws for weak interactions. *Nucl. Phys.* , 3:127–131, 1957.

[7] T. D. Lee and C. N. Yang. Parity Nonconservation and a Two Component Theory of the Neutrino. *Phys. Rev.* , 105:1671–1675, 1957. [,245(1957)].

[8] A. Salam. On parity conservation and neutrino mass. *Il Nuovo Cimento (1955-1965)*, 5(1):299–301, Jan 1957.

[9] M. Goldhaber, L. Grodzins, and A. W. Sunyar. Helicity of Neutrinos. *Phys. Rev.* , 109:1015–1017, Feb 1958.

[10] B. T. Cleveland et al. Measurement of the solar electron neutrino flux with the homestake chlorine detector. *Astrophysical Journal* , 496(1):505–526, mar 1998.

[11] J. N. Abdurashitov et al. Results from sage (the russian-american gallium solar neutrino experiment). *Phys. Lett.* **B**, 328(1):234 – 248, 1994.

[12] P. Anselmann et al. Solar neutrinos observed by gallex at gran sasso. *Phys. Lett.* **B**, 285(4):376 – 389, 1992.

[13] V. Gribov and B. Pontecorvo. Neutrino astronomy and lepton charge. *Phys. Lett.* **B**, 28(7):493 – 496, 1969.

[14] Y. Fukuda et al. Evidence for Oscillation of Atmospheric Neutrinos. *Phys. Rev. Lett.* , 81:1562–1567, Aug 1998.

[15] Q. R. Ahmad et al. Measurement of the rate of $\nu_e + d \to p + p + e^-$ interactions produced by ^8b solar neutrinos at the sudbury neutrino observatory. *Phys. Rev. Lett.*, 87:071301, Jul 2001.

[16] M. H. Ahn et al. Measurement of neutrino oscillation by the k2k experiment. *Phys. Rev. D* , 74:072003, Oct 2006.

[17] P. Adamson et al. Measurement of neutrino and antineutrino oscillations using beam and atmospheric data in minos. *Phys. Rev. Lett.* , 110:251801, Jun 2013.

[18] K. Abe et al. Precise measurement of the neutrino mixing parameter θ_{23} from muon neutrino disappearance in an off-axis beam. *Phys. Rev. Lett.* , 112:181801, May 2014.

[19] F. P. An et al. Spectral measurement of electron antineutrino oscillation amplitude and frequency at daya bay. *Phys. Rev. Lett.* , 112:061801, Feb 2014.

[20] J. K. Ahn et al. Observation of reactor electron antineutrinos disappearance in the reno experiment. *Phys. Rev. Lett.* , 108:191802, May 2012.

[21] Y. Abe et al. First measurement of θ_{13} from delayed neutron capture on hydrogen in the double chooz experiment. *Phys. Lett.* **B**, 723(1):66 – 70, 2013.

[22] C. Giunti and C. W. Kim. *Fundamentals of Neutrino Physics and Astrophysics*. 2007.

[23] C. Giganti, S. Lavignac, and M. Zito. Neutrino oscillations: The rise of the PMNS paradigm. *Prog. Part. and Nucl. Phys.* , 98:1 – 54, 2018.

[24] F. Capozzi et al. Global constraints on absolute neutrino masses and their ordering. *Phys. Rev. D* , 95:096014, May 2017.

[25] S. K. Agarwalla and P. Hernández. Probing the neutrino mass hierarchy with Super-Kamiokande. *Journal of High Energy Physics*, 2012(10):86, Oct 2012.

[26] O. Mena, S. Palomares-Ruiz, and S. Pascoli. Determining the neutrino mass hierarchy and CP-violation in NOνA with a second off-axis detector. *Phys. Rev. D* , 73:073007, Apr 2006.

[27] K. Abe et al. Neutrino oscillation physics potential of the T2K experiment. *Progress of Theoretical and Experimental Physics*, 2015(4), 04 2015.

[28] A. Ghosh, T. Thakore, and S. Choubey. Determining the neutrino mass hierarchy with ino, t2k, nova and reactor experiments. *Journal of High Energy Physics*, 2013(4):9, Apr 2013.

[29] S. Adrian-Martinez et al. Letter of intent for KM3NeT 2.0. *J. Phys.*, G43(8):084001, 2016.

[30] V. N. Aseev et al. An upper limit on electron antineutrino mass from Troitsk experiment. *Phys. Rev.* , D84:112003, 2011.

[31] Ch. Kraus et al. Final results from phase II of the Mainz neutrino mass searching tritium β decay. *Eur. Phys. J.* **C**, 40(4):447–468, Apr 2005.

[32] A. Osipowicz et al. KATRIN: A Next generation tritium beta decay experiment with sub-eV sensitivity for the electron neutrino mass. Letter of intent. 2001.

[33] L. Bornschein et al. Status of the karlsruhe tritium neutrino mass experiment katrin. *Fusion Science and Technology*, 71(4):485–490, 2017.

[34] M. Aker et al. An improved upper limit on the neutrino mass from a direct kinematic method by KATRIN. submitted to Phys. Rev. Letter, arXiv:1909.06048, 2019.

[35] P. A. R. Ade et al. Planck 2015 results. XIII. Cosmological parameters. *Astron. Astrophys.*, 594:A13, 2016.

[36] M. Agostini et al. Probing Majorana neutrinos with double-β decay. supmitted to Science, arXiv:1909.02726.

[37] S. Mertens. Direct Neutrino Mass Experiments. *J. Phys.: Conf. Ser.* , 718:022013, may 2016.

[38] M. Thomson. *Modern particle physics*. Cambridge University Press, New York, 2013.

[39] P. Minkowski. $\mu \to e\gamma$ at a rate of one out of 10^9 muon decays? *Phys. Lett.* **B**, 67(4):421 – 428, 1977.

[40] M. Gell-Mann, P. Ramond, and R. Slansky. Complex Spinors and Unified Theories. *Conf. Proc.*, C790927:315–321, 1979.

[41] N. R. Mohapatra and G. Senjanovic. Neutrino Mass and Spontaneous Parity Nonconservation. *Phys. Rev. Lett.* , 44:912, 1980. [,231(1979)].

[42] S. Dell'Oro et al. Neutrinoless Double Beta Decay: 2015 Review. *Adv. High Energy Phys.*, 2016:2020–2023, 2016.

[43] S. R. Elliott, A. A. Hahn, and M. K. Moe. Direct evidence for two-neutrino double-beta decay in ^{82}Se. *Phys. Rev. Lett.* , 59:2020–2023, Nov 1987.

[44] W. H. Furry. On transition probabilities in double beta-disintegration. *Phys. Rev.* , 56:1184–1193, Dec 1939.

[45] E. Majorana. Teoria simmetrica dell'elettrone e del positrone. *Nuovo Cim.*, 14:171–184, 1937.

[46] N. R. Mohapatra. New contributions to neutrinoless double-beta decay in supersymmetric theories. *Phys. Rev. D* , 34:3457–3461, Dec 1986.

[47] M. Hirsch, H. V. Klapdor-Kleingrothaus, and O. Panella. Double beta decay in left-right symmetric models. *Phys. Lett.* **B**, 374(1):7 – 12, 1996.

[48] M. Lindner, F. S. Queiroz, and W. Rodejohann. Dilepton bounds on left-right symmetry at the LHC run II and neutrinoless double beta decay. *Phys. Lett.* **B**, 762:190 – 195, 2016.

[49] H. Päs and W. Rodejohann. Neutrinoless double beta decay. *New Journal of Physics*, 17(11):115010, nov 2015.

[50] F. Simkovic, J. Vergados, and A. Faessler. Few active mechanisms of the $0\nu\beta\beta$ decay and effective mass of majorana neutrinos. *Phys. Rev. D* , 82, 12 2010.

[51] W. Rodejohann. Neutrino-less double beta decay and particle physics. *International Journal of Modern Physics* **E**, 20(09):1833–1930, 2011.

[52] G. Benato. Effective majorana mass and neutrinoless double beta decay. *Eur. Phys. J.* **C**, 75(11):563, Nov 2015.

[53] C. Giunti and E. M. Zavanin. Predictions for neutrinoless double-beta decay in the $3+1$ sterile neutrino scenario. *J. Phys.: Conf. Ser.* , 718:062074, may 2016.

[54] M. Agostini, G. Benato, and J. A. Detwiler. Discovery probability of next-generation neutrinoless double-β decay experiments. *Phys. Rev. D* , 96:053001, Sep 2017.

[55] J. Schechter and J. W. F. Valle. Neutrino Masses in SU(2) x U(1) Theories. *Phys. Rev.* , D22:2227, 1980.

[56] F. Simkovic and A. Faessler. Distinguishing the $0\nu\beta\beta$-decay mechanisms. *Prog. Part. and Nucl. Phys.* , 48(1):201 – 209, 2002.

[57] R. G. H. Robertson. Empirical Survey of Neutrinoless Double Beta Decay Matrix Elements. *Mod. Phys. Lett.*, A28:1350021, 2013.

[58] J. Engel and J. Menendez. Status and future of nuclear matrix elements for neutrinoless double-beta decay: a review. *Rep. Progr. Phys.* , 80(4):046301, mar 2017.

[59] J. Suhonen and O. Civitarese. Probing the quenching of g_a by single and double beta decays. *Phys. Lett.* **B**, 725(1):153 – 157, 2013.

[60] I. Ostrovskiy and K. O'Sullivan. Search for neutrinoless double beta decay. *Mod. Phys. Lett.* **A**, 31(18):1630017, 2016.

[61] S. R. Elliott and P. Vogel. Double Beta Decay. *Ann. Rev. Nucl. Part. Sci.* , 52(1):115–151, 2002.

[62] E. Fiorini, A. Pullia, G. Bertolini, F. Cappellani, and G. Restelli. A search for lepton non-conservation in double beta decay with a germanium detector. *Phys. Lett.* **B**, 25(10):602 – 603, 1967.

[63] N. Abgrall et al. The MAJORANA DEMONSTRATOR neutrinoless double-beta decay experiment. *Adv. High Energy Phys.*, 2014, 08 2013.

[64] N. Abgrall et al. The Large Enriched Germanium Experiment for Neutrinoless Double Beta Decay (LEGEND). *AIP Conference Procs.* , 1894(1):020027, 2017.

[65] K. Alfonso et al. Search for Neutrinoless Double-Beta Decay of ^{130}Te with CUORE-0. *Phys. Rev. Lett.* , 115(10):102502, 2015.

[66] O. Azzolini et al. Final result of CUPID-0 phase-I in the search for the ^{82}Se Neutrinoless Double Beta Decay. *Phys. Rev. Lett.* , 123(3):032501, 2019.

[67] G. Anton et al. Search for Neutrinoless Double-Beta Decay with the Complete EXO-200 Dataset. 2019.

[68] S. Kharusi et al. nEXO Pre-Conceptual Design Report. 2018.

[69] C. Chambers et al. Imaging individual barium atoms in solid xenon for barium tagging in nexo. *Nature*, 569(7755):203–207, 2019.

[70] J. J. Gomez-Cadenas. Status and prospects of the NEXT experiment for neutrinoless double beta decay searches. 2019.

[71] A. Gando et al. Search for Majorana Neutrinos near the Inverted Mass Hierarchy Region with KamLAND-Zen. *Phys. Rev. Lett.* , 117(8):082503, 2016. [Addendum: Phys. Rev. Lett.117,no.10,109903(2016)].

[72] S. Andringa et al. Current Status and Future Prospects of the SNO+ Experiment. *Adv. High Energy Phys.*, 2016:6194250, 2016.

[73] M. Agostini et al. Background-free search for neutrinoless double-β decay of ^{76}Ge with Gerda. *Nature*, 544:47, April 2017.

[74] A. Caldwell, D. Kollár, and K. Kröninger. BAT - the Bayesian Analysis Toolkit. *J. Phys.: Conf. Ser.* , 219(3):032013, Apr 2010.

[75] C. Hu. *Modern Semiconductor Devices for Integrated Circuits*. 01 2010.

[76] Glenn F. Knoll. *Radiation detection and measurement*. Wiley, 4th ed edition, 2010.

[77] H. V. Klapdor-Kleingrothaus and I. V. Krivosheina. The evidence for the observation of $0\nu\beta\beta$ decay: The identification of $0\nu\beta\beta$ events from the full spectra. *Mod. Phys. Lett.* **A**, 21(20):1547–1566, 2006.

[78] K.-H. Ackermann et al. The Gerda experiment for the search of $0\nu\beta\beta$ decay in ^{76}Ge. *Eur. Phys. J.* **C**, 73:2330, 2013.

[79] G. Heusser. Low-Radioactivity Background Techniques. *Ann. Rev. Nucl. Part. Sci.* , 45(1):543–590, 1995.

[80] M. Agostini et al. Upgrade for Phase II of the Gerda experiment. *Eur. Phys. J.* **C**, 78(5):388, May 2018.

[81] K. Freund. *Muonic Background in the Gerda $0\nu\beta\beta$ Experiment*. PhD thesis, U. Tübingen, 2014.

[82] K. Freund et al. The performance of the Muon Veto of the Gerda experiment. *Eur. Phys. J.* **C**, 76(5):298, May 2016.

[83] H. V. Klapdor-Kleingrothaus et al. Latest results from the Heidelberg-Moscow double beta decay experiment. *Eur. Phys. J.* **A**, 12:147–154, 2001.

[84] C. E. Aalseth et al. Igex ^{76}Ge neutrinoless double-beta decay experiment: Prospects for next generation experiments. *Phys. Rev. D* , 65:092007, May 2002.

[85] M. Agostini et al. Production, characterization and operation of ^{76}Ge enriched BEGe detectors in Gerda. *Eur. Phys. J.* **C**, 75:39, 2015.

[86] Z. He. Review of the Shockley–Ramo theorem and its application in semiconductor gamma-ray detectors. *Nucl. Instr. Methods* **A**, 463:250–267, 05 2001.

[87] M. Agostini et al. Characterization of 30 ^{76}Ge enriched Broad Energy Ge detectors for GERDA Phase II. 2019.

[88] M. Agostini, L. Pandola, and P. Zavarise. Off-line data processing and analysis for the GERDA experiment. *J. Phys.: Conf. Ser.* , 368:012047, jun 2012.

[89] P. Benetti et al. Measurement of the specific activity of ^{39}Ar in natural argon. *Nucl. Instr. Methods* **A**, 574(1):83 – 88, 2007.

[90] Laboratoire National Henri Becquerel. Recommended data. http://www.nucleide.org/DDEP_WG/DDEPdata.htm.

[91] L. Pandola et al. Monte Carlo evaluation of the muon-induced background in the Gerda double beta decay experiment. *Nucl. Instr. Methods* **A**, 570:149–158, 2007.

[92] L. Vanhoefer. *Limitations of rare event HPGe experiments due to neutron induced backgrounds*. PhD thesis, Max Planck Institut für Physik, München, 2018.

[93] A. Wegmann. *Characterization of the liquid argon veto of the Gerda experiment and its application for the measurement of the ^{76}Ge half-life*. PhD thesis, U. Heidelberg, 2017.

[94] V. Wagner. *Pulse Shape Analysis for the Gerda Experiment to Set a New Limit on the Half-life of $0\nu\beta\beta$ Decay of ^{76}Ge*. PhD thesis, U. Heidelberg, 2017.

[95] A. Kirsch. *Search for the neutrinoless double β-decay in* GERDA *Phase I using a Pulse Shape Discrimination technique*. PhD thesis, U. Heidelberg, 2014.

[96] B. Raz and J. Jortner. Wannier type impurity excited states in liquid rare gases. *Chem. Phys. Lett.*, 4(8):511 – 514, 1970.

[97] M. Agostini et al. LArGe: active background suppression using argon scintillation for the Gerda $0\nu\beta\beta$-experiment. *Eur. Phys. J.* **C**, 75(10):506, Oct 2015.

[98] P. Peiffer et al. Pulse shape analysis of scintillation signals from pure and xenon-doped liquid argon for radioactive background identification. *J. Instrum.* , 3:P08007, 2008.

[99] M. Agostini et al. Pulse shape discrimination for Gerda Phase I data. *Eur. Phys. J.* **C**, 73(10):2583, Oct 2013.

[100] A. Hocker et al. TMVA - Toolkit for Multivariate Data Analysis. 2007.

[101] M. Agostini et al. Measurement of the half-life of the two-neutrino double beta decay of ^{76}Ge with the GERDA experiment. *J. Phys. G: Nucl. Part. Phys.* , 40(3):035110, feb 2013.

[102] L. Pertoldi, A.-K. Schuetz, B. Schneider, K. von Sturm, and T. Wester. Monte carlo simulations and probability density functions for GERDA Phase II background model. *GERDA Scientific Technical Reports*, GSTR-18-009, 2018.

[103] M. Boswell et al. Mage-a Geant4-Based Monte Carlo Application Framework for Low-Background Germanium Experiments. *IEEE Trans. Nucl. Sci.*, 58(3):1212–1220, June 2011.

[104] M. Agostini et al. Modeling of GERDA Phase II data. supmitted to J. High Energ. Phys., arXiv:1909.02522.

[105] W. Maneschg, M. Salathe, and E. Andreotti. Density of germanium: predictions and measurements. *GERDA Scientific Technical Reports*, GSTR-13-008, 2013.

[106] I. Barabanov et al. Shielding of the Gerda experiment against external gamma background. *Nucl. Instr. Methods* **A**, 606(3):790 – 794, 2009.

[107] L. Baudis et al. Production and characterization of228th calibration sources with low neutron emission for GERDA. *J. Instrum.* , 10(12):P12005–P12005, dec 2015.

[108] N. Becerici-Schmidt. *Results on Neutrinoless Double Beta Decay Search in Gerda: Background Modeling and Limit Setting*. PhD thesis, Max Planck Institut für Physik, München, Jul 2014.

[109] S. Hemmer. *Study of Lepton Number Conserving and Non-Conserving Processes Using GERDA Phase I Data*. PhD thesis, Dipartimento di Fisica e Astronomia dell'Universit'a di Padova and INFN Padova, 2014.

[110] K. von Sturm. High energy background modeling - Phase II. *GERDA Scientific Technical Reports*, GSTR-18-015, 2018.

[111] T. Wester. K-model. *GERDA Scientific Technical Reports*, GSTR-18-014, 2018.

[112] F. Beaujean et al. p-values for model evaluation. *Phys. Rev. D* , 83:012004, Jan 2011.

[113] L. Lista. *Statistical Methods for Data Analysis in Particle Physics*. Lecture Notes in Physics. Springer International Publishing, 2015.

[114] A. Caldwell, D. Kollár, and K. Kröninger. BAT - The Bayesian analysis toolkit. *Computer Physics Communications*, 180(11):2197 – 2209, 2009.

[115] M. Agostini. *Signal and background studies for the search of neutrinoless double beta decay in GERDA*. PhD thesis, Technischen Universität München, April 2013.

[116] A. Lubashevskiy et al. Mitigation of ^{42}ar ^{42}k background for the GERDA Phase II experiment. *Eur. Phys. J.* **C**, 78(1):15, Jan 2018.

[117] M. Agostini et al. Results on $\beta\beta$ decay with emission of two neutrinos or Majorons in ^{76}Ge from GERDA Phase I. *The European Physical Journal C*, 75(9):416, Sep 2015.

[118] O. Ponkratenko, V. Tretyak, and Y. Zdesenko. Event Generator DECAY4 for Simulating Double-Beta Processes and Decays of Radioactive Nuclei. *Phys. Atom. Nucl.* , 63:1282–1287, 07 2000.

[119] M. Agostini et al. Parameters and facts from the analysis dataset of the $0\nu\beta\beta$ decay of Gerda Phase IIc. *GERDA Scientific Technical Reports*, GSTR-18-011, 2018.

[120] A. Vasenko, I. Kirpichnikov, V. Kuznetsov, A. Starostin, A. Dzhanian, et al. New Results in the Itep / Yepi Double Beta Decay Experiment With Enriched Germanium Detector. *Mod. Phys. Lett.*, A5:1299–1306, 1990.

[121] H. Miley, F. Avignone, R. Brodzinski, J. Collar, and J. Reeves. Suggestive evidence for the two-neutrino double-β decay of ^{76}Ge. *Phys. Rev. Lett.* , 65:3092–3095, Dec 1990.

[122] F. Avignone et al. Confirmation of the observation of $2\nu\beta\beta$ decay of ^{76}Ge. *Phys. Lett.* **B**, 256(3):559 – 561, 1991.

[123] F. Avignone. Double-beta decay: Some recent results and developments. *Prog. Part. and Nucl. Phys.* , 32:223 – 245, 1994.

[124] Angel Morales. Review on double beta decay experiments and comparison with theory. *Nucl. Phys. Proc. Suppl.* , 77(1):335 – 345, 1999.

[125] M. Günther et al. Heidelberg-Moscow $\beta\beta$ experiment with^{76}Ge: Full setup with five detectors. *Phys. Rev. D* , 55:54–67, Jan 1997.

[126] C. Dörr and H. V. Klapdor-Kleingrothaus. New Monte-Carlo simulation of the HEIDELBERG-MOSCOW double beta decay experiment. *Nucl. Instr. Methods* **A**, 513(3):596 – 621, 2003.

[127] A. Bakalyarov, A. Balysh, S. Belyaev, V. Lebedev, and S. Zhukov. Results of the experiment on investigation of Germanium-76 double beta decay: Experimental data of Heidelberg-Moscow collaboration November 1995 - August 2001. *Phys. Part. Nucl. Lett.*, 2010:91299, 2008.

[128] B. Pritychenko. Proc. Nuc. Struc. 2008, June 3-6 2008, East Lansing, MI. *Brookhaven National Laboratory Report*, BNL-91299-2010, 2010.

[129] NNDC. 2β-decay Data Project. *Available from http://www.nndc.bnl.gov/bbdecay*.

[130] A. Barabash and B. Cheremushkinskaya. Precise half-life values for two-neutrino double-β decay. *Phys. Rev. C* , 81, 03 2010.

[131] A. Barabash. Average and recommended half-life values for two-neutrino double beta decay. *Nucl. Phys.* **A**, 935:52 – 64, 2015.

[132] M. Agostini et al. Limits on uranium and thorium bulk content in gerda phase i detectors. *Astroparticle Physics*, 91, 11 2016.

[133] R. B. Firestone and V. S. Shirley. *Table of Isotopes*. 1996.

Acknowledgements

Such a thesis is never the work of a single person. With this in mind, I want to thank all the people who made it possible for me to write my dissertation. First of all, I want to express my gratitude to my supervisors Peter Graymayr and Josef Jochum who guided me through the development of this thesis with their subject matter expertise and wide range of scientific experience.

My personal thank goes to all the members of the GERDA collaboration which set up such an exciting, unique and incredible experiment. I would like to acknowledge Bernhard Schwingenheuer for his assistance and suggestions. Our constructive discussions inspired many arguments in my dissertation. I appreciate the background modeling group including Luigi Pertoldi, Katharina von Sturm, and Thomas Wester. A special thanks is dedicated to Luigi for refurbishing and prettying-up all our plots. And to Matteo for providing us valuable assistance and input as analysis coordinator.

Another word of thanks is addressed to Tobias Lachenmaier for all the answers he provided to my questions concerning Statistics and Neutrino Physics and, last but not least, for teaching me self-management skills during the preparation of exercises despite stressful and busy weeks.

A special thanks to the members of the AG Jochum and Lachenmaier for the inspiring working atmosphere, including Marc Breisch, David Blum, Jessica Eck, Alexander Göggelmann, Khushbakht Habib, Tobias Heinz, Büsra Heß, Katharina Kilgus, Axel Müller, Lukas Rauscher, Vincent Schipperges, Christian Strandhagen, Tobias Sterr, Alex Tietzsch, Andreas Zschocke and my former colleagues Gerhard Deuter, Raphael Falkenstein, Kai Freund, Alexander Hegai, Markus Röhrling, Klemens Rottler, Christopher Schmitt, Stefan Scholl and Martin Uffinger. And to many more people at the Physics Institute of the University of Tübingen. Not to forget, Gaby Behring and Torsten Hehl.

I would like to say thank you to all the proof-readers of my dissertation for their technical support, editing and correcting. In saying this, I would like to stress the incredible efforts of Christian Strandhagen.

For support in myriad ways - Le Gentlemens Club: Tobias Heinz, Marc Breisch, Katja Wuster, Büsra Heß, Lukas Wolz, Lukas Rauscher and Tobias Sterr. The past few years have been no less stressful for them. Nevertheless, they gave me all possible support in the form of coffee, open ears and expedient discussions at any time. You have my very special thanks.

I would like to take the opportunity to give warm thanks to my wonderful family: Mama, Papa, Sabrina, and Juliane, you're the balance and the foundation of my life.

And loving thanks to Matthias. During the long days of writing this dissertation, you fed me. Literally and metaphorically. You saved me from hunger and fatigue. You animated and centered me at all the right moments. This dissertation is dedicated to you.